JOINT MOVEMENT MODELS FOR ANGUS L. MACDONALD SUSPENSION
BRIDGE

by

Philip G. Vickers

Submitted in partial fulfilment of the requirements
for the degree of Master of Applied Science

at

Dalhousie University
Halifax, Nova Scotia
September 2014

Table of Contents

List of Tables

List of Figures

Abstract

The Angus L. Macdonald (ALM) Suspension Bridge spans the Halifax Harbour linking the Halifax Peninsula with Dartmouth, Nova Scotia. The ALM was first opened in 1955 and currently accommodates approximately 50,000 crossings on a typical workday. As with any aging infrastructure the need for maintenance and rehabilitation exists, which requires adequate engineering knowledge of the structure. This study will investigate the expansion joint movement at the main tower locations of the bridge. Halifax Harbour Bridges (HHB) wishes to understand the range of the expansion joint movement and thereby minimize the cost of future joints. There is uncertainty as to whether the Canadian Highway Bridge Design Code (CHBDC CAN/CSA S6-06) over estimates the required range of movement of the expansion joints for long span structures.

In late June of 2012, a field-monitoring program was developed to monitor the joint movement. The deck at each tower of the ALM was instrumented with displacement sensors to measure and record longitudinal movement of the main and side spans with respect to the main towers. Weather conditions were also recorded by a weather station located at the midpoint of the bridge.

In order to better understand the actual in-service movement ranges, numerical models were developed to characterize movements at the expansion joint locations for variations in thermal, wind, and traffic loads. Analysis of the collected monitoring data was completed to identify correlations between movement and different loading variations. Thermal variations were found to have the largest effect on expansion joint movement. Wind was also found to have a significant effect on expansion joint movement while traffic loads were found to have the least impact on movement.

Extreme environmental conditions were fed into the numerical models to determine extreme movement ranges for thermal, wind, and traffic loads.

List of Abbreviations and Symbols Used

ALM	Angus L. Macdonald Bridge
B&T	Buckland and Taylor Ltd.
BP$_{MS}$	Main Span Bearing Position
BP$_{SS}$	Side Span Bearing Position
CHBDC	Canadian Highway Bridge Design Code
DAL	Dalhousie University
DMT	Dartmouth Main Tower
E.J.G	Expansion Joint Gap
HHB	Halifax Harbour Bridges
HMT	Halifax Main Tower
MS	Main Span
REF	Reference Measurement
RMS	Root Mean Square
RSB	Runyang Suspension Bridge
SHM	Structural Health Monitoring
SS	Side Span

C_{1i} / C_{2i}	Rotational conversion factors	
$f_x(X)$	Probability density function	
G_i	Sensor identification	
n	Number of residual data points in averaged subset	
n_eff	Number of effective independent observations	
N_T	Number of traffic events for the selected period	
R^2	Coefficient of determination	
T	Structural temperature at expansion joint location	(°C)
u_n	Characteristic largest value of X	
v	Wind velocity	(km/hr)
x_i	Residual data	
X_T	Window average subset	

α_n	Inverse measure of the dispersion of X_n	
β_T	Longitudinal movement thermal y-intercept	(mm)
β_W	Plan rotation wind offset	(°)
$\beta_{\theta T}$	Vertical rotation thermal y-intercept	(°)
δ_L	Longitudinal translation	(mm)
δ_T	Longitudinal displacement due to thermal variations	(mm)
θ	Correlation length	
θ_P	Plan rotation	(°)
$\theta_{P,LL}$	Hourly average live load plan rotation	(°)
$\theta_{P,wind}$	Plan rotation due to wind variations	(°)
θ_{PT}	Plan rotation due to thermal variations	(°)
θ_V	Vertical rotation	(°)
$\theta_{V,LL}$	Hourly average live load vertical rotation	(°)
$\theta_{V,max}$	Maximum expected vertical rotation	(°)
θ_{VT}	Vertical rotation due to thermal variations	(°)
λ	Exponential distribution rate parameter	
λ_T	Longitudinal movement thermal coefficient	(mm/°C)
λ_w	Wind direction coefficient	
$\lambda_{\theta T}$	Vertical rotation thermal coefficient	(°/°C)
$\rho(\tau)$	Theoretical correlation model	
τ	Distance between data points	

Acknowledgements

Chapter 1: Introduction

As most of our infrastructure ages over time, the need for maintenance and rehabilitation exists. Maintenance and rehabilitation requires adequate engineering knowledge of the structure in question. Decisions must be made based on the best available information. Traditionally, theoretical and code-based approaches were developed to generate an approximate representation of the structure and generic loading conditions. Code-based approaches can lead to very conservative designs or less than optimal economic designs when an existing structure is to undergo rehabilitation. The use of structural monitoring can aid in the design by developing numerical models that are specific to the individual structure. This can lead to more efficient and economical decisions.

1.1   Project Background

In 2015, the Angus L. Macdonald Bridge, located in Halifax Nova Scotia, is scheduled to under go a complete re-decking project. The project will replace and raise the road deck by approximately 2.1 meters. This will require a new bearing and expansion joint system to be designed to accommodate the new deck. There is uncertainty as to whether the Canadian Highway Bridge Design Code (CHBDC CAN/CSA S6-06) over estimates the required range of movement of the expansion joints for long span structures.

Halifax Harbour Bridges (HHB), owner and operator of the bridge, wishes to minimize the provided range of the expansion joint movement and thereby minimize the cost of the joints. In late June of 2012, a field-monitoring program was developed to monitor the joint movement to obtain a better understanding of the bridge's response to thermal, wind, and traffic load variations at the expansion joint locations. The use of this data will aid in the design of the new systems. Traffic load will be considered as the live load for the purpose of this thesis.

1.2   Objectives

The primary objective of this research was to develop general movement equations that model the deck movement at the expansion joint locations by using structural health monitoring (SHM) data. Three types of movements were monitored: longitudinal translation, vertical rotation, and plan rotation. Three types of loading phenomena were investigated as movement sources: thermal, wind, and live load.   Each movement component has three loading cases, which can be seen below in Table 1.1.

Table 1.1: Break down of loading cases for each movement component

Longitudinal Translation (δ_L)	Vertical Rotation (θ_V)	Plan Rotation (θ_P)
Thermal	Thermal	Thermal
Wind	Wind	Wind
Live Load	Live Load	Live Load

The development of the movement equations consisted of the following four phases:

1. Identify how each movement type responds to variations in thermal, wind, and live load;
2. Characterize the identified movement responses using numerical models;
3. Combine individual movement models to develop general sensor equations that can predict sensor readings from the monitored data knowing environmental conditions;
4. Combine sensor equations to define design equations that can predict movements of the sliding bearing and the expansion joint gap.

Extreme environmental conditions were fed into the design equations to predict extreme movement ranges for each source of movement: thermal, wind, and live load.

1.3 Thesis Layout

The thesis begins with a review of the general history and components that make up todays' modern suspension bridge. Special review of the typically bearing and expansion joint systems will be presented. A review of relevant literature pertaining to the causes of deck movement and how this movement correlates to the behaviour of the expansion joint location will be discussed.

Chapters Three and Four describe the Angus L. Macdonald Suspension Bridge and the main objectives of this research. Chapters Five and Six layout the structural health-monitoring program installed on the bridge and discuss the analysis techniques used in the data processing. Chapters Seven and Eight compare the models to the actual in-field monitoring data and account for any errors within the models. Chapter Nine uses the models created in Chapter Six to determine 75-year extreme movement predictions and Chapter Ten presents the conclusions and recommendations from this study.

Chapter 2: Literature Review

This chapter will explore the relevant literature pertaining to movement of the suspended deck segments of a typical suspension bridge. A brief background of the development of the modern suspension bridge will be presented along with the main components that make up a suspension bridge. Focus will be on the suspended deck system and how it responds to variations in temperature, wind, and live loads. The functions of the bearing system and expansion joints will be explored, as this is the main focus of this research. Finally, a few cases studies related to the monitoring of deck movement will be discussed and the conclusions from these studies will be presented.

2.1 Suspension Bridges

2.1.1 History of Suspension Bridges

The origins of the suspension bridge go back a long way in history. Primitive suspension bridges (Figure 2.1), or simple crossing devices were the forebears to today's modern suspension bridge structures (Harazaki, 2000). Primitive bridges consisted of ropes made of natural vines that were strung across valleys and small waterways. The iron suspension bridge first appeared in Europe in the 17th century and the structural design was developed into the 19th century. A rapid expansion of the central span length took place in the latter half of the 20th century initiated by the invention of steel. Today, the suspension bridge is most suitable type for very long spans (Kawada, 2010). The modern suspension bridge originated in the 19th century when the development of the bridge structure and the production of iron started on a full-scale basis. Jacobs Creek Bridge (Figure 2.2) was the first iron-chain suspension bridge constructed in the United States in 1801 (Kawada, 2010). The bridge's distinguishing feature was the adoption of a truss-stiffening girder, which gave rigidity to the bridge to distribute the load through the hanger ropes and thus prevent excessive deformation of the main cable.
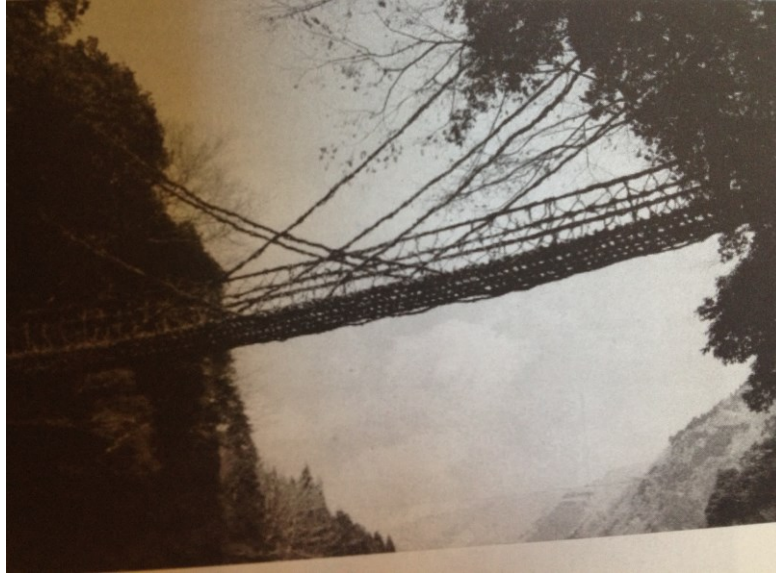
Figure 2.1: Primitive bridge of a native tribe in Asia (Harazaki 2000)
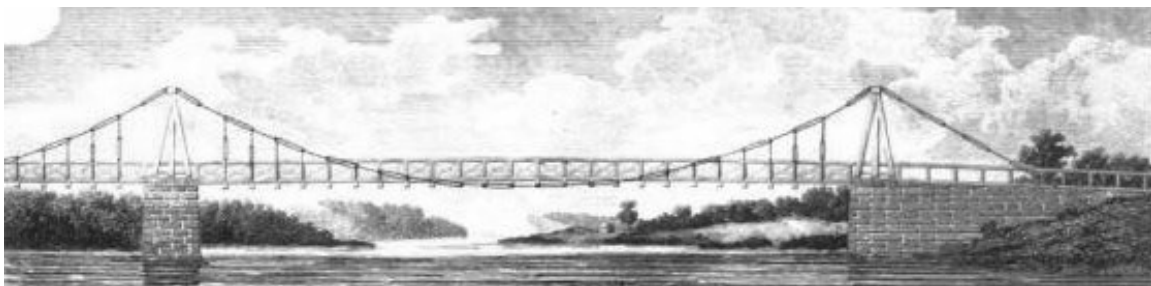
Figure 2.2: Jacobs Creek Bridge, Pennsylvania, United States, 1801 (Kawada 2010)

The Brooklyn Bridge, New York City, was the first suspension bridge to use steel wires, which is hailed as the first modern suspension bridge (Blockley, 2010). At the time, wind-resistant design was not taken into account. It wasn't until the collapse of the Tacoma Narrows Bridge (Figure 2.3) in 1940 that wind-resistant design became curial for suspension bridges. Tacoma Narrows collapsed just four months after completion under winds of 19 m/s (Harazaki, 2000). The failure of the Tacoma Narrows Bridge influenced subsequent bridge engineering worldwide and the science of bridge aerodynamics was born (Kawada, 2010). Today, the Akashi Kaikyō Bridge (Figure 2.4) has the longest central span of any suspension bridge in the world. The central span is 1,991 m and side spans of 960 m each.

Figure 2.3: Tacoma Narrows during collapse, 1940 (Blockley 2010)

Figure 2.4: The Akashi Kaikyō Bridge, Japan (Kawada 2010)

2.1.2 Main Components of Suspension Bridges

The general layout of a modern suspension bridge can be seen in Figure 2.5. The following subsections will detail the main components.
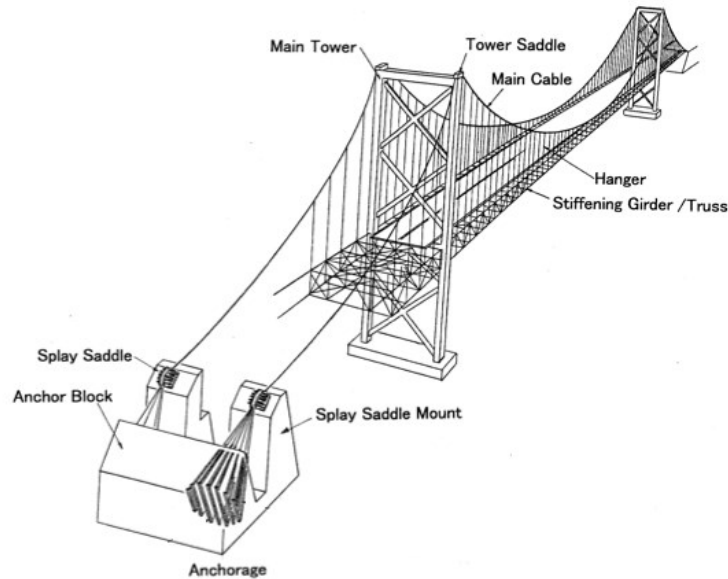
Figure 2.5: Main components of the modern suspension bridge (Harazaki, 2000)

2.1.2.1 Main Towers

The main towers support the main cable at a height sufficient to provide the required main cable sag above the level of the stiffening girder. They also support the end bearings of the stiffening girders. The primary loading on the towers is compression, combined with longitudinal and transverse bending from wind and traffic loading. (ICE, 2008) The leg of the tower's cross-section may be T-shaped, rectangular, or cross-shaped. The multi cell made up of small box sections has been used for some time, however single cells have become noticeable in more recent suspension bridges (Harazaki, 2000). Cable saddles (Figure 2.6) sit atop the main towers where the main cable is supported. They transfer load from the main cable to the supporting tower structure through a longitudinally curved trough. The main cable is deflected through the trough to the required angle (ICE, 2008).

Figure 2.6: Cable saddles atop main towers, Williamsburg Bridge (ICE 2008)

2.1.2.2 Main Cable

The main cables are the primary structural element of a suspension bridge. The basic element for all cables is high-strength steel wire having a diameter between 5 and 5.5 mm. Wire of this size is generally produced with a tensile strength of 1570 N/mm^2 but higher-strength wire with a minimum of 1800 N/mm^2 is becoming more popular for longer span structures. This higher-strength wire was used for the cables of Akashi Kaikyō Bridge. The high tensile strength is obtained by cold drawing through a series of dies to reduce its diameter from the initial rod size down to the final wire size. This produced a wire that has consistently accurate dimensions, and a smooth flaw free surface (ICE, 2008).

For convenience in construction, individual wires are divided into groups called strands with each strand containing between 200 to 550 wires. Strands are grouped together in a hexagonal shape and the strands are squeezed together to form a single compact mass of wires with a nominally circular cross section. It is essential to protect the main cables from corrosion. Corrosion is prevented by using galvanized zinc wires, wrapping the main cable with tightly spaced galvanized steel wire, and a final series of paint coats.

2.1.2.3 Anchorages

The safety of a suspension bridge depends upon the security of the anchorages (Steinman, 1957). The anchorages secure the ends of the main cables and transfer their force into the ground. At the anchorages a splay saddle separates the main cable into its individual strands, deviating them both laterally and vertically to their individual connection points within the anchorage. The direction of the cable forces is predominantly horizontal with a smaller upward component (ICE, 2008). The individual strands of the main cable are anchored into sound unfaulted rock so that sufficient mass can be mobilized to resist the cable force with the required degree of safety. In most cases sufficient rock is not available for anchorage so a gravity anchorage is required. Where the ground is suitable, the anchorage can be partially or wholly embedded in the ground. The development of the necessary resistance against sliding by base friction requires the anchorage to have a very large mass.

2.1.2.4 Suspended Deck

The primary function of the suspended deck is to provide a stable and level traffic platform with acceptable deflection characteristics. The deck is supported from vertical hangers attached to the main cables. The required stiffness of the deck is effectively related to the hanger spacing and as this is a small proportion of the span length, the contribution of the deck bending stiffness to the overall stiffness of the structure is generally insignificant in comparison to the cable system (ICE, 2008). In design, it is optimal to minimize the self-weight of the suspended deck, as it will produce savings in other element of the cable system (hangers, towers and anchorages).

In order to provide sufficient flexural and torsional stiffness to the suspended deck, vertical truss girders are used. Their function is to equalize deflections due to concentrated live loads and distributes these loads to the main cable. These truss girders run along the length of the suspended span and are positioned at or near deck edges. The optimum arrangement of this layout is to have the stiffening trusses below deck level so that the deck structure can provide the upper bracing function by acting as a horizontal web plate between the truss upper chord members (ICE, 2008). Transverse truss arrangements provide lateral bracing of the deck system.

2.2   Deck Movement

Motions of the bridge deck initiate from thermal changes, wind forces, live loads, and the physical properties of the materials that make up the bridge (Pugsley, 1968). The following subsections will explore the different mechanisms of movement and how modern suspension bridges accommodate this movement.

2.2.1   Temperature Effects

Bridge decks are subjected to daily and seasonal environmental temperature effects induced by solar radiation and ambient air temperature. Variation in temperature in bridge components significantly influences the overall deflection and deformation of the bridge. The temperature effects on a structure are dependent on the temperature distribution, structural configuration and boundary conditions, and material mechanical properties of the structure. The local climatic conditions, structural orientation, structural configuration and material thermal properties will affect the structural temperature distribution. Uniform changes in temperature in the suspended deck's cross-section cause a horizontal translation (Ramburger, 2002). The main suspension system is self-accommodating to temperature effects as the cables are free to adjust themselves by alterations in sag of the bridge deck (Banks, 1941). This results in a change in vertical rotation at the end of the spans due to the alterations in sag of the bridge deck.

Traction rods are typically used at mid span to transfer traction forces in the suspended structure into the main cables. High tensile rods are adjustable by turnbuckles to apply the appropriate traction force. These rods prevent rigid body movements of the suspended span longitudinally and cause the expansion and contraction of the span to take place equally at both ends (Banks, 1941).

2.2.2   Wind Effects

When a long span suspension bridge is built in a wind prone region, wind environment around and wind effects on the bridge must be monitored to ensure the functionality and

safety of the bridge in high winds (Xu, 2012). The effect of wind loading causes the suspended spans to rotate laterally out of plane. Wind loads cause rotation of the end of floor beams resulting in the leeward truss-ends of adjacent spans to approach each other while the windward ends retreat from one another (Banks, 1941). To prevent excessive stress at the main tower locations, provisions must be made to accommodate this movement.

2.2.3 Live Load Effects

Live load (traffic) causes bending of the suspended bridge deck, which results in rotational movement. As the suspended deck bends under live loading the bottom chords of the stiffening truss extend, resulting in additional translational movements (ICE, 2008). The amount of deflection depends on the amount and the loading pattern of traffic as well as the relative stiffness of the suspended deck.

2.2.4 Bearings

In early bridge construction, movement of the deck was not considered as they were built of stones, bricks or timber. Elongation and shortening occurred in these bridges however the temperature gradients were small due to the high mass of stone resulting in minimal expansion and contraction. Timber bridges were typically small and had natural joints within the members (Ramberger, 2002).

In the modern age it is necessary to design for changes in the long horizontal length of the truss and deck system of each span. The angular end movements, both lateral and vertical must be accounted for as well (Banks, 1941). The role of bearings is to transfer the bearing reaction from the superstructure to the substructure, fulfilling the design requirements concerning forces, displacements and rotations. The bearings must accommodate the displacements and rotations required with very low resistance during the entire lifetime. Bearings must be able to withstand external forces, thermal actions, air moisture changes and weather conditions (Ramberger, 2002). If for any reason the

bearing movement is impaired, there is a danger of damage to the suspended deck and main tower (Ryall, 2010).

Bridge bearings are of two general types: expansion and fixed. Bearings can be fixed in the longitudinal and transverse directions, fixed in one direction and expansion in the other or expansion in both directions. Expansion bearings provide rotational movements of the girders or truss system, as well as longitudinal expansion and contraction of the bridge spans. If an expansion bearing develops a large resistance to the longitudinal movement due to corrosion or other causes, this frictional force within the span could become larger than its original design load which could cause potential damage to the structure. The function of a fixed bearing is to allow rotation at the supports but prevent the superstructure from moving longitudinally off the substructure. Table 2.1 describes the common bearing types, including the possible bearing forces and displacements. Figure 2.7 illustrates the common bearing types (Ramberger, 2002).

Table 2.1: Common bearing types

Function	Common Name
All translation fixed, Rotation all around	Pot bearing; Fixed elastomeric bearing; Spherical Bearing
Horizontal movement in one direction, Rotation all around	Sliding bearing; Pot sliding bearing; Elastomeric bearing; Spherical Sliding Bearing
Horizontal movement in all directions, Rotation all around	Free point rocker bearing; Free pot sliding bearing; Free elastomeric bearing; Link bearing with universal joints
All translation fixed, Rotation about one axis	Line rocker bearing; Leaf bearing
Horizontal movement in one direction, Rotation about one axis	Roller bearing; Link bearing; Constant line rocker sliding bearing
Horizontal movement in all directions, Rotation about one axis	Free rocker sliding bearing; Free roller bearing; Free link bearing
All horizontal translation fixed, Rotation all around	Horizontal force bearing
Horizontal movement in one direction, Rotation all around	Guide Bearing
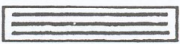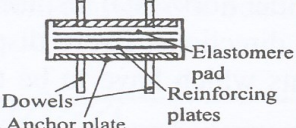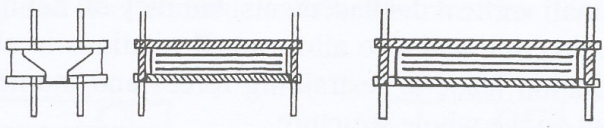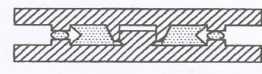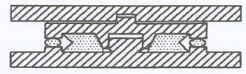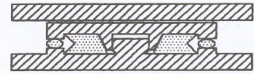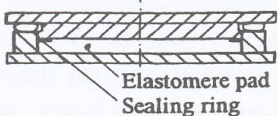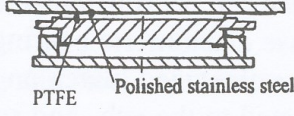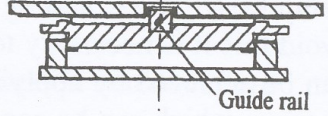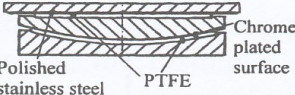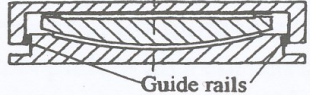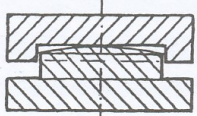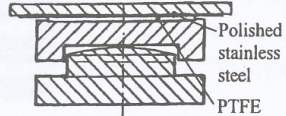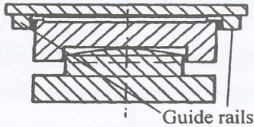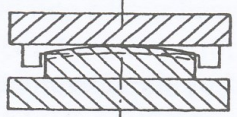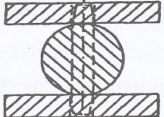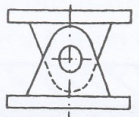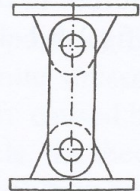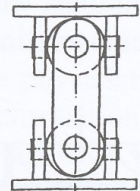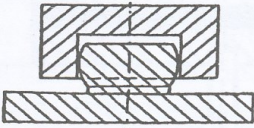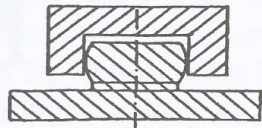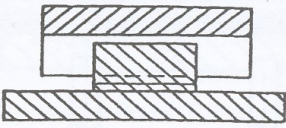
		Standard type	Combinations	
Bearing	Elastomeric	Reinforced elastomeric bearing	Elastomeric bearing with fixing device	
		Anchored elast. bearing Elastomere pad Dowels Reinforcing plates Anchor plate	all translations fixed	movement in one dir.
	Disc	Fixed bearing	Uni-directional guided	Multi-directional non-guided
	Pot	Pot bearing Elastomere pad Sealing ring	Free pot sliding bearing PTFE Polished stainless steel	Constr. pot sliding bearing Guide rail
	Spherical	Free spherical bearing Chrome plated surface Polished stainless steel PTFE	Fixed spherical bearing	Constr. spherical bearing Guide rails
	Point rocker	Point rocker bearing	Free point rocker bearing Polished stainless steel PTFE	Constr. point rocker bearing Guide rails
	Line rocker	Line rocker bearing	Roller bearing	
	Leaf, Link	Leaf bearing	Link bearing	Link bearing with universal (cardan) joints
	Horiz. force	Horizontal force bearing	Guide bearing	

Figure 2.7: Common bearing types (Ramburger, 2002)

13

2.2.5 Expansion Joints

Traditionally, openings are provided between rigid sections of the superstructure equal to or greater than the anticipated movement. These openings permit the deck to move or rotate freely within limitations to accommodate the anticipated movement. This however results in a discontinuity in the roadway surface of the deck and creates an impaired riding quality.

The function of a bridge deck expansion joint is to accommodate motions that occur in the superstructure and provides a level transition between deck spans. Expansion joints are the most vulnerable parts of the a bridge as they are exposed to direct impact loads from traffic, effects of the environment such as severe temperature changes, UV light from the sun, and salt laden water in the winter months (Ryall, 2010). The joint opening can also act as a path through which damaging materials are deposited, such as road salts, on supporting elements beneath the deck (Ramberger, 2002).

A variety of devices have been incorporated in the design of bridge deck expansion joints to bridge the opening in the deck and to seal the opening. The first expansion joints were built for steel railway bridges. As road traffic loads and speed increased, closing the gaps became necessary for safety reasons, especially at the moveable bearings. Initially, cover plates were used for expansion joints but this became insufficient for longer bridges. Finger joints and sliding plate joints were used for these bridges. All joints mentioned above were not watertight causing the water to run down onto the bearings and to the main towers causing corrosion problems. The first watertight expansion joints were built using steel rails between rubber tubes to absorb the movement and provide protection to the bridge elements below the deck (Ramberger, 2002). Figure 2.8 shows a typical expansion joint using the combination of steel rails and rubber tubes.
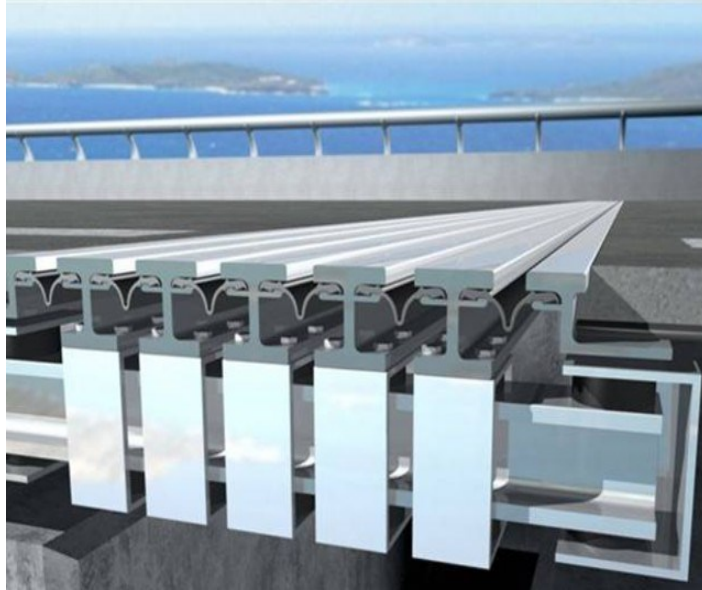
Figure 2.8: Typical suspension bridge expansion joint (Mageba)

2.3   Structural Health Monitoring

Structural health monitoring (SHM) has been used for thousands of years by engineers examining the ongoing performance of their structures in an effort to prolong structures' service lives and ensure public safety. SHM is defined as a non-destructive in-situ structural evaluation method that uses any of several types of sensors, which are attached to, or embedded in, a structure. Theses sensors obtain various types of data (either continuously or periodically), which are then collected, analyzed and stored for future analysis and reference. The data can be used to assess the safety, integrity, strength, or performance of the structure, and to identify damage as its onset. SHM is an important tool in the current and future design, analysis, and maintenance of modern civil engineering structures and systems (ISIS 2004).

2.4 Case Studies

Many studies have been completed in an attempt to accurately model the movement at the expansion joint locations under variations in loads. The three main mechanisms discussed in the previous section, thermal, wind and live load, are the main focus of research. The following subsections will briefly detail a few studies and their conclusions that are relevant to the research to be presented in later chapters.

2.4.1 SHM of Runyang Suspension Bridge

Miao et al. (2013) conducted a study on the Runyang Suspension Bridge (RSB), a single-span steel suspension bridge that crosses the Yangtze River. The bridge is a suspension bridge with a main span of 1,490 m, which can be seen in Figure 2.9. At the time of opening in 2005, RSB was the longest suspension bridge in China and the third longest in the world. To get a comprehensive understanding of the performance of RSB during its service life, a SHM system was installed to real-time monitor the structural responses, environmental conditions and mobile loads.

Figure 2.9: Runyang Suspension Bridge (Miao et al. 2013)

The study of the variations in the expansion joint displacements was presented as a function of temperature, traffic loadings and wind speed based on which simple regression models were established and the dominant environmental factors were decided. Displacement sensors were used to measure displacements of two expansion joints located at the north and south abutments at the level of the bridge. A total of 130-

days of data were used for analysis, which covered measurements from January to June 2006. The multiple linear regression models were obtained to describe the correlation between the expansion joint displacements and the dominant environmental factors. The authors only considered longitudinal displacements and ignored rotations.

The monitored displacements and temperatures were averaged daily to exclude the effects of traffic and wind on the displacements. A linear regression analysis was performed to fit to the averaged daily data. The expression of the linear regression function of the displacement versus temperature can be seen in Table 2.2.

Before measured displacements were used for correlation analysis of traffic-displacement and wind-displacement, the temperature effect on the measured displacements was removed. An accelerometer located at mid span was used to represent the intensity of the bridge's traffic. The root mean square (RMS) of the vertical acceleration responses showed that the larger the acceleration RMS is, the greater the traffic intensity is. Data points for traffic analysis were selected when the wind speed was less than 2 m/s in order to minimize the effect of wind. The expression of the linear regression function of the displacement versus traffic can be seen in Table 2.2.

Similarly, the traffic effect on the measured displacement was removed. Normalizing the displacement due to traffic to a fixed reference acceleration RMS enabled the removal of traffic effects from the displacement measures; therefore only effects of wind should remain. A linear regression analysis was performed to obtain the correlation models between displacement and wind speed. These can also be seen in Table 2.2.

In order to get a quantitative analysis to the effects of the three environmental factors, temperature, wind, and traffic, on the expansion joint displacement, the range of the environmental factors were fed to the regression functions shown in Table 2.2. The results are listed in Table 2.3.

Table 2.2: Linear regression functions between displacements and environmental factors

Abutment	Temperature	Traffic	Wind
North	$d_M = 1.01T - 17.68$ $R^2 = 0.9994$	$d^T = -0.54V + 2.88$ $R^2 = 0.0032$	$d^V = -0.014W + 2.20$ $R^2 = 0.1522$
South	$d_M = 1.02T - 15.50$ $R^2 = 0.9988$	$d^T = -0.67V + 5.62$ $R^2 = 0.0007$	$d^V = -0.007W + 4.72$ $R^2 = 0.2044$

where: d_M = displacement due to temperature

d^T = displacement due to traffic

d^V = displacement due to wind

T = temperature

V = acceleration RMS

W = wind speed

Table 2.3: Displacement ranges for environmental factors

	Temperature (cm)		Traffic (cm)		Wind (cm)	
	North	South	North	South	North	South
Max Value	18.95	21.31	2.84	5.57	2.20	4.72
Min Value	-19.28	-17.11	1.42	3.81	1.99	4.61
Abs (max –min)	38.23	38.42	1.42	1.76	0.21	0.11

Miao et al. were able to conclude the following:

1) Temperature is the critical source causing displacement variability, and there is a linear increase in displacement with the temperature increase.
2) Although the RMS-displacement correlation is weaker than temperature-displacement correlation, it cannot be ignored because it is still notable enough.
3) The correlation between displacement and wind speed is very weak so the effect of wind on displacement can be ignored.

2.4.2 SHM of Ting Kau Bridge

Ni et al. (2007) presented a procedure for condition assessment based on long-term monitoring of expansion joint displacement and bridge temperature. This procedure was applied to the cable-stayed Ting Kau Bridge (Figure 2.10), located in Hong Kong, with the use of one-year of measurement data. The bridge is a 1,177 m long cable-stayed bridge having its longest span at 448 meters.

Figure 2.10: Ting Kau Bridge

The data were used to determine a correlation between longitudinal movement and temperature. Linear trends were fitted to the collected data and were used to compare to design movements calculated for the bridge. Extreme temperatures were computed by fitting a Gumbel distribution to the monitored temperature data and extremes were calculated for the design life of the bridge, 120 years. Ni et al. (2007) concluded three main points:

1) Movements of the expansion joints are highly correlated with the effective temperature. A linear regression model with an appropriate confidence interval can be formulated.
2) Prediction results of the maximum displacement range and the extreme temperature agree well with the design values, justifying the design assumptions
3) Cumulative displacements of the expansion joints are approximately in linear proportion to the service time.

2.4.3 SHM of Tamar Suspension Bridge

Battista et al. (2011) investigated the longitudinal movement of the road deck on Tamar Suspension Bridge (Figure 2.11) in Plymouth, UK over a period of six months. The Tamar Bridge opened in 1961 providing a vital transportation link over the River Tamar between Saltash and Plymouth. The structure was a symmetrical suspension bridge with a main span of 335 m and side spans of 114 m.

The expansion joint of the bridge deck was instrumented with pull-wire type extensometers. Environmental data, such as the temperature, and structural data, such as cable tension, were acquired from other monitoring systems located throughout the bridge. Temperature sensors were located on the main suspension cable and at deck level near the expansion joint. Battista et al. determined that there was a linear correlation between longitudinal movement of the road deck and deck temperature. They also found a relationship between longitudinal movement and main cable temperature, however this relationship was determined to be bi-linear. They concluded that future work needed to be done to compare deck movement to other load variations; wind and live load.

Figure 2.11: Tamar Suspension Bridge (Battista et al. 2011)

2.5 Discussion

In general many researchers find that thermal variations are the main source of longitudinal movement of the bridge deck. Although wind effects have been looked at in previous research, many authors concluded that the effects are minimal and can be ignored. Of the case studies reviewed, no investigation about rotations of the bridge deck at expansion joint locations was completed.

This thesis will explore the correlations between thermal, wind, and live load variations with respect to longitudinal translations and rotations. In the context of this work, live loads will be considered as the traffic loading. Once the correlations between loadings and expansion joint response have been identified, models will be fitted to characterize each type of response, translation or rotation. These models will be compiled into one general equation to characterize the total movement at the expansion joint locations. Finally extreme movement predictions will be determined for a 75-year design life.

Chapter 3: Angus L. Macdonald Suspension Bridge

3.1   Overview

The Macdonald Bridge, Halifax Nova Scotia is the sister bridge to the Lions Gate Bridge in Vancouver, British Columbia. The Macdonald Bridge opened 15 years after the Lions Gate and was designed by the same engineering firm, P.L. Pratley.

The Macdonald Bridge first opened in 1955 providing the first direct link between Dartmouth Nova Scotia and downtown Halifax. It consisted of two lanes with a narrow sidewalk. In 1999, the bridge underwent a major retrofit converting it to a three-lane structure with a pedestrian walkway and bicycle lane (Figure 3.1). Widening the roadway and placing the sidewalk and bike lane outside of the suspended structure accommodated the third lane.

The Macdonald Bridge sees approximately 50,000 crossings on an average workday (HHB). Vehicles over 3,200 kg are not permitted to cross the bridge and must cross the neighbouring A. Murray MacKay Bridge. Transit buses are the largest source of vehicle load on the bridge. The bridge has a reversible centre lane to help accommodate the direction of rush hour traffic flow. In the morning there are two lanes to Halifax and in the afternoon two lanes to Dartmouth.

Figure 3.1: Alternating center lane, Halifax approach span looking towards Dartmouth

3.2 Structural Description

The Macdonald Bridge (Figure 3.2) is approximately 1,346 m in total length, consisting of two approach spans and three suspended spans. The span, which is suspended between the two main towers, is considered the main span (MS) with a length of 441 m. The spans between the approach span and the main tower are considered as the side spans (SS) each having a length of 160 m.
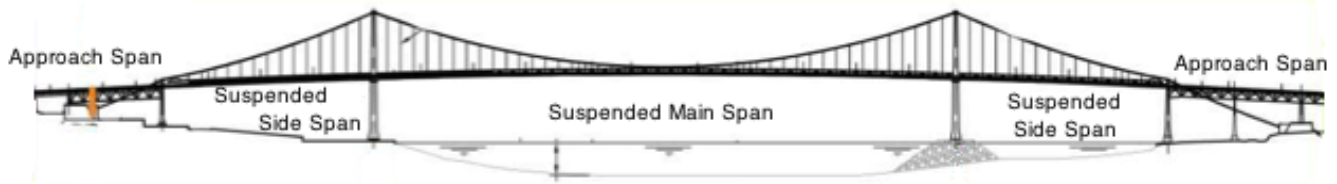
Figure 3.2: Layout of spans (Adapted from B&T)

3.2.1 Main Towers

The Halifax Main Tower (HMT) and the Dartmouth Main Tower (DMT) support the suspended spans of the bridge. These towers are formed from a build up of steel plates and angles constructed in a cruciform. Each leg of the towers consists of a rectangular core flanked by two symmetrical wings. The tower legs are joined by four sets of diagonal bracing. The bracing is continuous except for the portal opening where the roadway passes. Three visible cross struts are located at the top and bottom of each tower, and over the roadway portal. The tops of the main towers contain the main cable saddles, approximately 99 m above sea level. Figure 3.3 shows the HMT looking from Halifax.

Figure 3.3: Halifax Main Tower

3.2.2 Cables

The main cables of the Macdonald Bridge are composed of 61 strands of 37 mm diameter galvanized wire, laid in a hexagonal form (Figure 3.4). The circular forms of the cables are obtained by using cedar wood as filler and the entire cable in wrapped in 3 mm galvanized annealed soft steel wire. The cable is then painted with several layers. The suspender cables (hangers) consist of 6 galvanized strands twisted together forming a 54 mm diameter cable. These cables pass over the main cables via a custom cast cable band, allowing each hanger to be anchored only at deck level. Figure 3.5 shows the suspender cables connecting to the stiffening trusses.
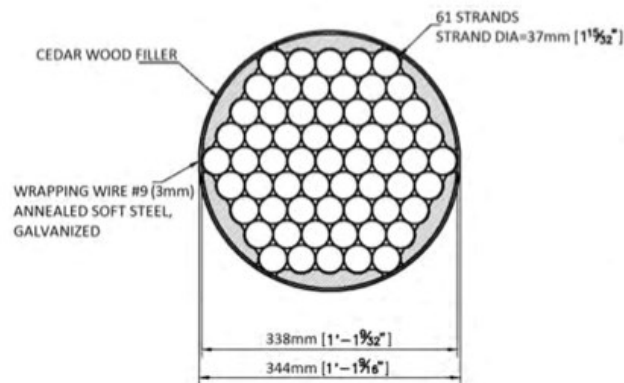
Figure 3.4: Cross-section of main suspension cable (Adapted from B&T)

24
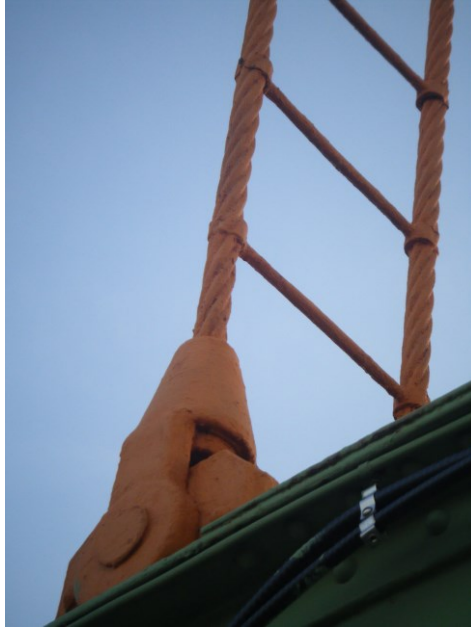
Figure 3.5: Suspender cables connecting south truss to main cable

3.2.3 Deck System

The deck system is composed of a Teegrid, which is supported on longitudinal stringers and transverse floor beams (Figure 3.6). A deck stiffening truss, a "through truss" (Figure 3.7), adds additional stiffens to the deck system on both the north and south face of the bridge. The stiffening truss is comprised of steel angles and flat plate riveted together.
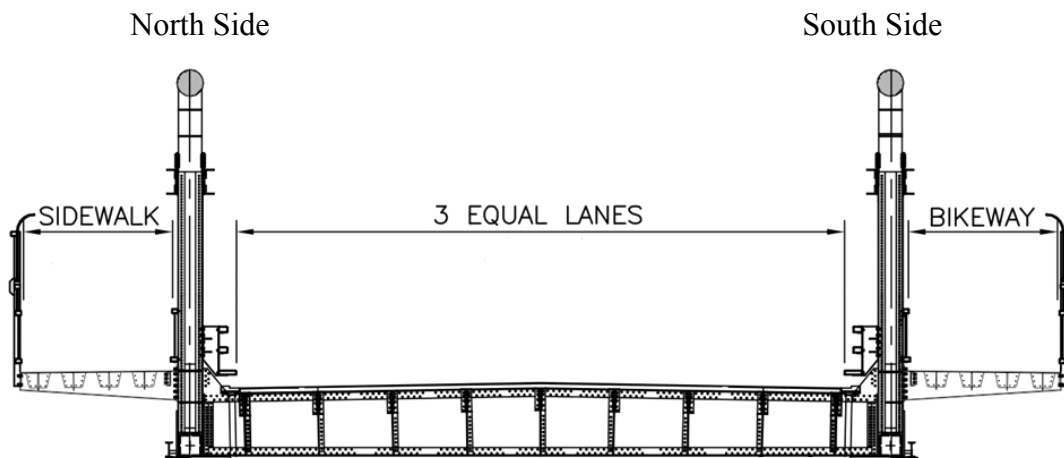
Figure 3.6: Cross-section of deck system looking towards Halifax (Adapted from B&T)

Figure 3.7: Stiffening truss, looking towards Dartmouth from walkway

3.2.4 Bearing System

At the tower locations, longitudinal expansion of the suspended spans is accommodated through the use of a bearing system. Longitudinal movement is only accommodated at the main tower locations; the side spans are fixed to the cable bents therefore all of the longitudinal movement is accommodated at the main towers. Figure 3.8 shows the provided gap between the side span and main span to accommodate longitudinal movement. Traction rods at mid span prevent rigid body movement of the bridge deck causing the total longitudinal movement of the main span to be shared between the two main towers. Figure 3.9 shows the location of the traction rods. The Macdonald Bridge uses a conventional sliding bearing (Figure 3.10) system to handle the longitudinal movement of the suspended deck spans. A horizontal pin is located within the bearing crosshead to allow limited rotation in the vertical direction. Chamfering of the sliding bearings, which can be seen in Figure 3.11, accommodates the necessary plan rotation.
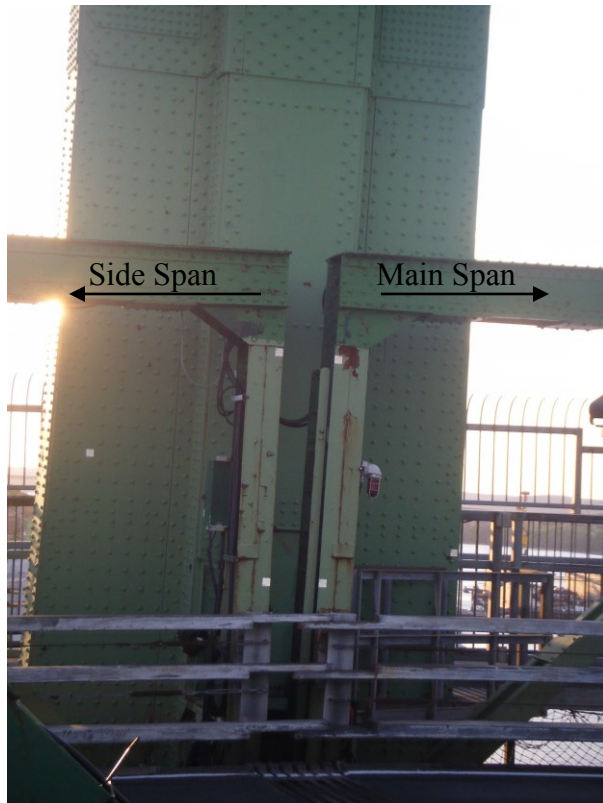
Figure 3.8: Gap between side span and main span stiffening trusses at HMT

Figure 3.9: Tractions rods for Main Span

Figure 3.10: Sliding bearing at DMT MS, South side
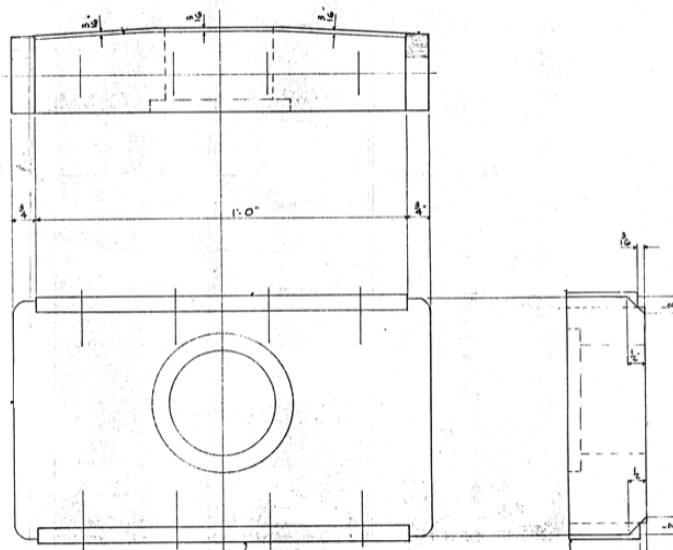
Figure 3.11: Sliding bearing profile with chamfered edges (Adapted from B&T)

3.2.5 Expansion Joint

An expansion joint is located at each main tower to bridge the gap between the side span roadway and the main span roadway. The expansion joints consist of steel rails with rubber tubes in-between to absorb the movements of the spans. Figure 3.12 shows the expansion joint located at HMT.
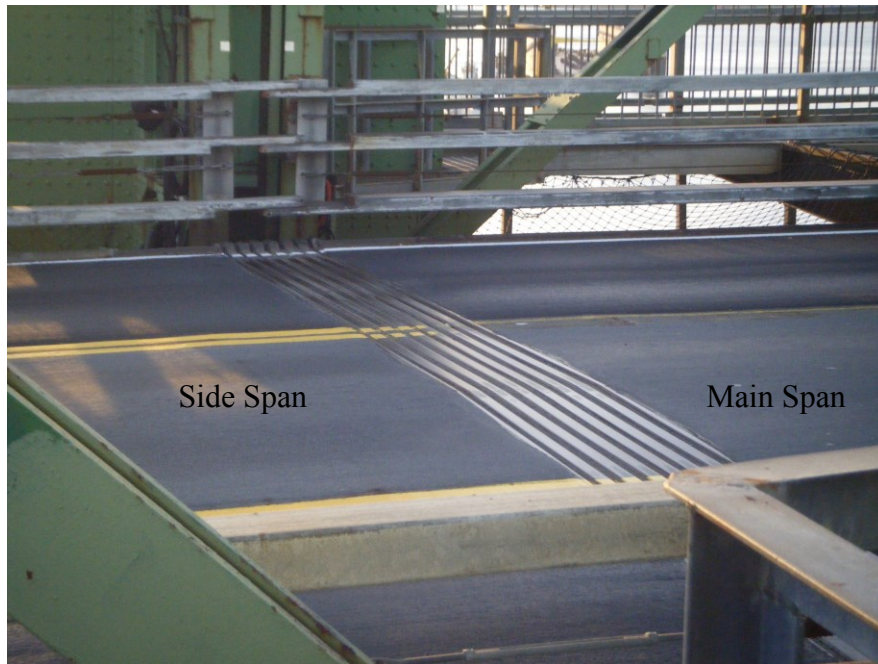
Figure 3.12: Expansion joint at Halifax Main Tower

Chapter 4: Project Objectives

4.1 Structural Health Monitoring

The main focus of this research was to identify the response of the bridge deck at the expansion joint locations due to variations in thermal, wind, and live load. This was done through the use of a structural health-monitoring program. The details of the monitoring program will be discussed in Chapter 5.

4.2 Development of Movement Models

Once it was identified how the bridge deck responses to variations in thermal, wind, and live load, numerical models were developed to characterize these responses. This was done by fitting trends to the monitored data with respect to the three sources of movement. The analysis of collected data and model development will be detailed in Chapter 6.

4.3 Extreme Movement Predictions

Lastly, the extreme range of movement of the bridge deck, which would occur during its design life, was computed. This consisted of design values recommend through design code as well as a statistical analysis of extremes. Extreme movement predictions will be discussed in Chapter 9.

Chapter 5: Macdonald Bridge Expansion Joint Monitoring System

The chapter will discuss the details of the structural health monitoring system. The monitoring system design and installation was not part of this thesis work. A partnership with Halifax Harbour Bridges (HHB) enabled Dalhousie (Dal) to obtain the monitoring data to conduct detailed analytical work. The design and installation of the monitoring system was done by Mageba as per the requirements set by Buckland and Taylor Ltd (B&T). This system was installed in mid June of 2012 and was fully operational by August 2012.

5.1   Instrumentation Layout

In order to determine the response from the expansion joint locations due to variations in thermal, wind, and live load, the expansion joints were instrumented at the main tower locations. Halifax Main Tower (HMT) and Dartmouth Main Tower (DMT) were both instrumented with eight longitudinal wire displacement sensors. At each tower, four sensors were monitoring the main span movement and four sensors monitored the side span movement. The typical sensor layout can be seen in Figure 5.1. Table 5.1 provides the sensor identifications along with its corresponding location. All sensors will be referenced by tower, HMT or DMT, and sensor location, North or South, top or bottom.

Table 5.1: Sensor identification scheme

Sensor ID	Sensor Location
G-1	Main Span South Top
G-2	Main Span South Bottom
G-3	Main Span North Top
G-4	Main Span North Bottom
G-5	Side Span South Top
G-6	Side Span South Bottom
G-7	Side Span North Top
G-8	Side Span North Bottom
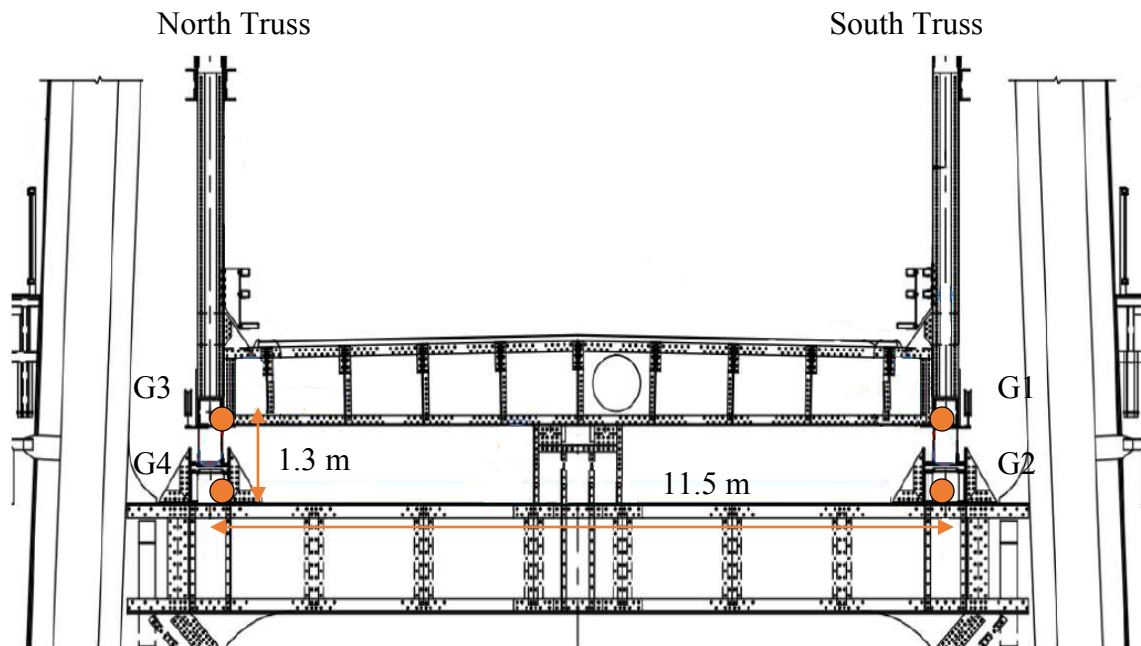
Figure 5.1: Typical sensor layout for all spans

5.2 Wire Displacement Sensors

Wire displacement sensors were used to monitor the longitudinal movement of the suspended spans at the expansion joint locations. In an attempt to provide protection for the sensors from the harsh environment, the wire displacement sensors were equipped with a diverter pulley in order to position the wire downwards. This provided protection against water intrusion but at the same time allowed horizontal displacement measurements. In order to reduce damages to the structure caused by drilling such as corrosion, powerful magnets were used to fix the sensors to the structure. Bottom sensors were attached directly to the bearing crosshead and the wire end was attached to a fixed location on the main tower (Figure 5.2). Similarly the top sensors were attached to the end floor beam of the deck system above the bearing crosshead and the wire end was attached to a fixed location (Figure 5.3). This arrangement allowed longitudinal movement to be monitored as well as rotations to be calculated. As the bearing crosshead moved longitudinally the wire would lengthen or shorten resulting in a change in displacement.

Figure 5.2: Typical bottom wire displacement sensor mounted to bearing crosshead

Figure 5.3: Typical top wire displacement sensor mounted to floor beam of deck system

5.3 Structural Temperature Sensors

Temperature sensors were installed to provide the structural temperature at the expansion joint locations (Figure 5.4). The sensors were attached to bare steel. Each tower had two temperature sensors, one measuring on the north side and one measuring on the south side.

Figure 5.4: Typical structural temperature sensor

5.4   Data Acquisition

Data was acquired and stored using Mageba's provided data software. A monitoring box (Figure 5.5) was located at each tower to collect and store eight longitudinal wire displacement sensors and two structural temperature sensors. All computer components of the monitoring box were contained in water-resistant enclosures. Automatic measurements were taken at a rate of 1 Hz for all sensors. Data was transmitted wirelessly to Mageba's ROBO® CONTROL web interface where authorized users could view data in real time. Data was transmitted every five minutes to the web interface and represented the measurement taken at the five-minute mark. This data was useful to monitor the state of the sensors (failures, computer failures, etc.). For analysis purposes of this thesis, the raw 1 Hz data was used and was downloaded on-site by connecting a field laptop to the monitoring box.

Figure 5.5: Monitoring box and field laptop for manual download

5.5 Sensor Calibration

After installation, all displacement sensors were calibrated to ensure reliability in the recorded data. All wire sensors were attached to three different positions with fixed distances (30 mm, 70 mm, and 110 mm). The measured data was stored and evaluated to compare to the fixed distances. An example calibration plot for DMT MS North Bottom sensor can be seen in Figure 5.6.
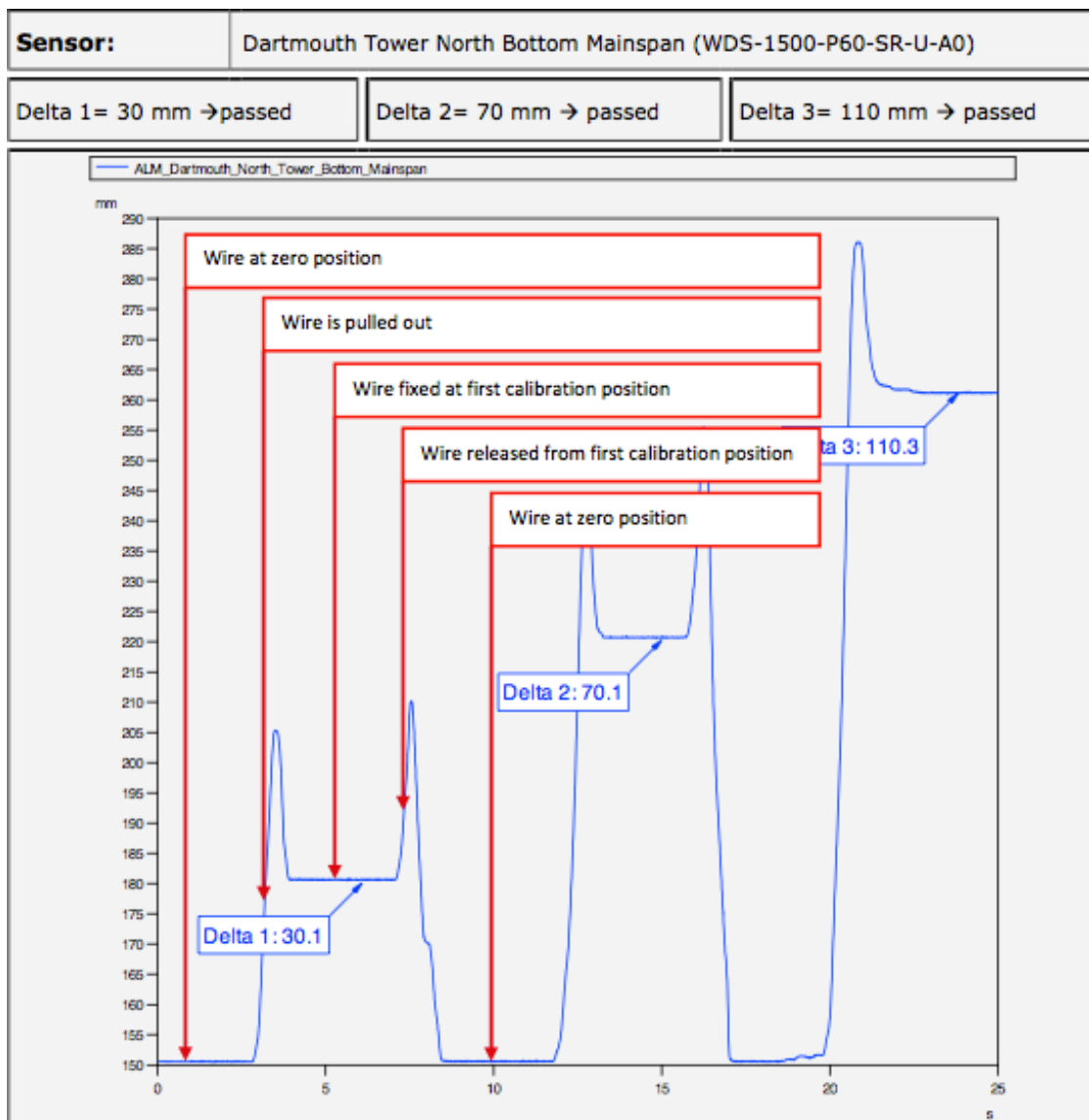
Figure 5.6: Example calibration for DMT MS North Bottom sensor (Mageba)

5.6 Weather Station

Environmental conditions were monitored and provided through HHB's on-site weather station. It was located at mid point of the main span and was mounted above the traffic level to avoid any vehicular interference (Figure 5.7). The weather station provided the following information;

- Air temperature (^{o}C);
- humidity (%);
- average sustained wind speed (km/hr);
- maximum gust (km/hr);
- wind direction corresponding to average sustained wind (degrees);
- pressure (hPa); and
- visibility (m).

Figure 5.7: Halifax Harbour Bridges' Macdonald weather station

For the purpose of this research only air temperature, maximum gust, and average sustained wind speed with its associated wind direction were used. Air temperature was used to compare to structural temperature. The weather station contained a Vaisala WAA151 wind anemometer (Figure 5.8) for the collection of wind speed. Wind speeds were monitored at a frequency of 1 Hz and sustained wind speeds were computed by using 3-second averages. Average sustained wind speed represented the wind speed averaged over a monitored duration, either 8 or 12 minutes. This meant that at the 8-minute mark, the wind speeds were averaged over the previous 8 minutes and a line of data was stored. Then at the next 12-minute mark, the wind speeds were averaged over the previous 12 minutes and another line of data was stored. This pattern is repeated (8, 12, 8, 12, 8…) to produce the averaged sustained wind speed data. Maximum gust represented the largest wind speed magnitude observed during the monitored duration.

Figure 5.8: Vaisala WAA151 wind speed anemometer (Vaisala)

Chapter 6: Data Analysis

6.1 Data Collection

Data analysis was completed for a monitoring period of one year, beginning September 1st, 2012 and ending August 31st, 2013. Table 6.1 and Table 6.2 show the amount of data collected for each sensor throughout the monitoring period as well as the amount of acceptable data. Data was considered acceptable after passing through an outlier detection algorithm. This algorithm will be discussed in Section 6.2.2.

Table 6.1: Collected and acceptable data at Dartmouth Main Tower

Sensor (ID)	Collected Data	Acceptable Data	Percent Acceptable
MS North Top (G1)	31,535,700	31,190,100	99%
MS North Bottom (G2)	31,535,700	31,535,700	100%
MS South Top (G3)	31,535,700	31,535,700	100%
MS South Bottom (G4)	31,535,700	31,233,300	99%
SS North Top (G5)	31,535,700	31,535,700	100%
SS North Bottom (G6)	31,535,700	31,535,700	100%
SS South Top (G7)	31,535,700	31,535,700	100%
SS South Bottom (G8)	31,535,700	31,535,700	100%

Table 6.2: Collected and acceptable data at Halifax Main Tower

Sensor (ID)	Collected Data	Acceptable Data	Percent Acceptable
MS North Top (G1)	31,536,700	31,222,199	99%
MS North Bottom (G2)	31,536,700	30,872,748	98%
MS South Top (G3)	31,536,700	31,222,200	99%
MS South Bottom (G4)	31,536,700	31,222,199	99%
SS North Top (G5)	31,536,700	31,222,200	99%
SS North Bottom (G6)	31,536,700	31,222,200	99%
SS South Top (G7)	31,536,700	31,222,200	99%
SS South Bottom (G8)	31,536,700	30,977,200	98%

Due to the high volume of collected data, it was required to use a piece of computational software that could process the data in a reasonable amount of time. MATLAB® R2012b was chosen for the processing of data. MATLAB® was run on a 64-bit windows operating machine with 12 GB of ram allocated to the software to optimize computational time. A small set of data was first analyzed and the analysis scripts were developed. Once the analysis of the small data set was deemed acceptable the scripts were performed on the full one-year set of data. A flow chart can be seen in Figure 6.1 showing the process used for post-processing of the collected data. Each component of the flow chart will be discussed throughout this chapter.
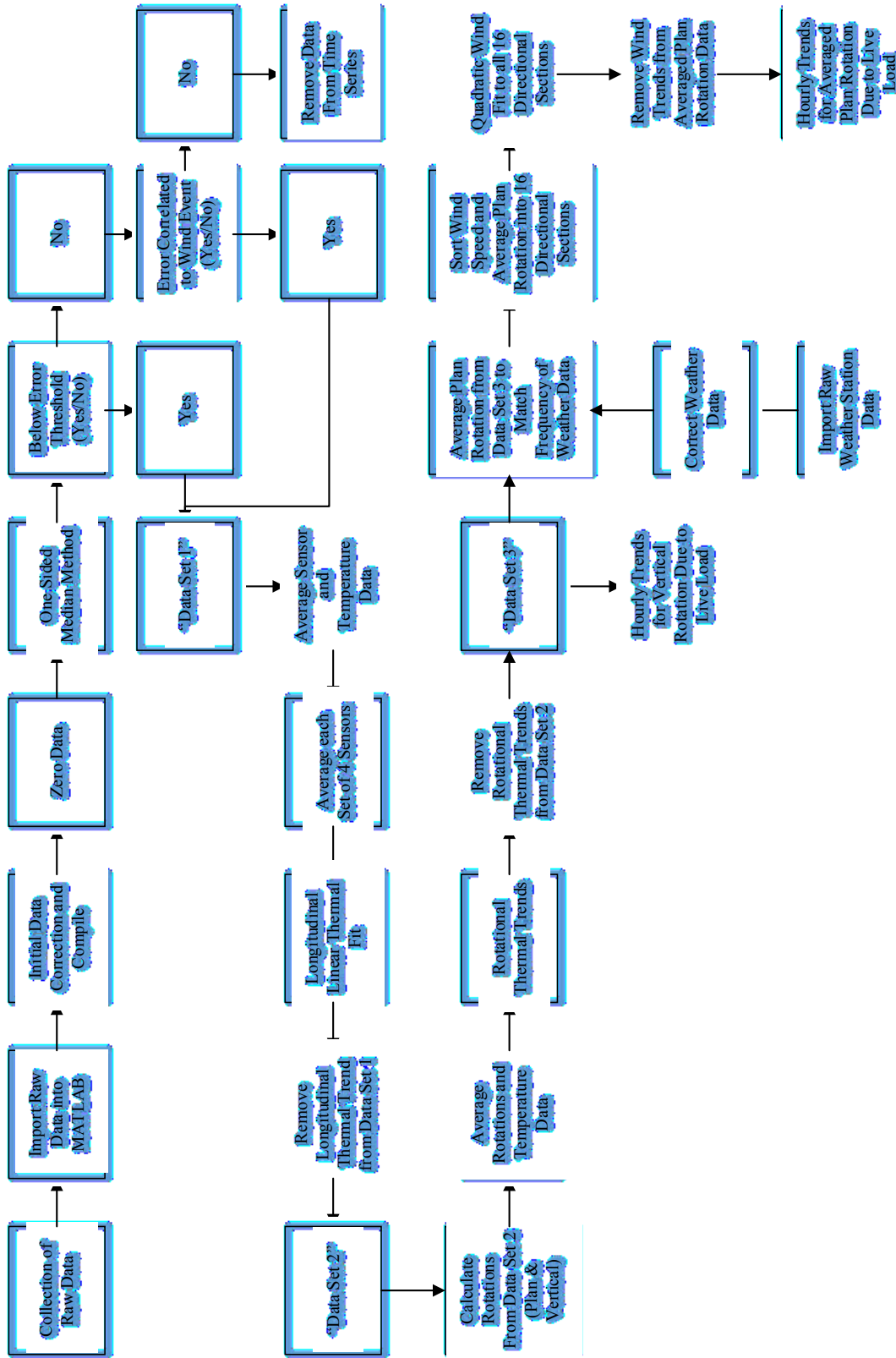
Figure 6.1: Flow chart of analysis process

6.2   Data Correction

Once the raw data had been collected from the on-site data loggers, it was then imported into MATLAB for analysis. Initial data correction was completed to correct label headings, unit conversion for displacement measurements, and compile individual sensor data into monthly and yearly data sets.

6.2.1   Zeroed Reference Point

In order to establish a baseline reference for the displacement sensors, all sensors were zeroed to a known reference point. This gives a reference point that will be used after the analysis has been completed. The reference point represents the distance from the centerline of the main tower to the centerline of the bearing at the time of zeroing. Table 6.3 and Table 6.4 show the measured reference distances as well as time of zeroing and reference wind speed and temperature for DMT and HMT, respectively. All measurements took place on October 23rd, 2012.

Table 6.3: DMT zeroed reference measurements

South Truss	Main Span	9:20 am	336 mm	Wind	Temp
	Side Span	9:20 am	415 mm		
North Truss	Main Span	9:35 am	338 mm	23.1 km/hr	6.86 °C
	Side Span	9:35 am	420 mm		

Table 6.4: HMT zeroed reference measurements

South Truss	Main Span	2:47 pm	324 mm	Wind	Temp
	Side Span	2:47 pm	389 mm		
North Truss	Main Span	2:50 pm	301 mm	25.6 km/hr	7.98 °C
	Side Span	2:50 pm	418 mm		

6.2.2 Outlier Detection Method

Basu and Meckesheimer (2007) define an outlier as a data point in a time series that is significantly different from the rest of the data points. Outliers are unusual observations that affect the analysis of the data and therefore must be treated appropriately. Sudden changes in observations in a time series due to sensor and equipment failures, sensor reconfiguration, and sudden changes in structure behaviours can be causes for erroneous data. In order for any analysis to be performed, one should have the confidence that the analyzed data is correct and free of erroneous data and anomalies.

Basu and Meckesheimer (2007) purposed an outlier detection method named the one-sided median method. This method uses the past data to determine whether a current data point is an outlier or not.

Two parameters for this method must be specified: the window size (k) and the threshold (τ). Window size refers to the number of past points to be used in computing a predicted data point. Window size defines a neighbourhood of points where 2k is the size of the neighbourhood window, starting at $t - 2k$ and ending at $t - 1$. Basu and Meckesheimer's study on the window size (k = 3, 4, 5, 6) shows that the window size does not have a great impact on the performance of the one-sided median method.   The threshold represents a limit where any prediction larger than +/- τ is considered an anomaly. Basu and Meckesheimer found that reducing the threshold value reduced the number of outliers that were not detected, but also increased the number of non-outliers that were mistaken as outliers.

Basu and Meckesheimer define the one-sided median method as:

For a time series $y_t = (y_1, y_2, \dots, y_n)$, define $m_y = $ median $\{y_{t-2k}, \dots, y_{t-1}\}$, and $m_z = $ median $\{z_{t-2k}, \dots, z_{t-1}\}$, where $z_t = y_t - y_{t-1}$. Calculate $m_t = m_y + k*m_z$ where m_t is the predicted value for y_t. Define the prediction error $d_t = y_t - m_t$. If $|d_t| < \tau$, y_t is not an outlier and if $|d_t| > \tau$, y_t is considered an anomaly and must be investigated further.

Before this method could be applied to the collect data, a window width and threshold value needed to be arbitrarily chosen. A window width of k = 3 was chosen. An appropriate threshold value was determined by looking at daily sensor data over the one

year of data. It was determined that all displacement sensors data were deemed acceptable between +/- 3 mm. A threshold of +/- 0.5 °C was chosen for temperature sensors. Figure 6.2 shows a typical monthly plot of the zeroed data for DMT MS north bottom sensor for the month of August 2012. Figure 6.3 shows the corresponding computed one-sided median errors plotted for the same sensor and month. It can be seen that the large spike on August 23rd in the time series of Figure 6.2 corresponds to a large spike on the one-sided median results in Figure 6.3. This large spike was known to be a sensor replacement. Therefore it was determined that the one-sided median method had the capability of identifying sudden jumps in the data. It can also be seen in Figure 6.3 that smaller spikes occur occasionally. If a small spike exceeded the threshold, the data would be matched against the collected weather data and if it was determined that it was indeed windy at the time, the data was considered acceptable. If there was no correlation to a sudden jump in data, the data was removed from the time series. Refer to Appendix A for example plots of the one-sided median method for all spans.
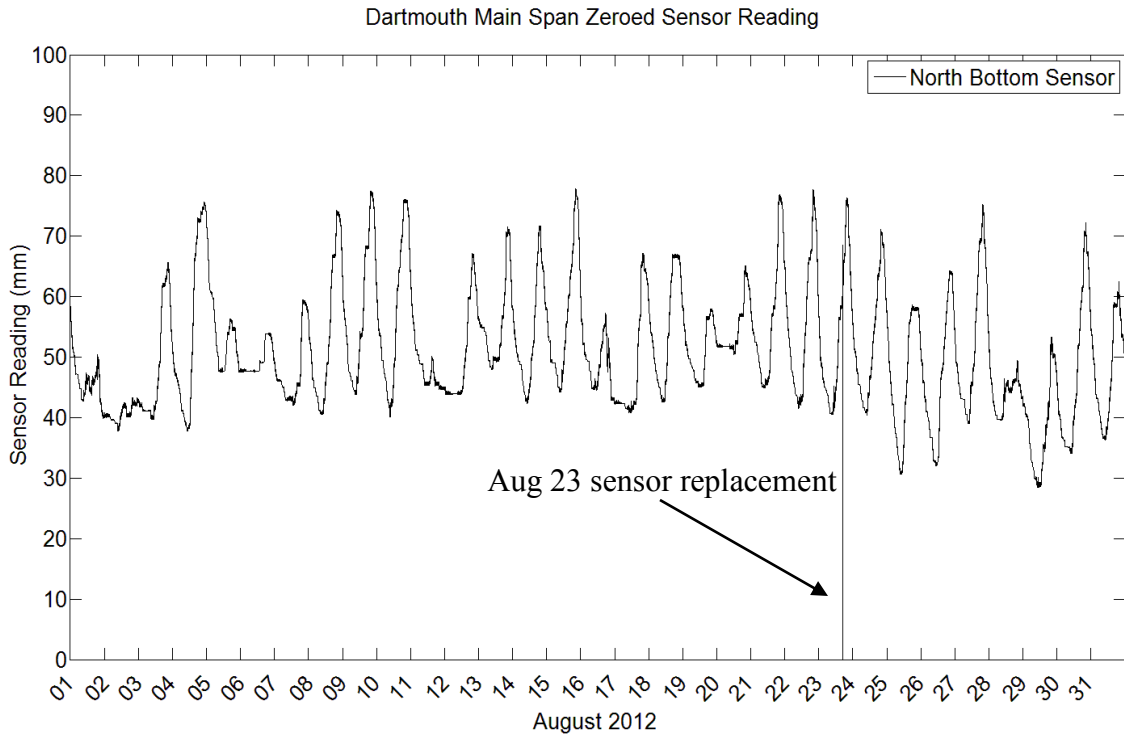
Figure 6.2: North bottom sensor readings for DMT MS, August 2012
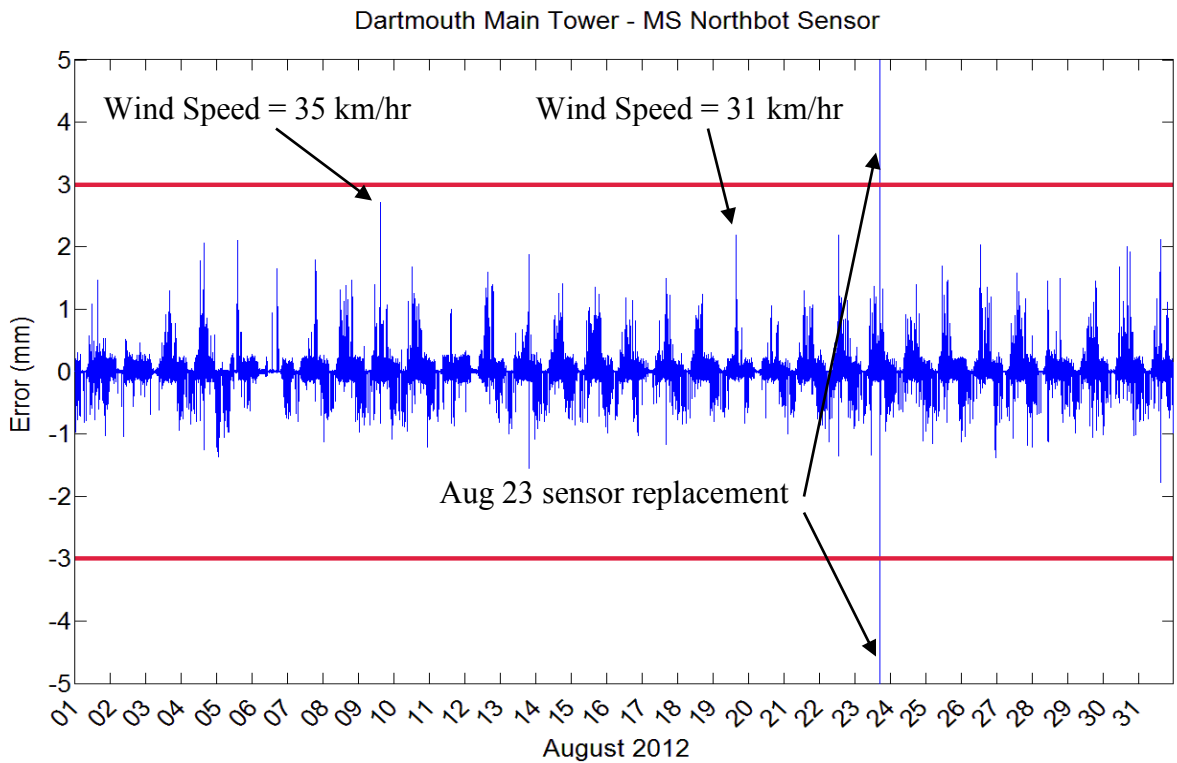
Figure 6.3: One-sided median method results - DMT MS north bottom, August 2012

45

6.3 Longitudinal Thermal Trend

As mentioned previously in Chapter 5, temperature sensors were installed at each tower of the bridge. The temperature reading of the north side was averaged with the temperature reading of the south side at each expansion joint location. The average temperatures were used for the analysis of thermal trends. Figure 6.4 to Figure 6.6 shows daily, monthly, and yearly sensor plots for all sensors monitoring DMT MS. It should be noted that due to the configuration of the longitudinal sensors, a negative change in sensor reading refers to the suspended deck moving away from the main tower. Based on these plots it was confirmed that thermal changes had a strong correlation with longitudinal movement. Refer to Appendix B for yearly sensor plots for all spans.
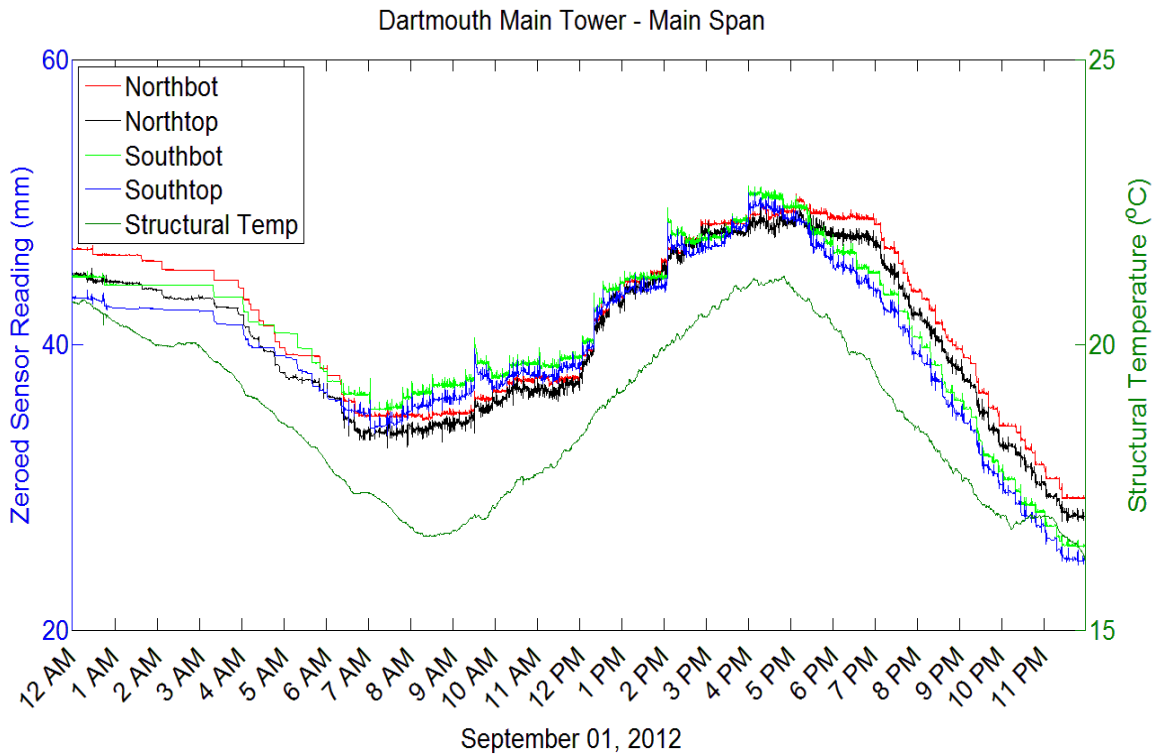
Figure 6.4: Daily record of sensor readings for DMT MS, September 01, 2012
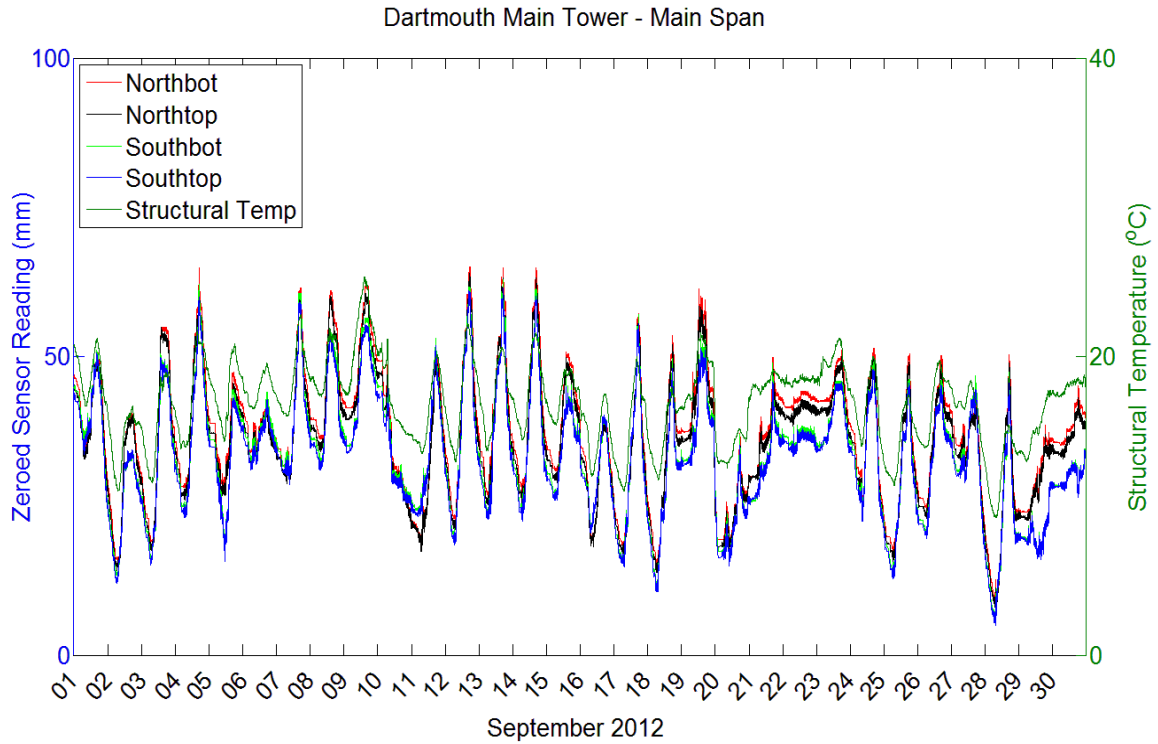
Figure 6.5: Month record of sensor readings for DMT MS, September 2012
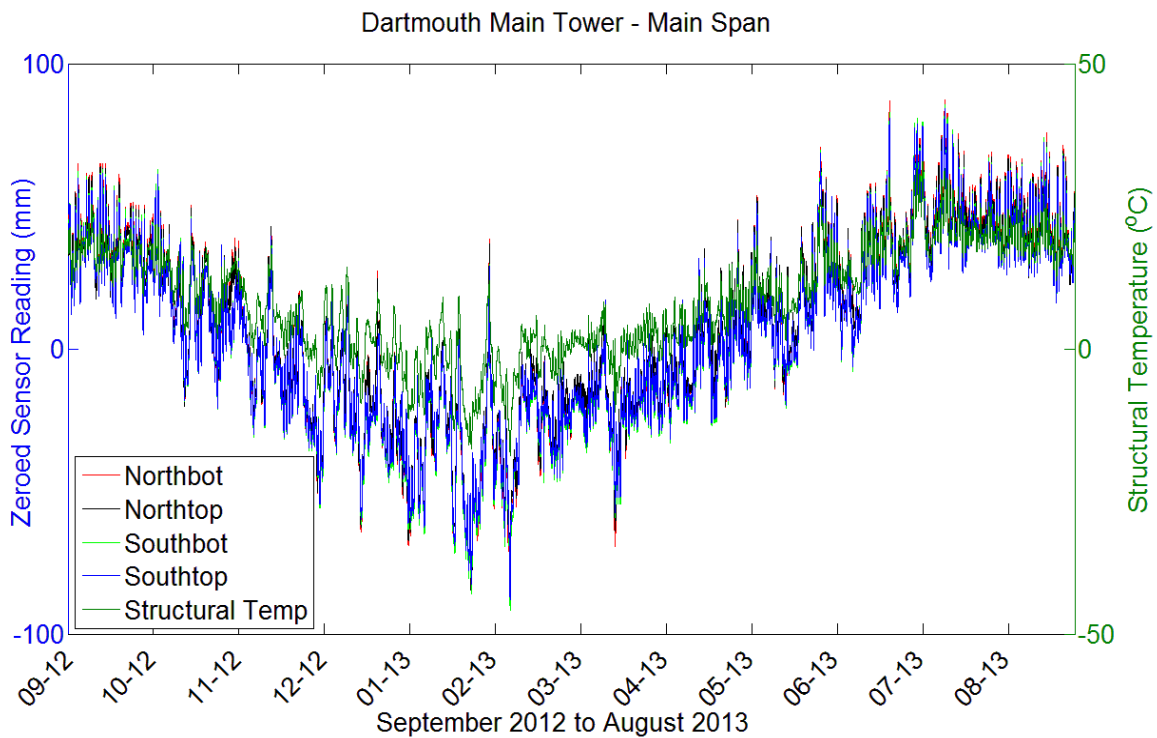
Figure 6.6: Record of sensor readings for DMT MS, September 2012 to August 2013

47

6.3.1 Effects of Averaging Data

Due to the high volume of collected data, it was thought to be acceptable to average the collected data over a time interval. By averaging the data, the effects of wind and live load would be reduced and the thermal trend of the bridge deck at the expansion joint location would be best represented. An appropriate averaging window was selected by investigating the impacts of averaging over different time intervals. Two months of displacement and temperature data, September 2012 and October 2012, were averaged over intervals of 1, 5, 30, 60, 120, and 360 minutes. A linear regression (Kutner et al. 2005) analysis was used to fit the thermal trend to the monitoring data collected from the months of September and October of 2012. MATLAB® uses the method of least squares where the sum of squared residuals is minimized. The fitted linear trends for each averaging interval can be seen below in Table 6.5 and Table 6.6 for September 2012 and October 2012, respectively. It appears that any interval less than 60 minutes does not have a large impact of the thermal trend. This seems appropriate since a significant change in temperature would be expected over an interval exceeding 1 hour.

Table 6.5: Thermal trends for different average time intervals – September 2012 - DMT

Averaged Time Interval	Main Span	Side Span
1 min	$3.48T - 24.3$	$2.08T - 15.9$
5 min	$3.48T - 24.3$	$2.08T - 15.9$
30 min	$3.48T - 24.3$	$2.08T - 15.9$
60 min	$3.48T - 24.3$	$2.08T - 15.9$
2 hr	$3.21T - 17.1$	$2.14T - 20.3$
6 hr	$3.39T - 13.3$	$2.19T - 22.6$

Table 6.6: Thermal trends for different average time intervals – October 2012 - DMT

Averaged Time Interval	Main Span	Side Span
1 min	$3.43T - 24.8$	$2.05T - 14.5$
5 min	$3.43T - 24.8$	$2.05T - 14.5$
30 min	$3.43T - 24.8$	$2.05T - 14.5$
60 min	$3.43T - 24.8$	$2.05T - 14.5$
2 hr	$3.31T - 17.6$	$2.01T - 19.2$
6 hr	$3.24T - 17.1$	$1.94T - 17.2$

6.3.2 Early Morning Data

Another method to extract the thermal trend out of the raw data was to take daily 3 am readings. Data readings from 3 am were compiled from each day for the monitoring year for DMT MS and HMT MS, September 2012 to August 2013. The rational for this was to minimize the effects of wind and live load. Daily 3 am data points were only collected when the averaged sustained wind speed was recorded below 15 km/hr. It would also be unlikely to observe high traffic volumes at this time. A linear regression analysis was conducted on the 3 am data. The two thermal trends determined from the two investigated data sets can be seen in Figure 6.7 and Figure 6.8. Table 6.7 shows the fitted linear yearly thermal trends.

Table 6.7: Thermal trends for 3 am morning data

Span	Thermal Trend
Dartmouth Main Span	$3.33T - 24.1$
Halifax Main Span	$3.71T - 36.5$
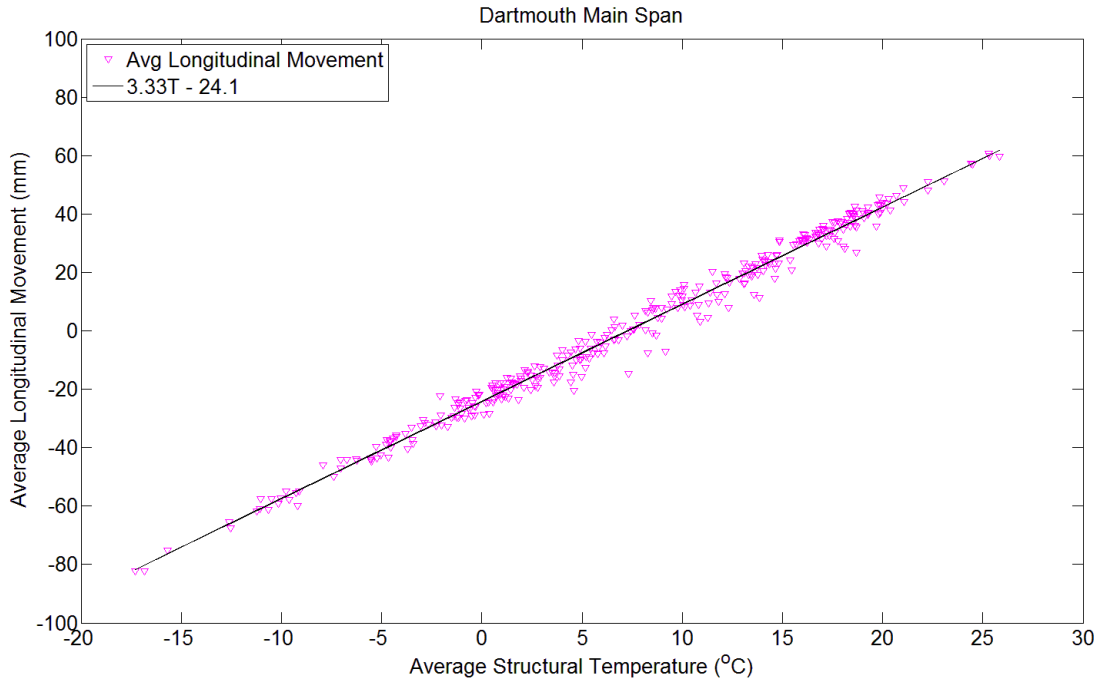
Figure 6.7: Thermal trend for DMT MS, 3am data
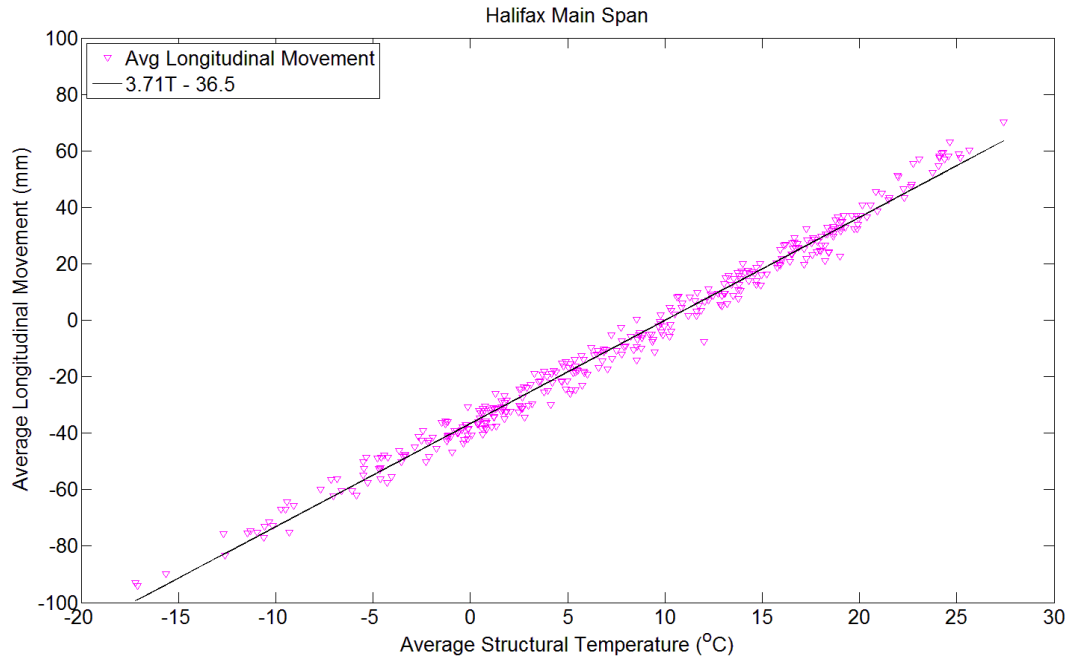
Figure 6.8: Thermal Trend for HMT, 3am data

6.3.3 Longitudinal Thermal Models

Longitudinal displacement and temperature readings were averaged over duration of 1000 data points (16.67 minutes). Although in the previous section it was shown that averaging up to one hour did not have an impact on the thermal trend, 1000 data points was chosen out of convenience. Also a large change in temperature would not be expected over this duration. Figure 6.9 shows a typical monthly thermal plot for the main span of DMT for the month of September 2012. It can be seen that the individual sensor thermal responses fall reasonably atop one another. For each span, all four longitudinal sensors were averaged together to represent the longitudinal displacement at the expansion joint location. Monthly trends were computed for each span and then compared to the yearly thermal trend. Table 6.8 and table 6.9 show the monthly thermal trends for main span and side span, respectively. Figure 6.10 shows the yearly thermal trend for Dartmouth main span for the monitoring year, September 2012 to August 2013. Refer to Appendix C for all longitudinal thermal trend plots for all spans.

50
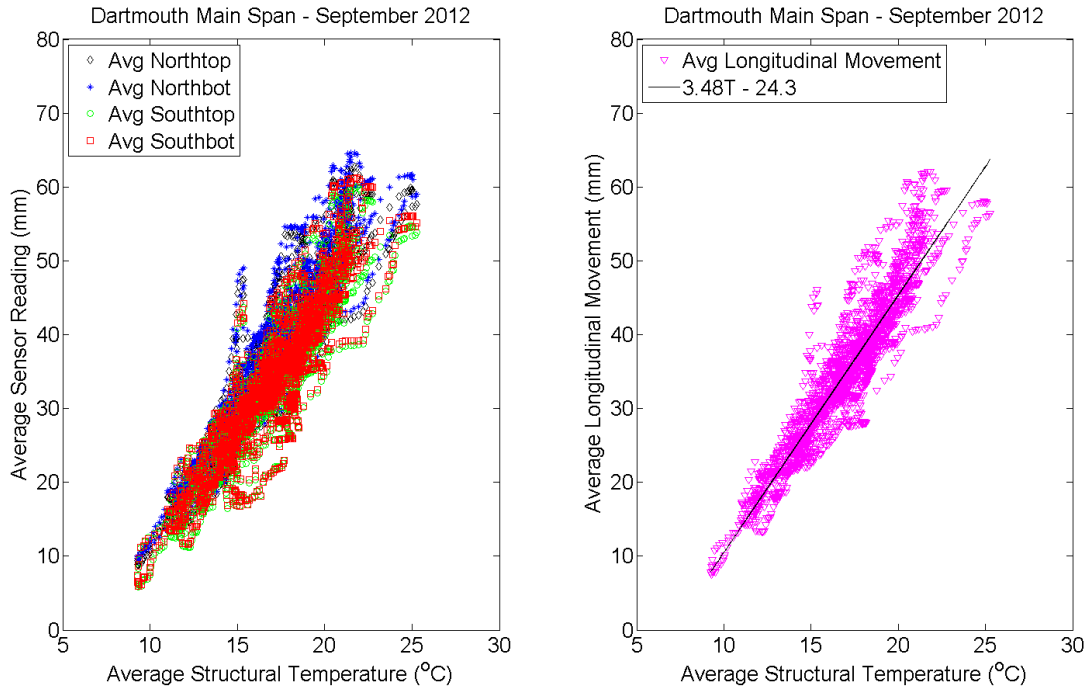
Figure 6.9: Monthly longitudinal thermal trend – DMT MS – September 2012

Table 6.8: Monthly main span thermal trend for HMT and DMT

Month	HMT MS Thermal Trend	DMT MS Thermal Trend
September	3.78T – 37.4	3.48T – 24.3
October	3.42T – 32.0	3.43T – 24.7
November	3.36T – 31.6	3.35T – 24.7
December	3.36T – 34.8	3.15T – 25.0
January	3.32T – 37.7	3.12T – 24.5
February	3.45T – 36.9	3.42T – 23.5
March	3.24T – 37.0	3.47T – 22.6
April	3.62T – 37.0	3.42T – 21.9
May	3.85T – 38.8	3.61T – 24.1
June	3.92T – 36.4	3.61T – 29.0
July	3.74T – 35.0	3.28T – 22.1
August	3.61T – 39.1	3.75T – 22.8
Monthly Average	**3.56T – 36.1**	**3.42T – 24.1**

Table 6.9: Monthly side span thermal trend for HMT and DMT

Month	HMT SS Thermal Trend	DMT SS Thermal Trend
September	1.79T – 16.4	2.08T – 15.9
October	1.74T – 15.1	1.65T – 14.5
November	1.59T – 13.3	1.75T – 12.9
December	1.47T – 15.3	1.88T – 12.2
January	1.51T – 16.4	1.99T – 11.8
February	1.48T – 16.4	1.85T – 12.2
March	1.64T – 16.7	2.04T – 11.2
April	1.91T – 17.0	2.10T – 12.5
May	1.67T – 15.3	1.90T – 12.9
June	1.52T – 12.2	1.94T – 12.0
July	1.45T – 13.1	1.89T – 11.3
August	1.85T – 19.1	2.01T – 16.1
Monthly Average	**1.64T – 15.5**	**1.92T – 12.9**
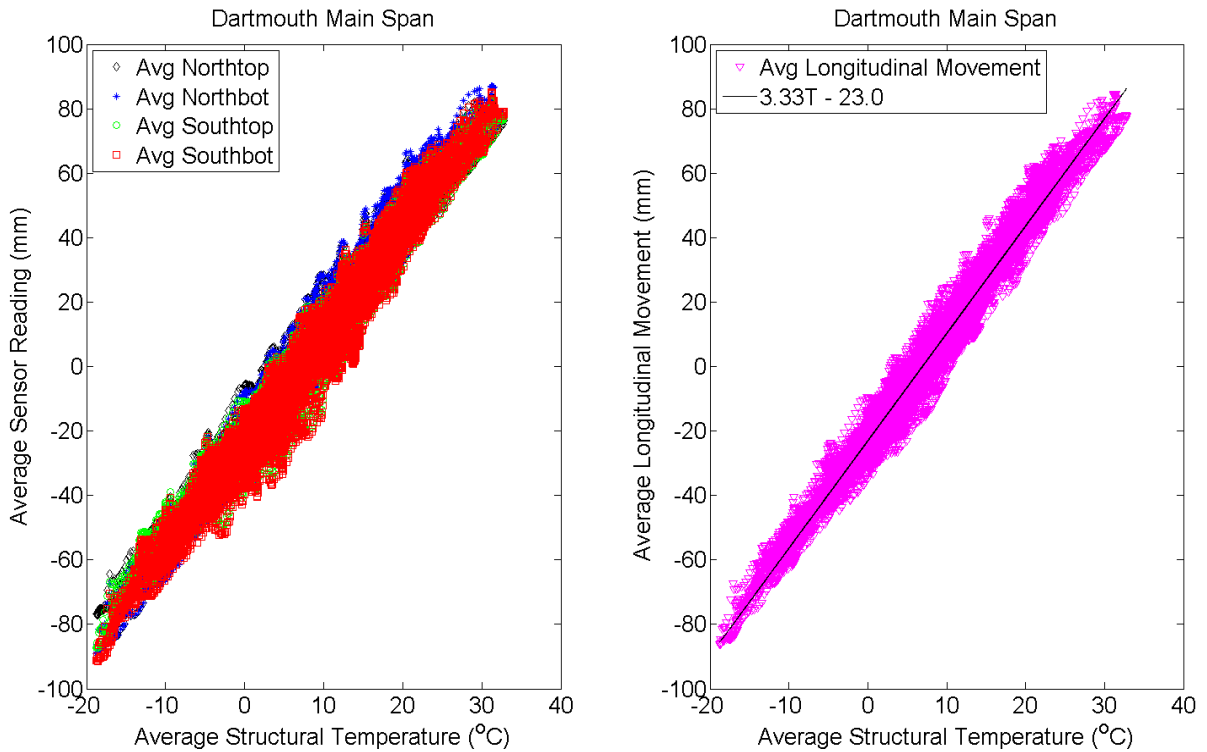
Figure 6.10: Longitudinal thermal trend for DMT MS – September 2012 to August 2013

52

6.3.4 Longitudinal Thermal Summary

Two approaches were used in an effort to extract the thermal movement from the collected data. First was the 3am data and secondly was averaging the data. It was shown that both of these methods were acceptable and produced similar results. In the end the method of averaging the yearly data was chosen since more data could be included in a single regression analysis for each span. Table 6.10 shows the final yearly longitudinal thermal trends for each main and side span. The variable, δ_T, represents the longitudinal displacement due to thermal changes, and T represents the structural temperature at the expansion joint location. As mentioned previously, Appendix C should be referred to for yearly longitudinal thermal trend plots for all spans. Table 6.11 shows the comparison of thermal expansion coefficients between the Runyang Suspension Bridge, Ting Kau Cable Stayed Bridge, and the Macdonald Suspension Bridge. Thermal expansion coefficients were determined by normalizing the thermal slope to the expansion length.

Table 6.10: Longitudinal displacement thermal models

Span	Longitudinal Thermal Model	Coefficient of Determination (R^2)
DMT MS	$\delta_T = 3.33T - 23.0$	0.9845
HMT MS	$\delta_T = 3.74T - 35.8$	0.9818
DMT SS	$\delta_T = 1.88T - 12.0$	0.9528
HMT SS	$\delta_T = 1.67T - 15.4$	0.9664

Table 6.11: Comparison of longitudinal thermal trends to case studies

Bridge	Location	Thermal Slope (mm/ºC)	Expansion Length (m)	Thermal Expansion Coefficients (/ºC)
Runyang (Miao et al.)	North Abutment	10.1	745	13.6
	South Abutment	10.2	745	13.7
Ting Kau (Ni et al.)	Left Span	8.13	575	14.1
	Right Span	7.08	602	11.8
Macdonald	DMT MS	3.33	220.5	15.1
	HMT MS	3.74	220.5	17.0
	DMT SS	1.88	160	11.8
	HMT SS	1.67	160	10.4

6.4 Rotational Thermal Trend

The longitudinal thermal trends were removed from the original non-averaged sensor data. The remaining monitoring data was assumed to be the result of plan and vertical rotation responses from wind and live load variations. Based on the sensor layout presented in Chapter 5, two possible rotations could be calculated. Figure 6.11 shows the orientation of the calculated rotations. Rotation about the y-axis was considered as plan rotation (θ_P) and rotation about the x-axis as vertical rotation (θ_V). Two calculations for each rotation could be calculated providing all four sensors were functional. These can be seen in Equation 6-1 and Equation 6-3. The average of the two were used to define the plan and vertical rotation at the point (0,0). The plan rotation calculated in Equation 6-2 and the vertical rotation calculated in Equation 6-4 are the rotations used for the analysis of rotational movement. Refer to Appendix B for yearly vertical and plan rotation plots for all spans.
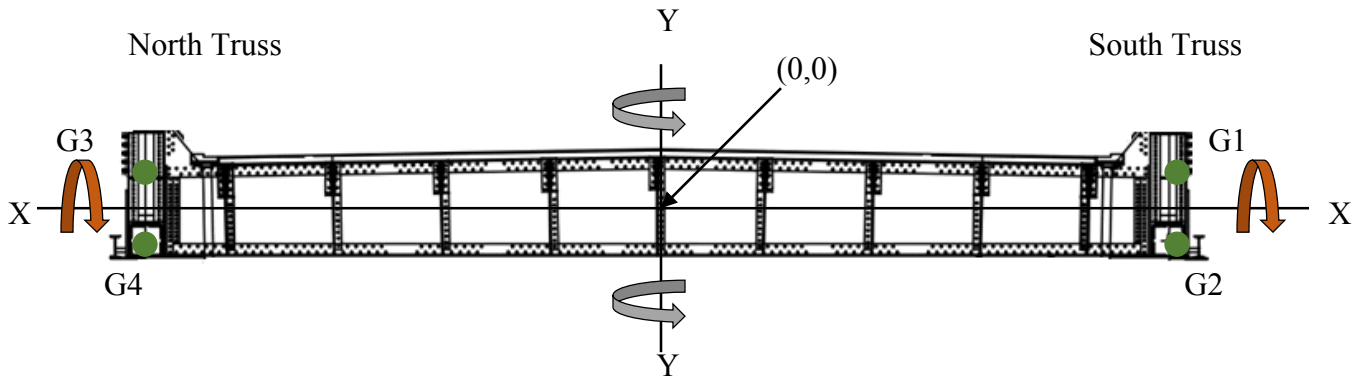
Figure 6.11: Orientation of calculated rotations

$$\theta_{V,North} = \tan^{-1}\left(\frac{G4-G3}{1280}\right) \quad \theta_{V,South} = \tan^{-1}\left(\frac{G2-G1}{1280}\right) \qquad [6\text{-}1]$$

$$\theta_V = \left(\frac{\theta_{V,North}+\theta_{V,North}}{2}\right) \qquad [6\text{-}2]$$

$$\theta_{P,Top} = \tan^{-1}\left(\frac{G1-G3}{11500}\right) \quad \theta_{P,Bottom} = \tan^{-1}\left(\frac{G2-G4}{11500}\right) \qquad [6\text{-}3]$$

$$\theta_P = \left(\frac{\theta_{P,Top}+\theta_{P,Bottom}}{2}\right) \qquad [6\text{-}4]$$

6.4.1 Vertical Rotation Thermal Models

From the literature discussed in Chapter 2, we would expect a vertical rotational change due to thermal variations. This is a result of the thermal expansion and contraction of the vertical hangers connecting the deck to the main cable. As the hangers adjust length due to thermal variations this causes a change in sag of the deck. Change in sag results in a rotational change at the expansion joint locations. Figure 6.12 shows the vertical rotation for DMT MS for the monitoring year, September 2012 to August 2013. It shows an annual change in vertical rotation similar to the annual change of longitudinal movement. The same analysis techniques were used on the vertical rotation data as the longitudinal movement data to determine the thermal trends for each span. Figure 6.13 shows DMT MS vertical rotation thermal trend. Refer to Appendix C for vertical rotation thermal trend plots for all spans.
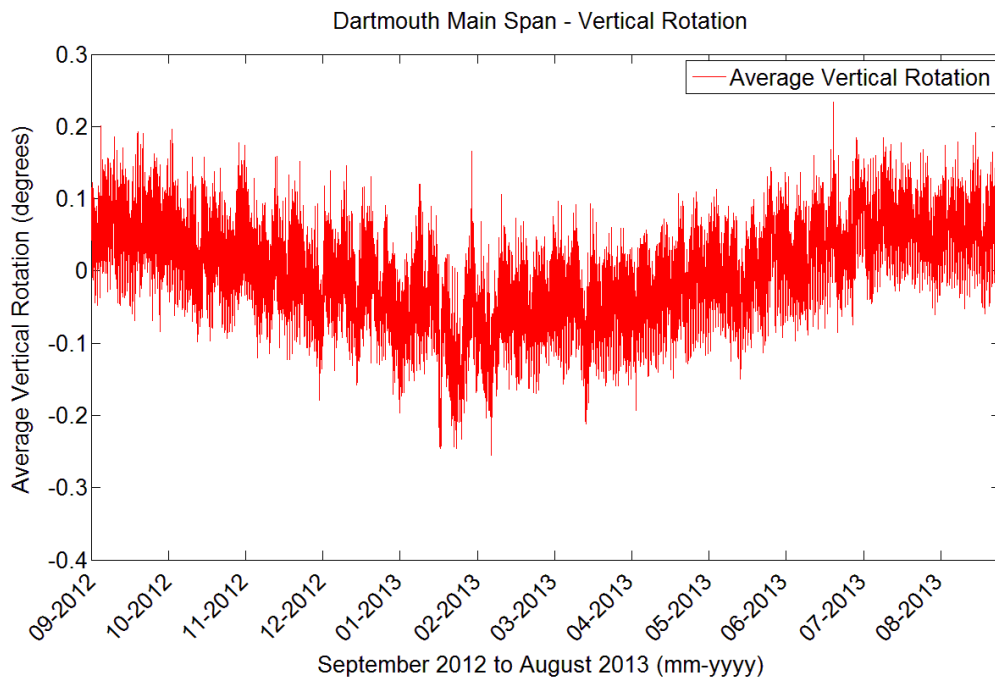
Figure 6.12: Vertical rotation for DMT MS, September 2012 to August 2013
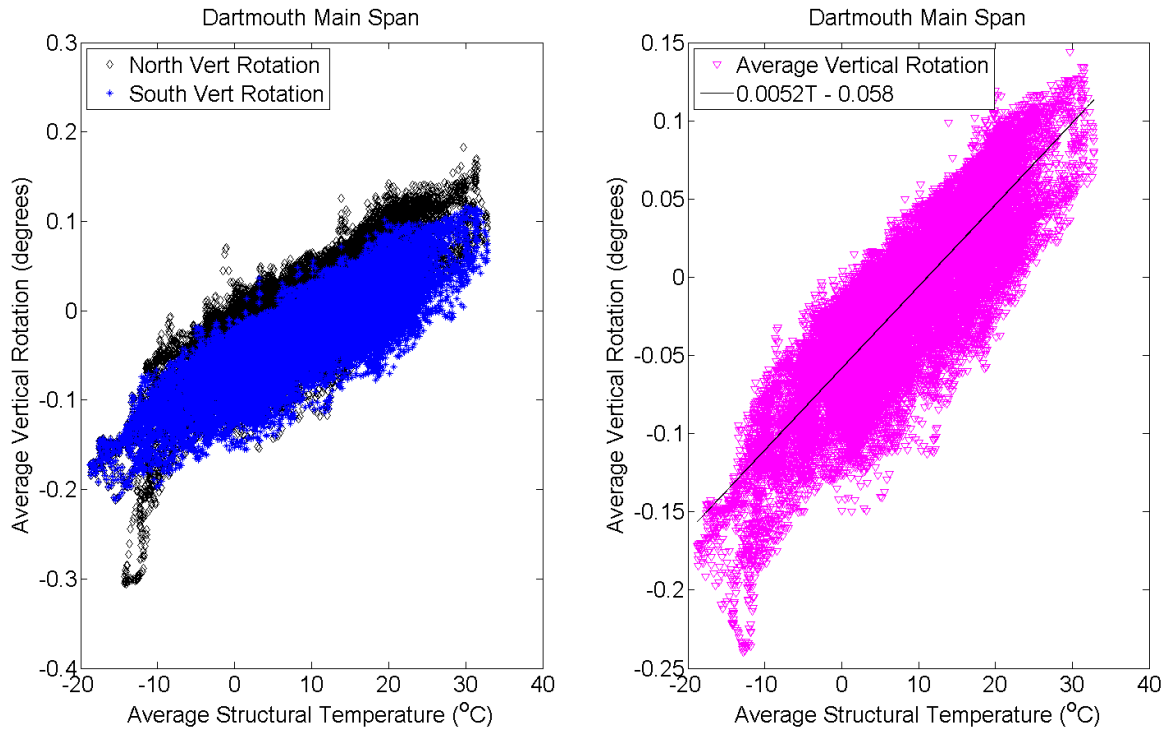
Figure 6.13: Vertical rotation thermal trend for DMT MS, September 2012 to September 2013

6.4.2 Plan Rotation Thermal Models

Similarly, plan rotation was investigated for an annual thermal trend. Figure 6.14 shows the plan rotation for DMT MS for the monitoring year, September 2012 to August 2013. From Figure 6.14 there are no visible signs of a thermal trend, however the data was analyzed using the same techniques as vertical. Figure 6.15 shows the plan rotation thermal trend for DMT MS. Refer to Appendix C for plan rotation thermal trend plots for all spans.
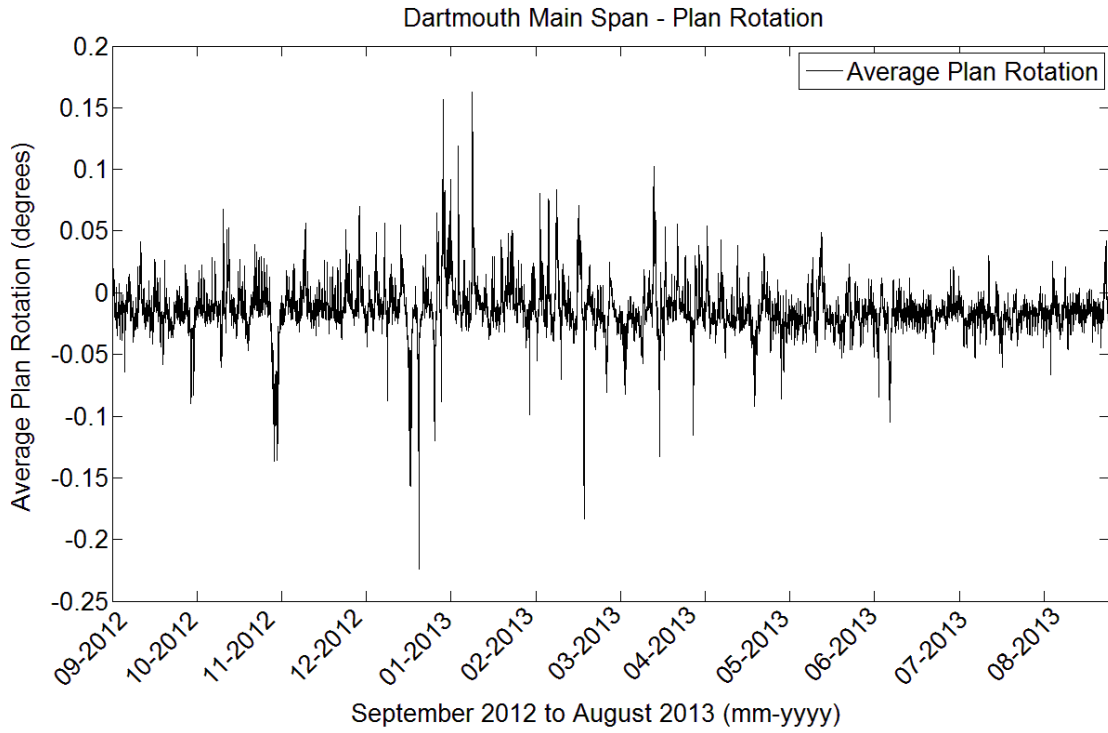
Figure 6.14: Plan rotation for DMT MS, September 2012 to August 2013
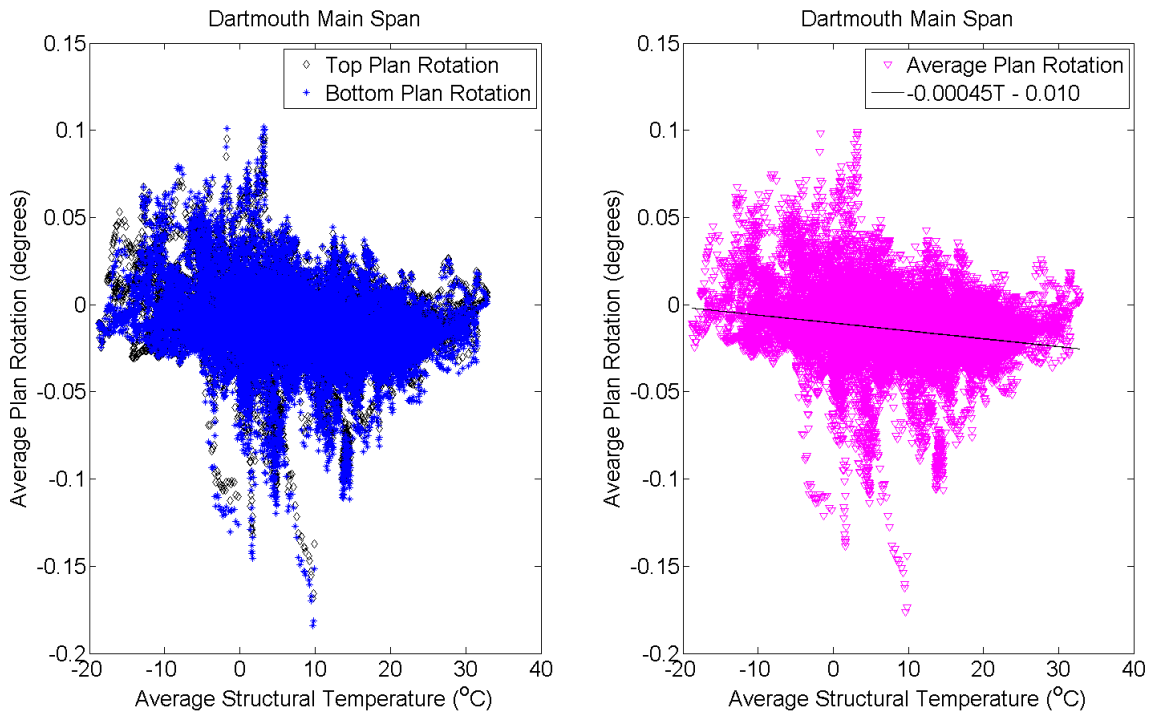
Figure 6.15: Plan rotation thermal trend for Dartmouth Main Span

6.4.3 Rotational Thermal Trend Summary

Linear regression methods were completed on both the vertical and plan rotations of all spans. Table 6.12 and Table 6.13 list the vertical rotation thermal models (θ_{VT}) and the plan rotation thermal models (θ_{PT}) for all spans. It can be seen that the response from plan rotation due to thermal variations is extremely small and for this reason these trends were neglected in the remainder of this analysis. The vertical rotational thermal models were removed from the original vertical rotation data, presumably leaving only effects of wind and live load. Since the plan rotation thermal models will not be accounted for, the plan rotation data was not altered.

Table 6.12: Vertical rotation thermal models

Span	Rotational Thermal Model	Coefficient of Determination (R^2)
DMT MS	$\theta_{VT} = 0.0052T - 0.058$	0.7663
HMT MS	$\theta_{VT} = 0.0040T - 0.039$	0.5981
DMT SS	$\theta_{VT} = 0.0022T - 0.019$	0.4766
HMT SS	$\theta_{VT} = 0.0007T + 0.003$	0.0763

Table 6.13: Plan rotation thermal models

Span	Rotational Thermal Model	Coefficient of Determination (R^2)
DMT MS	$\theta_{PT} = -0.00045T - 0.010$	0.0527
HMT MS	$\theta_{PT} = -0.00045T - 0.010$	0.0520
DMT SS	$\theta_{PT} = -0.00022T - 0.003$	0.1516
HMT SS	$\theta_{PT} = -0.00015T + 0.006$	0.0280

6.5 Wind Trend

As mentioned in the previous chapter, wind data was readily available through HHB's on-site weather station. In the context of plan rotation response to wind variations, averaged sustained wind speed and their corresponding directions were used in the analysis of wind trends. Although maximum gust data was available it was deemed to be very inconsistent, as the gust speeds were only recorded in significant storms and were sporadic at best. In most cases, gust data cannot be depended upon to crosscheck design wind speed predictions (Burton, 2011). For the remainder of this chapter, when wind speed is discussed it will be considered as the average sustained wind speed.

A histogram of wind speeds can be seen for the 12-month period in Figure 6.16 as well as a histogram for high wind speeds (> 30 km/hr) in Figure 6.17. The months containing large wind events occur roughly in late fall and during the winter months. This correlates to spikes in Figure 6.14. From this visual correlation it was deemed that plan rotation was primarily driven by wind events. Plan rotations were averaged to match the frequency of the provided weather data.
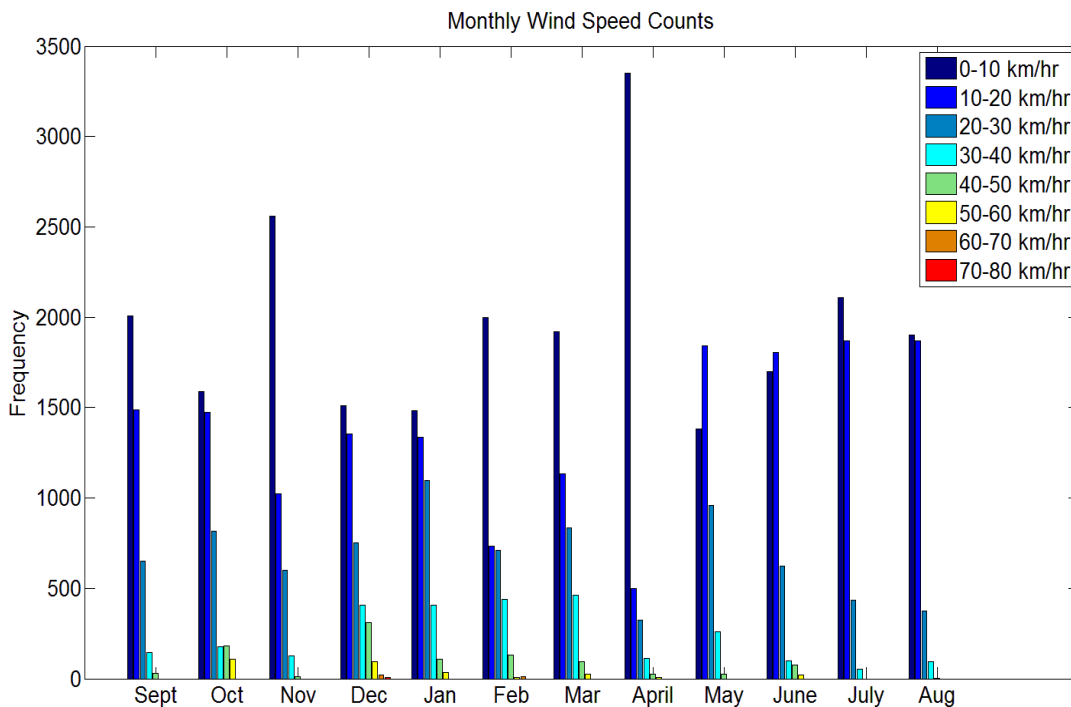
Figure 6.16: Monthly Wind Speed Counts
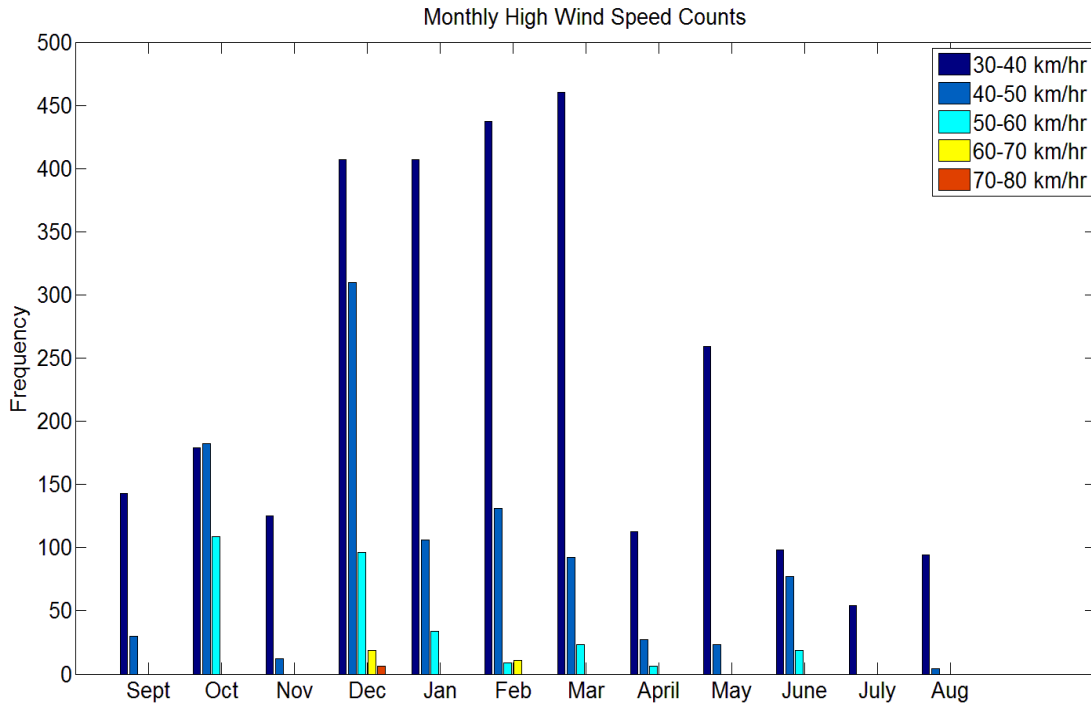
Figure 6.17: Monthly high (> 30 km/hr) wind speed counts

6.5.1 Wind Directions

Since the Macdonald Bridge is located in a very exposed location, all wind directions were considered. To aid in the trending of wind variations, the standard compass rose was divided into sixteen 22.5-degree directional sections (Figure 6.18). These 16 directional sections can be seen below in Table 6.14. For example, Perpendicular 1 refers to winds blowing into the Harbour and Perpendicular 2 refers to winds blowing out of the Harbour. Figure 6.19 shows the frequency of wind directions during the monitoring period.
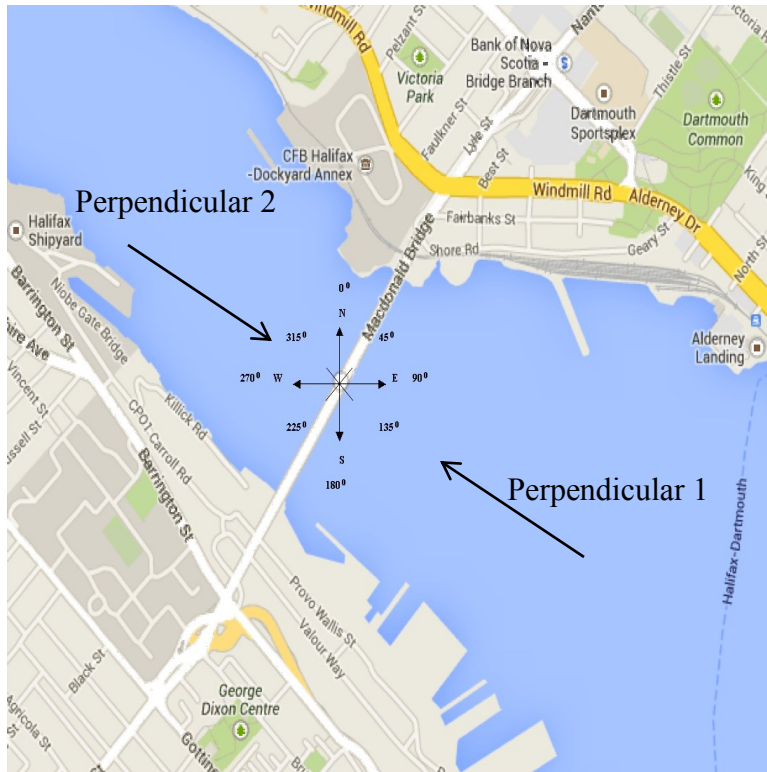
Figure 6.18: Compass coordinated of bridge (Google Maps)

Table 6.14: Sixteen directional sections for plan rotation wind analysis

Direction (ID)	Direction Range (degrees)
Parallel 1	22.75 – 45.25
Direction 1	42.25 – 67.75
Direction 2	67.75 – 90.25
Direction 3	90.25 – 112.75
Perpendicular 1	112.75 – 135.25
Direction 4	135.25 – 157.75
Direction 5	157.75 – 180.25
Direction 6	180.25 – 202.75
Parallel 2	202.75 – 225.25
Direction 7	225.25 – 247.75
Direction 8	247.75 – 270.25
Direction 9	270.25 – 292.75
Perpendicular 2	292.75 – 315.25
Direction 10	315.25 – 337.75
Direction 11	337.75 – 360
Direction 12	0 – 22.75

Figure 6.19: Wind direction counts

6.5.2 Plan Rotation Wind Trend

Plan rotation was plotted against wind speed for all wind events associated with each directional section. For each directional section, a polynomial regression was performed using MATLAB's® curve fitting toolbox. It was noticed that during the time of zeroing the raw data, average sustained winds were recorded to be approximately 35 km/hr. This resulted in the original quadratic fits to not pass through 0, therefore the data was adjusted by offset values to account for this wind at time of zeroing. Table 6.15 shows the plan rotation wind offsets for each span. These offsets were removed from the plan rotation data and the quadratic fits were reanalyzed. Monthly wind trends were first analyzed for DMT MS. Unlike monthly temperature trends, the monthly wind trends do differ from month to month. This monthly difference of the wind trend depends on two factors: amount of wind events associated with the direction in question and the magnitude of wind events. Figure 6-19 shows the monthly wind trends associated with perpendicular direction 1 for DMT MS. It can be seen that the majority of months all

follow the same trend, however a few months (November, January, May, and July) show different trends. This is the result of having minimal number of wind events associated with perpendicular direction 1 during these months and the wind events that were recorded were small in magnitude. The black dots in Figure 6.20 represent the maximum wind recorded during that month. These months of poor wind correlation are however still important data with respect to the entire monitoring year. Figure 6.21 shows the yearly fitted wind trend associated with perpendicular direction 1 for DMT MS where the variable, v, represents wind velocity (km/hr). The fitted quadratic constant will be labeled as the wind direction coefficient. Table 6.16 to Table 6.19 show the wind direction coefficients for all directional sections for DMT MS, HMT MS, DMT SS, and HMT SS, respectively. Refer to Appendix D for directional wind plots for all spans.

Table 6.15: Plan rotation wind offsets

Span	Plan Rotation Offset (Degrees)
DMT MS	-0.015
HMT MS	-0.014
DMT SS	-0.003
HMT SS	-0.004
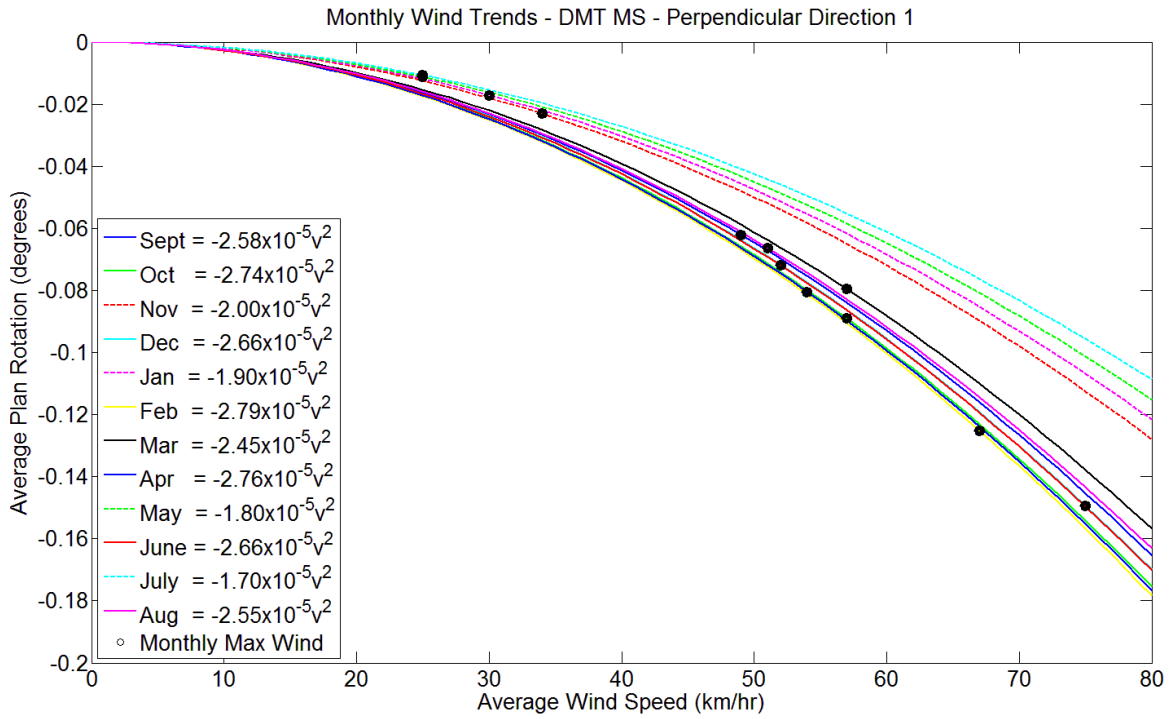
Figure 6.20: Monthly wind trends for perpendicular direction 1 - DMT MS
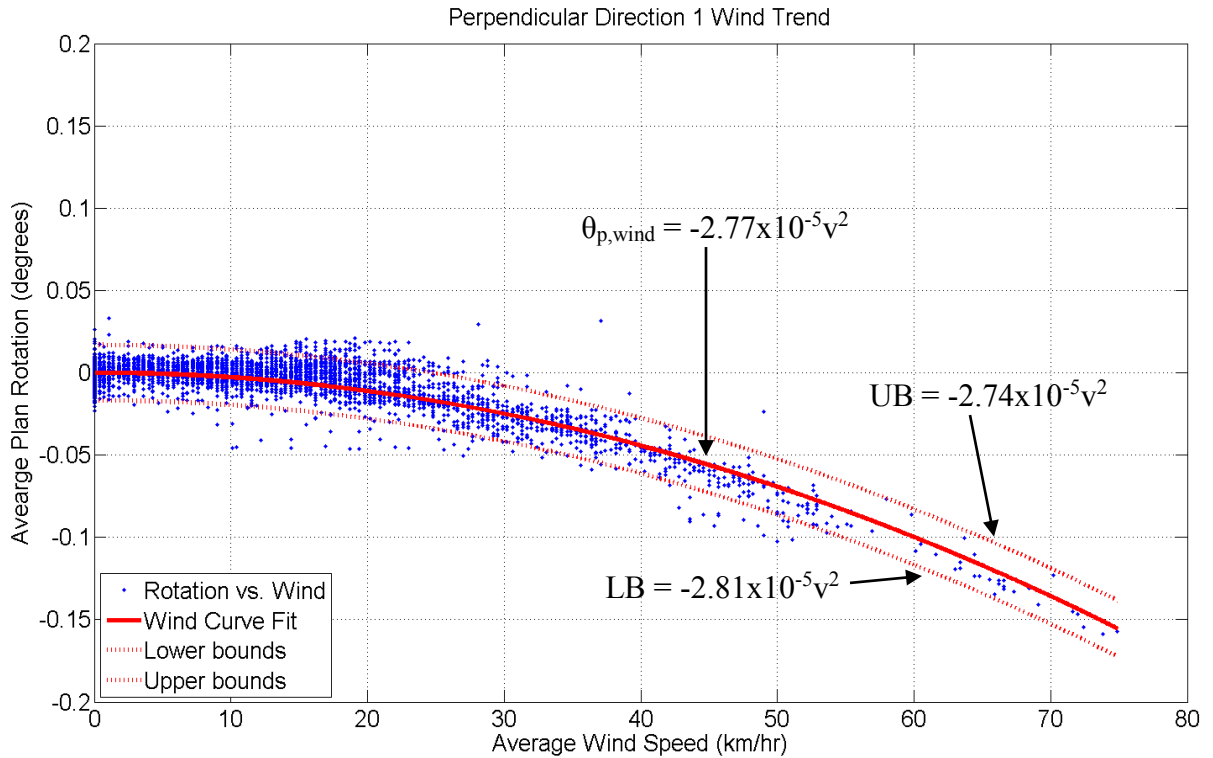
Figure 6.21: Wind trend for perpendicular direction 1 for DMT MS - Year

64

Table 6.16: Wind direction coefficients for Dartmouth Main Span

Directional Section	Wind Direction Coefficient (x10^{-5})	95% Confidence Bounds	
		Upper Bound (x10^{-5})	Lower Bound (x10^{-5})
Parallel 1	3.68	3.72	3.60
Direction 1	2.78	2.84	2.72
Direction 2	-0.82	-0.71	-0.93
Direction 3	-2.57	-2.54	-2.60
Perpendicular 1	-2.77	-2.74	-2.81
Direction 4	-1.64	-1.60	-1.69
Direction 5	-1.20	-1.13	-1.27
Direction 6	-0.44	-0.35	-0.52
Parallel 2	0.57	0.66	0.49
Direction 7	0.64	0.71	0.56
Direction 8	2.07	2.17	1.98
Direction 9	3.50	3.58	3.42
Perpendicular 2	3.95	3.99	3.90
Direction 10	3.74	3.79	3.68
Direction 11	3.08	3.17	2.98
Direction 12	3.66	3.70	3.62

Table 6.17: Wind direction coefficients for Halifax Main Span

Directional Section	Wind Direction Coefficient (x10^{-5})	95% Confidence Bounds	
		Upper Bound (x10^{-5})	Lower Bound (x10^{-5})
Parallel 1	3.64	3.68	3.59
Direction 1	2.87	2.94	2.80
Direction 2	-1.02	-0.91	-1.13
Direction 3	-2.49	-2.46	-2.52
Perpendicular 1	-2.54	-2.50	-2.58
Direction 4	-1.46	-1.41	-1.51
Direction 5	-1.02	-0.95	-1.10
Direction 6	0.04	0.12	-0.05
Parallel 2	1.00	1.09	0.91
Direction 7	1.16	1.26	1.06
Direction 8	2.28	2.43	2.13
Direction 9	3.44	3.54	3.34
Perpendicular 2	4.23	4.29	4.17
Direction 10	4.09	4.15	4.02
Direction 11	3.40	3.51	3.30
Direction 12	3.64	3.68	3.60

Table 6.18: Wind direction coefficients for Dartmouth Side Span

Directional Section	Wind Direction Coefficient (x10^{-6})	95% Confidence Bounds	
		Upper Bound (x10^{-6})	Lower Bound (x10^{-6})
Parallel 1	4.89	5.11	4.67
Direction 1	7.34	7.61	7.06
Direction 2	0.52	0.90	0.14
Direction 3	-1.62	-1.49	-1.74
Perpendicular 1	-3.12	-2.95	-3.30
Direction 4	-6.89	-6.56	-7.22
Direction 5	-2.81	-2.28	-3.34
Direction 6	-3.66	-2.96	-4.33
Parallel 2	-7.78	-7.12	-8.45
Direction 7	-0.36	0.18	-0.91
Direction 8	3.97	4.62	3.32
Direction 9	7.37	7.82	6.92
Perpendicular 2	5.67	5.94	5.40
Direction 10	1.10	1.45	0.75
Direction 11	-0.39	0.13	-0.91
Direction 12	0.91	1.14	0.67

Table 6.19: Wind direction coefficients for Halifax Side Span

Directional Section	Wind Direction Coefficient (x10^{-6})	95% Confidence Bounds	
		Upper Bound (x10^{-6})	Lower Bound (x10^{-6})
Parallel 1	0.33	0.68	-0.03
Direction 1	-1.41	-1.00	-1.82
Direction 2	-2.17	-1.55	-2.78
Direction 3	-4.75	-4.53	-4.98
Perpendicular 1	-5.52	-5.18	-5.85
Direction 4	-5.49	-4.92	-6.06
Direction 5	-6.31	-5.38	-7.23
Direction 6	-14.1	-12.92	-15.37
Parallel 2	-17.8	-1.64	-1.91
Direction 7	-9.93	-8.52	-11.35
Direction 8	-8.59	-7.07	-9.99
Direction 9	-7.51	-6.77	-8.25
Perpendicular 2	1.75	2.13	1.38
Direction 10	-6.28	-5.73	-6.84
Direction 11	-2.99	-2.12	-3.87
Direction 12	1.75	2.13	1.38

6.5.3 Vertical Rotation Wind Trend

As mentioned in Section 6.4.5, the vertical rotation thermal trend was removed from the original rotation data. The same procedure was applied to vertical rotation as applied to plan rotation to determine the wind response. It was found that wind had no impact on vertical rotation. Figure 6.22 shows the average vertical rotation plotted against average wind speed for all events associated with perpendicular direction 1 for DMT MS. As seen in Figure 6.22 vertical rotation for the year after the thermal effects had been removed show no correlation to wind as was seen with plan rotation. This plot is typical for all directional sections. It general it was noted that the higher the recorded wind speed, the smaller the vertical rotation magnitude became. This would suggest that traffic would be less in volume during severe wind events. It was deemed that the remaining vertical rotation is a result of traffic loadings.
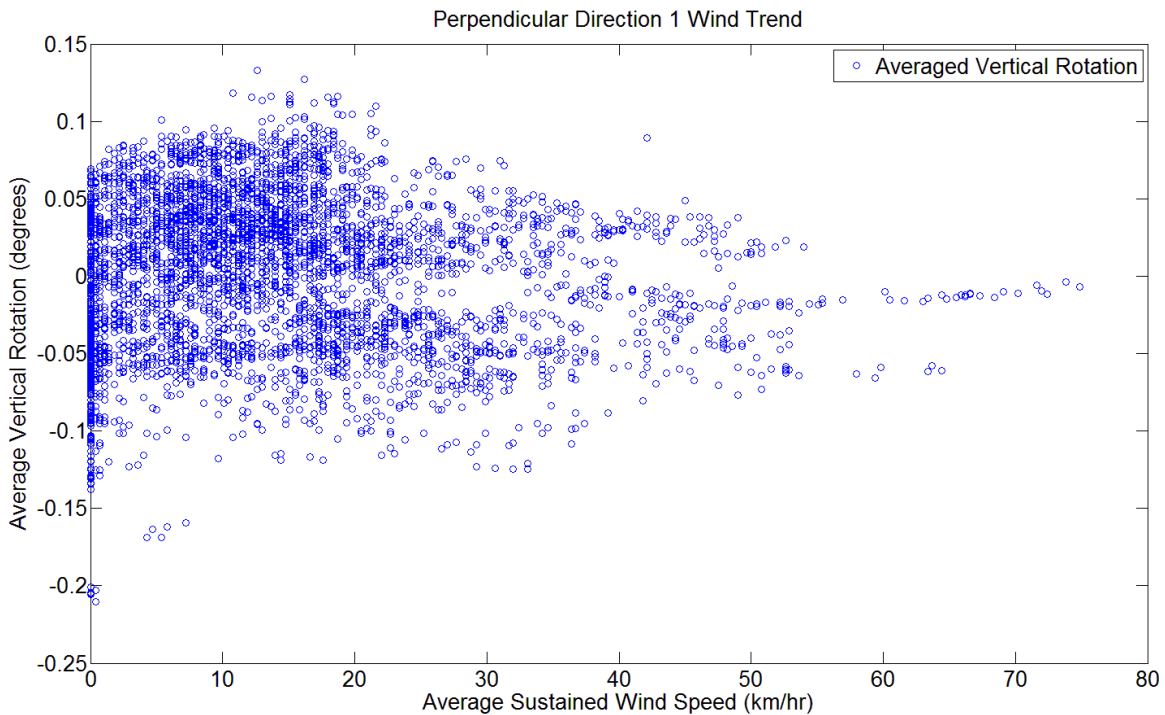
Figure 6.22: Scatter plot of all wind events for perpendicular direction 1 and averaged vertical rotation, DMT MS

67

6.5.4 Wind Trend Discussion

It was determined that wind variations predominantly influenced plan rotation while vertical rotation was not impacted. The wind trends were removed from the plan rotation presumably leaving only the effects of live load. Since there were no wind correlations with vertical rotation it was assumed that the remaining vertical rotation was a result of live load.

6.6 Live Load Trend

Once the effects of thermal and wind were removed from the original rotation data set, variations in live load were investigated for any correlation to rotational changes. Due to the unavailability of traffic data, it was difficult to relate traffic volumes and patterns to deck movement. An approach of correlating rotational changes with peak traffic hours and workdays versus non-work days, such as weekends and holidays was used.

6.6.1 Vertical Rotation Hourly Averages

Figure 6.23 shows a 24-hour vertical rotation plot for a typical workday. There appears to be a correlation between time of day and vertical rotation. Variations in vertical rotation were very small during the overnight hours (1am – 4am), which is expected, as minimal traffic would be anticipated during this time. There is a noticeable increase in vertical rotation patterns during the morning rush hour (6:30am – 9:30am) with rotation leveling off during the daytime hours (11am – 3am). Another increase occurs during the afternoon rush hour (4am – 6am). The spikes in the data can be related to the randomness of the traffic. Figure 6.24 shows a 24-hour vertical rotation plot for a typical non-workday. It can be seen that there are no rush hour peaks and the bandwidth of vertical rotation stays fairly consistent throughout the day light hours. Due to the difference in workdays and non-workdays, two sets of hourly vertical rotation averages were computed. These hourly averages can be seen below in Table 6.20 and Table 6.21 for DMT MS for workdays and non-workdays, respectively. The two plots shown represent DMT MS however similar trends were seen in HMT MS, and not as strong for DMT SS and HMT SS. Refer to Appendix E for all hourly vertical rotation average tables for all spans.

69
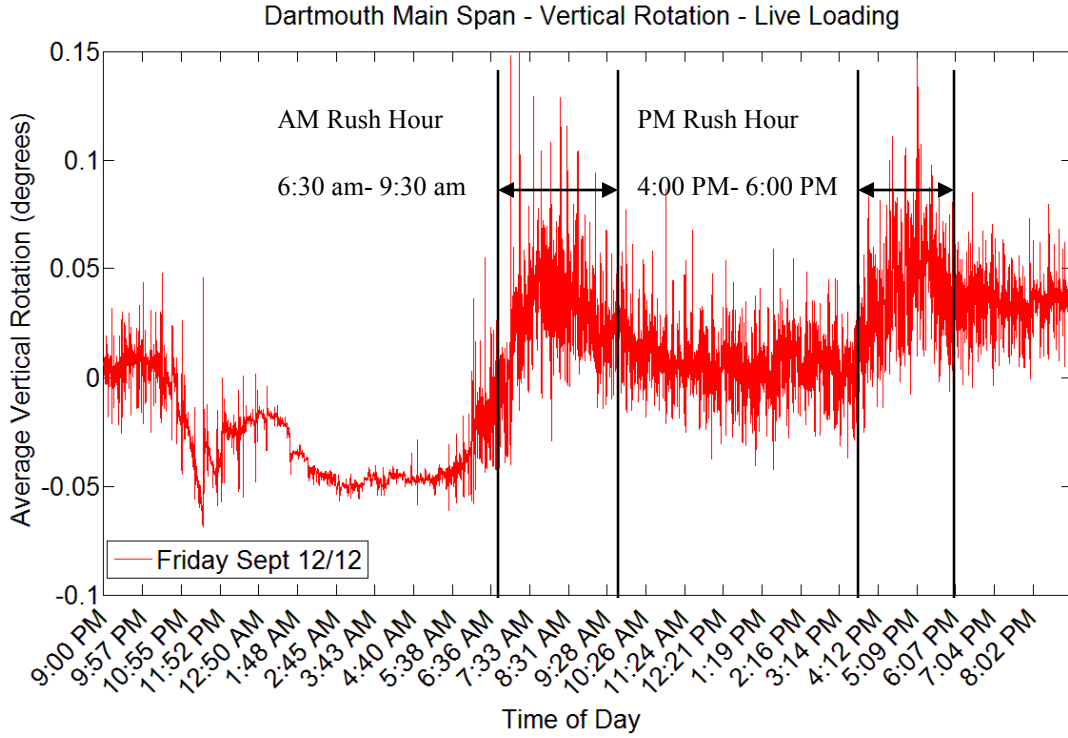
Figure 6.23: Typical 24-hour workday vertical rotation trend due to traffic – DMT MS
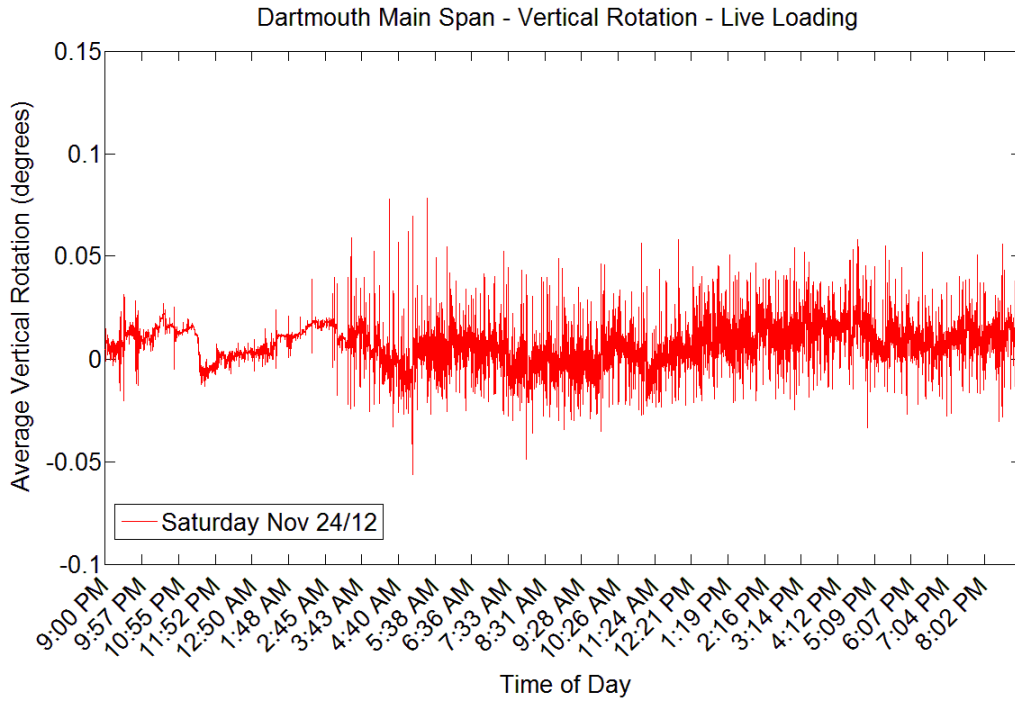
Figure 6.24: Typical 24-hour non-workday vertical rotation trend due to traffic – DMT MS

70

Table 6.20: Vertical Rotation Hourly Averages - Workday

TIME OF DAY	AVEARGE (Degrees)	STANDARD DEVIATION (Degrees)
12 AM	-0.015	0.021
1 AM	-0.013	0.015
2 AM	-0.025	0.012
3AM	-0.031	0.009
4AM	-0.021	0.015
5AM	-0.015	0.025
6 AM	-0.005	0.043
7 AM	0.035	0.061
8 AM	0.041	0.062
9 AM	0.025	0.061
10 AM	0.011	0.057
11 AM	0.019	0.045
12 PM	0.022	0.043
1 PM	0.015	0.048
2 PM	0.012	0.051
3 PM	0.022	0.055
4 PM	0.041	0.052
5 PM	0.051	0.065
6 PM	0.045	0.061
7 PM	0.035	0.063
8 PM	0.015	0.059
9 PM	0.006	0.042
10 PM	0.010	0.021
11 PM	-0.021	0.032

Table 6.21: Vertical Rotation Hourly Averages - Non-Workday

TIME OF DAY	AVEARGE (Degrees)	STANDARD DEVIATION (Degrees)
12 AM	-0.015	0.008
1 AM	-0.013	0.008
2 AM	-0.025	0.007
3AM	-0.031	0.008
4AM	-0.021	0.005
5AM	-0.015	0.009
6 AM	-0.005	0.011
7 AM	0.015	0.012
8 AM	0.011	0.010
9 AM	-0.005	0.010
10 AM	-0.001	0.015
11 AM	-0.016	0.015
12 PM	-0.012	0.016
1 PM	-0.007	0.017
2 PM	0.009	0.018
3 PM	0.012	0.021
4 PM	0.015	0.016
5 PM	0.011	0.014
6 PM	0.013	0.015
7 PM	0.015	0.016
8 PM	0.015	0.014
9 PM	0.006	0.019
10 PM	0.010	0.011
11 PM	0.011	0.005

6.6.2 Plan Rotation Hourly Averages

Similarly to vertical rotation, the remaining plan rotation was investigated for trends related to time of day. Unlike vertical rotation, there was not a significant difference between workdays and non-workdays; therefore hourly averages were not separated from workdays and non-workdays. It was noted that plan rotation changes from negative to positive at noon and vice versa at midnight. This was related to the fact that the center lane is changed direction at noon and midnight. This changes the loading pattern on the bridge and is reasonable to expect a change in plan rotation from this lane direction change. Table 6.22 shows the hourly plan rotation averages from DMT MS. Similar trends were noticed in HMT MS and not as strong for both side spans. Refer to Appendix E for all hourly plan rotation average tables for all spans.

Table 6.22: Plan Rotation Hourly Averages

TIME OF DAY	AVEARGE (Degrees)	STANDARD DEVIATION (Degrees)
12 AM	-0.0007	0.006
1 AM	-0.0006	0.006
2 AM	-0.0004	0.006
3AM	-0.0007	0.006
4AM	-0.0007	0.006
5AM	-0.0014	0.006
6 AM	-0.0015	0.006
7 AM	-0.0018	0.008
8 AM	0.0015	0.009
9 AM	-0.0013	0.007
10 AM	-0.0005	0.007
11 AM	-0.0004	0.007
12 PM	0.0016	0.007
1 PM	0.0034	0.008
2 PM	0.0039	0.009
3 PM	0.0032	0.009
4 PM	0.0022	0.012
5 PM	0.0012	0.011
6 PM	0.0017	0.018
7 PM	0.0031	0.014
8 PM	0.0026	0.012

9 PM	0.0004	0.009
10 PM	0.0007	0.007
11 PM	0.0002	0.007

6.6.3 Live Load Summary

Due to the lack of traffic data is was impossible to correlate live load patterns and volumes with rotations, therefore a time of day approach was taken. Although hourly averages may not be the most appropriate way to estimate its trend, the magnitude of rotations due to live load is very minimal in comparison to thermal and wind. Vertical rotation due to live load accounts for roughly +/- 2 mm of longitudinal movement while plan rotation due to live load accounts for roughly +/- 1 mm.

6.7 Discussion

This chapter discussed the analysis techniques performed on the collected data. From the results, it can be seen that thermal changes account for the majority of the longitudinal movement. Plan rotation is predominately influenced by wind loadings. The remaining plan rotation was attributed to live loads. Vertical rotation contains a dominating thermal trend and the remaining rotation was attributed to live loads where trends were observed based on time of day. The next chapter will assemble the individual models into a general equation and define design equations.

Chapter 7: Bearing Movement and Expansion Joint Displacement Models

This chapter will discuss the development of models for bearing movement and expansion joint displacement. Combing the individual load effects into a general sensor model must first develop sensor models.

7.1 Sensor Models from Load Effects

Individual sensor equations were assembled using the models determined in the previous chapter. Table 7.1 shows the breakdown of responses for each type of movement. Equation 7-1 shows the general sensor equation. Factors are required to convert rotations back into longitudinal displacements. These factors can be seen in Table 7.2.

Table 7.1: Breakdown of movement responses

Longitudinal Displacement (δ_L)	Plan Rotation (θ_p)	Vertical Rotation (θ_v)
Thermal	Wind	Thermal
	Live Load	Live Load

$$G_i = \delta_L + C_{1i}\tan(\theta_p) + C_{2i}\tan(\theta_v) \qquad \textbf{[7-1]}$$

where: G_i = sensor reading (i = 1-8 for each tower)

     δ_L = longitudinal movement (thermal)

     θ_p = plan rotation (wind + live load)

     θ_v = vertical rotation (thermal + live load)

     C_{1i} = plan rotation conversion factor (Table 7.2)

     C_{2i} = vertical rotation conversion factor (Table 7.2)

For each type of movement shown in Equation 7-1, three equations are defined to represent longitudinal movement and rotation. Equation 7-2 defines the longitudinal movement. As seen in Table 7.1, only thermal variations were found to significantly influence the longitudinal displacement. As seen in Chapter 6, it was determined that longitudinal movement responded linearly to thermal variations and the effects of wind

and live load could be ignored. Equation 7-2 requires an input of temperature (T) and the selection of linear thermal coefficients, λ_T and β_T, from Table 6-10 for the appropriate main or side span.

$$\delta_L = \lambda_T * T + \beta_T \qquad \text{[7-2]}$$

where: λ_T = thermal longitudinal movement coefficient (Table 6.10)

T = input temperature (°C)

β_T = thermal longitudinal movement y-intercept (Table 6.10)

Equation 7-3 defines the plan rotation, which is the combination of wind and live load variations. From Chapter 6 it was determined that plan rotation responded quadratically to wind speed variations while live load variations were correlated to time of day. Plan rotation responded linearly however it was found that the effects were minimal and could be ignored. The required known parameters are wind speed (v) and direction in degrees for the wind response portion and time of day for the live load. The appropriate wind offset, β_w, is selected from Table 6.14 depending on the span. Wind direction is required to reference the appropriate direction ID from Table 6.13 to correspond to the appropriate wind direction coefficient, λ_W (Table 6.15 to Table 6.18) depending on the main or side span. Hourly live load averages corresponding to the time of day are determined from Appendix E for the appropriate main or side span.

$$\theta_p = \lambda_W * v^2 + \beta_w + \theta_{pLL} \qquad \text{[7-3]}$$

where: λ_W = directional plan rotation wind coefficient (Table 6.15 to 6.18)

v = input wind velocity (m/s)

β_W = wind offset (Table 6.14)

θ_{pLL} = hourly average live load plan rotation (Appendix E)

Lastly, Equation 7-4 defines the vertical rotation, which is the combination of thermal and live load variations. Similar to longitudinal movement, it was determined that vertical rotation responded linearly to thermal variations. Live load was correlated to time of day. It was found the wind did not have a significant affect to vertical rotation. Temperature (T) is required as an input for thermal and time of day for live load. Linear thermal coefficients, $\lambda_{\theta T}$ and $\beta_{\theta T}$, for vertical rotation are selected from Table 6.11 for the appropriate span. Hourly live load averages corresponding to the time of day are determined from Appendix E for the appropriate main or side span.

$$\theta_v = \lambda_{\theta T}*T + \beta_{\theta T} + \theta_{vLL} \qquad \textbf{[7-4]}$$

where: $\lambda_{\theta T}$ = thermal vertical rotation coefficient (Table 6.11)

     T   = input temperature (°C)

    $\beta_{\theta T}$ = thermal vertical rotation y-intercept (Table 6.11)

    θ_{vLL} = hourly average live load plan rotation (Appendix E)

Table 7.2: Rotational conversion factors

Sensor ID (G_i)	Plan Rotation (C_{1i})	Vertical Rotation (C_{2i})
G1	-5750	-640
G2	-5750	640
G3	5750	-640
G4	5750	640
G5	-5750	-640
G6	-5750	640
G7	5750	-640
G8	5750	640

A flow chart can be seen in Figure 7.1 that shows the process of calculating a sensor reading with known temperature, wind speed and direction, and time of day. An example of the model can be seen in Figure 7.2. It shows the breakdown of each component for DMT MS north bottom sensor on March 3rd, 2013 at 12:32 pm.
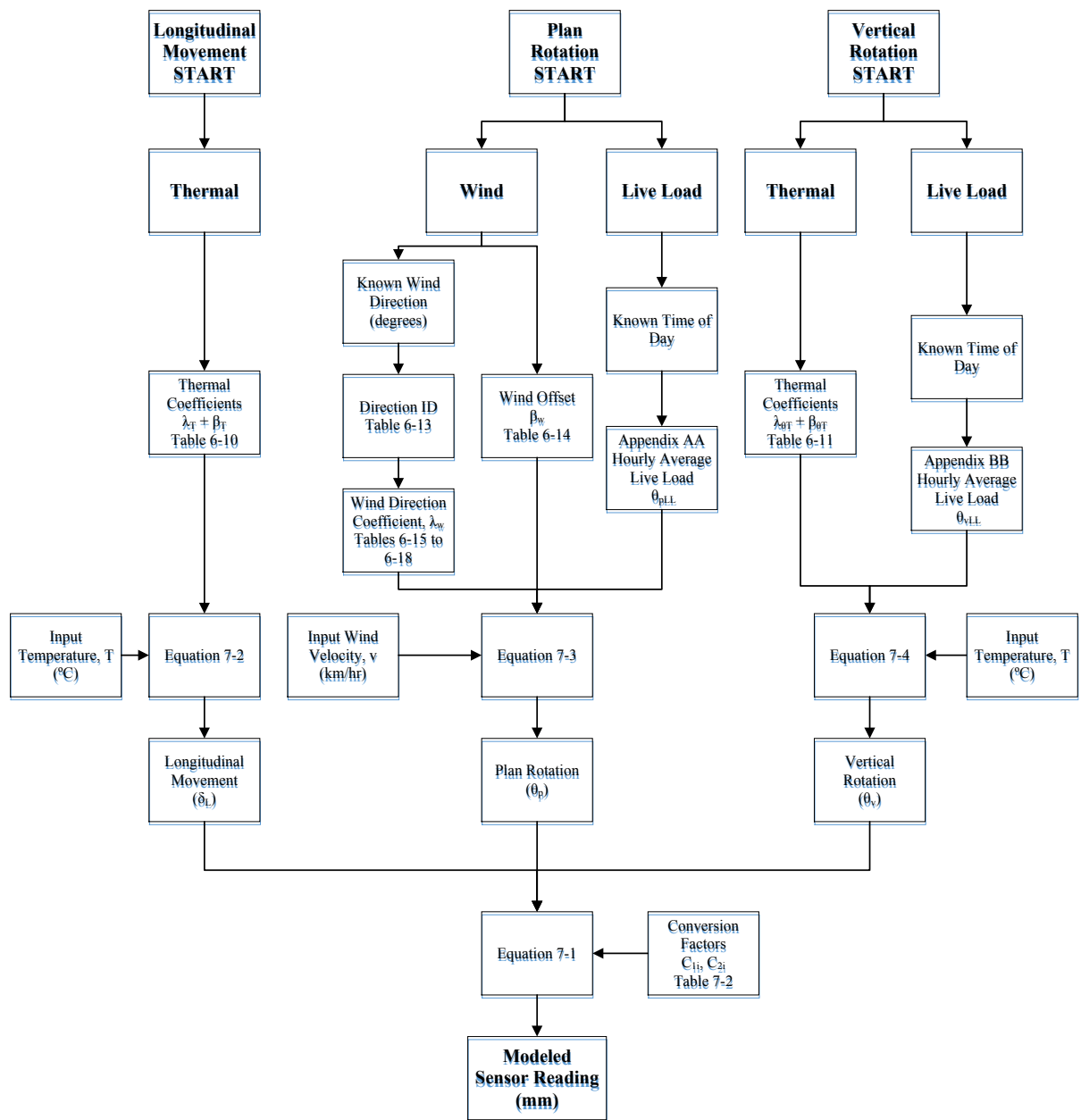
Figure 7.1: Flow chart of sensor model calculation process

Example of Sensor Model Calculation:

Dartmouth Main Span North Bottom Sensor (G2) Example:

March 3rd, 2013 12:32PM

Temperature = 1.7 °C

Wind = 27.7 km/hr

Direction = 55°

Longitudinal Movement

From Table 6.10 linear thermal coefficients for DMT MS

$$\lambda_T = 3.33$$

$$\beta_T = -23.0$$

$$\delta_L = \lambda_T * T + \beta_T$$

$$\delta_L = 3.33*(1.7°C) - 23.0$$

$$\boldsymbol{\delta_L = -17.34mm}$$

Plan Rotation

From Table 6.13 wind direction ID

55° = Direction 1

From Table 6.14 wind offset for DMT MS

$$\beta_W = -0.015°$$

From Table 6.15 wind direction coefficient for Direction 1 DMT MS

$$\lambda_W = 2.78 \times 10^{-5}$$

From Appendix E plan rotation hourly average for 1PM DMT MS

$$\theta_{pLL} = 0.0016°$$

$$\theta_p = \lambda_W * v^2 + \beta_W + \theta_{pLL}$$

$$\theta_p = 2.78\text{x}10^{-5}*(27.7\text{km/hr})^2 - 0.015° + 0.0016°$$

$$\boldsymbol{\theta_p = 0.0078°}$$

Vertical Rotation

From Table 6.11 linear thermal coefficients for DMT MS

$$\lambda_{\theta T} = 0.0052$$

$$\beta_{\theta T} = -0.058$$

From Appendix E vertical rotation hourly average non-working day for 1PM DMT MS

$$\theta_{vLL} = -0.012°$$

$$\theta_v = \lambda_T * T + \beta_T + \theta_{vLL}$$

$$\theta_v = 00.0052(1.7°C) - 0.058 - 0.012$$

$$\boldsymbol{\theta_v = -0.061°}$$

Rotational Conversion Factors

From Table 7.2 rotational conversion factors for DMT MS, G2

$$C_{12} = -5750$$

$$C_{22} = 640$$

Combine Movements

$$G_2 = \delta_L + C_{12}\tan(\theta_p) + C_{22}\tan(\theta_v)$$

$$G_2 = -17.34 + -5750*\tan(0.0078°) + 640*\tan(-0.061°)$$

$$G_2 = -17.34\text{mm} + -0.78\text{mm} + -0.68$$

$$\boldsymbol{G_2 = \textbf{-18.80 mm}}$$

Actual monitored reading = -18.42 mm

Figure 7.2: Example of sensor model – DMT MS G2

7.1.1 Comparison of Models

The models were compared to the original monitored data to assess their accuracy in predicting the overall sensor readings. As mentioned earlier, the weather data (wind speed and direction) was recorded at a different frequency than the sensor data. It was necessary to average the sensor data to match the frequency of the weather data in order to compare the models to monitored data. Figure 7.3 shows the comparison of the calculated sensor readings from the models to the averaged field measurements for DMT MS north bottom sensor. Differences were calculated as Actual Observation − Model Prediction. Figure 7.4 shows the distribution of differences between the actual data and the model. It can be seen that over 90% of the predicted data from the models falls within +/- 7.5 mm of the observed data. Since the total observed movement was approximately 180 mm it can be concluded that the DMT MS north bottom sensor is within 10% accuracy of the total annual movement, 90% of the time. Table 7.3 and Table 7.4 show the observed maximum and minimum sensor reading compared to the maximum and minimum calculated from the models for all main span sensors and side span sensors, respectively. All main span sensors, DMT and HMT, were found to be within the same accuracy as the shown DMT MS north bottom sensor. It was found that 90% of the predicted data from the side span sensor models fell within +/- 5 mm of the observed data. The total observed movement of the side span was approximately 100 mm therefore it can also be concluded that the side span sensor models are within 10% accuracy of the total annual movement, 90% of the time. Appendix F contains complete model comparison plots and distribution of differences for all sensors
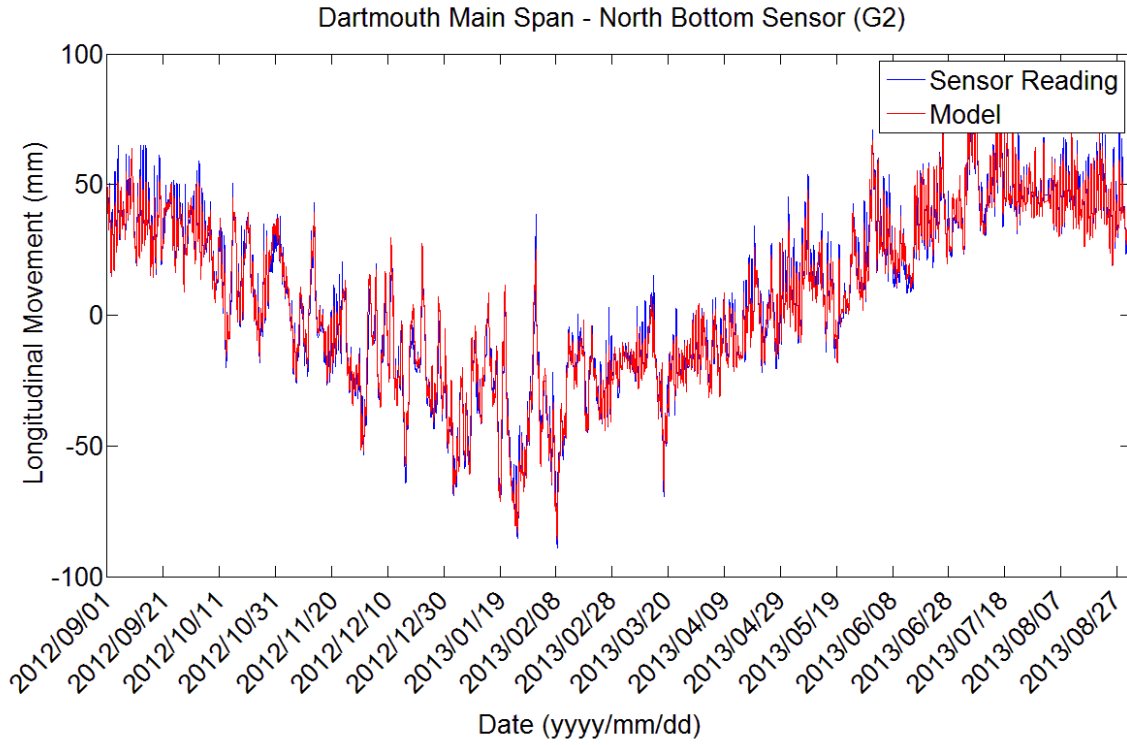
Figure 7.3: Comparison of modeled sensor data to actual data
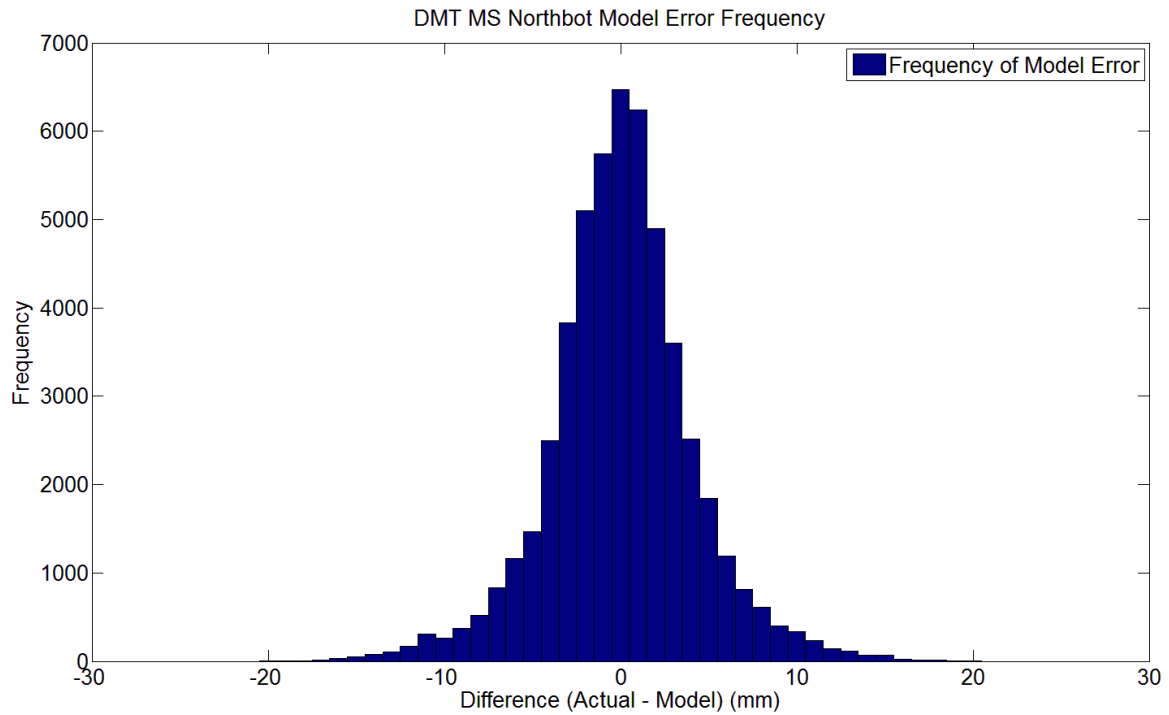
Figure 7.4: Histogram of model residuals for DMT MS North bottom sensor

82

Table 7.3: Comparison of observed max and min to modeled max and min – Main Span

Main Span Sensor	Observed		Modeled	
	Min (mm)	Max (mm)	Min (mm)	Max (mm)
DMT Northtop	-85	84	-85	86
DMT Northbot	-89	87	-86	88
DMT Southtop	-88	86	-85	86
DMT Southbot	-92	86	-89	89
HMT Northtop	-98	91	-105	89
HMT Northbot	-100	93	-105	90
HMT Southbot	-102	90	-109	91
HMT Southtop	-100	88	-105	89

Table 7.4: Comparison of observed max and min to modeled max and min – Side Span

Side Span Sensor	Observed		Modeled	
	Min (mm)	Max (mm)	Min (mm)	Max (mm)
DMT Northtop	-50	51	-47	50
DMT Northbot	-50	52	-47	50
DMT Southtop	-49	50	-47	49
DMT Southbot	-52	50	-48	50
HMT Northtop	-47	37	-47	40
HMT Northbot	-50	38	-49	41
HMT Southbot	-47	37	-47	40
HMT Southtop	-47	36	-47	40

The differences from observation and model will now be considered the residuals of the model and will be further investigated in the next chapter. A summary of the residuals for all sensors can be seen in Table 7.5 and Table 7.6 for main span sensors and side span sensors, respectively.

Table 7.5: Model residuals – Main Span

Main Span Sensor	Average Residuals (mm)	Standard Deviation of Residuals (mm)	Total Monitored Movement Range (mm)
DMT Northtop	-0.11	4.11	169
DMT Northbot	0.04	4.10	176
DMT Southtop	0.19	4.16	174
DMT Southbot	-0.22	4.23	178
HMT Northtop	-0.20	4.90	189
HMT Northbot	-0.19	4.98	193
HMT Southbot	0.22	5.03	192
HMT Southtop	-0.47	4.95	188

Table 7.6: Model residuals – Side Span

Side Span Sensor	Average Residuals (mm)	Standard Deviation of Residuals (mm)	Total Monitored Movement Range (mm)
DMT Northtop	0.09	3.55	101
DMT Northbot	0.83	3.35	102
DMT Southtop	0.47	3.19	99
DMT Southbot	-0.03	2.90	102
HMT Northtop	0.16	3.32	84
HMT Northbot	-0.04	3.24	88
HMT Southbot	0.28	3.07	84
HMT Southtop	0.02	3.21	83

7.2 Bearing and Expansion Joint Predictions from Sensor Models

For a design application, the sensor models can be used to define movements at two points of interest. The first point is the location of the sliding bearing relative to the centerline of the main tower, Figure 5.2. A diagram of this location can be seen below in Figure 7.5 where 'BP' represents bearing position, which is the distance from centerline of main tower to centerline of sliding bearing. The second point of interest the total gap opening at the deck level. This gap would be accommodated by the expansion joint to bridge between the ends of the main span roadway and the side span roadway at the main tower locations, Figure 3.12. Figure 7.6 shows the orientation of the expansion joint opening with respect to sensor locations. E.J.G represents the total expansion joint gap, which is the distance from the end of the main span to the end of the side span at the main tower locations.
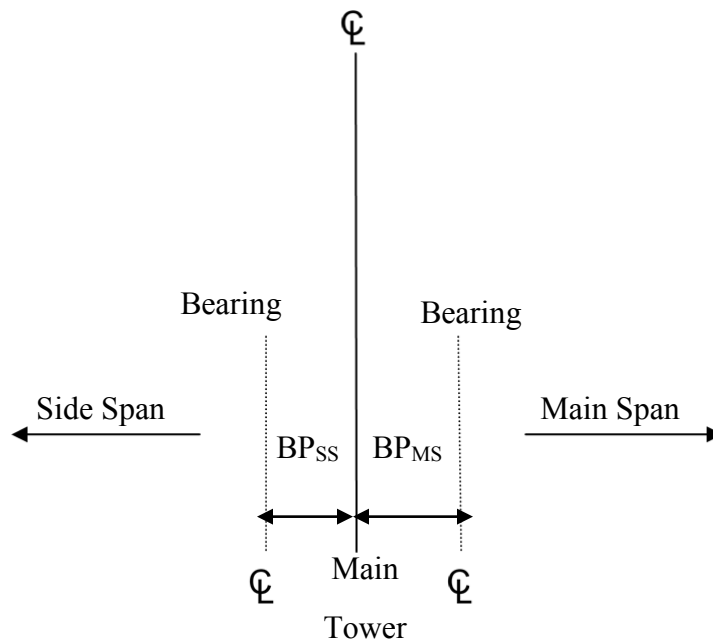
Figure 7.5: Orientation of bearing position (not to scale)
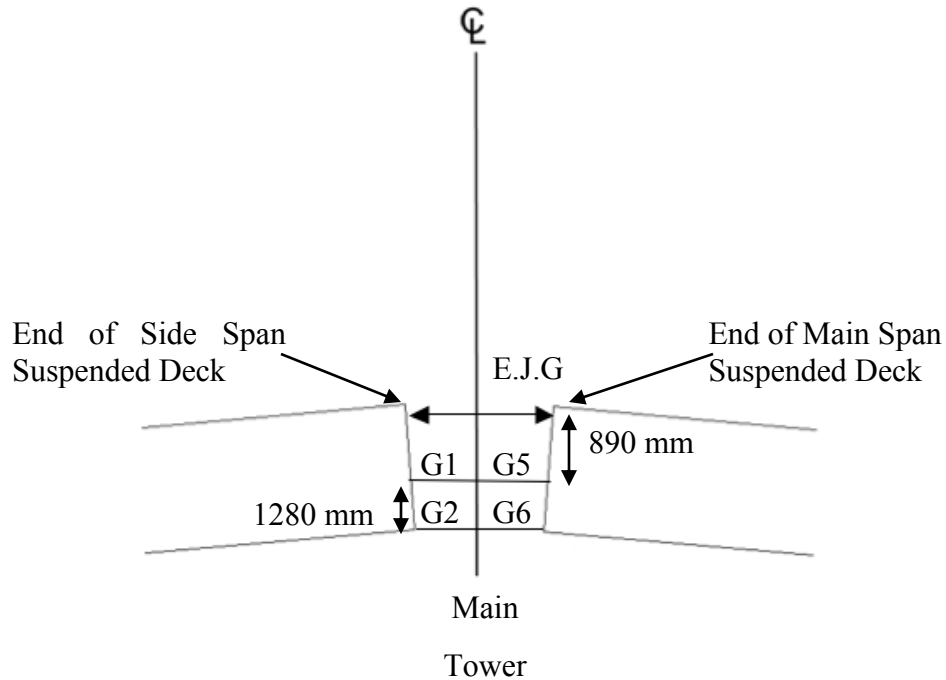
Figure 7.6: Orientation of expansion joint opening (not to scale)

7.2.1 Bearing Position

As outlined in Chapter 5, the bottom sensors were attached to the bearing crosshead; therefore these sensors are monitoring the bearing position. An equation can be developed for each bearing, north side and south side for each span. These can be seen below in Equation 7-5a to Equation 7-5d. It should be noted that these four equations could be used for either DMT or HMT, by using the appropriate span sensors. REF refers to the reference measurement taken at the time of zeroing the data. This reference measurement is the distance from the centerline of the bearing to the centerline of the main tower when the sensor reading was manually zeroed. The reference measurements can be seen below in Table 7.7.

$$BP_{MS, \text{South}} = REF - G2 \qquad \textbf{[7-5a]}$$

$$BP_{MS, \text{North}} = REF - G4 \qquad \textbf{[7-5b]}$$

$$BP_{SS, \text{South}} = REF - G6 \qquad \textbf{[7-5c]}$$

$$BP_{SS, \text{North}} = REF - G8 \qquad \textbf{[7-5d]}$$

where: BP   = bearing position – distance from centerline of bearing to centerline of main tower (mm)

REF   = reference measurement (mm)

Table 7.7: Reference measurements for bearing position equations

Bearing Location	Reference Measurement** (mm)
DMT MS South	336
DMT MS North	338
DMT SS South	415
DMT SS North	420
HMT MS South	324
HMT MS North	301
HMT SS South	389
HMT SS North	418

**Centerline of bearing to centerline of main tower

7.2.2 Expansion Joint Gap

The total expansion joint gap consists of the distance from the centerline of the tower to the end of the main span deck and the distance from the centerline of the tower to the end of the side span deck. By using simple geometry, equations can be formulated to define the total expansion joint opening at deck level for the north and south side at each tower. These equations can be seen below in Equation 7-6a and Equation 7-6b. REF refers to the expansion joint opening when the data was zeroed. These reference measurements can be seen in Table 7.8.

$$E.J.G_{\text{South}} = REF - (1.7*G1 - 0.7*G2) - (1.7*G5 - 0.7*G6) \qquad \textbf{[7-6a]}$$

$$E.J.G_{\text{North}} = REF - (1.7*G3 - 0.7*G4) - (1.7*G7 - 0.7*G8) \qquad \textbf{[7-6b]}$$

where: E.J.G = expansion joint gap – distance from end of main span roadway to side span roadway (mm)

Table 7.8: Reference measurements for expansion joint gap equations

Expansion Joint Location	Reference Measurement** (mm)
DMT South	751
DMT North	758
HMT South	713
HMT North	719

**End of main span deck to end of side span deck

Chapter 8: Discussion of Model Residuals

Figure 8.1 shows the residuals after subtracting the estimate given by Equation 7-1 from the observed values. The observed value is the averaged monitored sensor reading as discussed in Section 7.1.1. Similar residuals were calculated for each longitudinal displacement sensor. The residuals show an annual cyclic trend that can be predicted, as discussed next.

8.1 Annual Variation

In an attempt to identify whether there was an annual trend in the residual data and its parameters, a moving average was performed on each residual data set. A moving average is a method to smooth scattered data by averaging different subsets of data, creating a series of averages (Kutner et al., 2005). Equation 8-1 describes the moving average. The residuals for each longitudinal sensor were averaged using different window sizes until a relatively smooth curve was obtained. An example of the window averaged residuals for DMT MS north bottom sensor can be seen in Figure 8.2. For this sensor a window width, n, of 12,500 was found to be the best for an approximately smooth curve. As seen in Figure 8.2, a cosine curve is matched to the residuals from window averaging the data. A similar cosine curve was found for all sensors, both MS and SS. The cosine correlation function was fit to the residuals data (Figure 8.1) through MATLAB's curve fitting toolbox using the parameters from Figure 8.1 as original guesses. Table 8.1 lists the fitted correlation functions for each sensor. These functions will now be considered as the annual variation functions.

$$X_T(0) = \frac{1}{n}\sum_{i=1}^{n} x_i \qquad\qquad \textbf{[8-1]}$$

$$X_T(i) = X_T(i-1) - \frac{1}{n}(x_i - x_{n+i})$$

where: X_T = window averaged subset

       x_i = residual data

       n   = number of residual data points in averaged subset
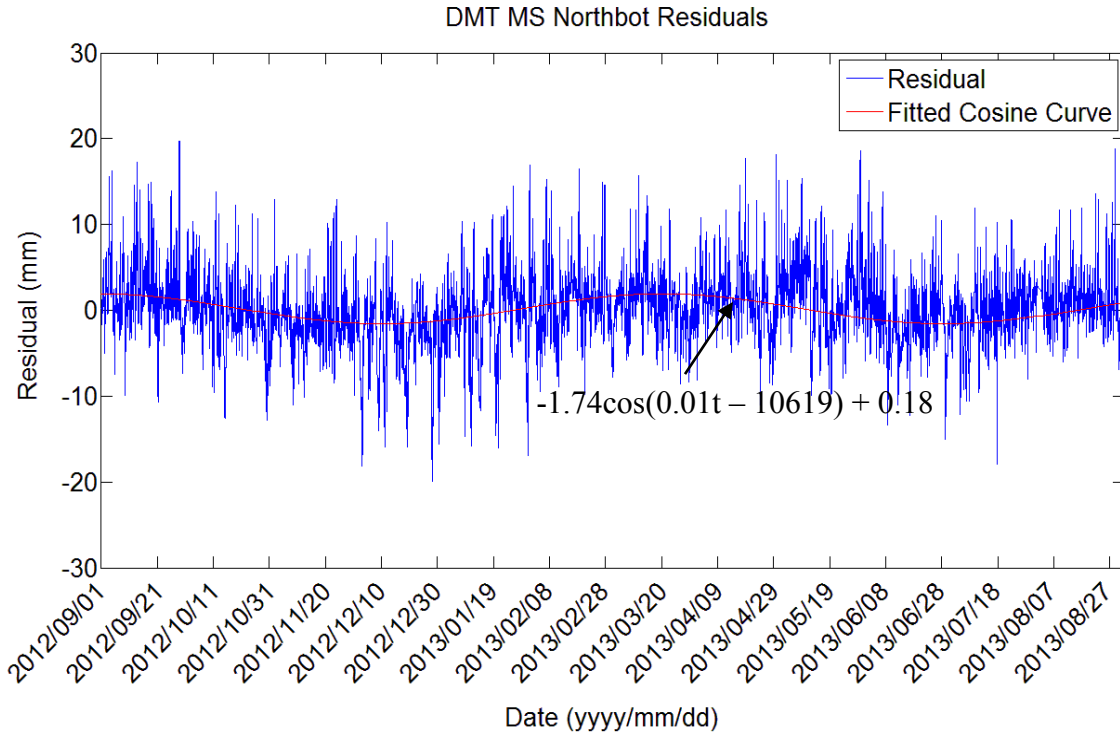
Figure 8.1: Fitted cosine function to model error data, DMT MS North bottom sensor
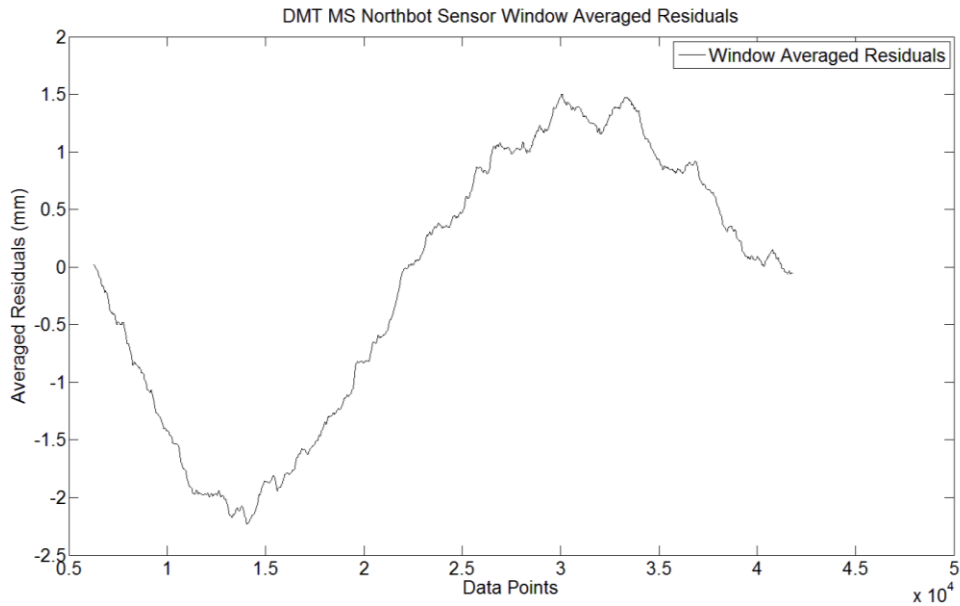
Figure 8.2: Window averaged model errors for DMT MS North bottom sensor

90

Table 8.1: Fitted cosine functions

Sensor	Annual Variation Function
DMT MS North top	$-1.89\cos(0.01t - 10613) + 0.08$
DMT MS North bottom	$-1.74\cos(0.01t - 10619) + 0.18$
DMT MS South top	$-1.58\cos(0.01t - 10629) + 0.27$
DMT MS South bottom	$-1.62\cos(0.01t - 10626) - 0.14$
HMT MS North top	$-1.99\cos(0.01t - 10379) - 0.58$
HMT MS North bottom	$-2.10\cos(0.01t - 10739) - 0.57$
HMT MS South top	$-2.07\cos(0.01t - 10389) - 0.83$
HMT MS South bottom	$-2.08\cos(0.01t - 10391) - 0.12$
DMT SS North top	$-1.23\cos(0.01t - 10614) - 0.04$
DMT SS North bottom	$-1.32\cos(0.01t - 10571) + 0.78$
DMT SS South top	$-0.80\cos(0.01t - 10596) + 0.43$
DMT SS South bottom	$-0.56\cos(0.01t - 10600) - 0.05$
HMT SS North top	$-1.55\cos(0.01t - 10250) + 0.33$
HMT SS North bottom	$-2.39\cos(0.01t - 10208) + 1.03$
HMT SS South top	$-1.24\cos(0.01t - 10313) - 0.24$
HMT SS South bottom	$-1.20\cos(0.01t - 10317) + 0.03$

8.2 Random Error

The annual variations along with the estimates from Equation 7.1 were removed from the original observations for each sensor to yield the final error. Figure 8.3 shows a typical plot of the error for DMT MS Northbot sensor that is to be modeled probabilistically.
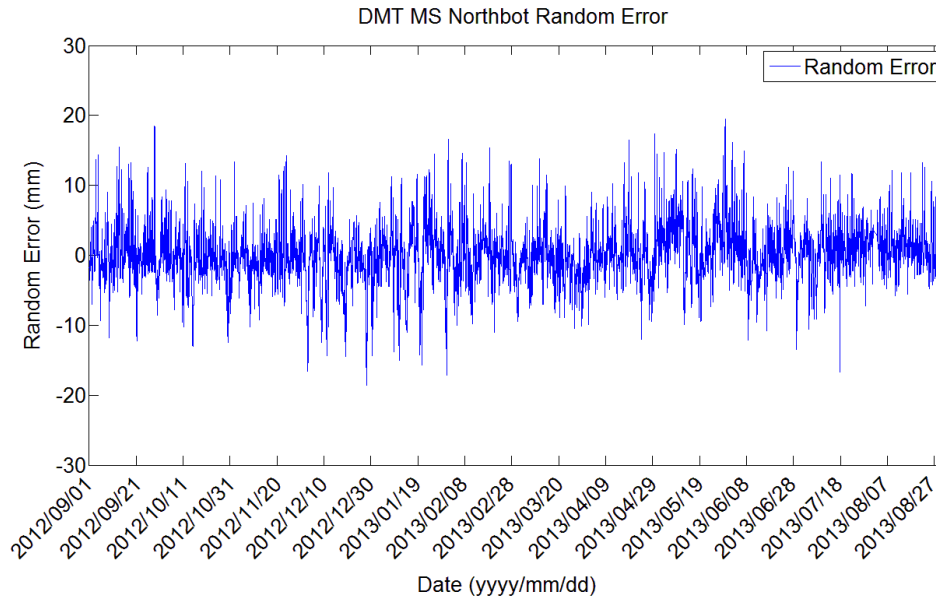
Figure 8.3: Random Error, DMT MS North bottom sensor

8.2.1 Distribution of Random Error

A histogram of the random error for DMT MS north bottom sensor can be seen in Figure 8.4. It can be seen that the random errors are roughly symmetric about 0; therefore the absolute value of the random error was used to determine an appropriate distribution to represent the random error magnitude (Figure 8.5). An exponential distribution was used to describe the relative likelihood that the random error would exceed a given value. The probability density function of the exponential distribution can be seen in Equation 8-2. A histogram of the absolute value of random error can be seen in Figure 8.5 for DMT MS north bottom sensor with its associated distribution. The rate parameter of the exponential distribution for each longitudinal sensor can be seen in Table 8.2.

$$f_x(x) = \lambda e^{-\lambda x} \quad \text{for } x \geq 0 \qquad \textbf{[8-2]}$$

where: λ = rate parameter
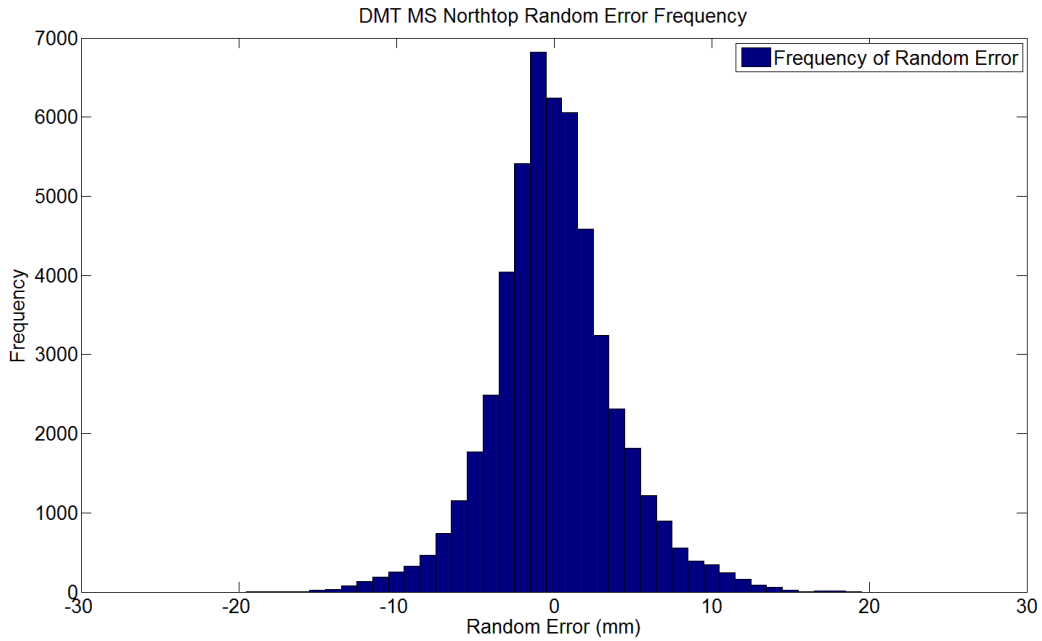
Figure 8.4: Histogram of random error, DMT MS North bottom sensor

$$f_x(x) = 0.346e^{-0.346x}$$
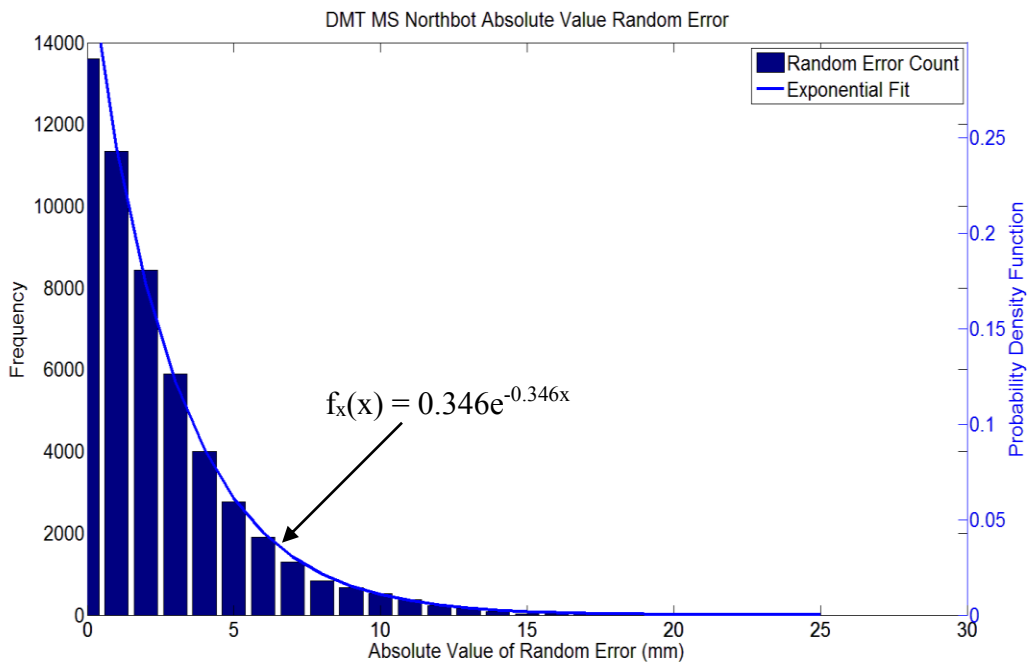
Figure 8.5: Histogram of absolute random error, DMT MS North bottom sensor

Table 8.2: Rate parameter (λ) for exponential distributions

Sensor	Rate parameter (λ)
DMT MS North top	0.344
DMT MS North bottom	0.346
DMT MS South top	0.334
DMT MS South bottom	0.332
HMT MS North top	0.277
HMT MS North bottom	0.273
HMT MS South top	0.275
HMT MS South bottom	0.271
DMT SS North top	0.281
DMT SS North bottom	0.296
DMT SS South top	0.308
DMT SS South bottom	0.332
HMT SS North top	0.434
HMT SS North bottom	0.447
HMT SS South top	0.434
HMT SS South bottom	0.447

Chapter 9: Discussion of Extreme Movement for Individual Model Inputs

The Canadian Highway Bridge Design Code (CHBDC CAN/CSA-S6-06) provides guidelines for the design of bearing and expansion joint systems. These guidelines are referenced in Section 11 of the code, which provides design values with respect to extreme environmental conditions such as thermal range and maximum expected wind events for different return periods. These extreme environmental conditions will be used to estimate extreme movement due to thermal and wind variations. In the case of extreme movements due to live load, a statistical approach will be used. A statistical approach was used due to the fact that traffic data was not available as mentioned previously. Movements due to traffic were considered to be random.

9.1   Extreme Temperature Range

CHBDC recommends that the design temperature range shall be the difference between the maximum and minimum effective temperatures specified in the code. The maximum and minimum mean effective temperature recommended for Halifax, Nova Scotia was 51°C and -36°C, respectively. The temperature values were used as inputs for the longitudinal and vertical rotation thermal models from Chapter 6. Table 9.1 shows the maximum and minimum longitudinal movement due to thermal effects computed using design temperatures specified by CHBDC. Table 9.2 shows the maximum and minimum vertical rotation due to thermal effects.

Table 9.1: Extreme longitudinal movements due to temperature

Span	Maximum (mm)	Minimum (mm)
DMT MS	147	-143
HMT MS	155	-170
DMT SS	84	-80
HMT SS	70	-76

Table 9.2: Extreme vertical rotation due to temperature

Span	Maximum (Degrees)	Minimum (Degrees)
DMT MS	0.21	-0.25
HMT MS	0.17	-0.18
DMT SS	0.10	-0.10
HMT SS	0.04	-0.02

9.2 Extreme Wind Event

CHBDC states that the hourly mean reference wind pressure shall be specified for a return period of 100 years for bridge structures with any span 125 m long or longer. The reference wind pressure for Halifax, Nova Scotia from the CHBDC is 670 Pa, which corresponds to 116 km/hr wind speed. The assumed wind direction is recommended to be perpendicular to the longitudinal axis for a straight structure. This would correspond to perpendicular directions 1 and 2 corresponding to 112.75° to 135.25° and 292.75° to 315.25°, respectively. Table 9.3 and 9.4 show the extreme plan rotations for all spans due to the 100-year return wind speed.

Table 9.3: Extreme plan rotation due to 100-year return wind speed – Perpendicular Direction 1

Perpendicular Direction 1 (112.75° to 135.25°)		
Span	Directional Coefficient	Plan Rotation (degrees)
DMT MS	-2.77×10^{-5}	-0.37
HMT MS	-2.54×10^{-5}	-0.34
DMT SS	-3.12×10^{-6}	-0.04
HMT SS	-5.52×10^{-6}	-0.07

Table 9.4: Extreme plan rotation due to 100-year return wind speed – Perpendicular Direction 2

Perpendicular Direction 2 (292.75° to 315.25°)		
Span	**Directional Coefficient**	**Plan Rotation (degrees)**
DMT MS	3.95×10^{-5}	0.53
HMT MS	4.23×10^{-5}	0.57
DMT SS	5.67×10^{-6}	0.08
HMT SS	1.75×10^{-6}	0.02

9.3   Gumbel Distribution of Live Load

Traffic data was not available for this project. Therefore it was not possible to correlate traffic loads with response in vertical and plan rotations. Once wind and thermal responses were removed from the rotations, the remainders were assumed to be caused by live load. These responses to live load can be considered random variables. A statistical approach was chosen to predict the extreme rotations due to live load using the monitored data.

Liu et al. (2009) investigated several possible distributions for modeling bridge responses due to changes in live load. They found that the Gumbel Distribution provided an acceptable fit to the monitored data. The Gumbel Distribution is as follows;

$$F_{Xn}(x) = \exp(\exp(-\alpha_n(x-u_n))) \qquad \textbf{[9-1]}$$

where: α_n = an inverse measure of the dispersion of X_n

   u_n = the characteristic largest value of X

The graphical approach outlined by Ang and Tang (1984) was used to estimate the Gumbel constants (α_n and u_n). In Ang and Tang's approach, the cumulative distribution function (CDF) of X_n is plotted on Gumbel Probability paper. The slope of the linear best-fit line represents α_n. The value read off the vertical axis at the point where the best-fit line intercepts the s-axis value of zero is equal to u_n.

9.3.1 Extreme Vertical Rotation Live Load

The procedure for extreme vertical rotation predication was adapted from Liu et al (2009). Their work dealt with extreme predication of strain due to live load variations. This method consisted of four main steps:

1. hourly maximum and minimum rotation;
2. histograms for maximum and minimum rotation;
3. Gumbel parameters for each histogram;
4. extreme value prediction.

The maximum and minimum vertical rotations were determined for each hour throughout the monitoring period from the vertical rotation data once the thermal trend had been removed. For each span, two histograms were created from the peak rotation data for both the negative rotation and positive rotation. Both positive and negative rotations were sorted into bins starting at bin 0 which represents zero vertical rotation with bin numbers increasing or decreasing bins for positive and negative directions respectively.   The cumulative distribution of peak vertical rotation in the positive direction was plotted on Gumbel Probability Paper to determine the Gumbel constants. Figure 9.1 shows an example of the Gumbel Probability plot for DMT MS positive vertical rotation. Table 9.5 show the determined Gumbel constants for all spans for the positive and negative vertical rotations. Once the Gumbel distributions were determined, extreme rotation predictions could be computed. The Gumbel Approximation in Equation 9-1 can be rearranged to result in a maximum expected rotation, shown in Equation 9-2. Refer to Appendix G for all vertical rotation Gumbel plots.

$$\theta_{V,max} = u_n - \frac{1}{\alpha_n} \ln\left[-\ln\left(1 - \frac{1}{N_T}\right)\right]$$ [9-2]

where: $\theta_{V,\,max}$ = most likely maximum vertical rotation (degrees)

N_T = number of traffic events for the selected period

N_T for the monitoring period was summed from the histogram data. It was assumed that the number of traffic events for the monitored year would remain constant with time. This was decided since there were no actual data to quantify the volume of traffic. Table 9.6 and Table 9.7 show the probably extreme vertical rotation magnitude determined for 1 through 75 years into the future using Equation [9-2] for positive and negative rotation, respectively.
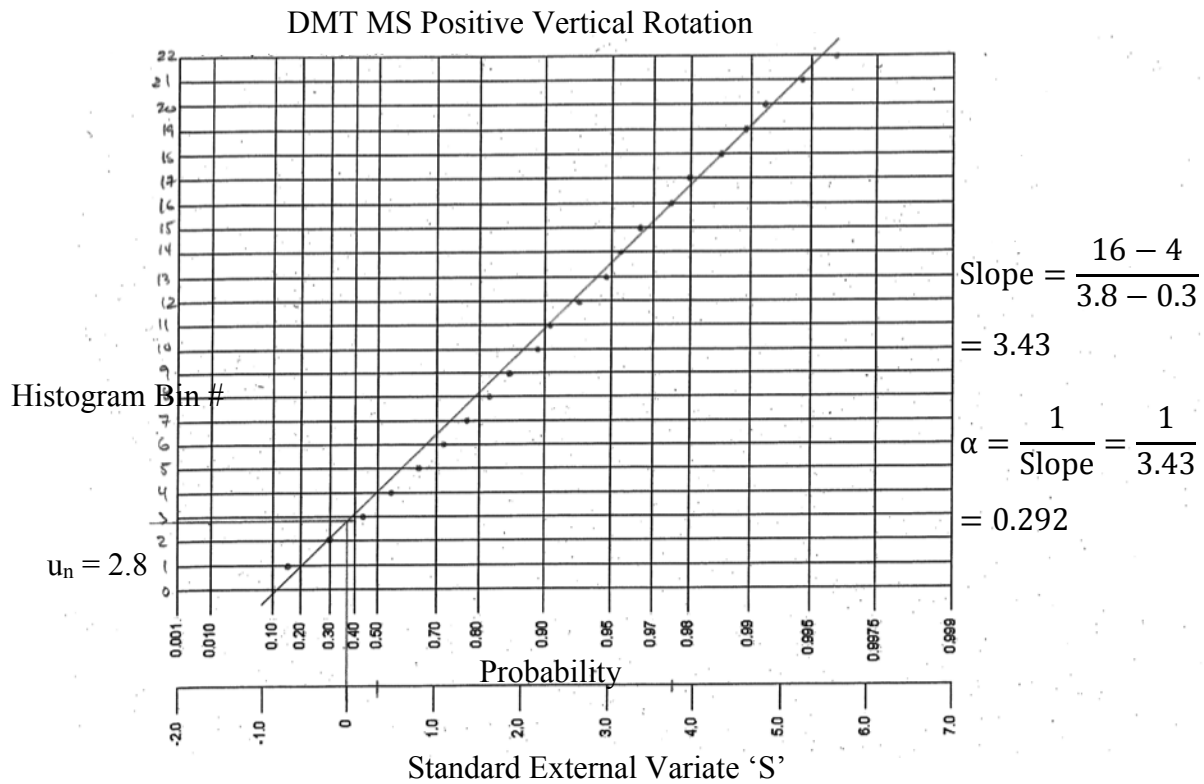
Figure 9.1: Gumbel distribution curve fit – DMT MS Positive Vertical Rotation

99

Table 9.5: Gumbel constants for positive and negative vertical rotation

Span	Vertical Rotation Gumbel Parameters			
	Positive Rotation		Negative Rotation	
	u_n	α_n	u_n	α_n
DMT MS	2.8	0.29	4.0	0.40
HMT MS	2.0	0.29	4.1	0.30
DMT SS	2.5	0.31	2.9	0.41
HMT SS	3.0	0.35	4.0	0.41

Table 9.6: Most likely maximum positive vertical rotation due to live load predictions

Extreme Positive Vertical Rotation (degrees)				
Years	DMT MS	HMT MS	DMT SS	HMT SS
1	0.205	0.195	0.175	0.185
2	0.215	0.205	0.180	0.195
3	0.225	0.215	0.190	0.200
5	0.235	0.225	0.195	0.210
10	0.245	0.235	0.205	0.220
20	0.255	0.245	0.215	0.230
50	0.270	0.265	0.230	0.245
75	0.280	0.270	0.235	0.255

Table 9.7: Most likely maximum negative vertical rotation due to live load predictions

Extreme Negative Positive Vertical Rotation (degrees)				
Years	DMT MS	HMT MS	DMT SS	HMT SS
1	-0.160	-0.190	-0.155	-0.155
2	-0.165	-0.205	-0.165	-0.165
3	-0.170	-0.210	-0.170	-0.170
5	-0.180	-0.220	-0.175	-0.175
10	-0.185	-0.230	-0.180	-0.185
20	-0.195	-0.240	-0.190	-0.195
50	-0.205	-0.255	-0.200	-0.205
75	-0.215	-0.265	-0.205	-0.210

9.3.2 Extreme Plan Rotation Live Load

The procedure for extreme plan rotation predications was identical to that for extreme vertical rotation predictions. In this case, maximum and minimum plan rotations were collected from the plan rotation data after the effects of wind variations was removed. Figure 9.2 shows an example of the Gumbel Probability plot for DMT MS positive plan rotation. Table 9.8 show the determined Gumbel constants for all spans for the positive and negative plan rotations. Table 9.9 and 9.10 show the probably extreme plan rotation magnitude determined for 1 through 75 years into the future using Equation [9-2] for positive and negative rotation, respectively. Refer to Appendix G for all plan rotation Gumbel plots.

$$\text{Slope} = \frac{16 - 4}{2.4 - 0.2}$$

$$= 5.45$$

$$\alpha = \frac{1}{\text{Slope}} = \frac{1}{5.45}$$

$$= 0.183$$
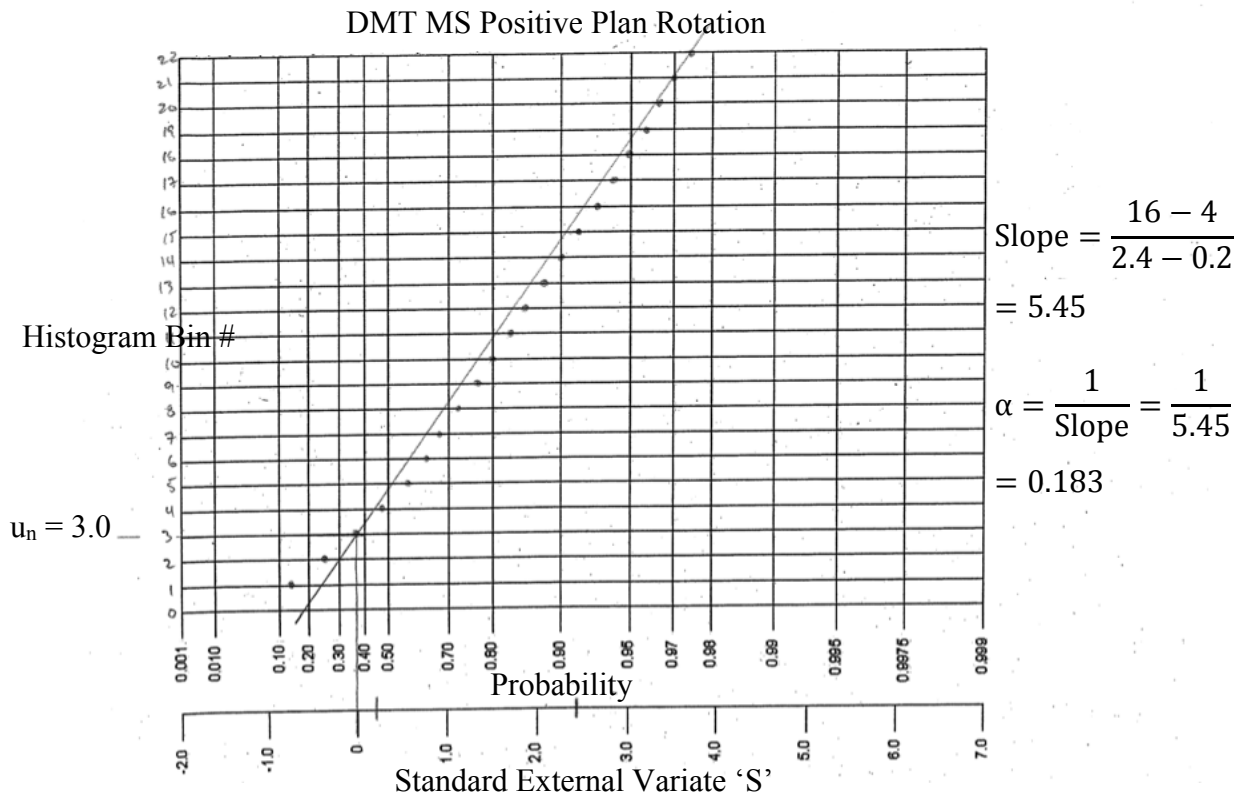
Figure 9.2: Gumbel distribution curve fit – DMT MS Positive Plan Rotation

Table 9.8: Gumbel Constants for Positive and Negative Plan Rotation

| Span | Plan Rotation Gumbel Parameters | | | |
| | Positive Rotation | | Negative Rotation | |
	u_n	α_n	u_n	α_n
DMT MS	3.0	0.18	2.8	0.24
HMT MS	4.0	0.19	3.5	0.27
DMT SS	3.8	0.21	4.1	0.20
HMT SS	7.3	0.17	8.2	0.17

Table 9.9: Most likely maximum positive plan rotation due to live load predictions

| Extreme Positive Plan Rotation (degrees) | | | | |
Years	DMT MS	HMT MS	DMT SS	HMT SS
1	0.058	0.058	0.027	0.034
2	0.062	0.062	0.028	0.036
3	0.064	0.064	0.029	0.038
5	0.067	0.067	0.030	0.039
10	0.071	0.070	0.032	0.041
20	0.075	0.074	0.034	0.043
50	0.080	0.079	0.036	0.046
75	0.082	0.081	0.038	0.047

Table 9.10: Most likely maximum negative vertical rotation due to live load predictions

| Extreme Negative Plan Rotation (degrees) | | | | |
Years	DMT MS	HMT MS	DMT SS	HMT SS
1	-0.044	-0.041	-0.027	-0.034
2	-0.047	-0.043	-0.029	-0.036
3	-0.048	-0.045	-0.030	-0.038
5	-0.051	-0.047	-0.031	-0.039
10	-0.053	-0.049	-0.033	-0.041
20	-0.056	-0.052	-0.035	-0.043
50	-0.060	-0.055	-0.037	-0.046
75	-0.062	-0.057	-0.038	-0.047

9.4 Extreme Random Error Prediction

The random errors are not independent of one another. In order to characterize the random error for extreme value predictions, the effective number of independent observations must be determined. To do so, the random errors must be modeled with correlation between random variables. Random field theory can be used to model these errors, which involves estimating the mean, variance, and correlation length. Mean and variance can be estimated from the exponential distributions discussed in Section 8.2.

Correlation length (θ) is a measure of the distance within which points are significantly correlated. Points separated by a distance smaller than θ will have a high degree of correlation while points separated by a distance much greater than θ will have little correlation. The approach used to estimate θ was based on the concept of best fitting the theoretical correlation model $\rho(\tau)$, Equation 9-4, to the estimated correlation function.

$$\rho(\tau) = exp\left\{\frac{-2|\tau|}{\theta}\right\}$$
[9-4]

where: τ　　　= distance between data points

The correlation function and correlation length is estimated from the random error process shown in Figure 8.3 according to the methodology suggested by Lloret-Cabot et al. (2014). Correlation lengths were determined for each sensor.

In order to use extreme value theory we need to know the effective number of independent random variables over any time interval of the random process. If we know the correlation length in units of number of observations, then the effective number of observations, n_eff, can be approximated. Since we know the number of observations, n, from the monitoring year, the number of effective observations can be approximated as n/θ. Table 9.11 and Table 9.12 show the correlation length and effective number of independent observations for all sensors.

Table 9.11: Correlation length and effective number of independent observations, MS

Main Span Sensor	Correlation Length (θ)	Number of Observations	Effective Number of Independent Observations
DMT MS North top	109.1	52213	479
DMT MS North bottom	96.4	52213	542
DMT MS South top	120.2	52213	435
DMT MS South bottom	105.9	52213	493
HMT MS North top	54.2	51637	953
HMT MS North bottom	59.5	51637	868
HMT MS South top	51.6	51637	1001
HMT MS South bottom	60.1	51637	860

Table 9.12: Correlation length and effective number of independent observations, SS

Side Span Sensor	Correlation Length (θ)	Number of Observations	Effective Number of Independent Observations
DMT SS North top	36.1	52213	1446
DMT SS North bottom	36.1	52213	1446
DMT SS South top	36.2	52213	1442
DMT SS South bottom	35.7	52213	1463
HMT SS North top	104.4	51637	495
HMT SS North bottom	115.3	51637	448
HMT SS South top	101.0	51637	511
HMT SS South bottom	127.3	51637	406

Assuming that the number of independent observations for one year remains constant for each sensor, we can predict the characteristic largest value of random errors over different time spans for each sensor. Table 9.13 and Table 9.14 show the number of independent observations for different time spans for main span and side span, respectively.

Table 9.13: Number of effective independent observations for different time spans, MS

Main Span Sensor	Effective Number of Independent Observations							
	Time Span (Years)							
	1	2	3	5	10	20	50	75
DMT MS North top	479	958	1,437	2,395	4,790	9,580	23,950	35,925
DMT MS North bottom	542	1,084	1,626	2,710	5,420	10,840	27,100	40,650
DMT MS South top	435	870	1,305	2,175	4,350	8,700	21,750	32,625
DMT MS South bottom	493	986	1,479	2,465	4,930	9,860	24,650	36,975
HMT MS North top	953	1,906	2,859	4,765	9,530	19,060	47,650	71,475
HMT MS North bottom	868	1,736	2,604	4,340	8,680	17,360	43,400	65,100
HMT MS South top	1,001	2,002	3,003	5,005	10,010	20,020	50,050	75,075
HMT MS South bottom	860	1,720	2,580	4,300	8,600	17,200	43,000	64,500

Table 9.14: Number of effective independent observations for different time spans, SS

Side Span Sensor	Effective Number of Independent Observations							
	Time Span (Years)							
	1	2	3	5	10	20	50	75
DMT SS North top	1,446	2,892	4,338	7,230	14,460	28,920	72,300	108,450
DMT SS North bottom	1,446	2,892	4,338	7,230	14,460	28,920	72,300	108,450
DMT SS South top	1,442	2,884	4,326	7,210	14,420	28,840	72,100	108,150
DMT SS South bottom	1,463	2,926	4,389	7,315	14,630	29,260	73,150	109,725
HMT SS North top	495	990	1,485	2,475	4,950	9,900	24,750	37,125
HMT SS North bottom	448	896	1,344	2,240	4,480	8,960	22,400	33,600
HMT SS South top	511	1,022	1,533	2,555	5,110	10,220	25,550	38,325
HMT SS South bottom	406	812	1,218	2,030	4,060	8,120	20,300	30,450

Since the absolute value of the random error generally followed an exponential distribution for all sensors, it was determined that the extreme random error distribution followed a Type 1 asymptotic distribution (Kutner et al., 2005). Table 9.15 and Table 9.16 show the predicted most likely extreme random error for different time spans for main span and side span, respectively.

Table 9.15: Predicted most likely extreme random error for different time spans, MS

Main Span Sensor	Predicted Extreme Random Error (mm) Years							
	1	2	3	5	10	20	50	75
DMT MS North top	18	20	21	23	25	27	29	31
DMT MS North bottom	18	20	21	23	25	27	29	31
DMT MS South top	18	20	21	23	25	27	29	31
DMT MS South bottom	19	21	22	24	26	28	30	32
HMT MS North top	25	27	29	31	33	36	39	40
HMT MS North bottom	25	27	29	31	33	36	39	41
HMT MS South top	25	27	29	31	33	36	39	41
HMT MS South bottom	25	27	29	31	33	36	39	41

Table 9.16: Predicted most likely extreme random error for different time spans, SS

Side Span Sensor	Predicted Extreme Random Error (mm) Years							
	1	2	3	5	10	20	50	75
DMT SS North top	26	28	30	32	34	37	40	41
DMT SS North bottom	25	27	28	30	32	35	38	39
DMT SS South top	24	26	27	29	31	33	36	38
DMT SS South bottom	22	24	25	27	29	31	34	35
HMT SS North top	14	16	17	18	20	21	23	24
HMT SS North bottom	14	15	16	17	19	20	22	23
HMT SS South top	14	16	17	18	20	21	23	24
HMT SS South bottom	13	15	16	17	19	20	22	23

9.4.1 Extreme Residual Discussion

This chapter discussed the residuals of the monitored data to the modeled predications and how these residuals were accounted for in the long-term joint movement predications. Extreme annual variation error is represented by the maximum and minimum of the sinusoidal correlation functions shown in Table 8-1. Although sinusoidal functions were fitted to each individual sensor, only one set of maximum and minimum values were determined for each span, which represents the maximum and minimum of the sinusoids over the four sensors for each span. The maximum and minimums for each span can be seen in Table 9.17. The most likely extreme random error is represented by the 75-year extreme prediction. Similar to annual variation, random error distributions were determined for each individual sensor however the most likely extreme random error selected for the spans is the largest obtained over the four sensors for each span. Since the random error is actually distributed symmetrical about 0, the 75-year extremes given in Table 9.18 represent the extreme in both directions, positive and negative.

Table 9.17: Extreme correlated error

Span	Extreme Correlated Error	
	Minimum (mm)	Maximum (mm)
DMT MS	1.97	-1.81
HMT MS	1.96	-2.90
DMT SS	2.10	-1.27
HMT SS	2.51	-1.48

Table 9.18: 75-year predicted most likely extreme random error

Span	75-Year Predicted Random Error (mm)
DMT MS	+/- 32
HMT MS	+/- 41
DMT SS	+/- 41
HMT SS	+/- 24

9.5 Summary of Extreme Movements

This chapter discussed the extreme movement predictions for the three sources of movement; thermal, wind, and live load. Table 9.19 shows a summary of the 75-year extreme bearing movement range predictions for each source of movement. The thermal component is the combination of longitudinal thermal movement and thermal vertical rotation for the extreme temperature range. The vertical rotation component was converted from rotational degrees to longitudinal millimeters. The wind component is the initial offset and plan rotation response to the extreme wind event. This plan rotation due to wind was converted from rotational degrees to longitudinal millimeters. The live load component is the 75-year extreme predicted to occur for plan and vertical rotation combined. The rotation due to live load was converted from rotational degrees to longitudinal movement. Figure 9.3 shows the comparison of movement ranges for all sources of movement for all spans.

Table 9.20 shows a summary of the 75-year extreme expansion joint gap range predictions for each source of movement. The only difference between Table 9-19 and Table 9-20 is the movements that contain vertical rotation, thermal and live load, have been adjusted to reflect the longitudinal expansion joint gap at road level. Figure 9.4 shows the comparison of expansion joint gap ranges for all sources of movement for all spans.

These movements all relate to the extreme conditions of thermal, wind, and live load. The likelihood of these extremes to occur simultaneously is extremely small. One would not expect an extreme live load condition to occur during a high wind event. It would be recommended to appropriately factor these extreme movements to account for a probability of occurrence.

Table 9.21 to table 9.23 show summaries of the extreme bearing movement range predictions for 1-year, 20 years, and 50 years, respectively. Table 9.24 to table 9.26 shows summaries of the extreme expansion joint gap range for 1-year, 20 years, and 50 years, respectively. Inputs for extreme temperature and wind for these three time durations were interpolated from the design code.

Table 9.19: 75-Year extreme movement range predictions

75-Year Extreme Bearing Movement Range Predictions (mm)				
Source of Movement	**Span**			
	DMT MS	**HMT MS**	**DMT SS**	**HMT SS**
Thermal[x]	302	333	168	148
Wind[y]	102	122	30	30
Live Load[z]	46	44	26	30
Annual Variation	4	5	4	4
Random Error	64	82	82	48

[x] Longitudinal thermal plus vertical rotation thermal converted to mm

[y] Plan rotation wind plus wind plan rotation offset, converted to mm

[z] Plan rotation plus vertical rotation, converted to mm

Table 9.20: 75-Year extreme expansion joint opening range predictions

75-Year Extreme Expansion Joint Opening Range Predictions (mm)		
Source of Movement	**Expansion Joint**	
	DMT	**HMT**
Thermal[x]	480	487
Wind[y]	132	152
Live Load[z]	87	91
Annual Variation	8	9
Random Error	146	130

[x] Longitudinal thermal plus vertical rotation thermal converted to mm

[y] Plan rotation wind plus wind plan rotation offset, converted to mm

[z] Plan rotation plus vertical rotation, converted to mm
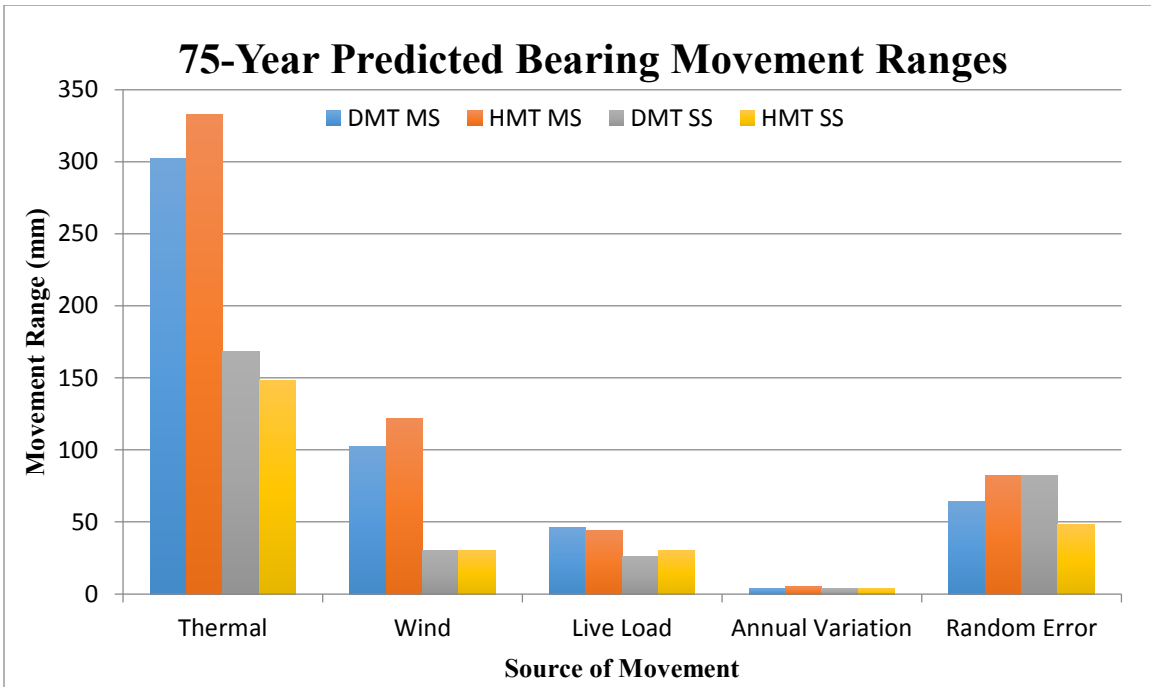
Figure 9.3: Comparison 75-year of bearing movement ranges for all spans
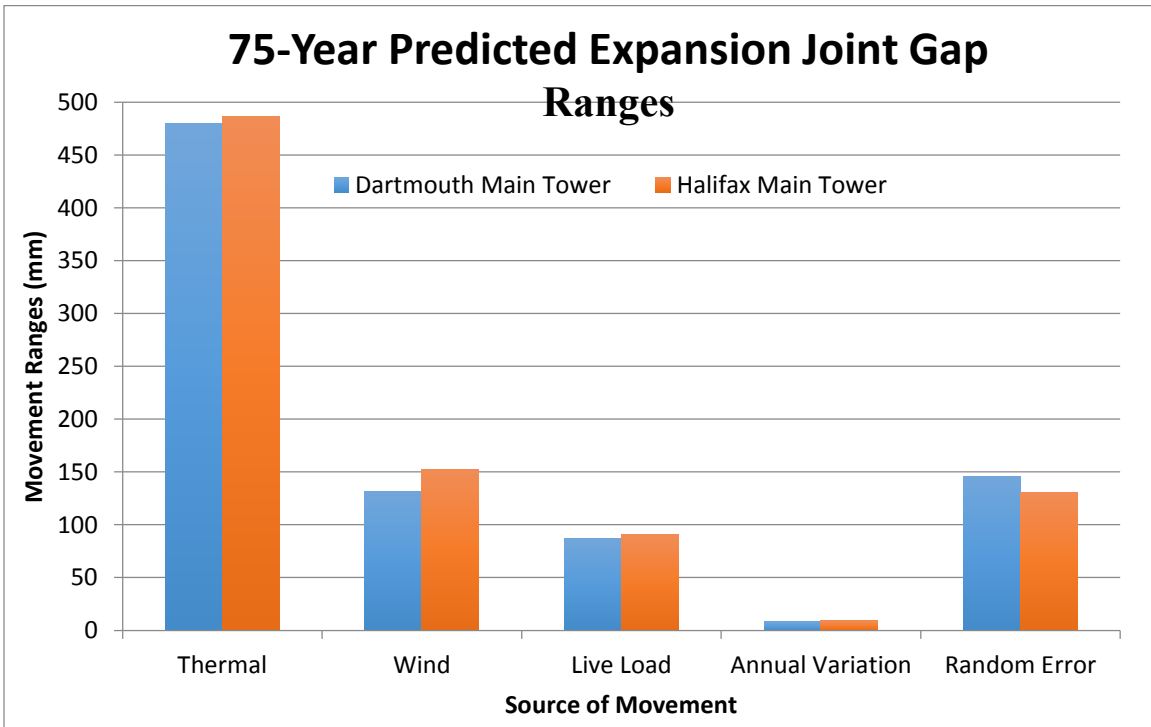
Figure 9.4: Comparison of 75-year expansion joint opening ranges for all spans

Table 9.21: 1-Year extreme movement range predictions

1-Year Extreme Bearing Movement Range Predictions (mm)				
Source of Movement	Span			
	DMT MS	HMT MS	DMT SS	HMT SS
Thermal[x]	180	200	100	87
Wind[y]	48	52	14	16
Live Load[z]	32	32	19	22
Annual Variation	4	5	4	4
Random Error	38	50	52	28

Table 9.22: 20-Year extreme movement range predictions

20-Year Extreme Bearing Movement Range Predictions (mm)				
Source of Movement	Span			
	DMT MS	HMT MS	DMT SS	HMT SS
Thermal[x]	215	238	120	104
Wind[y]	61	66	18	20
Live Load[z]	42	41	23	28
Annual Variation	4	5	4	4
Random Error	54	72	70	42

Table 9.23: 50-Year extreme movement range predictions

50-Year Extreme Bearing Movement Range Predictions (mm)				
Source of Movement	Span			
	DMT MS	HMT MS	DMT SS	HMT SS
Thermal[x]	259	288	145	125
Wind[y]	83	89	24	26
Live Load[z]	44	44	25	29
Annual Variation	4	5	4	4
Random Error	60	78	80	46

Table 9.24: 1-Year extreme expansion joint opening range predictions

1-Year Extreme Expansion Joint Opening Range Predictions (mm)		
Source of Movement	Expansion Joint	
	DMT	HMT
Thermal^x	280	287
Wind^y	62	68
Live Load^z	51	54
Annual Variation	8	9
Random Error	90	78

Table 9.25: 20-Year extreme expansion joint opening range predictions

20-Year Extreme Expansion Joint Opening Range Predictions (mm)		
Source of Movement	Expansion Joint	
	DMT	HMT
Thermal^x	335	342
Wind^y	79	86
Live Load^z	65	69
Annual Variation	8	9
Random Error	124	114

Table 9.26: 50-Year extreme expansion joint opening range predictions

50-Year Extreme Expansion Joint Opening Range Predictions (mm)		
Source of Movement	Expansion Joint	
	DMT	HMT
Thermal^x	404	413
Wind^y	107	115
Live Load^z	69	73
Annual Variation	8	9
Random Error	140	124

9.6 Cumulative Travel of Sliding Bearing

This research focused on the modelling of absolute position of the monitoring sensors. The sensor models were used to develop models for the sliding bearing and the expansion joint. These models can also be used to determine the cumulative travel of both the sliding bearing and the expansion joint. To get an accurate prediction of cumulative travel the necessary inputs of thermal, wind, and live load would require time intervals appropriate for each load case. Thermal changes occur over duration of minutes while wind effects occur over duration of seconds. Live load effects would require an even smaller time interval as the effects occur in a fraction of a second. Table 9.27 shows the cumulative travel of the sliding bearings for each span. Table 9.28 shows the breakdown of the percent movement that each load effect contributes to the total cumulative movement. Inputting the collected temperature data into the thermal models and summing the yearly movement determined the cumulative thermal movement. Summing the average 24-hour live load rotation plots and extrapolating for 365 days determined the cumulative live load. The remainder of cumulative movement was assumed to be caused by wind effects.

Table 9.27: Cumulative travel of sliding bearing for monitoring year

Span	Cumulative Movement (m)
DMT MS	447
HMT MS	314
DMT SS	251
HMT SS	371

Table 9.28: Breakdown of cumulative movement

Span	Thermal	Wind	Live Load
DMT MS	15%	19%	66%
HMT MS	21%	25%	54%
DMT SS	15%	22%	63%
HMT SS	10%	29%	61%

From table 9.21 it can be seen that thermal effects account for the largest amount of bearing position. It can also be seen that wind and live load have a lesser effect to overall bearing position. In context of cumulative movement, from Table 9.28 it can be seen that live load accounts for the largest amount of cumulative movement while wind and thermal have a lesser effect to overall cumulative bearing movement. Although the bearing position showed that live load accounts for minimal movement, live load effects occur at a quick interval. These small movements occurring at a fast rate will accumulate to substantial amount of cumulative movement.

Chapter 10:Conclusions and Recommendations

This thesis described the structural health monitoring system used to collect site-specific data pertaining to a long span bridge. The data was analyzed to identify how the structure responds to variations in thermal, wind, and live load at the expansion joint locations. Numerical models were developed to characterize the identified movement responses. Combining the individual numerical models developed the general sensor equation, Equation 7-1. By knowing the environmental conditions, sensor readings can be predicted by inputting the conditions into the general equation. From the general sensor equation, two design equations were developed for the movement of the sliding bearing and expansion joint gap. These equations were used to predict the extreme movement ranges for thermal, wind, and live load by inputting extreme environment conditions.

10.1 Conclusions

The results from this research have yielded the following conclusions:

- Confidence in the data is of the utmost importance, which can be gained through an outlier detection algorithm.

- Thermal variations account for the majority of movement.

- Longitudinal movement is primarily influenced by thermal variations and behaves linearly.

- Vertical rotation is also influenced by thermal variations and behaves linearly.

- Plan rotation is also influenced by thermal variations, however due to the small magnitude it can be ignored.

- Vertical rotation is primarily influenced by live load variations and was correlated to the time of day and day of the week.

- Plan rotation is primarily influenced by wind variations and behaves quadratically with wind speed. Wind variations should be accounted for as they account for a significant amount of bearing movement especially during extreme wind events.

- Plan rotation is also influenced by live load variations and were correlated to the time of day but showed no difference between a work and non-work day.

- Live loads account for minimal bearing movement resulting from both vertical and plan rotations.

10.2 Recommendations

Based on the objectives and results presented in this thesis, several recommendations and future work are proposed:

- Record keeping is essential when installing a structural monitoring system, including initial readings of sensors, record of time and dates of sensor installations and failures, and proper labeling of sensors.

- Algorithms could be included in the logging software for the on-site data logger to automatically correct for erroneous data in order to save time in the post processing of collected data.

- This analysis process can be applied to the A. Murray MacKay Suspension Bridge, as a similar structural health monitoring system was installed to the bridge for joint monitoring. The results can be used to compare the different bearing systems of the bridges.

- Access to traffic data would greatly assist in the correlation between joint movement and live load.

- In the case of extreme movement predictions, appropriate combination factors should be investigated to determine the appropriate range of movement allowed over the design life. It would be extremely unlikely to experience extreme temperature, extreme wind, and extreme live load conditions simultaneously.

References

Ang, A. and Tang, W. 1984. Probability Concepts in Engineering Panning and Design: Vol. II. John Wiley & Sons, New York. 562 pp.

Banks, S.R. 1942. The Lion's Gate Bridge. The Engineering Journal. The Engineering Institute of Canada.

Battista, N., Westgate, R., Koo, K., and Brownjohn, J. Wireless monitoring of the longitudinal displacement of the Tamar Suspension Bridge deck under changing environmental conditions. Proceedings of SPIE: Sensors and Smart Structures Technologies for Civil, Mechanical, and Aerospace.

Basu, S. and Meckesheimer, M. 2007. Automatic Outlier Detection for Time Series: an Application to Sensor data. Knowledge and Information Systems Vol II, Issue 2, pp 137-154.

Blockley, D. 2010. Bridges: The Science and Art of the World's Most Inspiring Structures. Oxford University Press. Oxford, NY.

CAN/CSA S6-06. 2006. Canadian Highway Bridge Design Code. Canadian Standards Association. Mississauga, Canada.

CAN/CSA S6.1-06. 2006. Canadian Highway Bridge Design Code Commentary. Canadian Standards Association. Mississauga, Canada.

Gumbel, E. 1958. Statistics of Extremes. Columbia University Press. 375 pp.

Institution of Civil Engineers (ICE). 2008. ICE manual of bridge engineering second edition. Thomas Telford Ltd. London, UK.

Liu, M., Frangopol, D., and Petcherdchoo, A. 2006. Probabilistic Lifetime Oriented Multiobjective Optimization of Bridge Maintenance: Combination of Maintenance Types. ASCE Journal of Structural Engineering 132(11):1821.

Lloret-Cabot, M., Fenton, G.A., and Hicks, M.A. 2014. On the estimation of scale of fluctuation in geostatics. Georisk Vol. 8, No. 2, 129-140.

Kawada, T. 2010. History of the Modern Suspension Bridge. American Society of Civil Engineers. Reston, Virginia.

Kutner, M., Nachtsheim, C., Neter, J., and Li, W. 2005. Applied Linear Statistical Models Fifth Edition. McGraw-Hill Irwin. New York, NY.

Miao, C., Deng, Y., Ding, Y., and Li, A. 2013. Damage alarming for bridge expansion joints using novelty detection technique based on long-term monitoring data. J. Cent. South Univ. 20: 226-235.

Ni, Y.Q., Hua, X.G., Wong, K.Y., and Ko, J.M. 2007. Assessment of Bridge Expansion Joints Using Long-Term Displacement and Temperature Measurement. ASCE Journal of Structural Engineering Vol 21, No. 2, 143-151.

Puglsey, A. 1968, The Theory of Suspension Bridges. London Edward Arnold (Publishers) Ltd. Great Britain.

Ramberger, G. 2002. Structural Bearings and Expansion Joints for Bridges. International Association for Bridge and Structural Engineering. Zurich, Switzerland.

Ryall, M. 2010. Bridge Management 2nd Edition. Elsevier Ltd. Oxford, UK.

Steinman, D.B. 1957. A Practical Treatise on Suspension Bridges: Their Design, Construction and Erection Second Edition. John Wiley & Sons Inc. New York, NY.

Xu, Y.L. and Xia, Y. 2012. Structural Health Monitoring of Long-Span Suspension Bridges. Spon Press. New York, NY.

Appendix A – Outlier Detection Plots
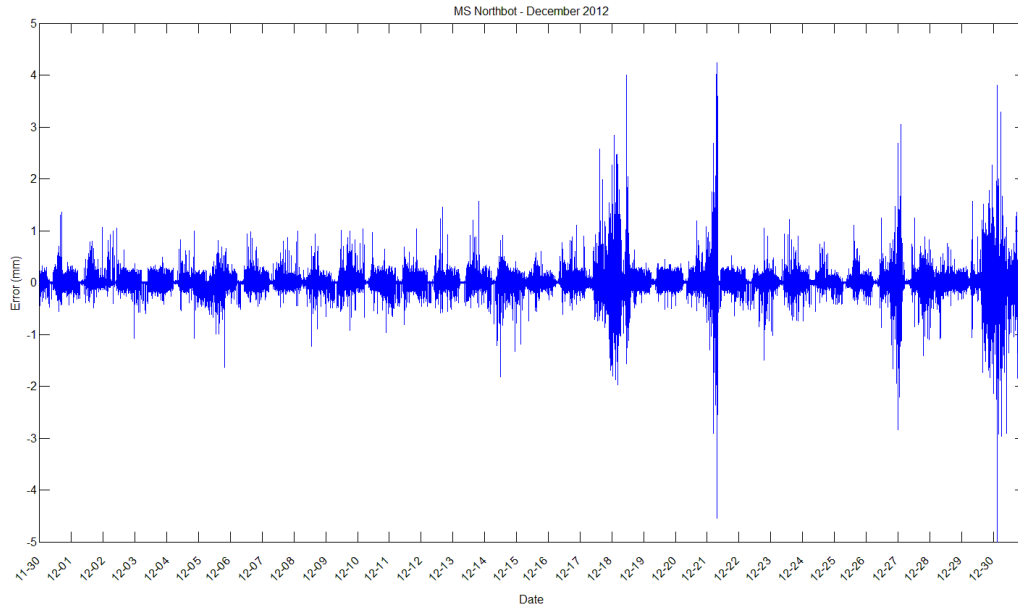
Figure A.1 – One sided median results – DMT MS Northbot – Dec 2012
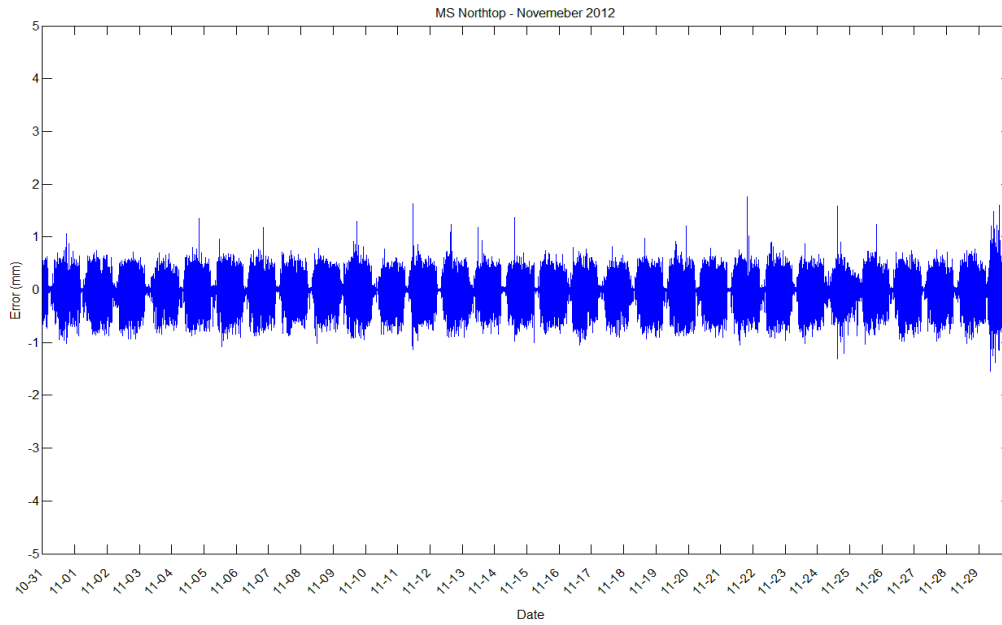
Figure A.2 – One sided median results – DMT MS Northtop – Nov 2012
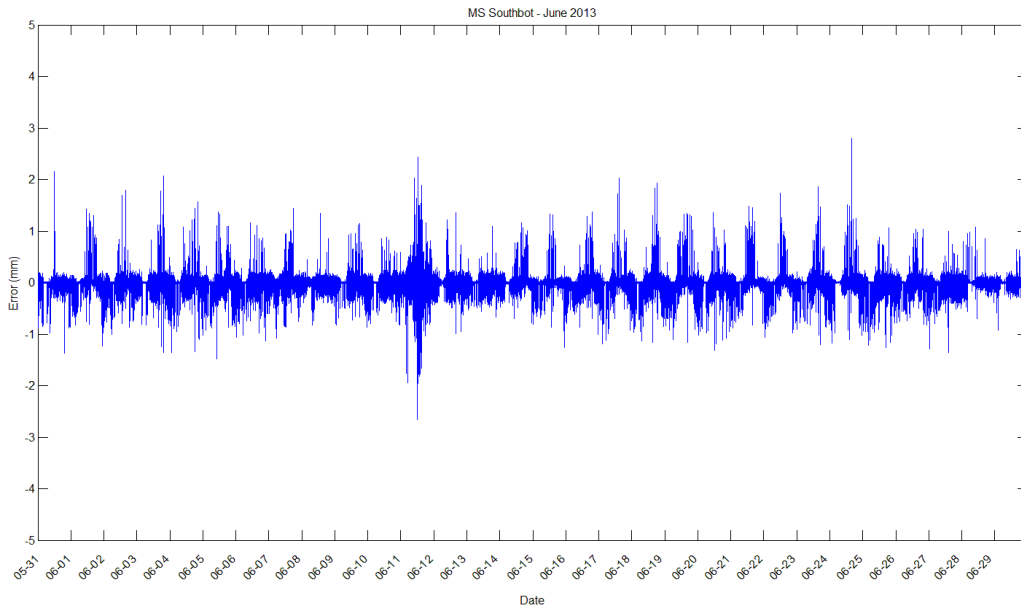
Figure A.3 – One sided median results – DMT MS Southbot – June 2013
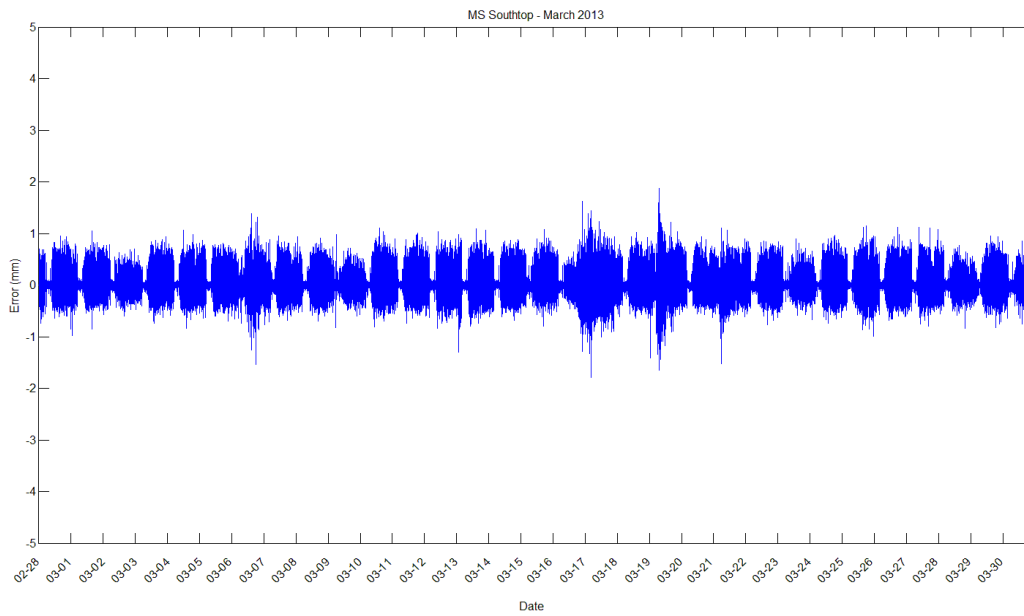
Figure A.4 – One sided median results – DMT MS Southtop – March 2013
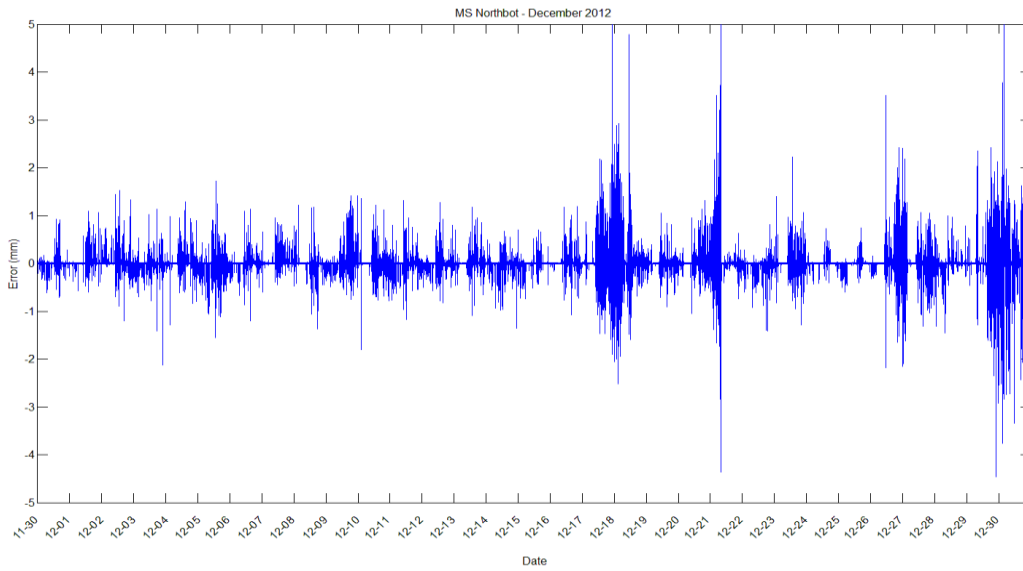
Figure A.5 – One sided median results – HMT MS Northbot – Dec 2012
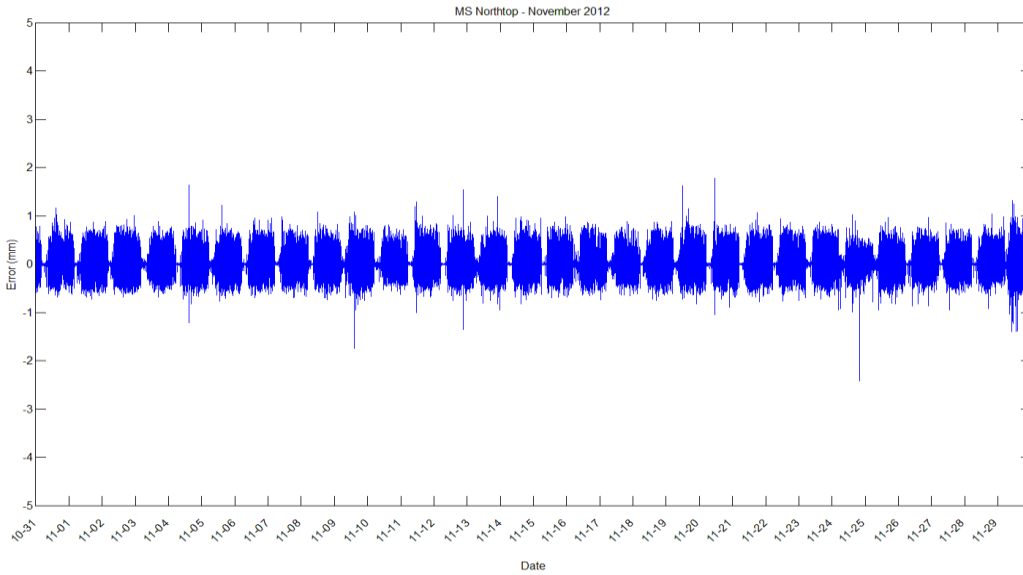
Figure A.6 – One sided median results – HMT MS Northtop – Nov 2012
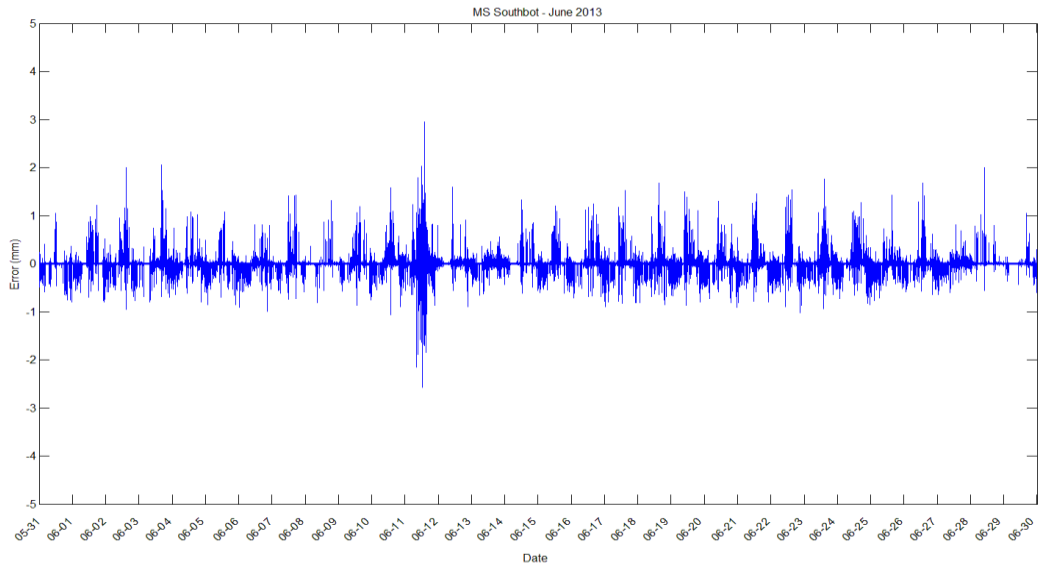
Figure A.7 – One sided median results – HMT MS Southbot – June 2013
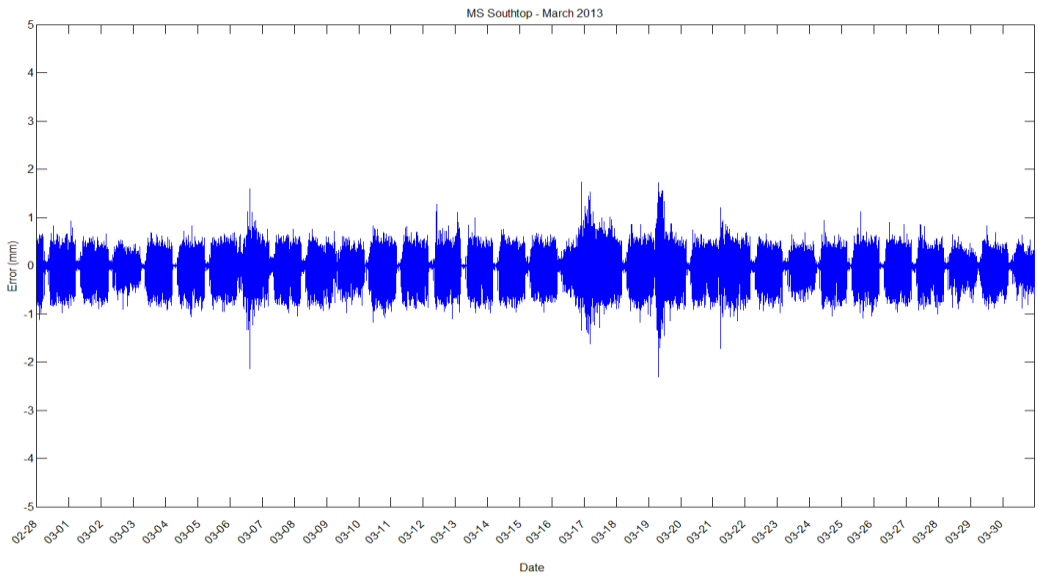
Figure A.8 – One sided median results – HMT MS Southtop – March 2013

123
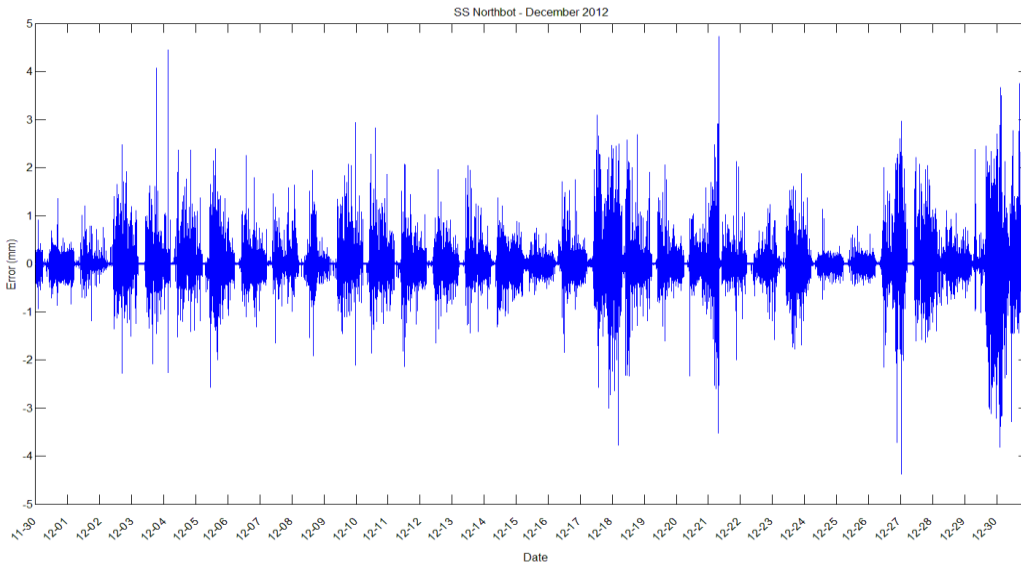
Figure A.9 – One sided median results – DMT SS Northbot – Dec 2012
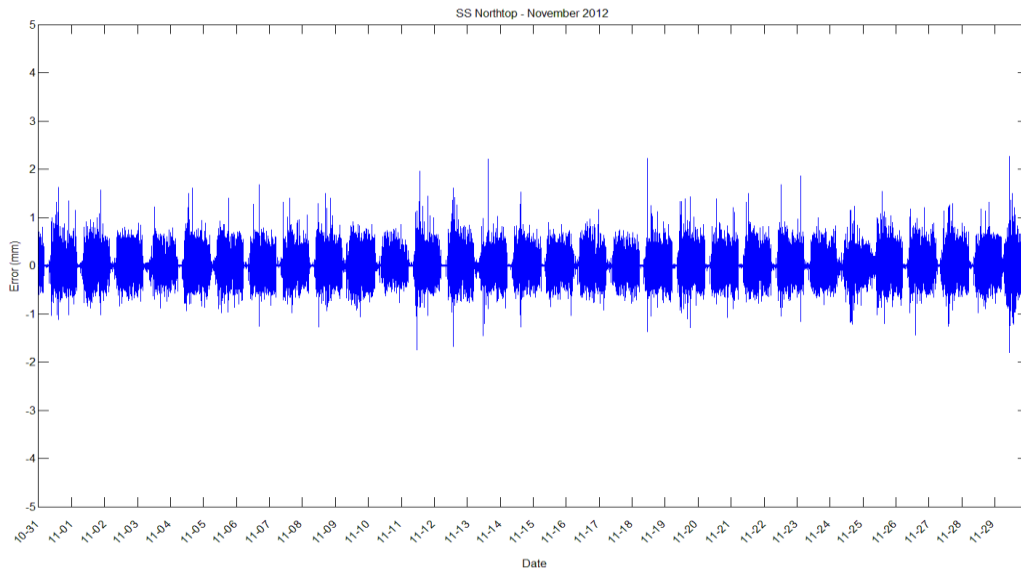
Figure A.10 – One sided median results – DMT SS Northtop – Nov 2012
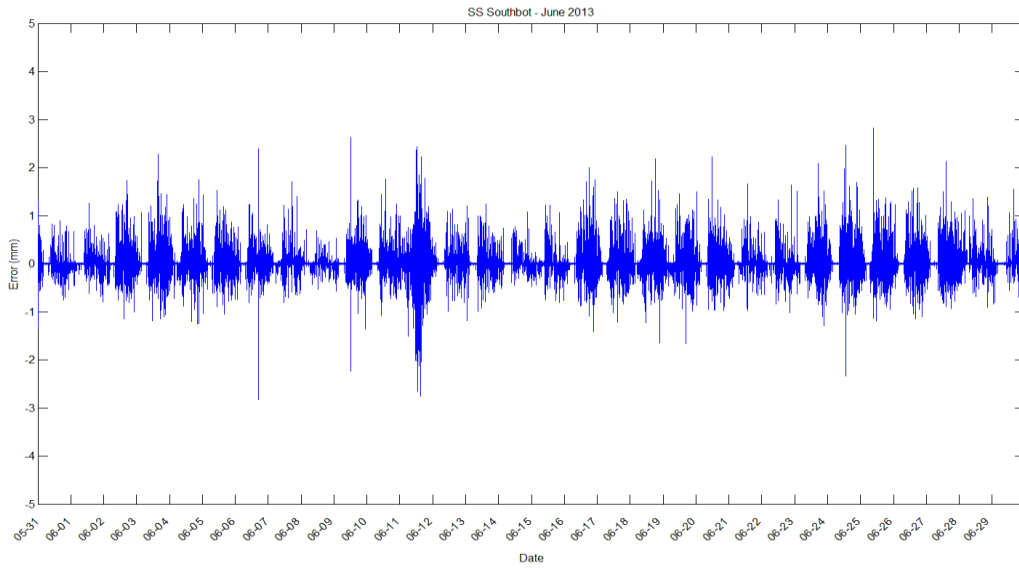
Figure A.11 – One sided median results – DMT SS Southbot – June 2013
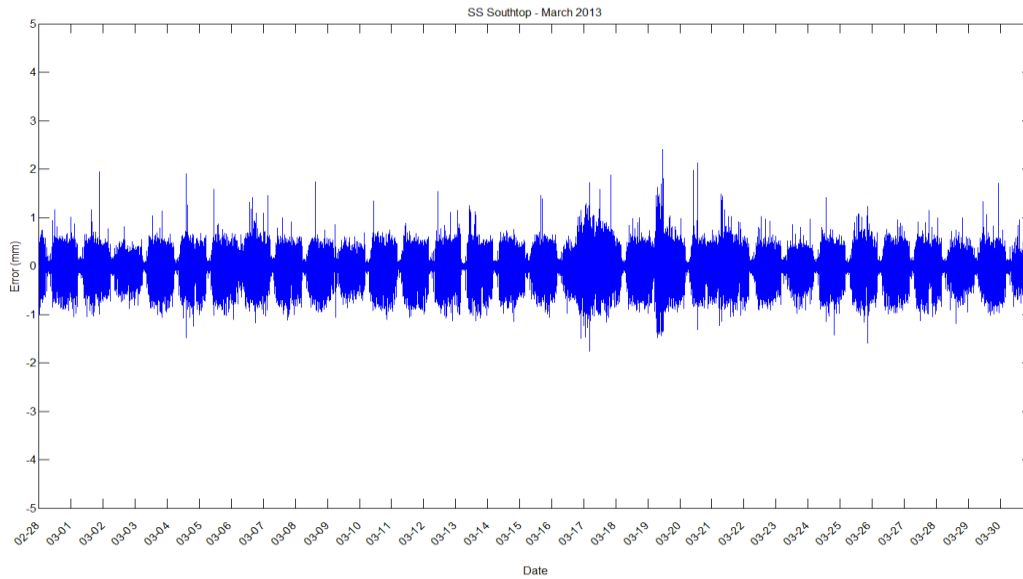
Figure A.12 – One sided median results – DMT SS Southtop – March 2013
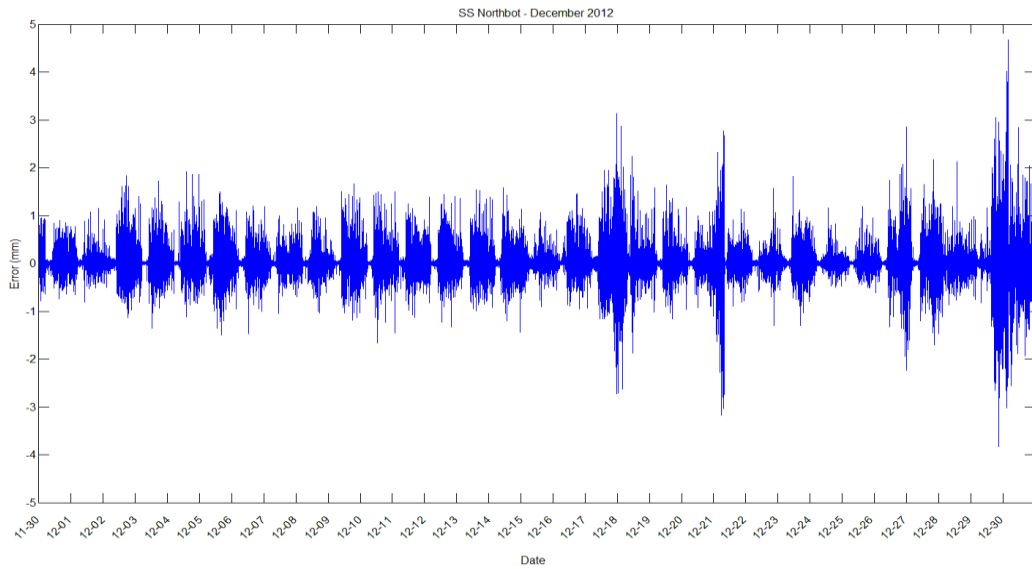
Figure A.13 – One sided median results – HMT SS Northbot – Dec 2012
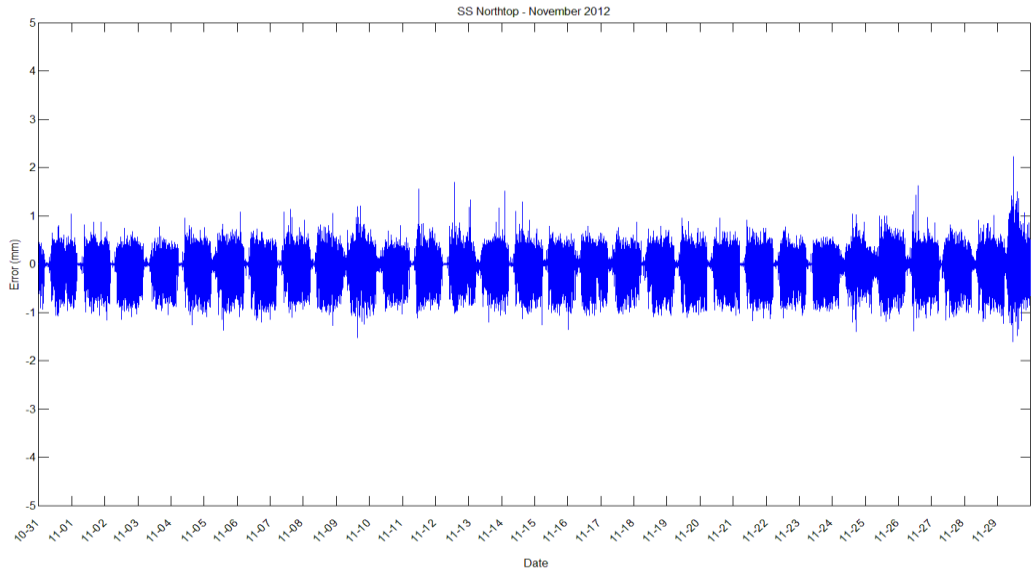
Figure A.14 – One sided median results – HMT SS Northtop – Nov 2012
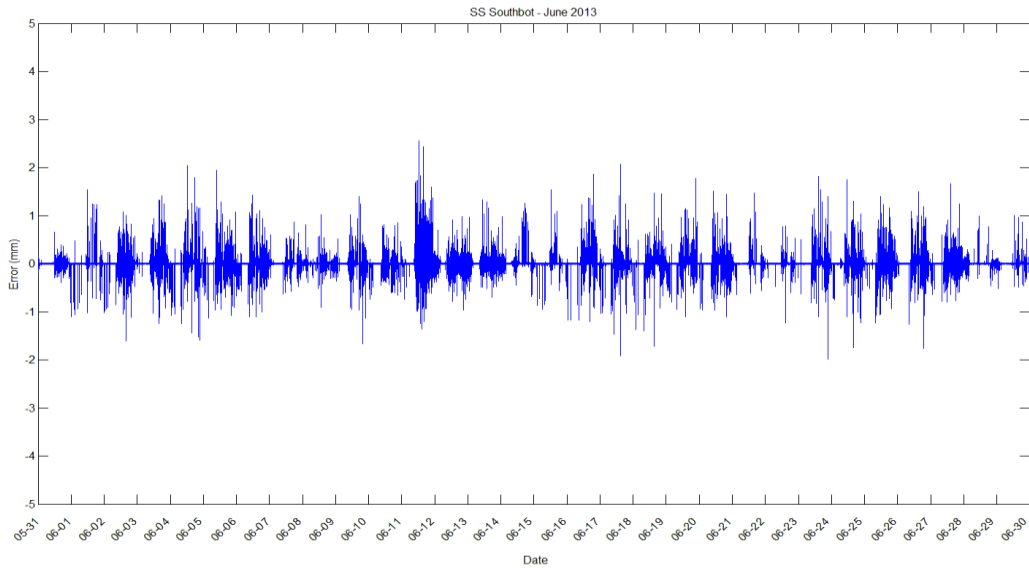
Figure A.15 – One sided median results – HMT SS Southbot – June 2013
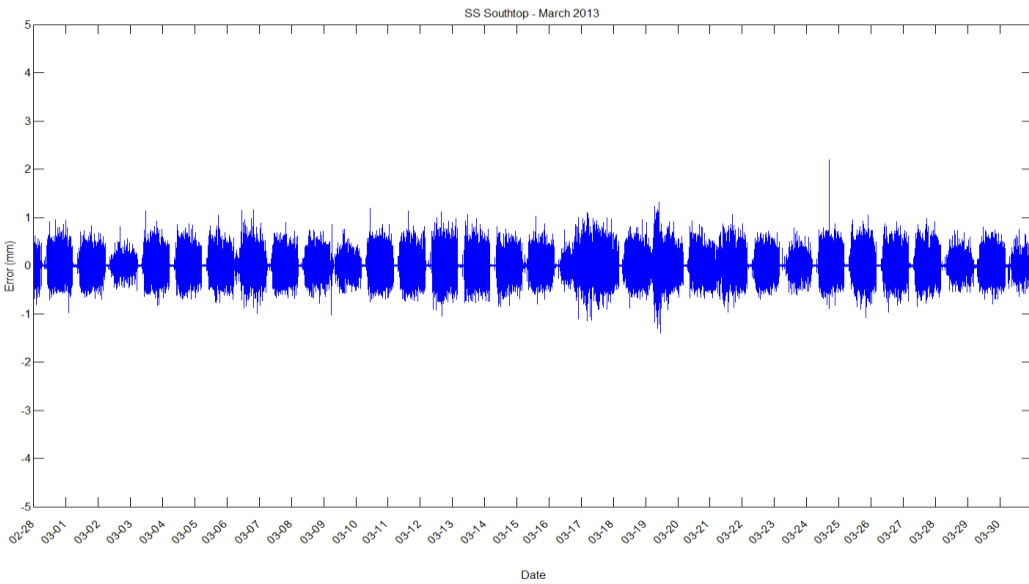
Figure A.16 – One sided median results – HMT SS Southtop – March 2013

Appendix B – Yearly Movement Plots
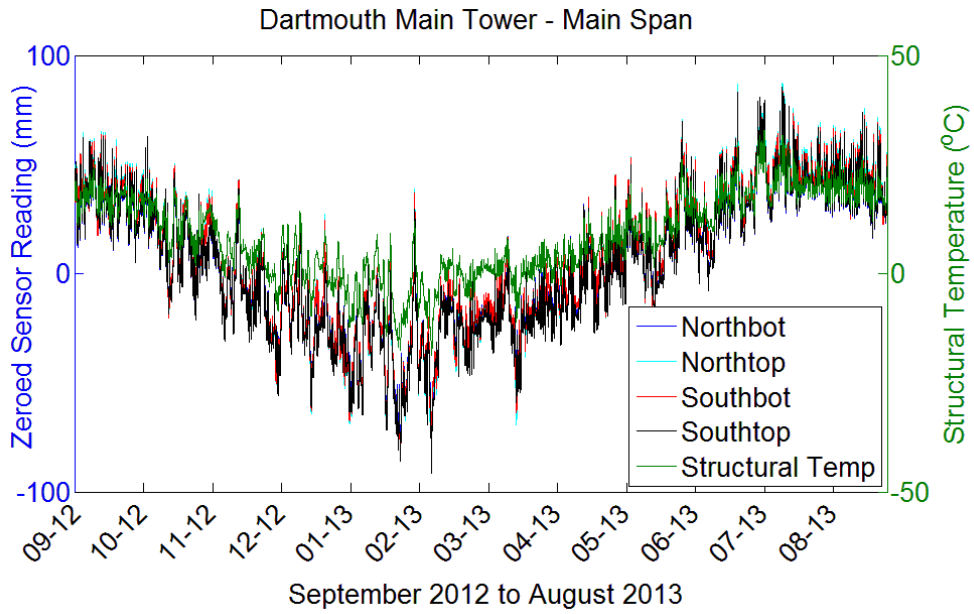
Figure B.1 – Yearly sensor readings, DMT MS
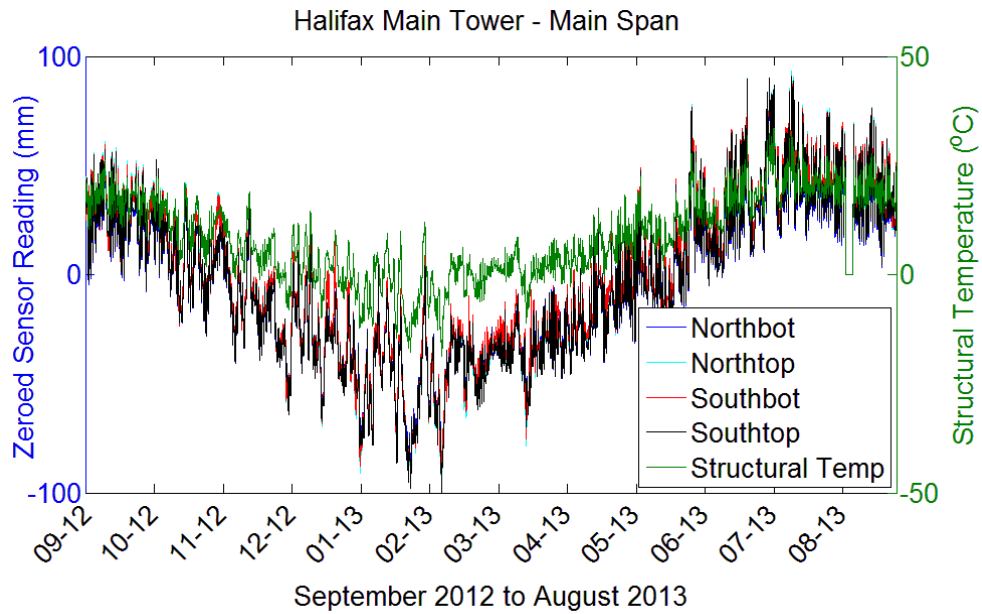
Figure B.2 – Yearly sensor readings, HMT MS
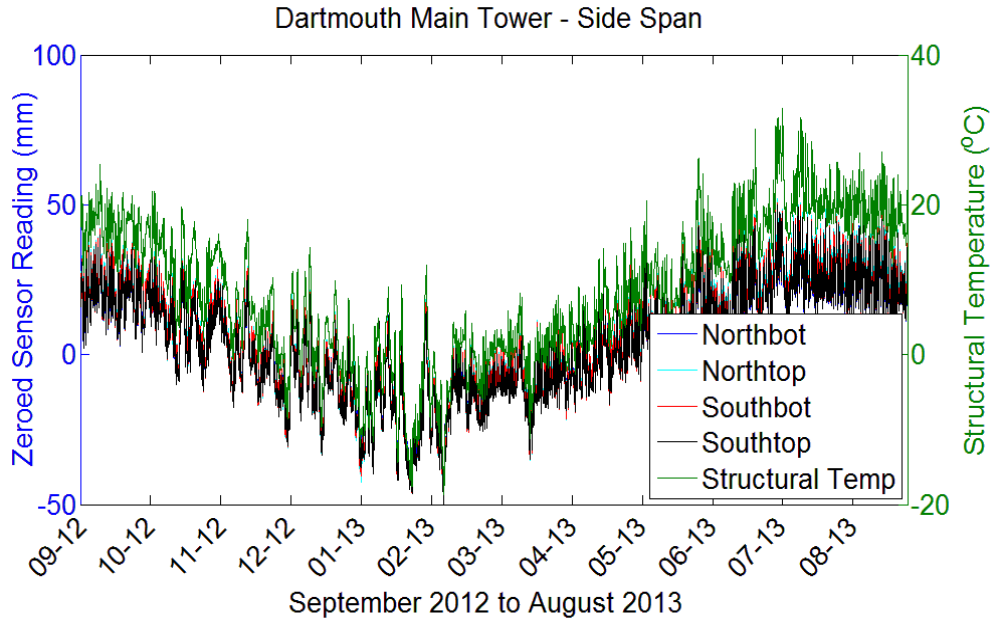
Figure B.3 – Yearly sensor readings, DMT SS
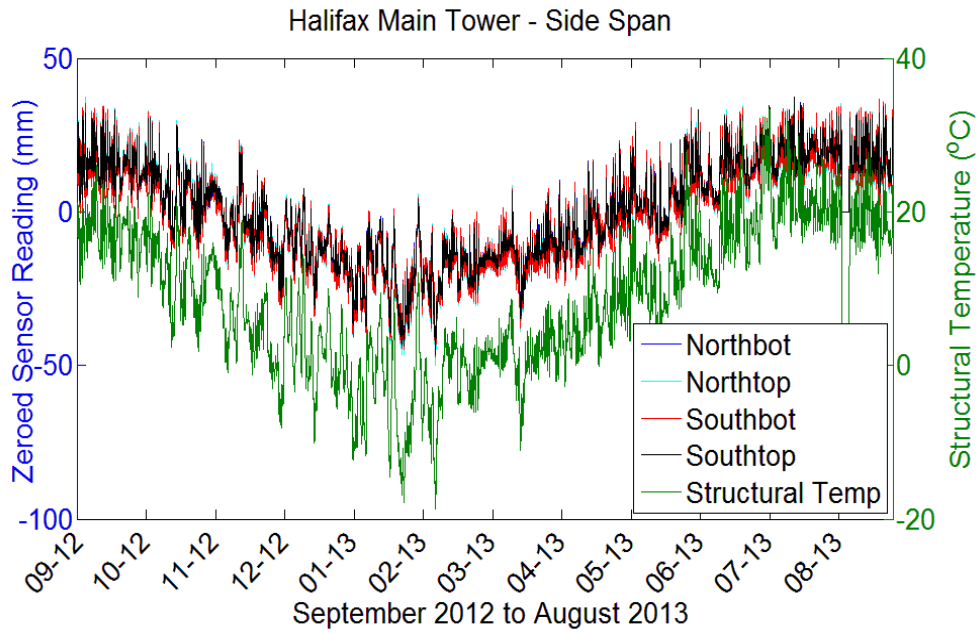
Figure B.4 – Yearly sensor readings, HMT SS
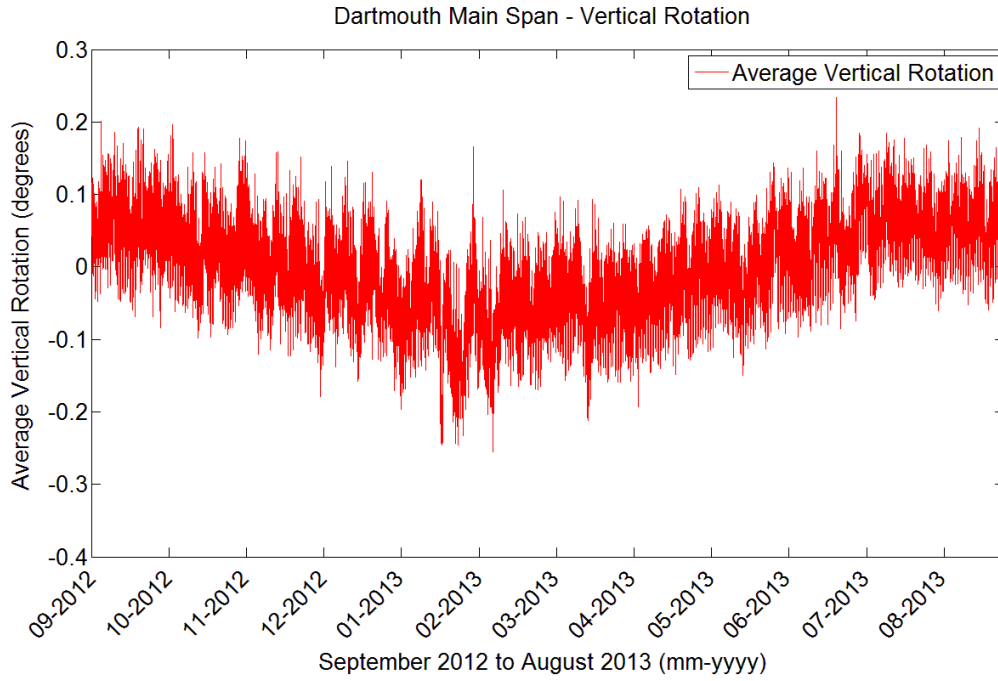
Figure B.5 – Yearly vertical rotation, DMT MS
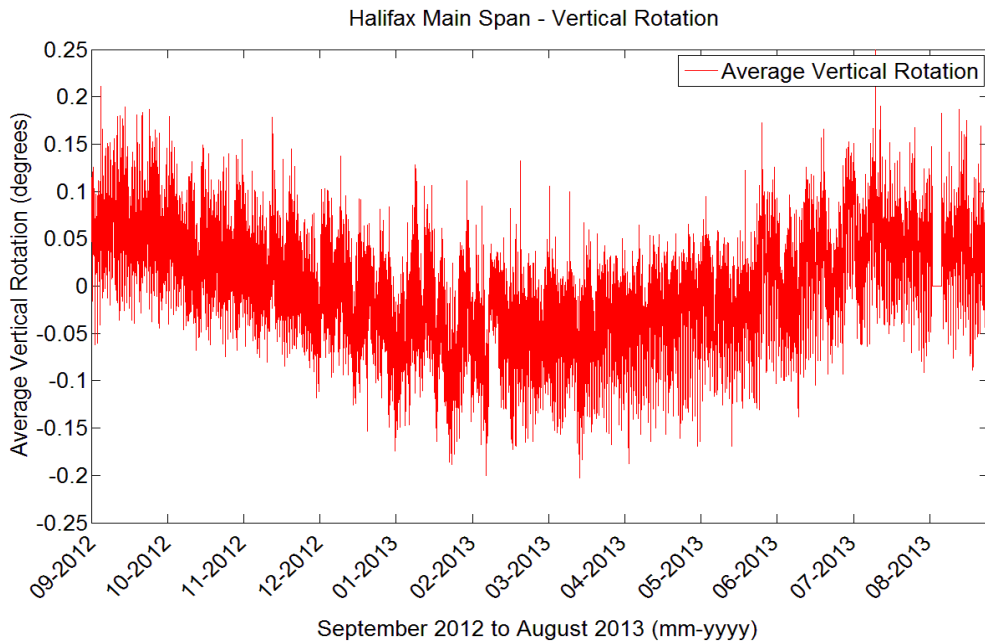
Figure B.6 – Yearly vertical rotation, HMT MS
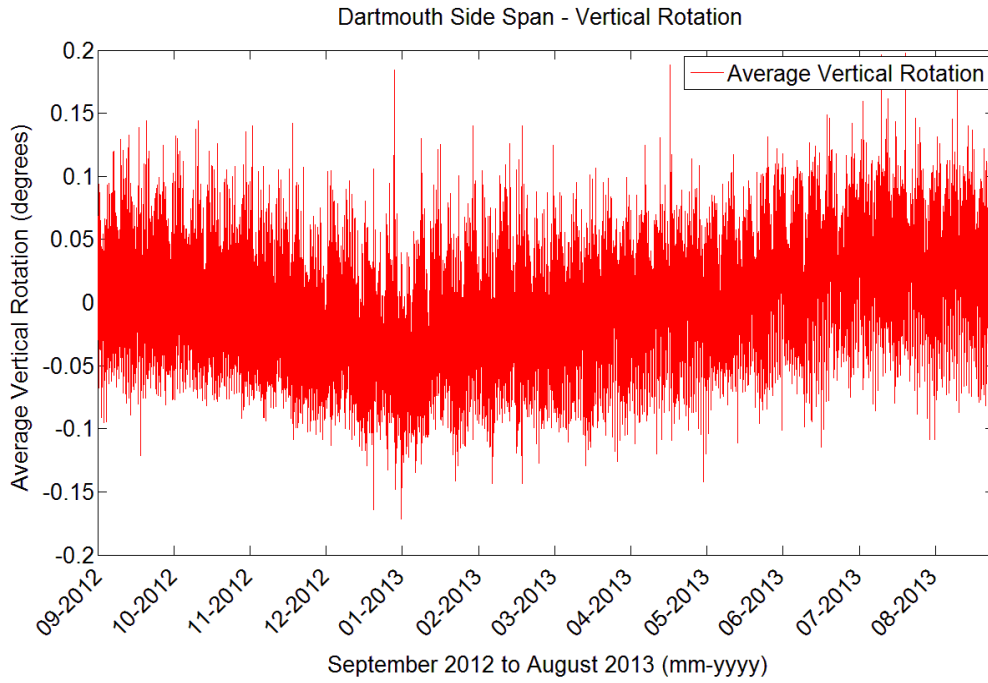
Figure B.7 – Yearly vertical rotation, DMT SS
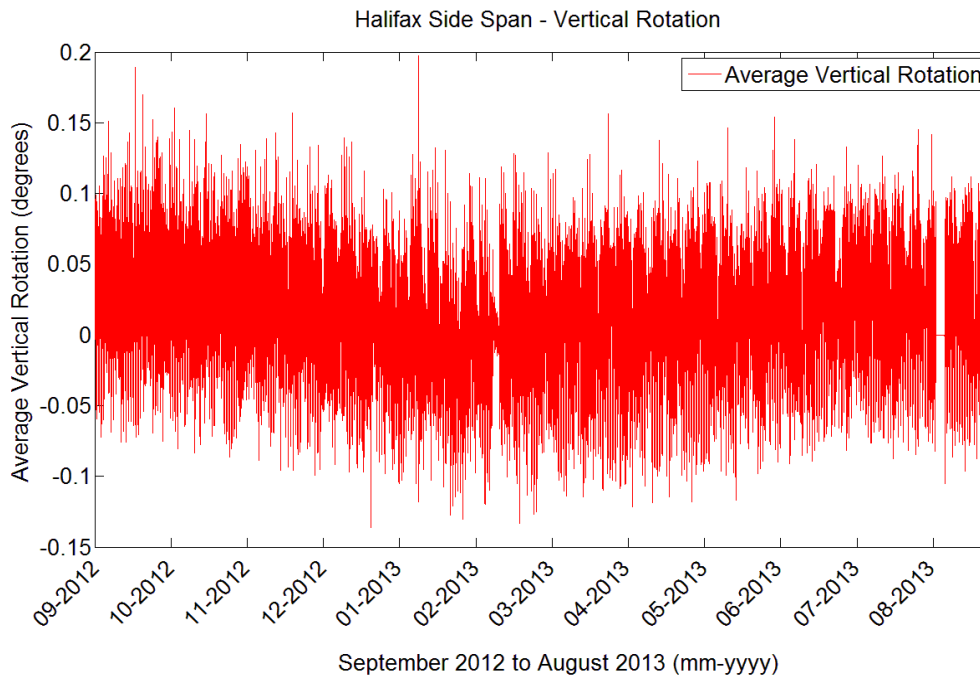
Figure B.8 – Yearly vertical rotation, HMT SS
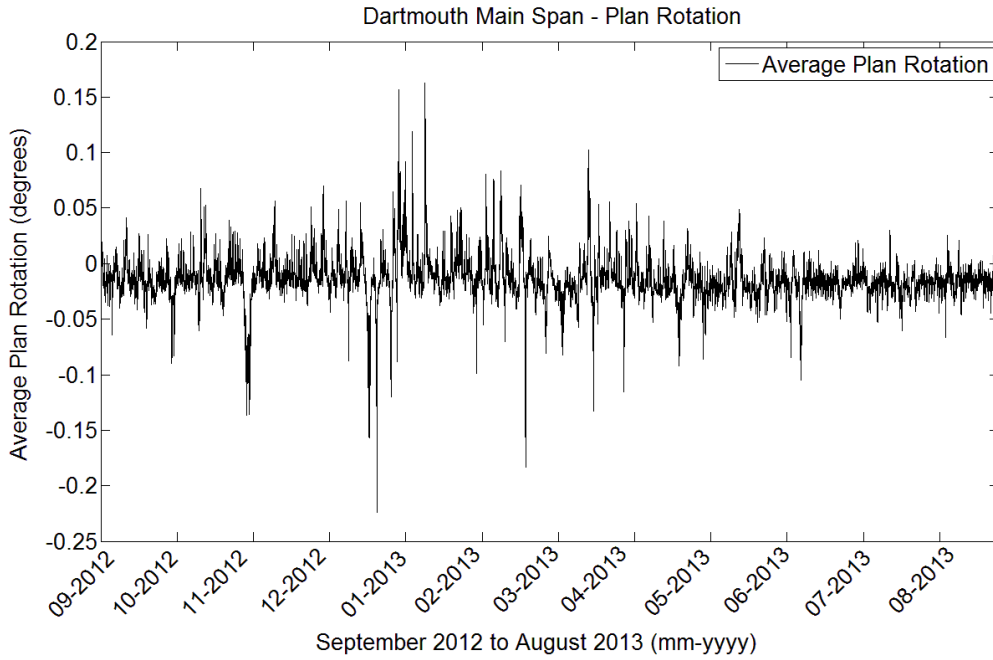
Figure B.9 – Yearly plan rotation, DMT MS
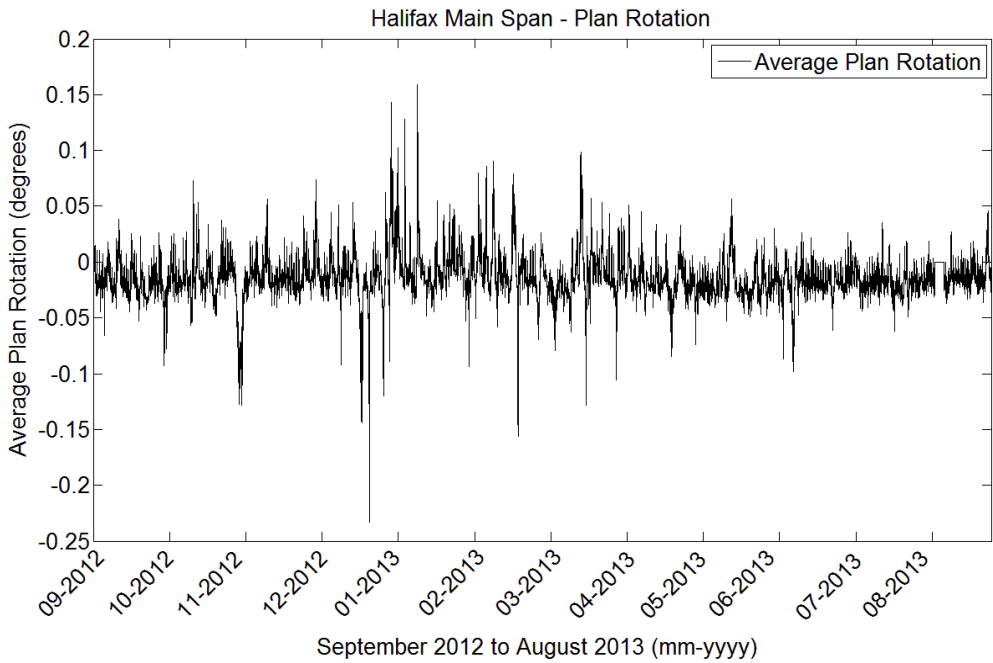
Figure B.10 – Yearly plan rotation, HMT MS

132
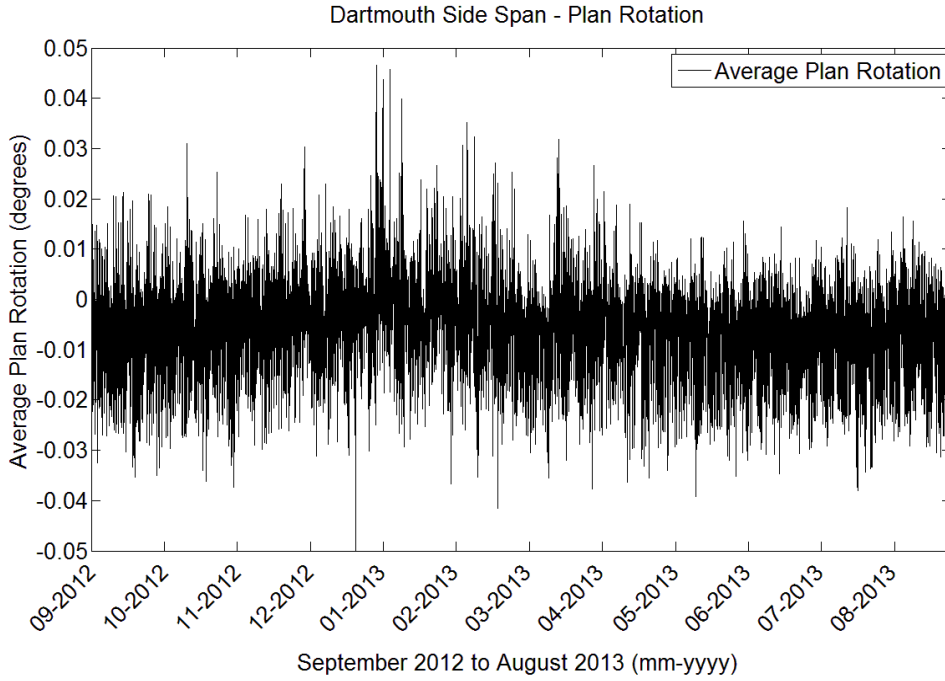
Figure B.11 – Yearly plan rotation, DMT SS
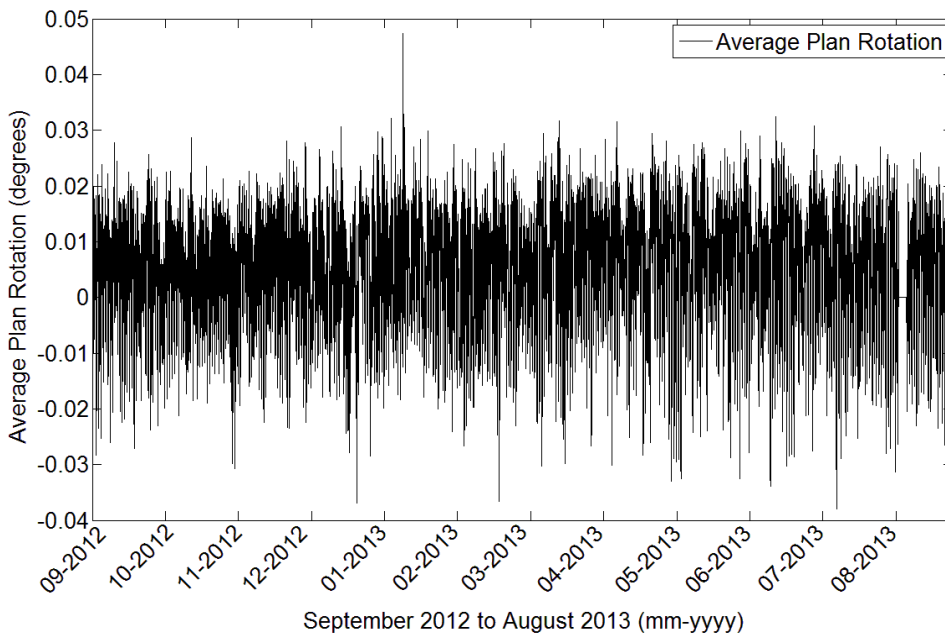
Figure B.12 – Yearly plan rotation, HMT SS

Appendix C – Thermal Trend Plots
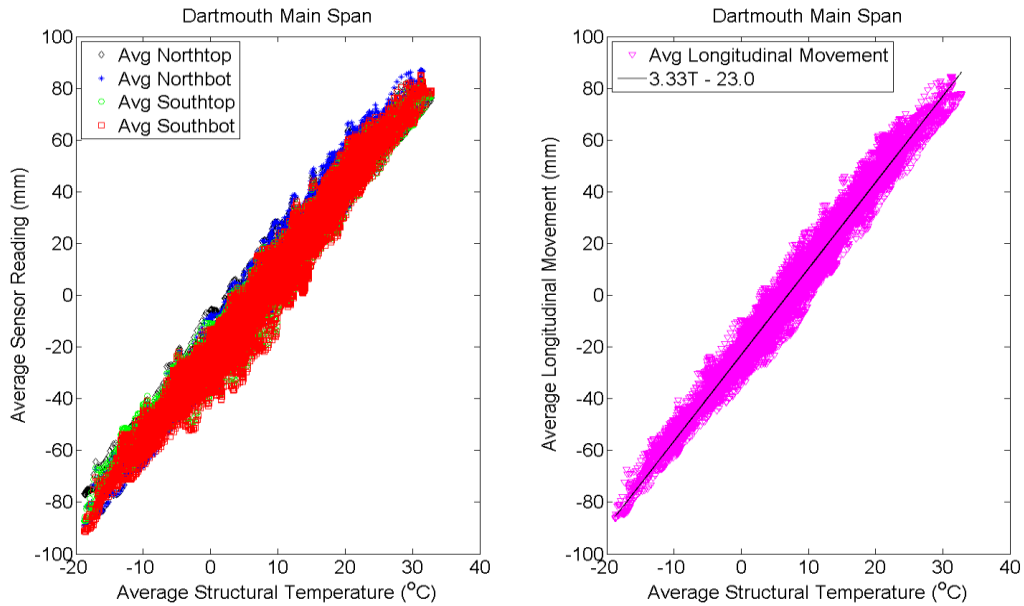
Figure C.1 –Longitudinal movement thermal trend, DMT MS
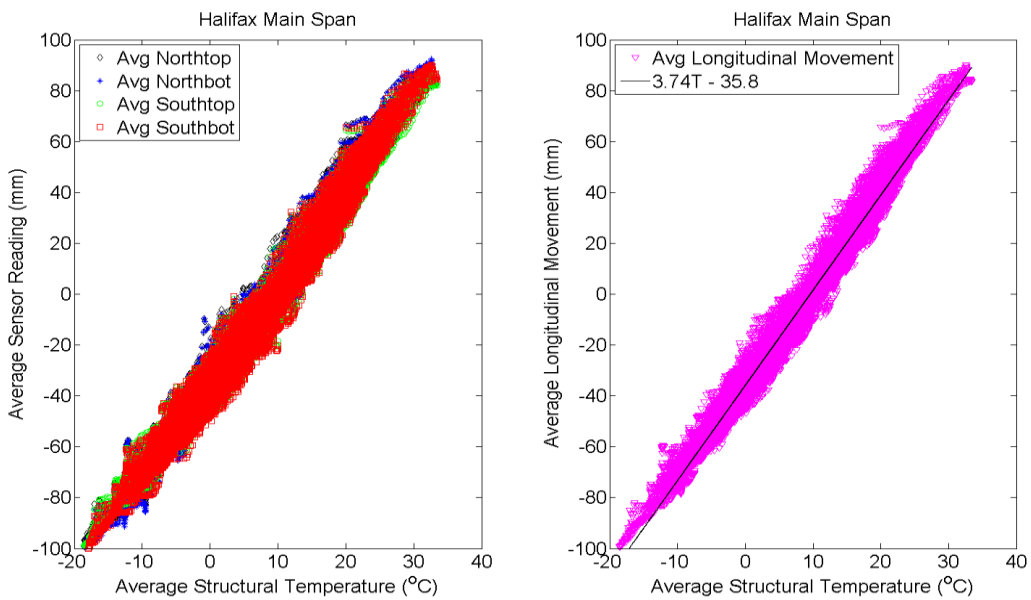
Figure C.2 –Longitudinal movement thermal trend, HMT MS
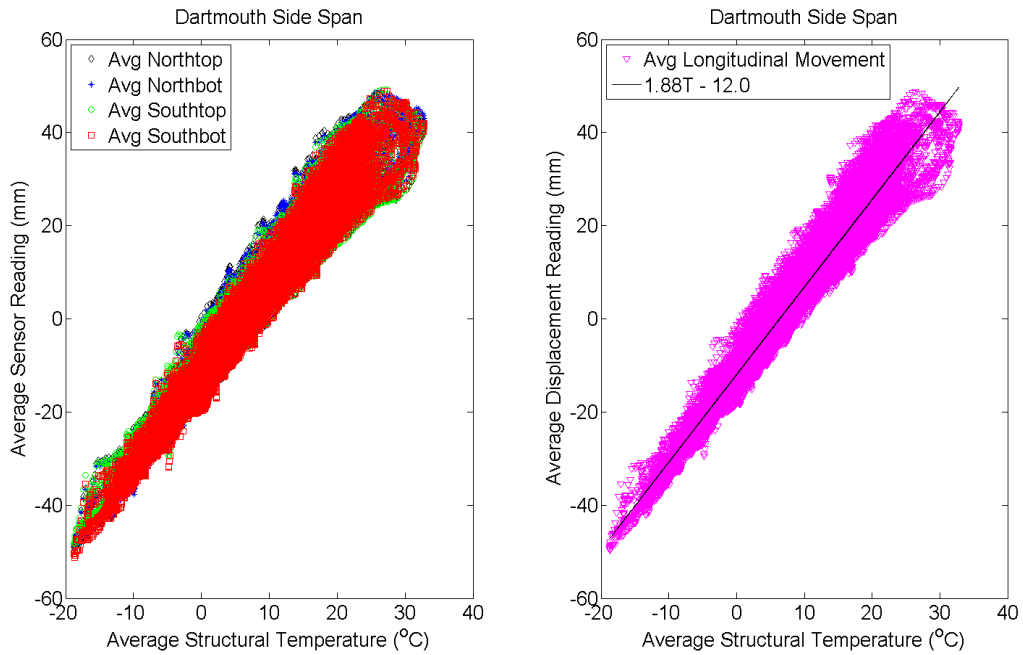
Figure C.3 –Longitudinal movement thermal trend, DMT SS
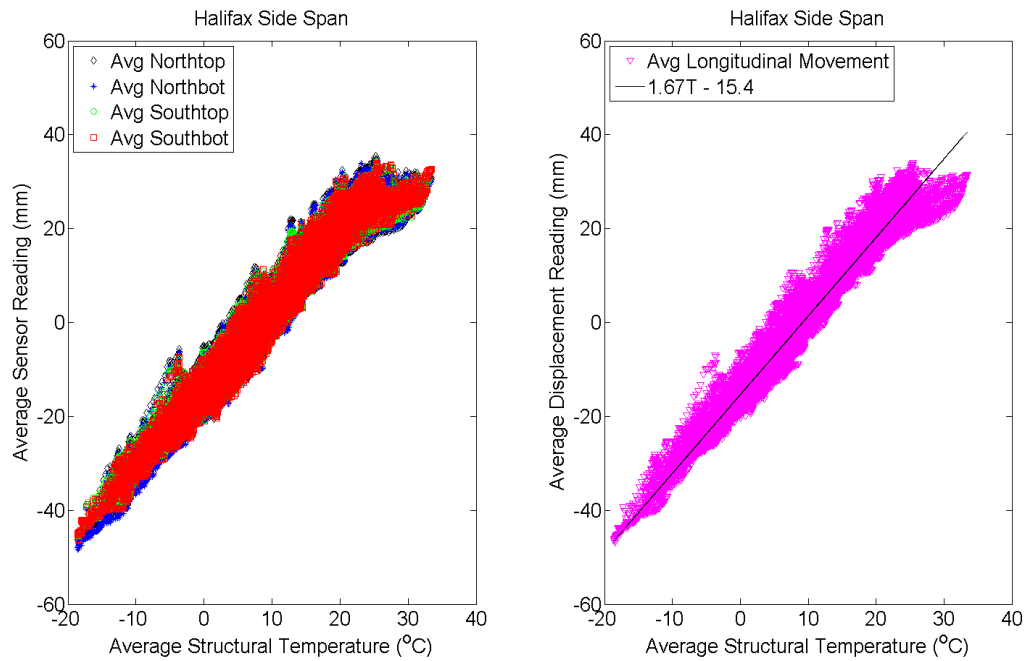
Figure C.4 –Longitudinal movement thermal trend, HMT SS
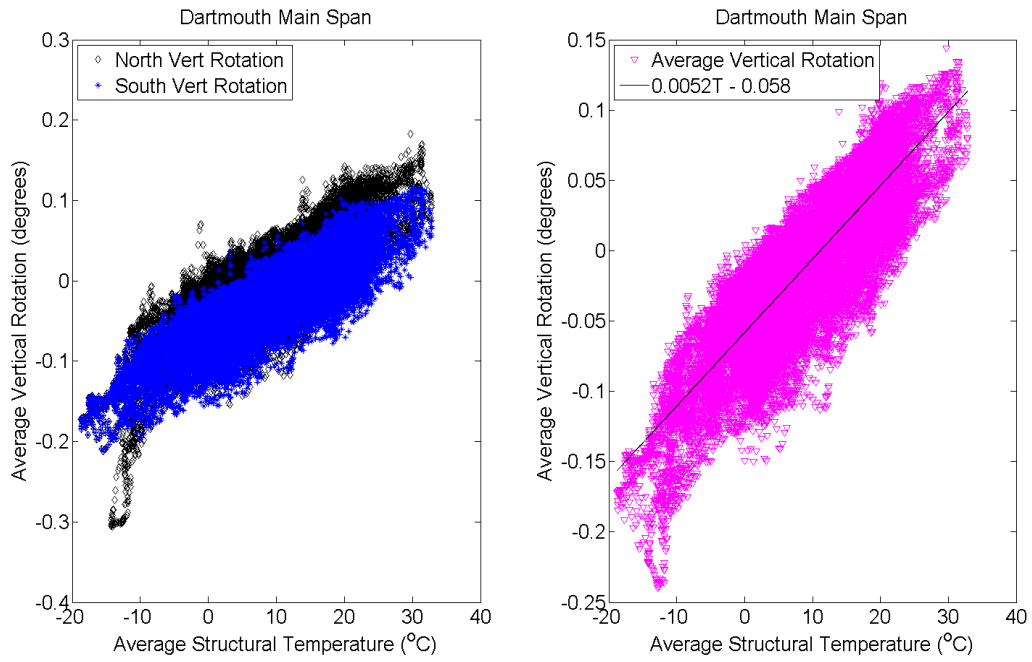
Figure C.5 –Vertical rotation thermal trend, DMT MS
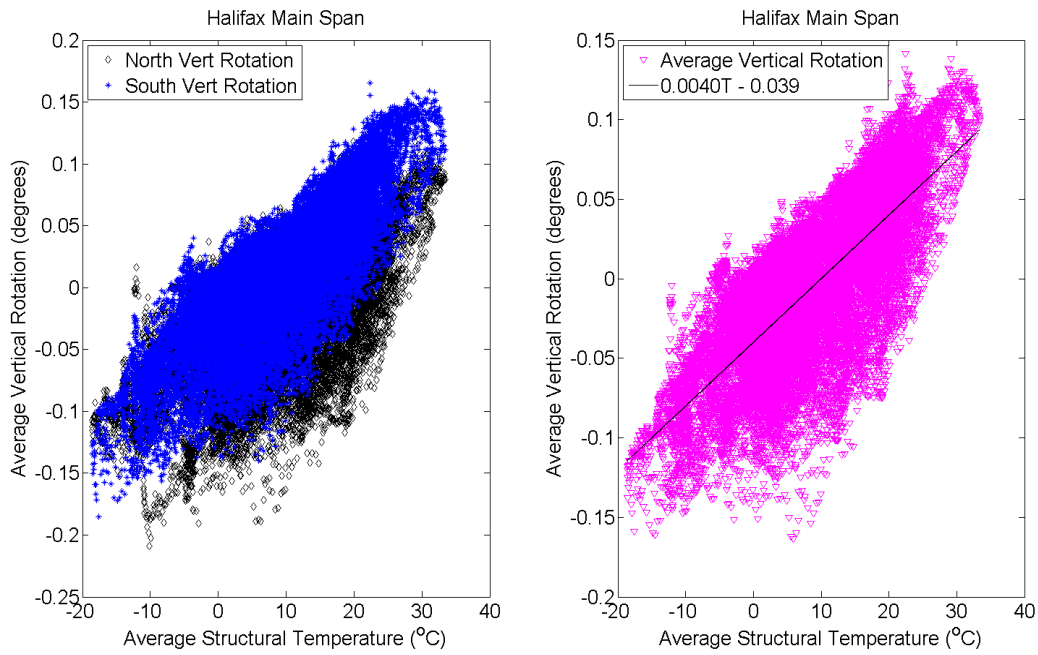
Figure C.6 –Vertical Rotation thermal trend, HMT MS
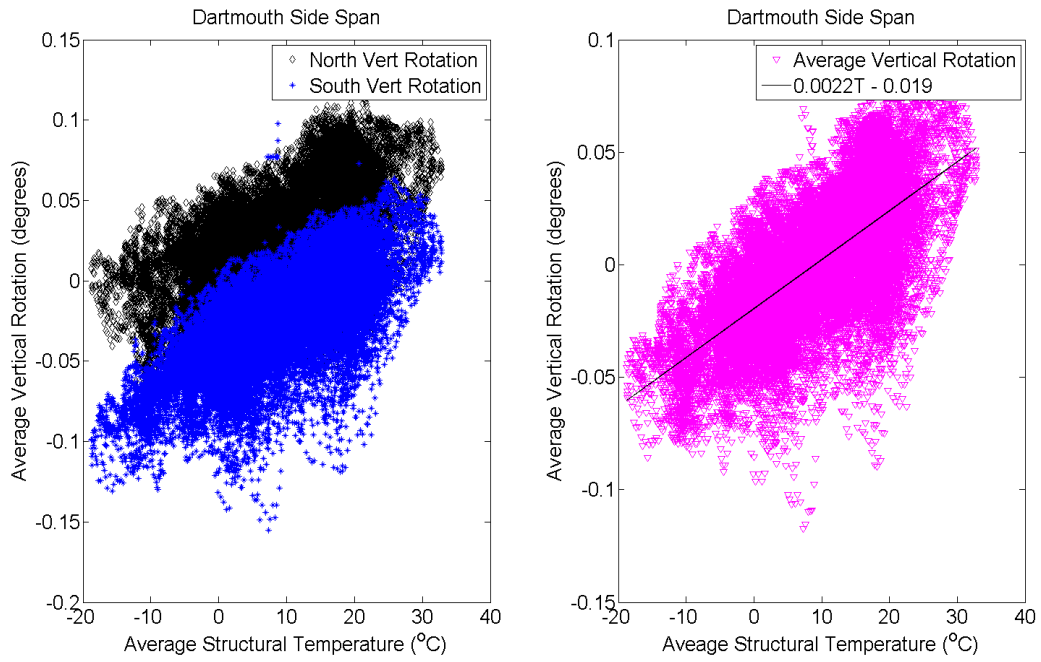
Figure C.7 –Vertical Rotation thermal trend, DMT SS
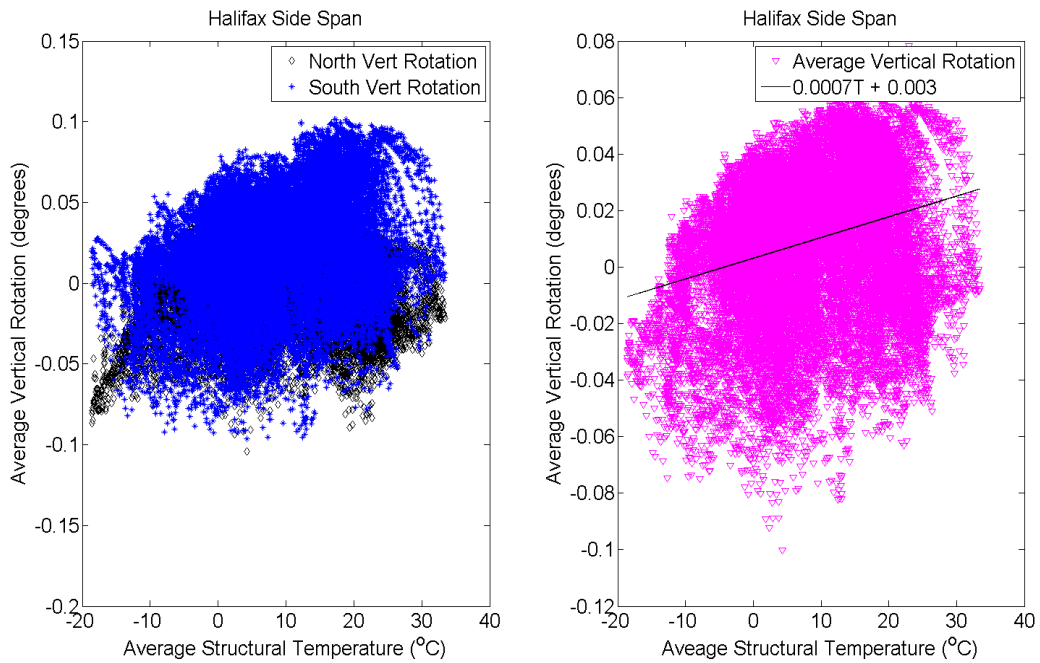
Figure C.8 –Vertical Rotation thermal trend, HMT SS
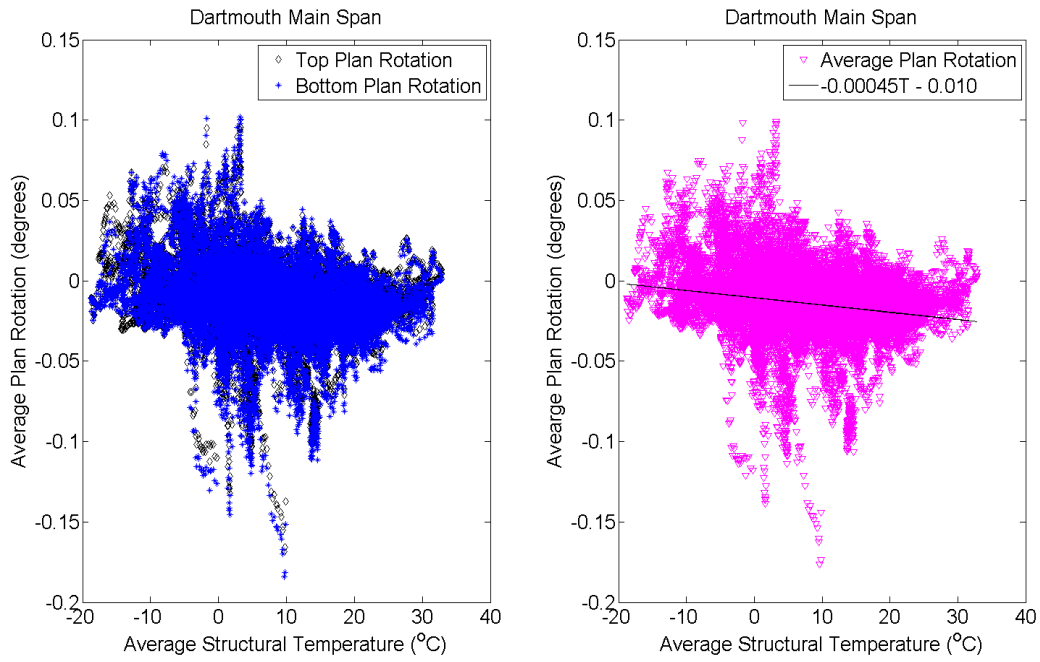
Figure C.9 –Plan Rotation thermal trend, DMT MS
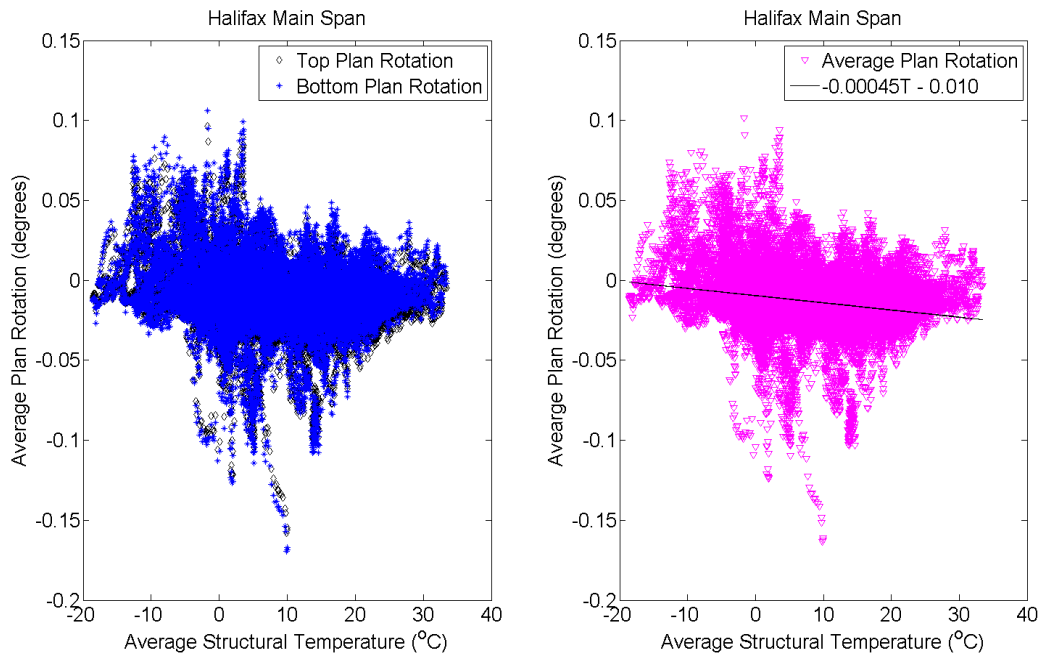
Figure C.10 –Plan Rotation thermal trend, HMT MS

138
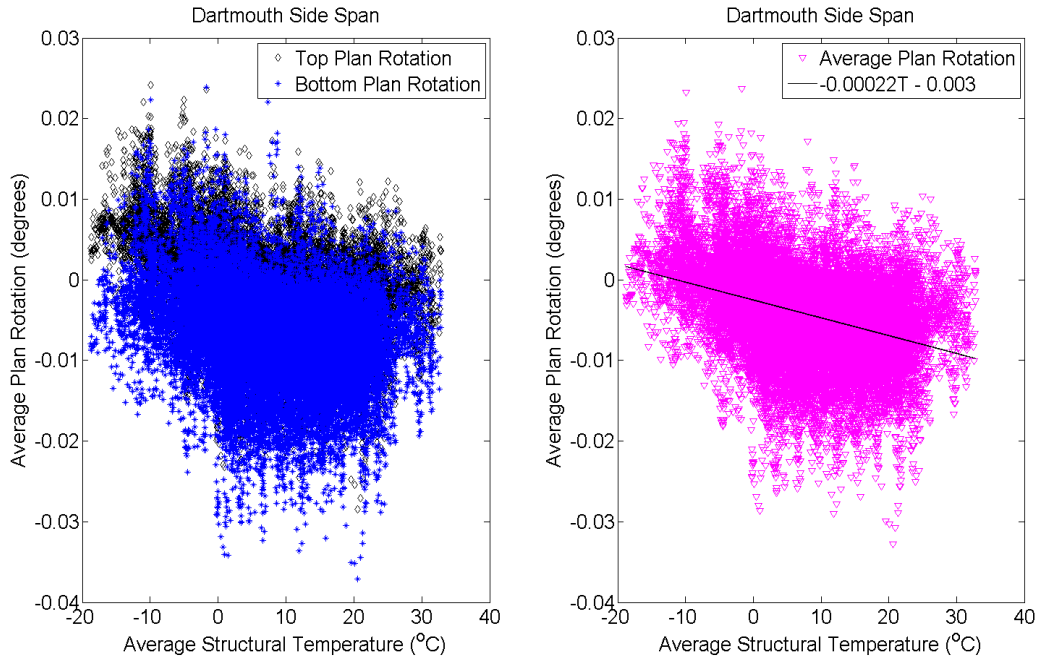
Figure C.11 –Plan Rotation thermal trend, DMT SS
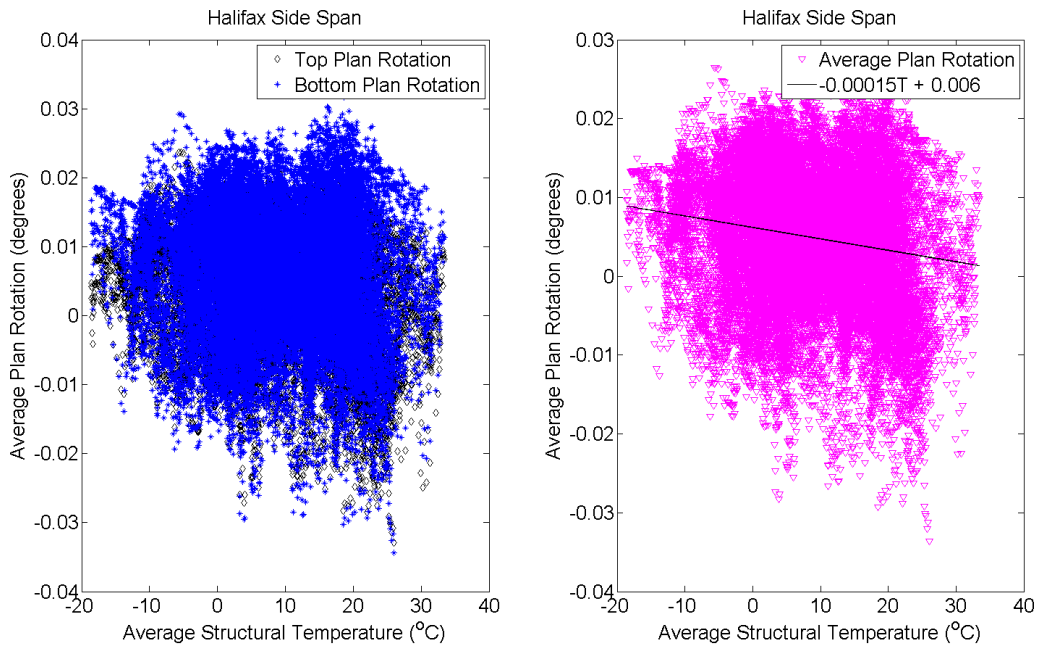
Figure C.12 –Plan Rotation thermal trend, HMT SS

Appendix D – Wind Trend Plots

Figure D.0: Compass coordinated of bridge (Google Maps)

Table D.0: Sixteen directional sections for plan rotation wind analysis

| Direction (ID)	Direction Range (degrees)
Parallel 1	22.75 – 45.25
Direction 1	42.25 – 67.75
Direction 2	67.75 – 90.25
Direction 3	90.25 – 112.75
Perpendicular 1	112.75 – 135.25
Direction 4	135.25 – 157.75
Direction 5	157.75 – 180.25
Direction 6	180.25 – 202.75
Parallel 2	202.75 – 225.25
Direction 7	225.25 – 247.75
Direction 8	247.75 – 270.25
Direction 9	270.25 – 292.75
Perpendicular 2	292.75 – 315.25
Direction 10	315.25 – 337.75
Direction 11	337.75 – 360
Direction 12	0 – 22.75

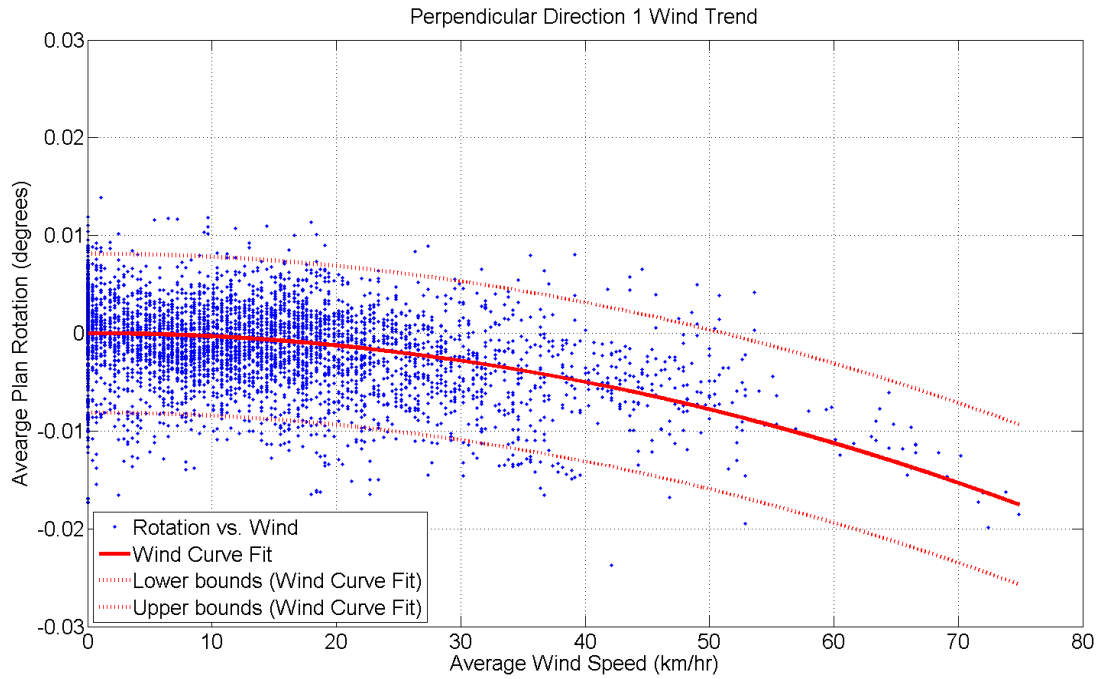**Figure D.1:** Plan rotation wind trend – Parallel Direction 1 – DMT MS
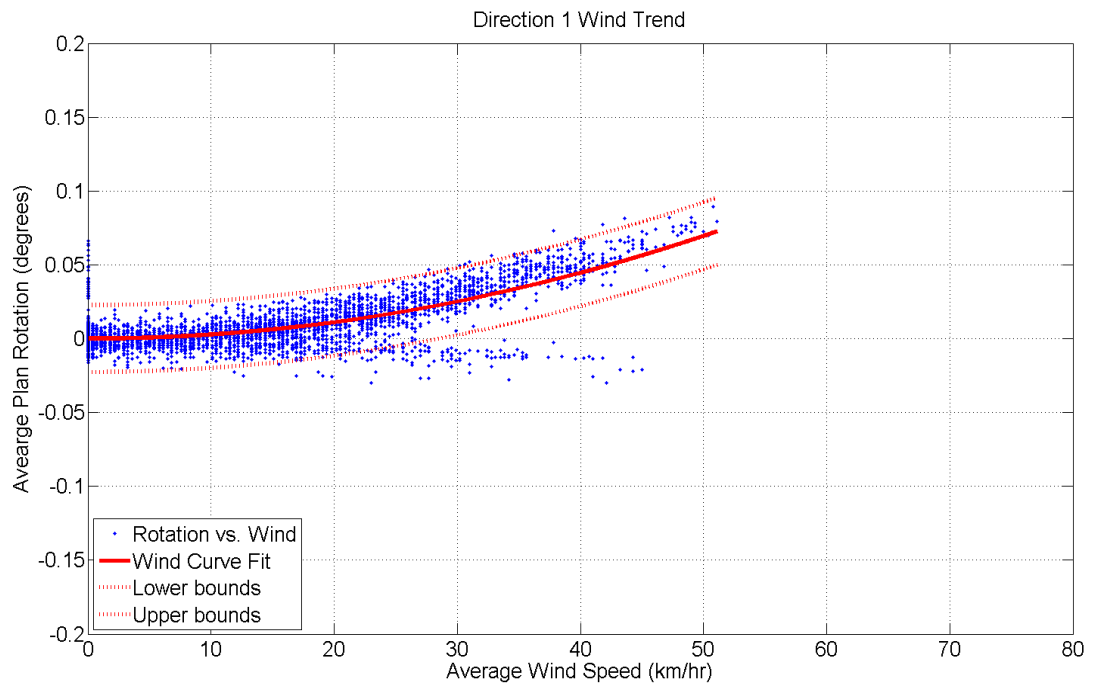
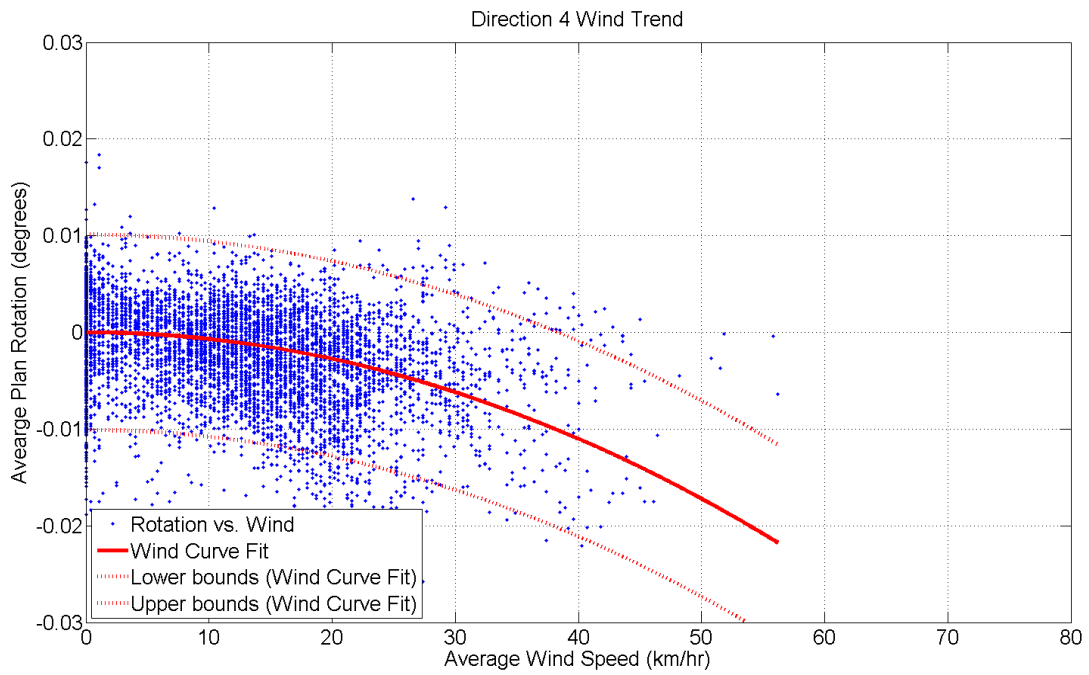**Figure D.2:** Plan rotation wind trend – Direction 1 – DMT MS
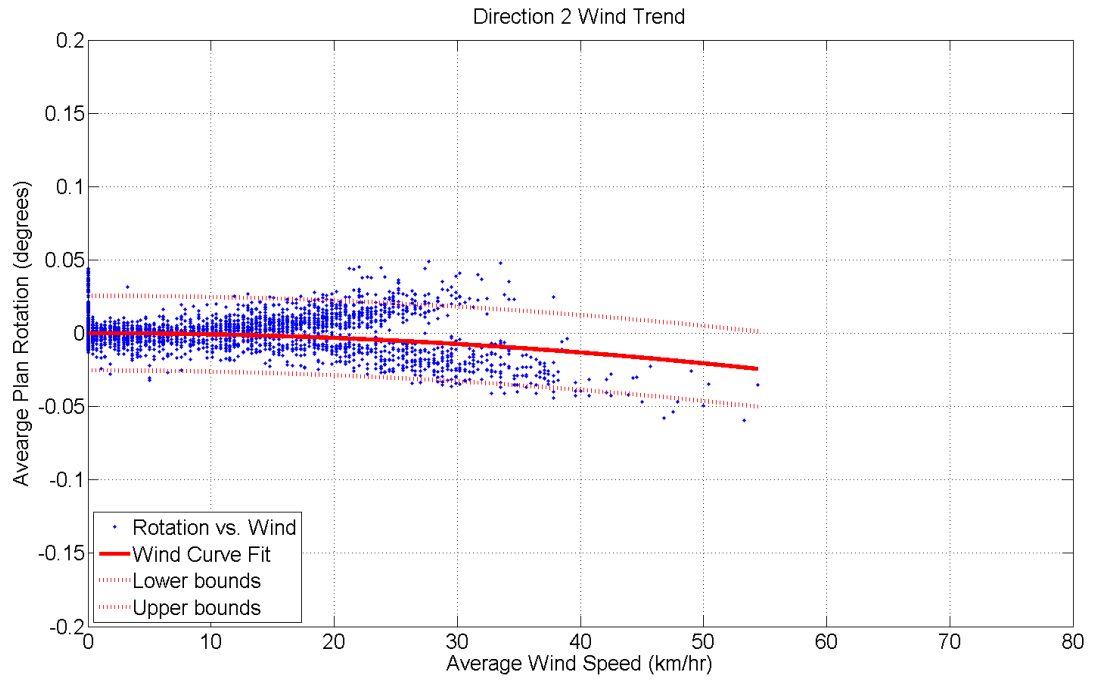
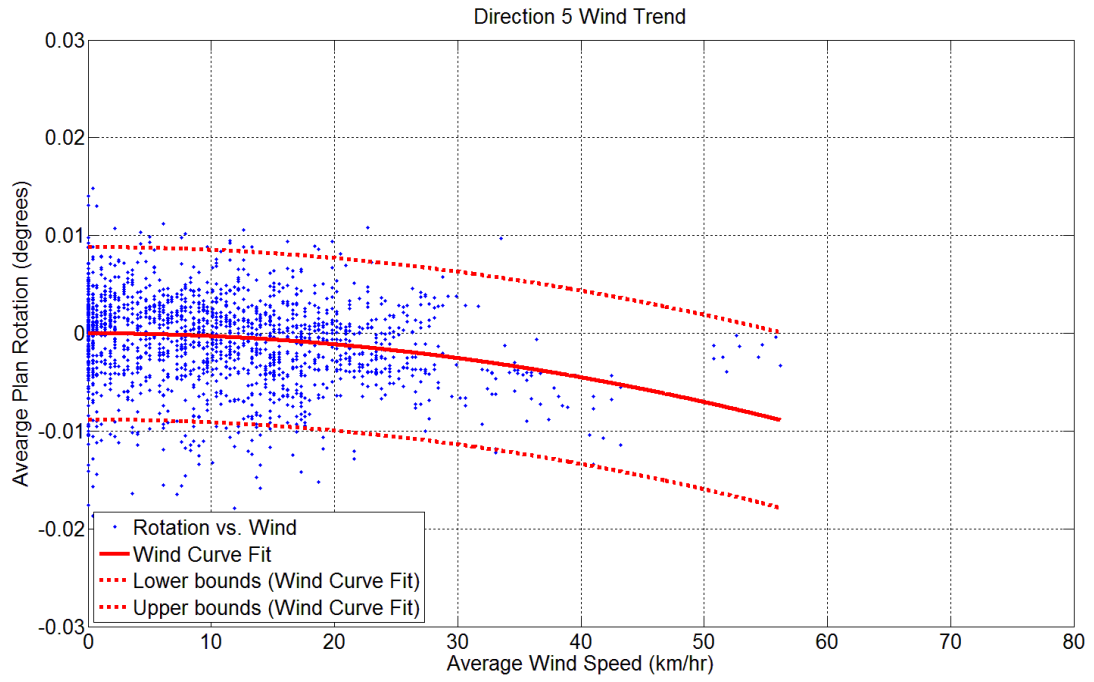**Figure D.3:** Plan rotation wind trend – Direction 2 – DMT MS
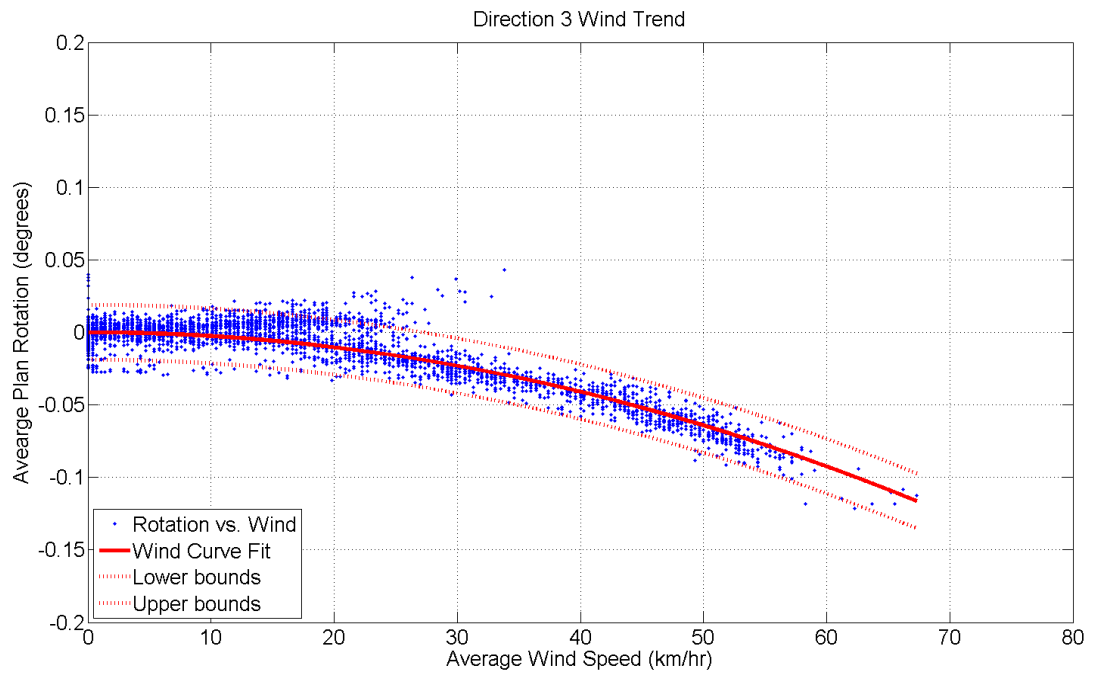
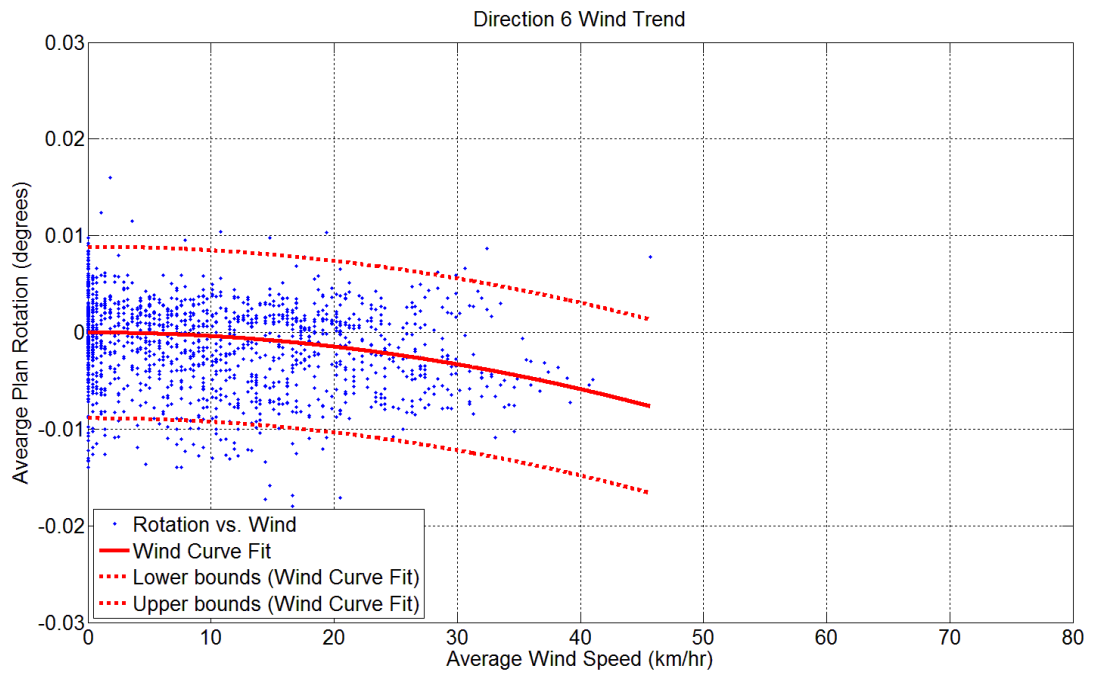**Figure D.4:** Plan rotation wind trend – Direction 3 – DMT MS
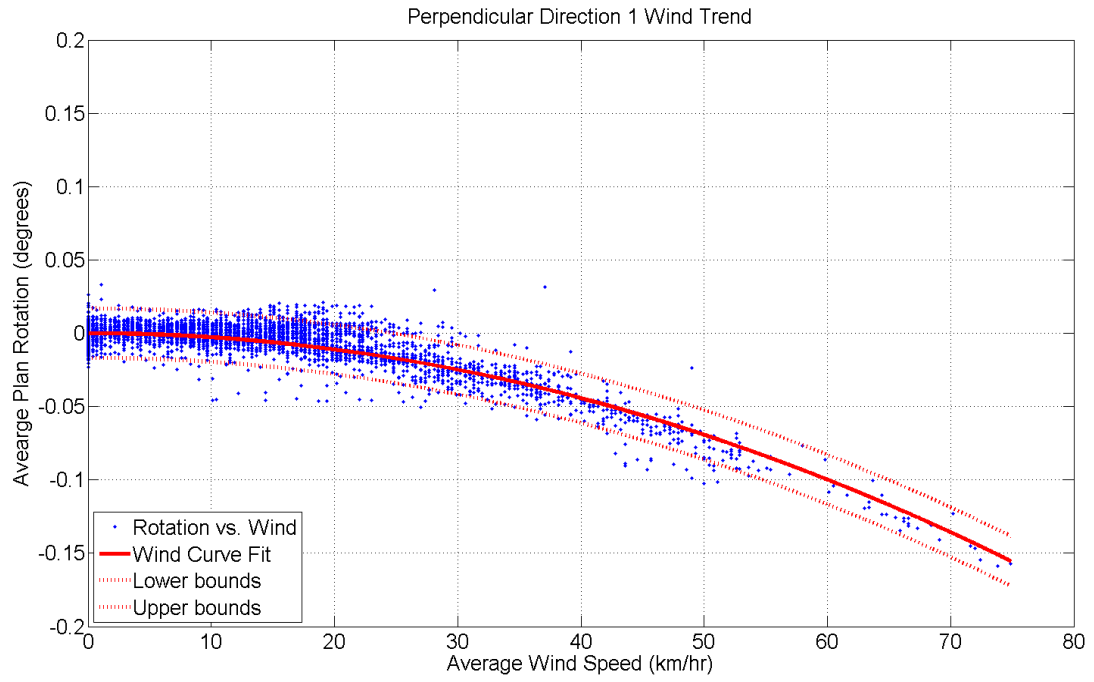
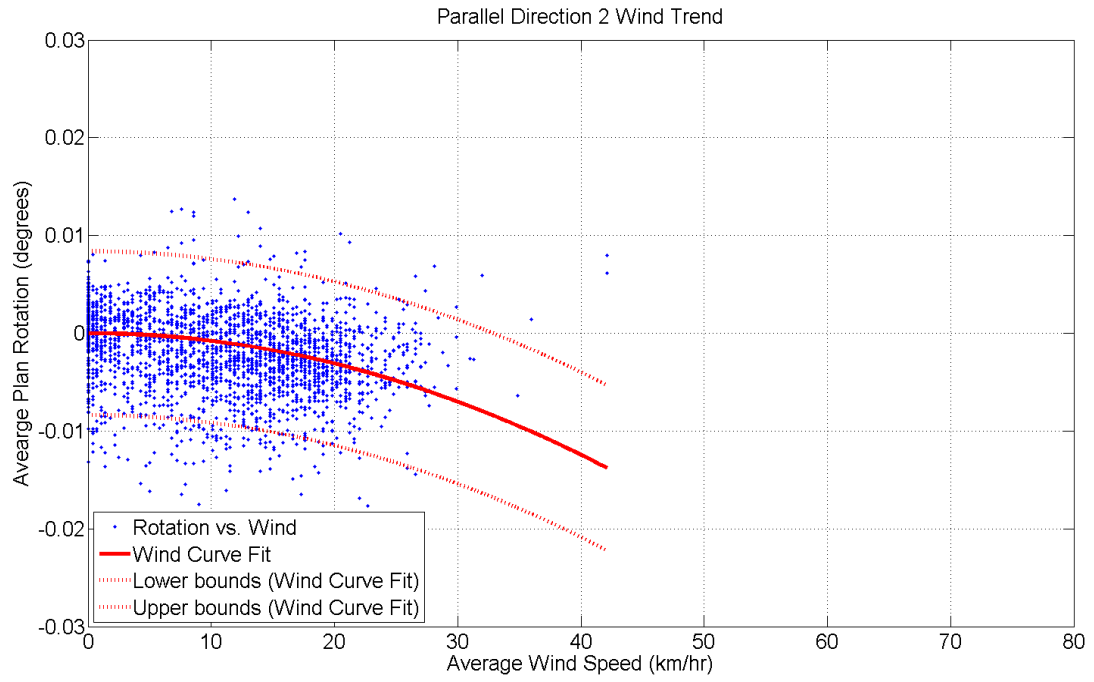**Figure D.5:** Plan rotation wind trend – Perpendicular Direction 1 – DMT MS
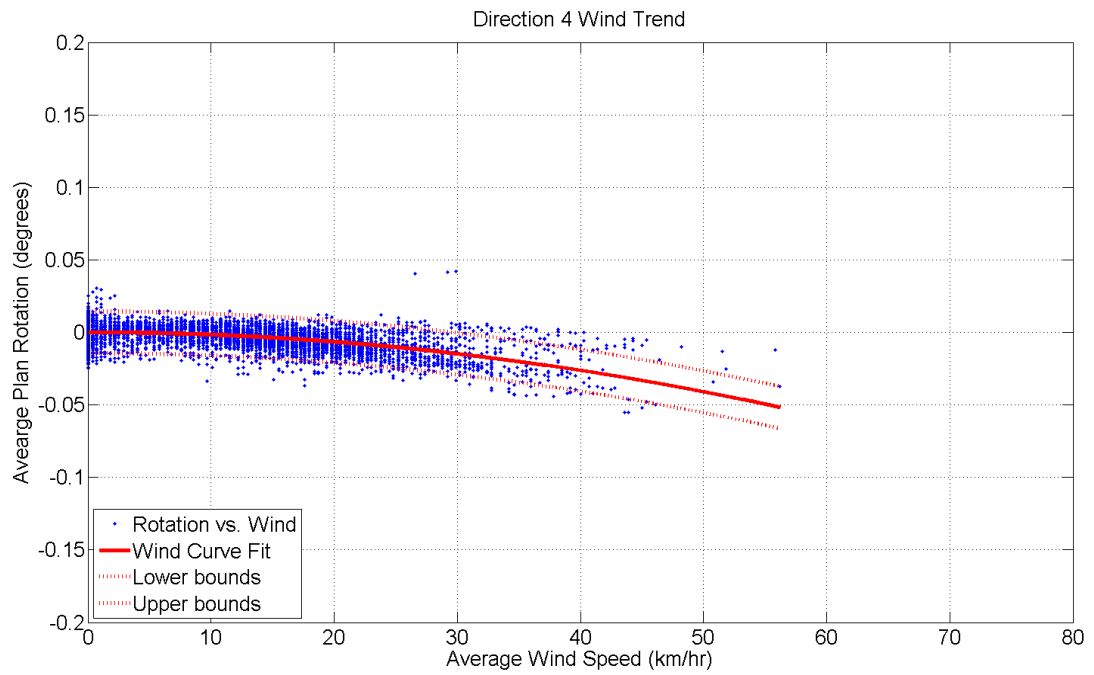
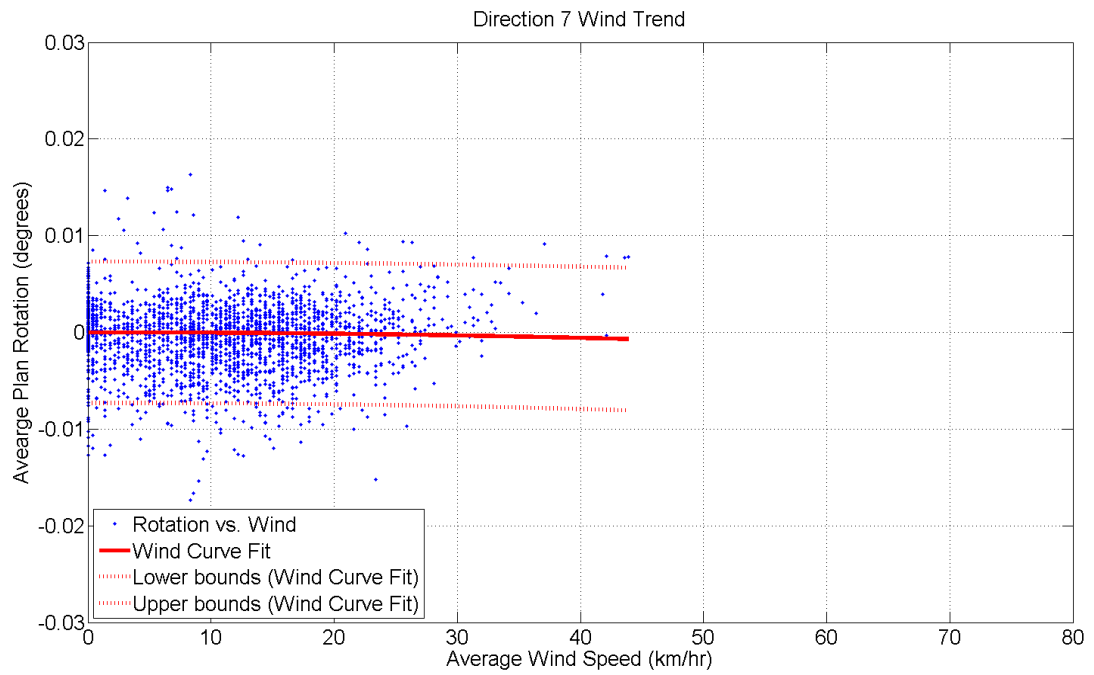**Figure D.6:** Plan rotation wind trend – Direction 4 – DMT MS
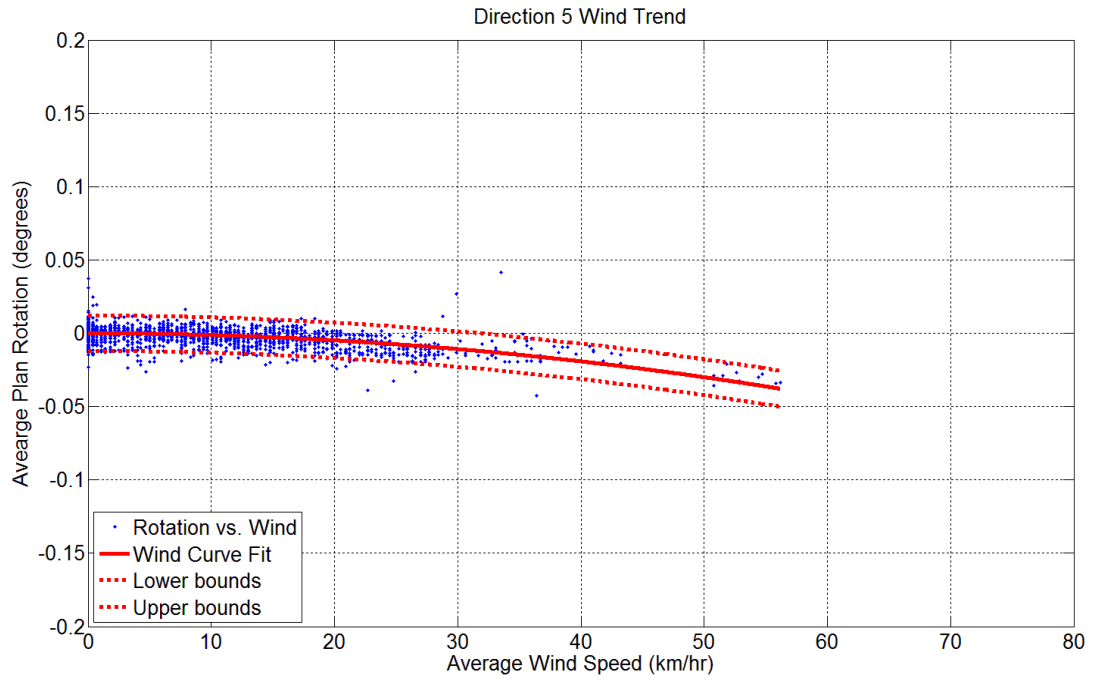
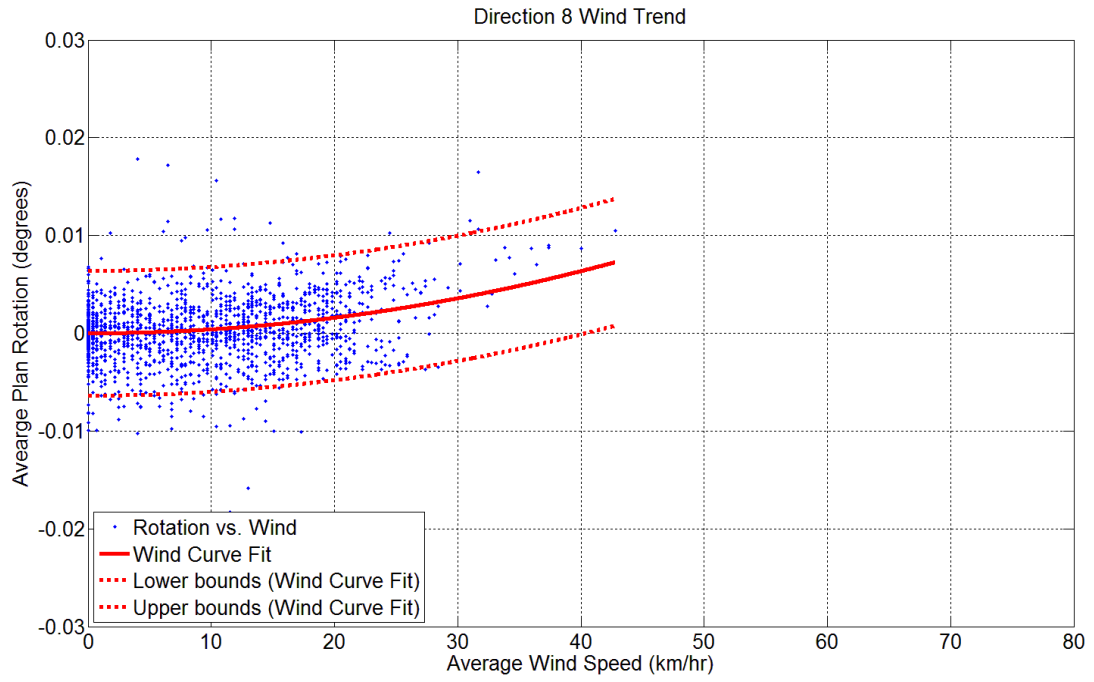**Figure D.7:** Plan rotation wind trend – Direction 5 – DMT MS
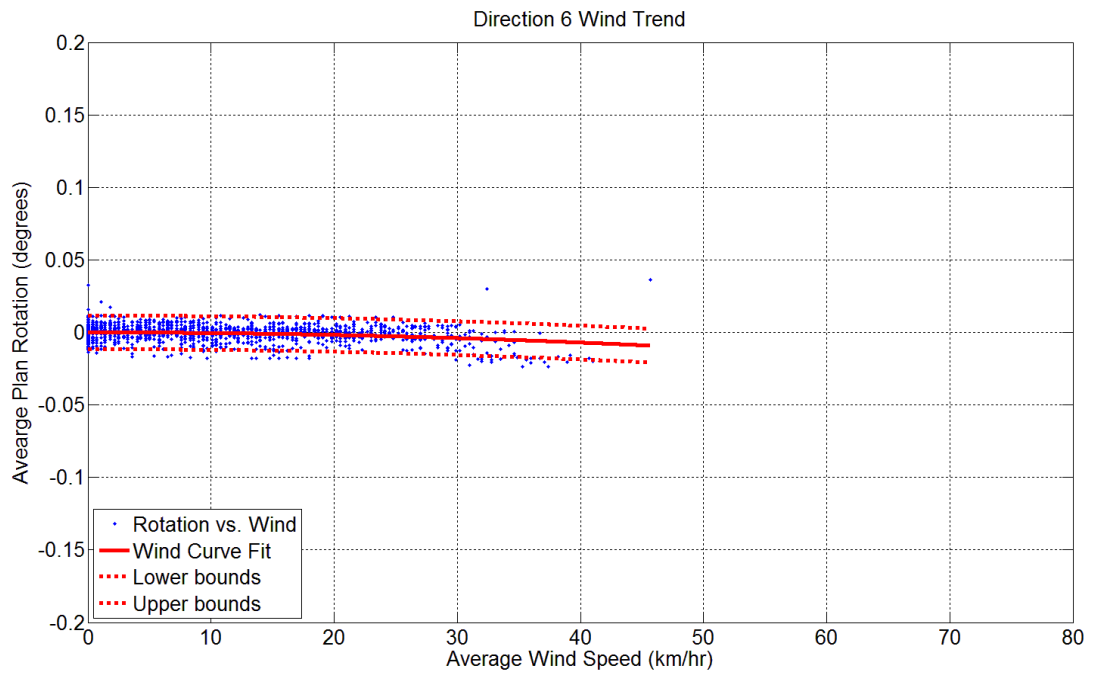
Figure D.8: Plan rotation wind trend – Direction 6 – DMT MS
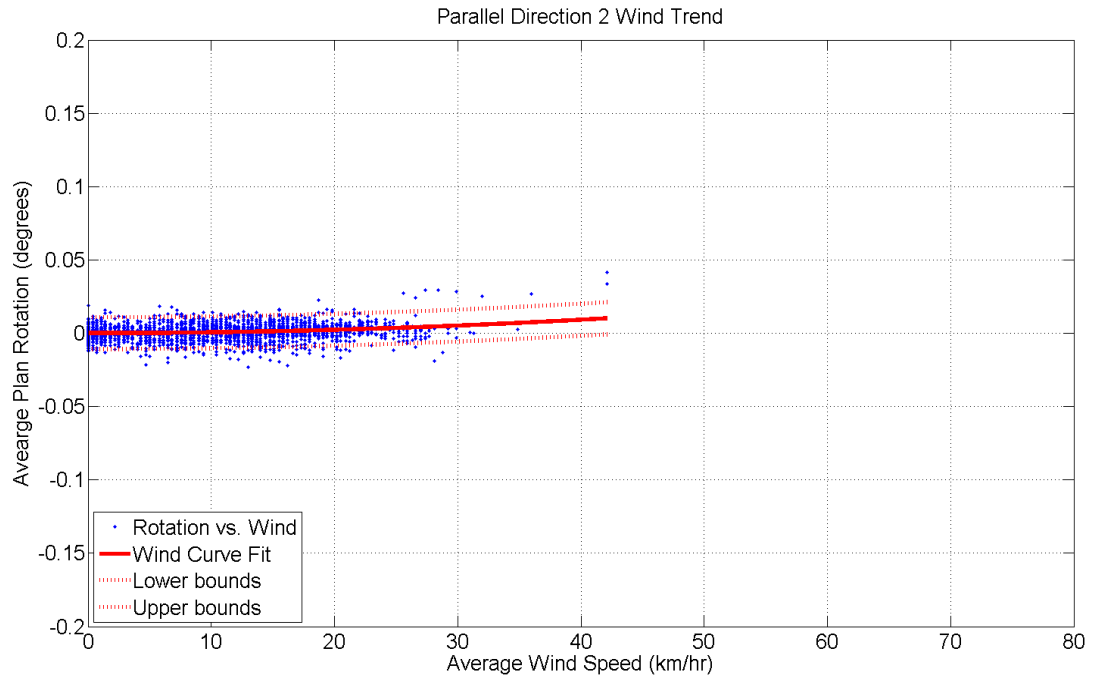
Figure D.9: Plan rotation wind trend – Parallel Direction 2 – DMT MS
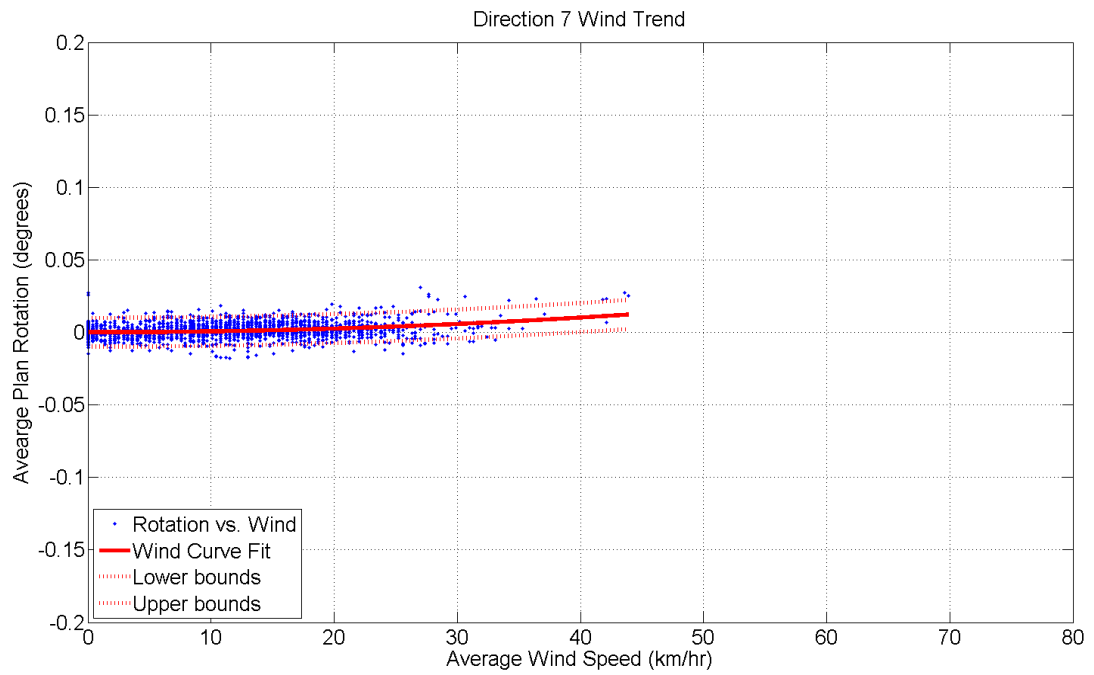
Figure D.10: Plan rotation wind trend – Direction 7 – DMT MS

145
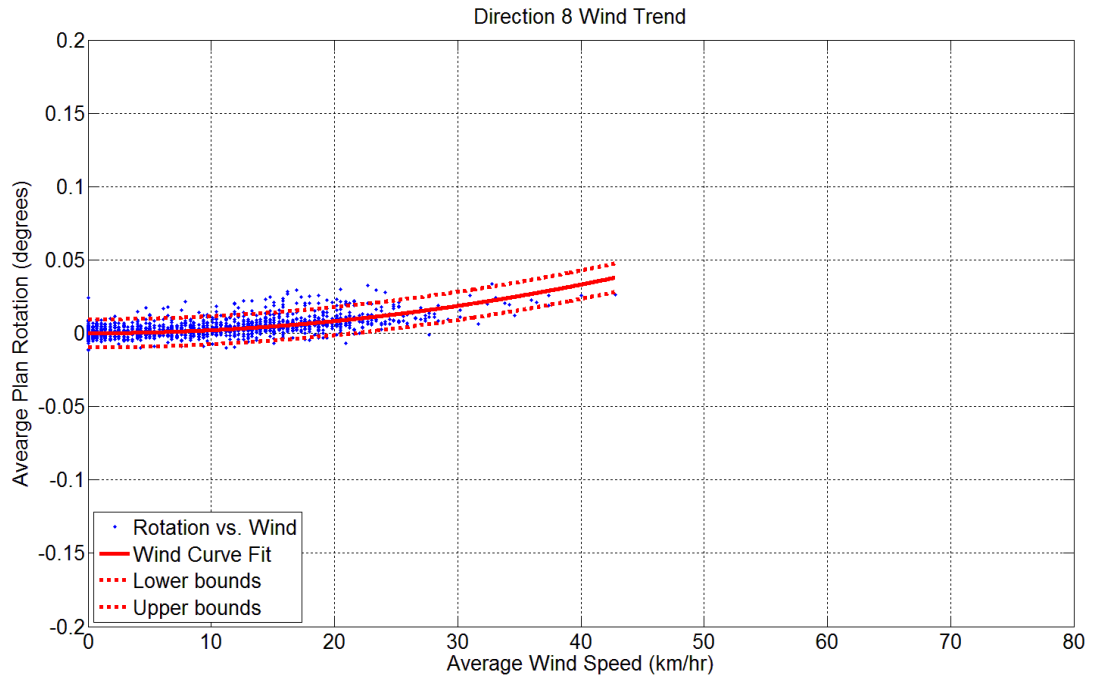
Figure D.11: Plan rotation wind trend – Direction 8 – DMT MS
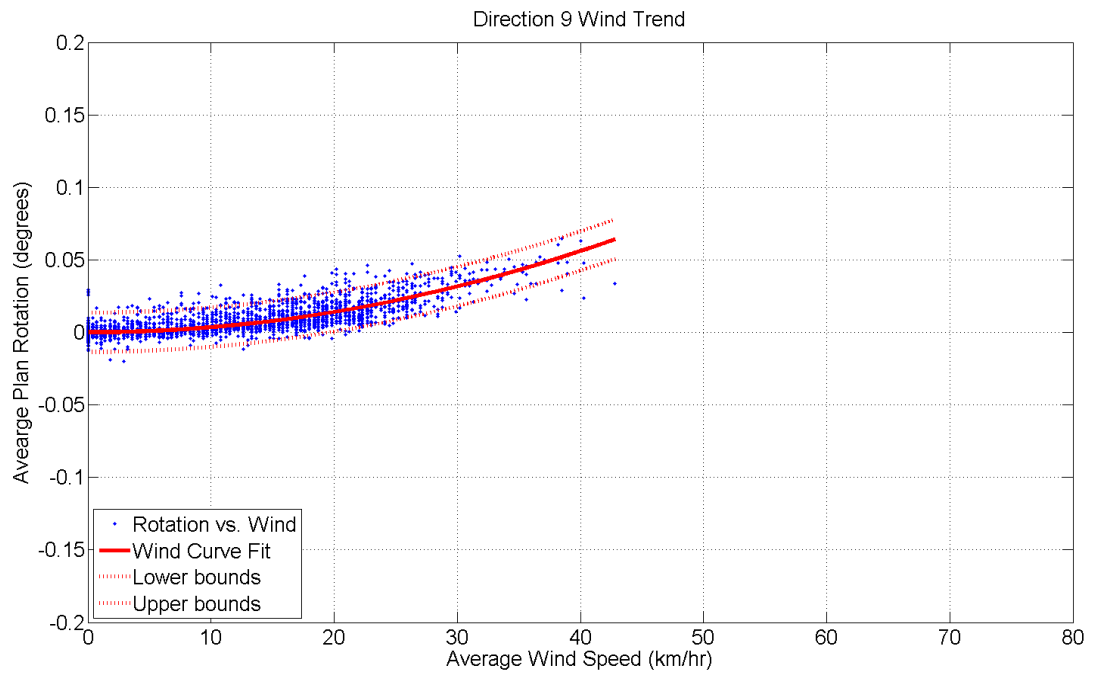
Figure D.12: Plan rotation wind trend – Direction 9 – DMT MS
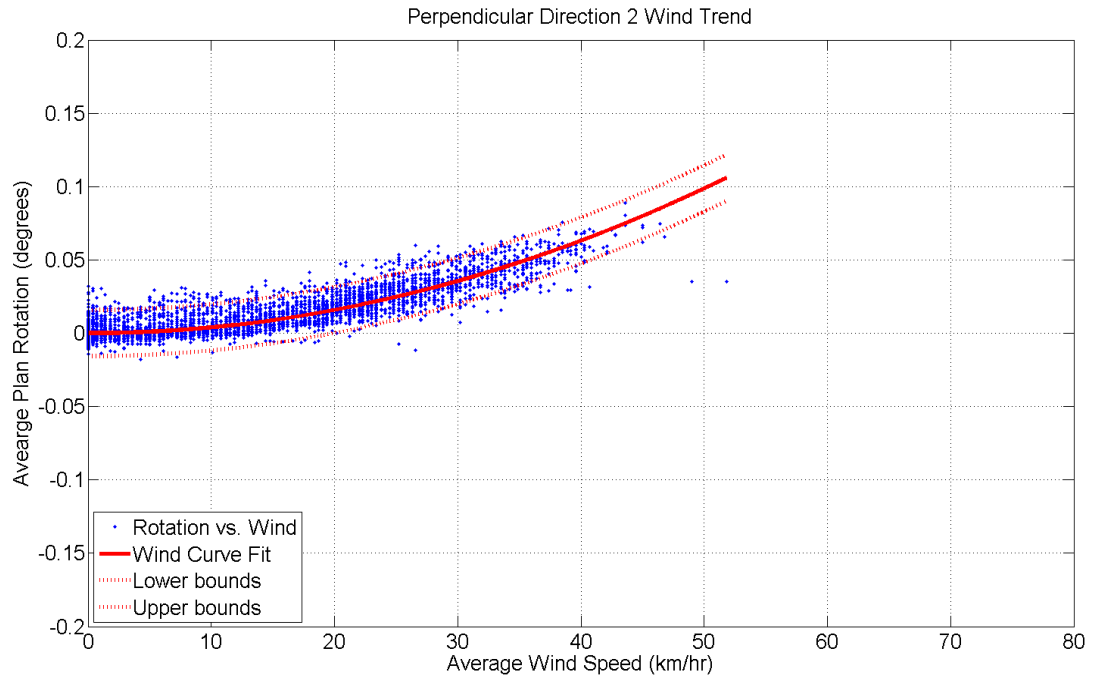
Figure D.13: Plan rotation wind trend – Perpendicular Direction 2 – DMT MS
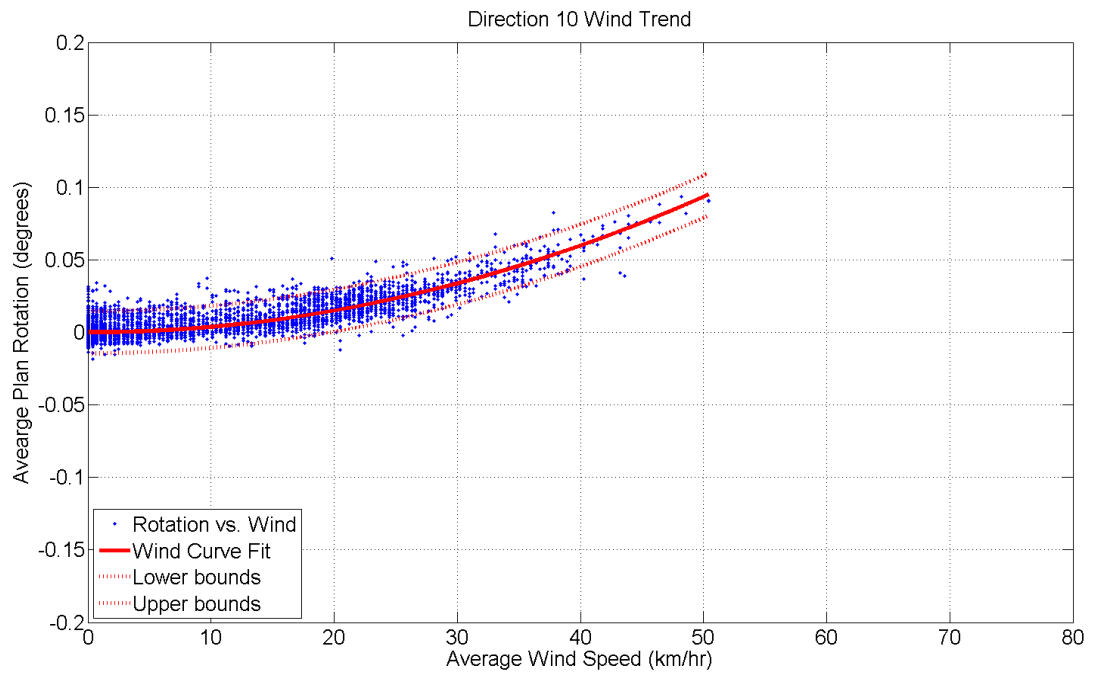
Figure D.14: Plan rotation wind trend – Direction 10 – DMT MS
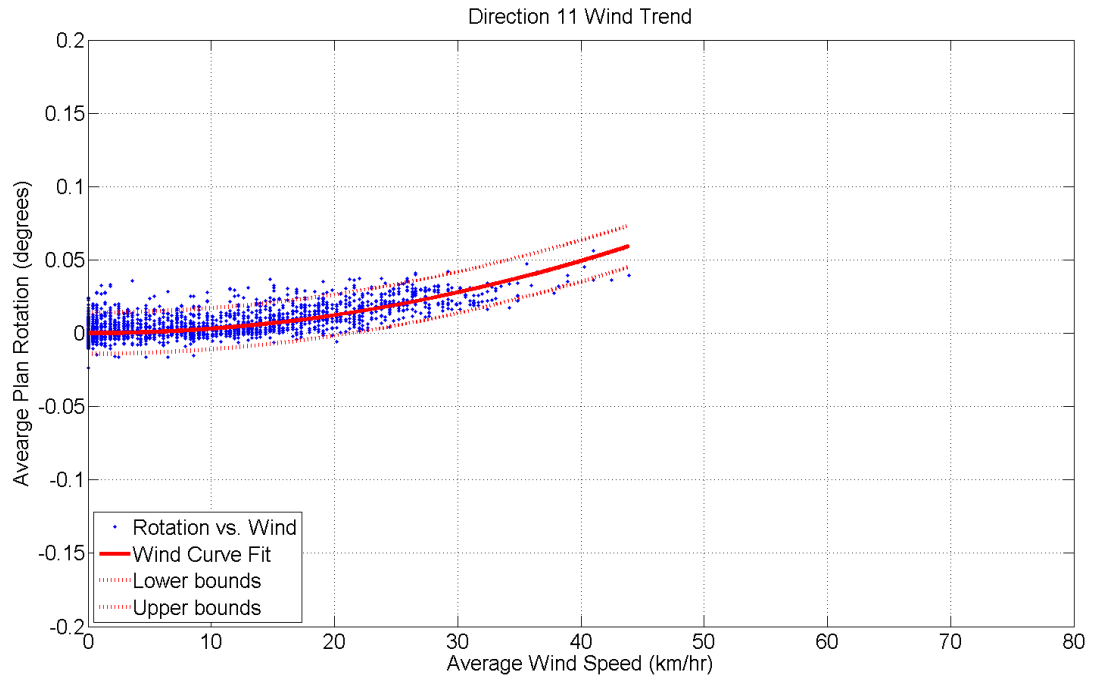
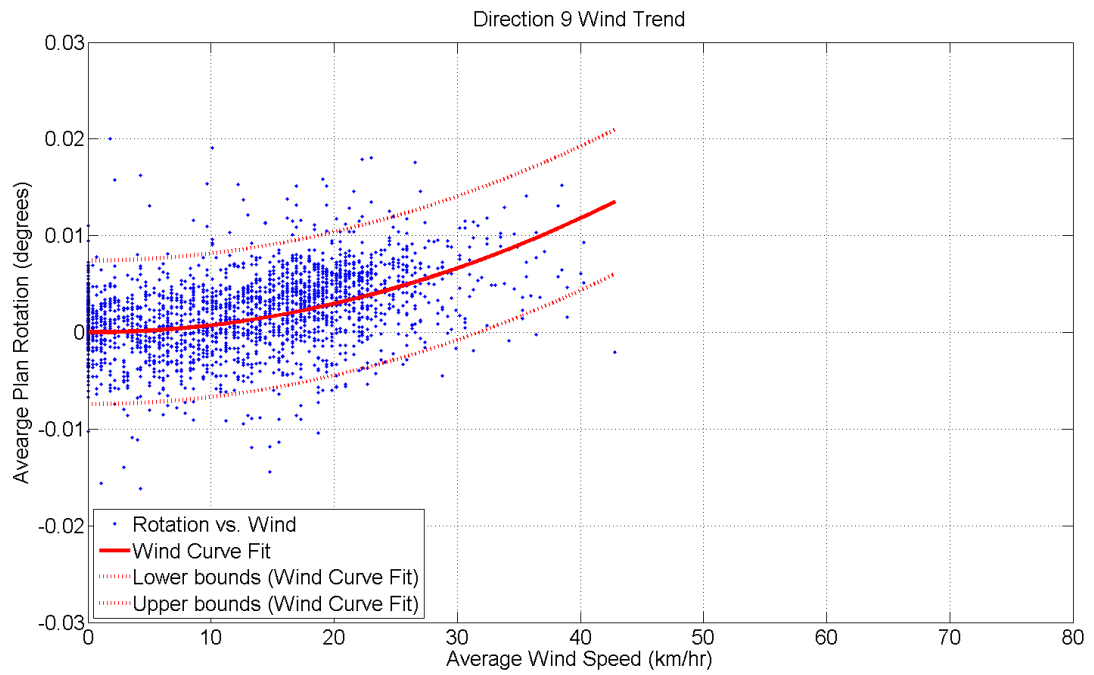**Figure D.15:** Plan rotation wind trend – Direction 11 – DMT MS
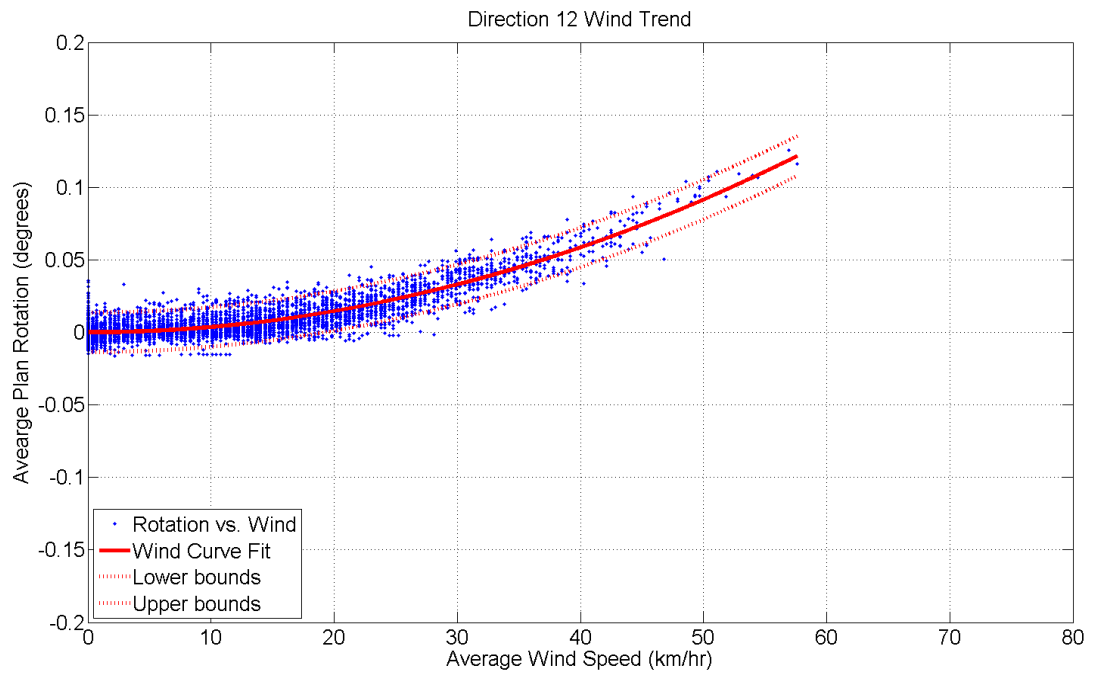
Figure D.16: Plan rotation wind trend – Direction 12 – DMT MS
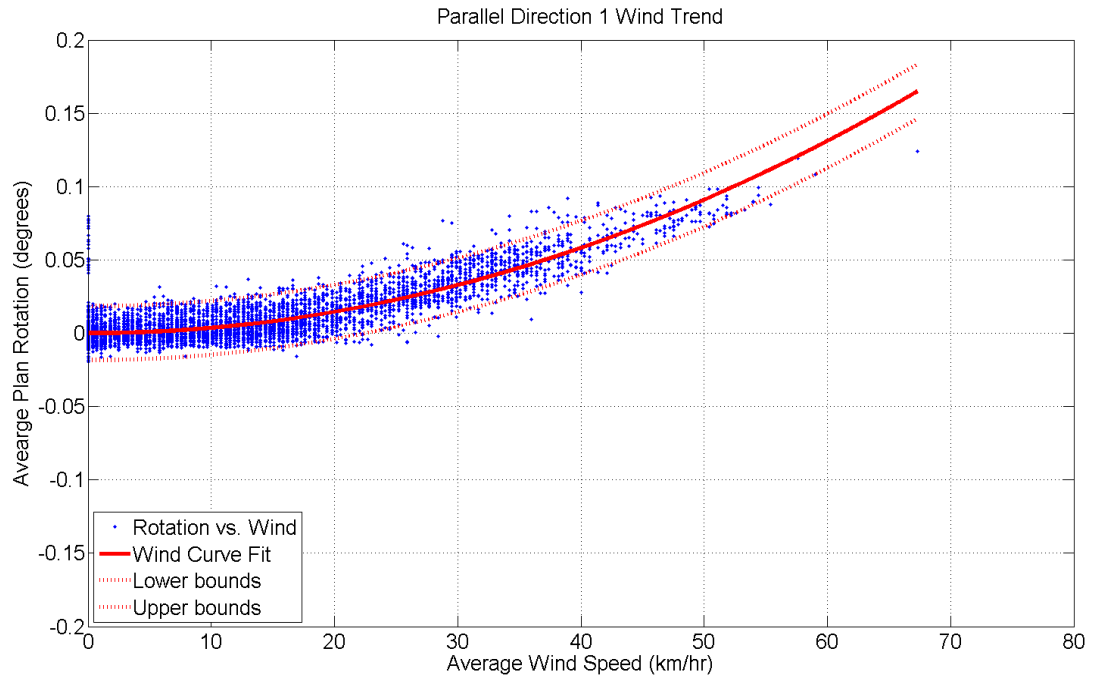
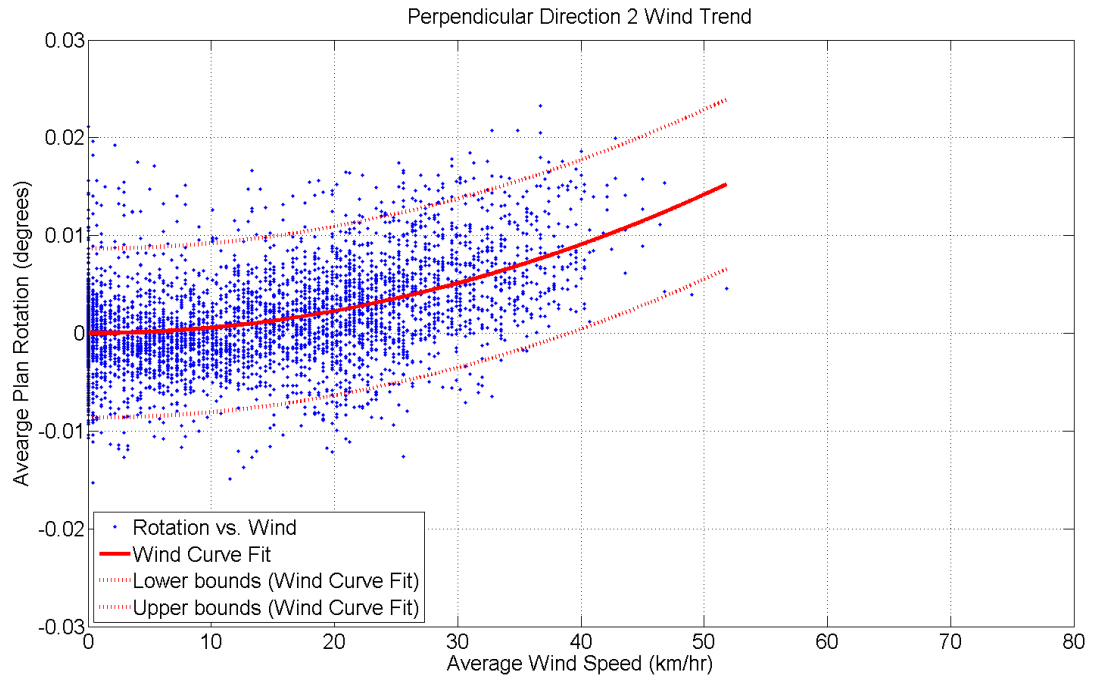**Figure D.17:** Plan rotation wind trend – Parallel Direction 1 – HMT MS
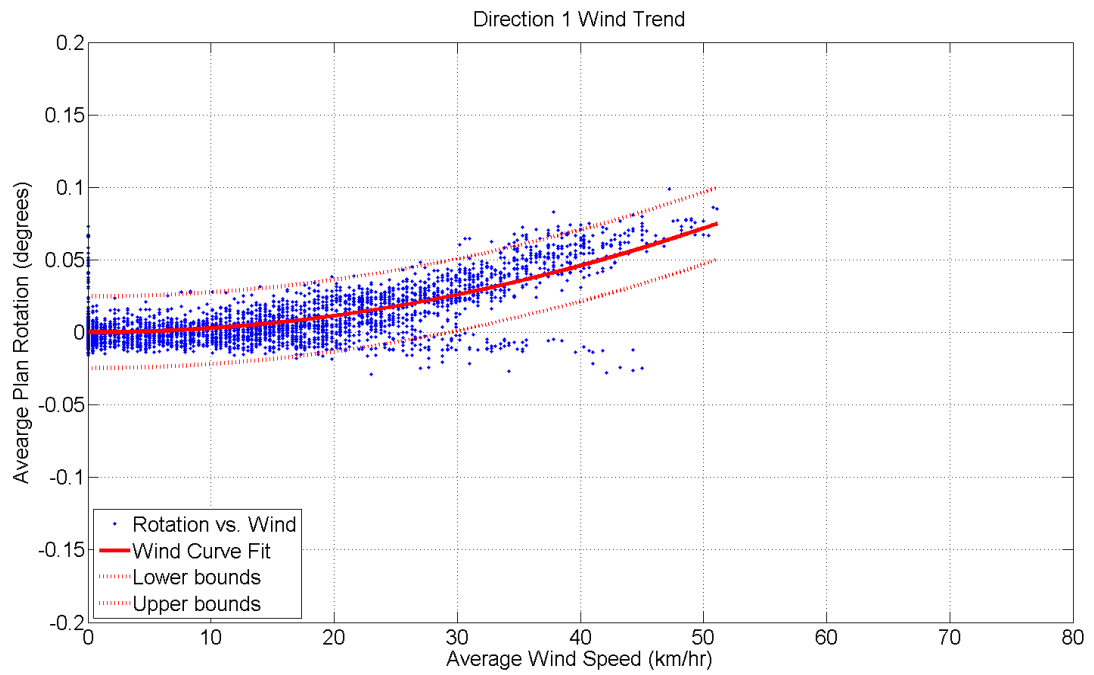
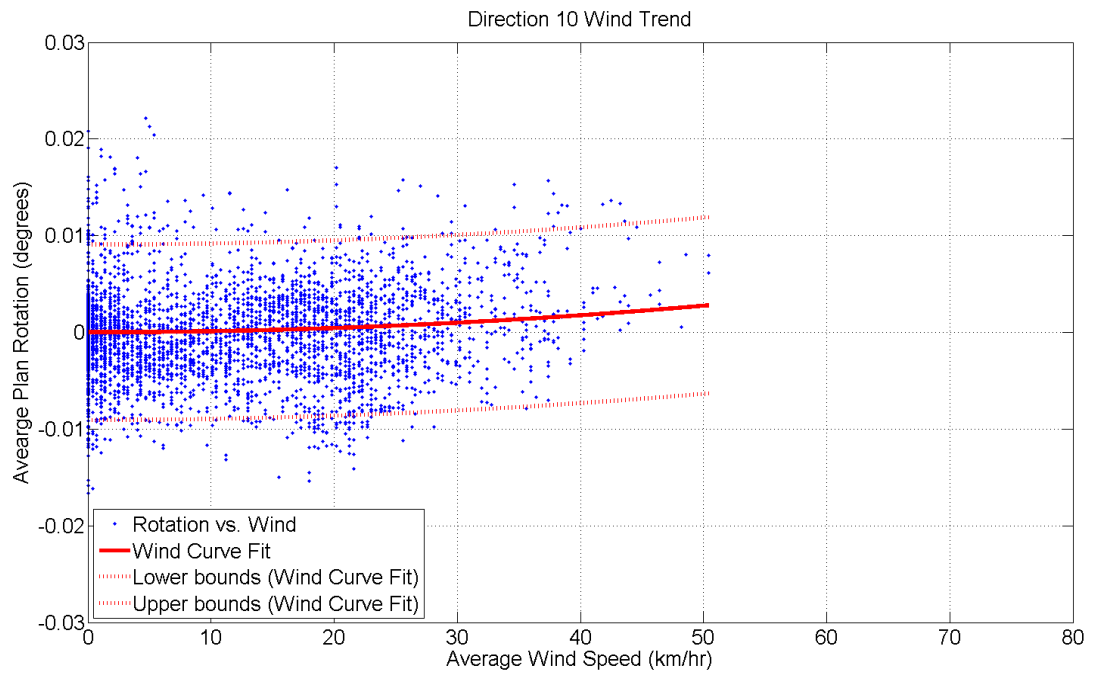**Figure D.18:** Plan rotation wind trend – Direction 1 – HMT MS
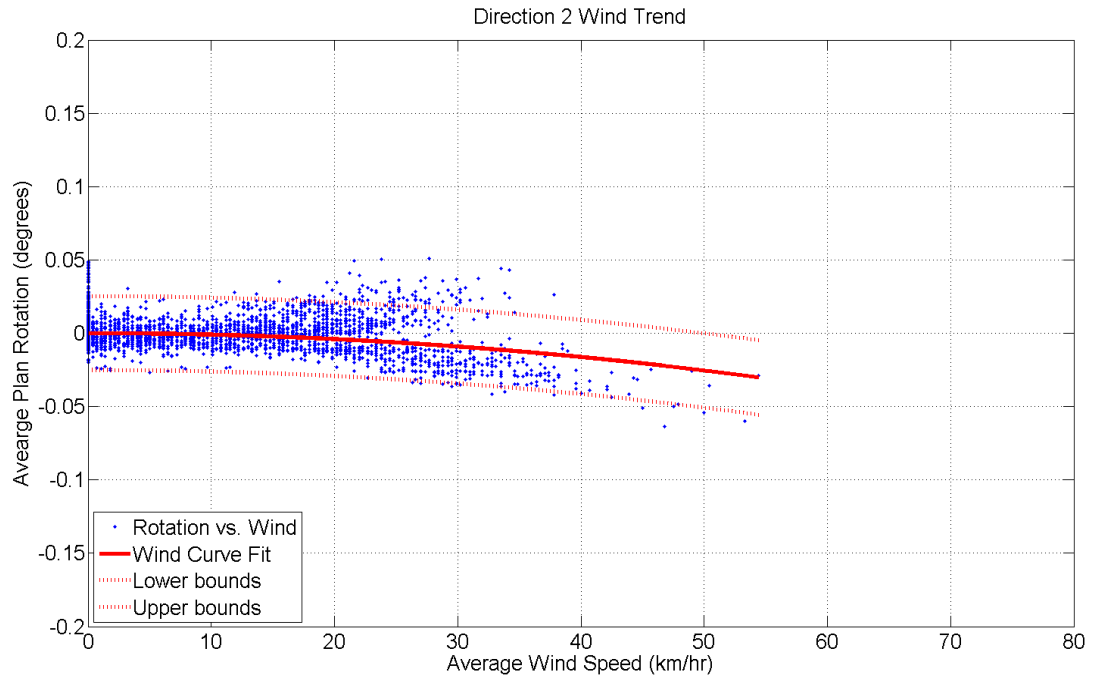
Figure D.19: Plan rotation wind trend – Direction 2 – HMT MS
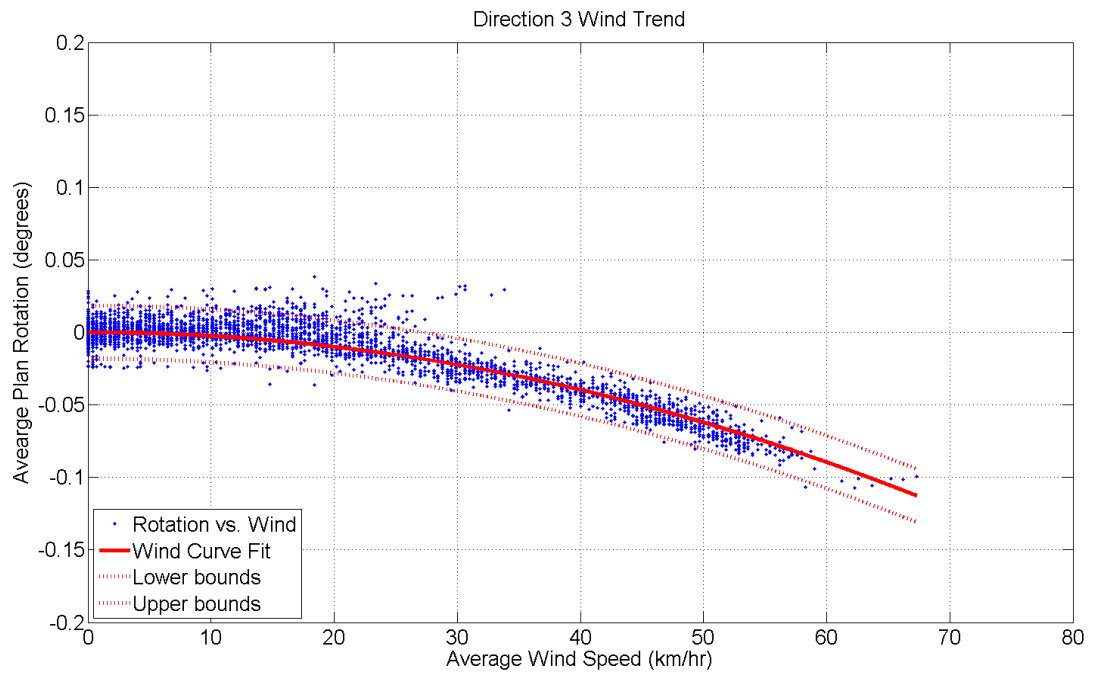
Figure D.20: Plan rotation wind trend – Direction 3 – HMT MS

150
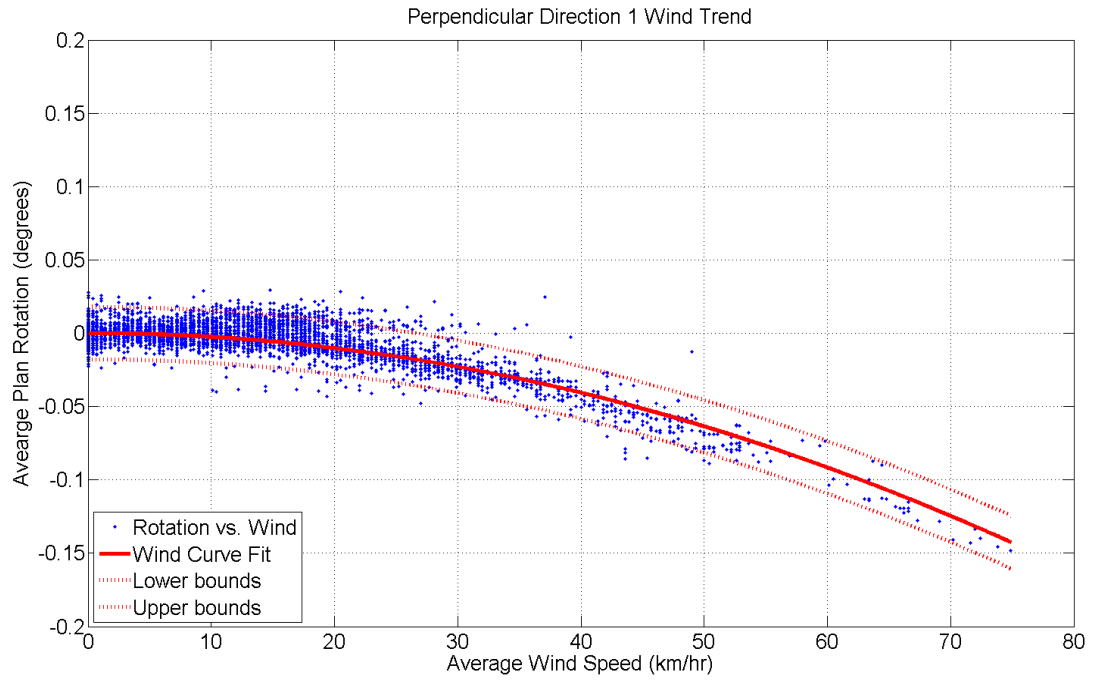
Figure D.21: Plan rotation wind trend – Perpendicular Direction 1 – HMT MS
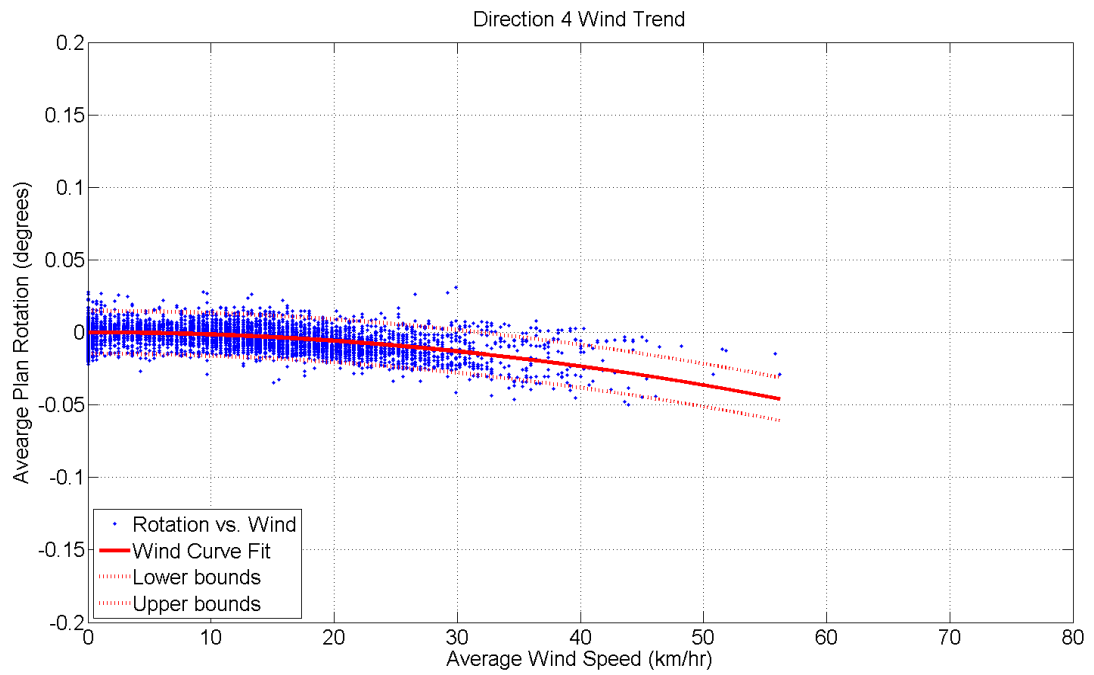
Figure D.22: Plan rotation wind trend – Direction 4 – HMT MS
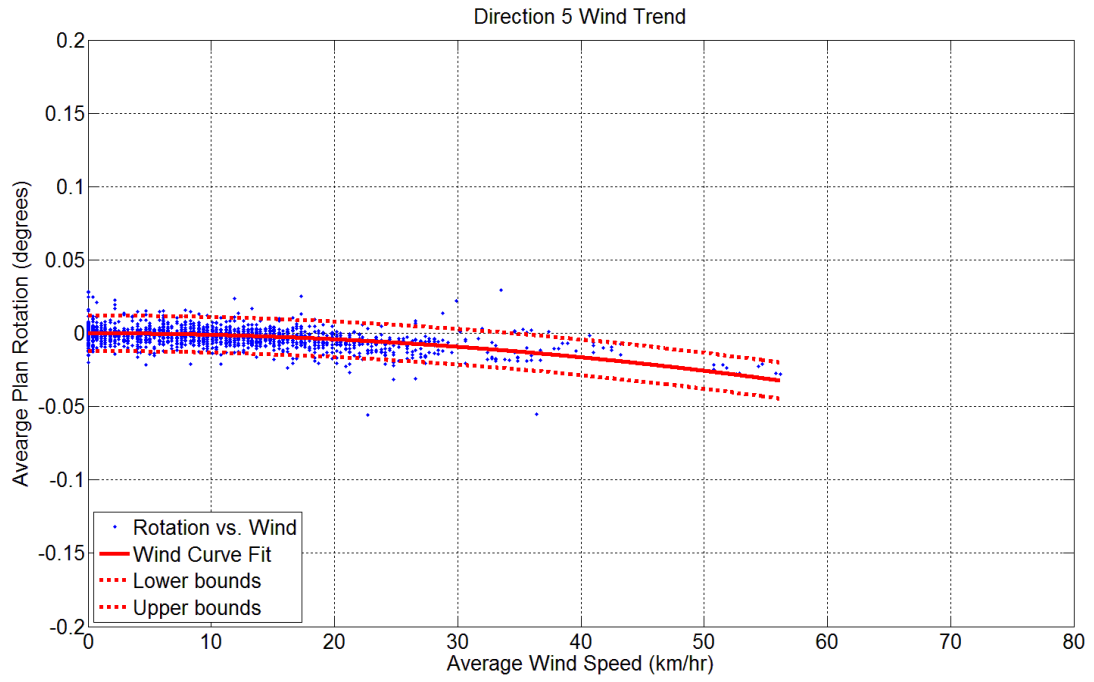
Figure D.23: Plan rotation wind trend – Direction 5 – HMT MS
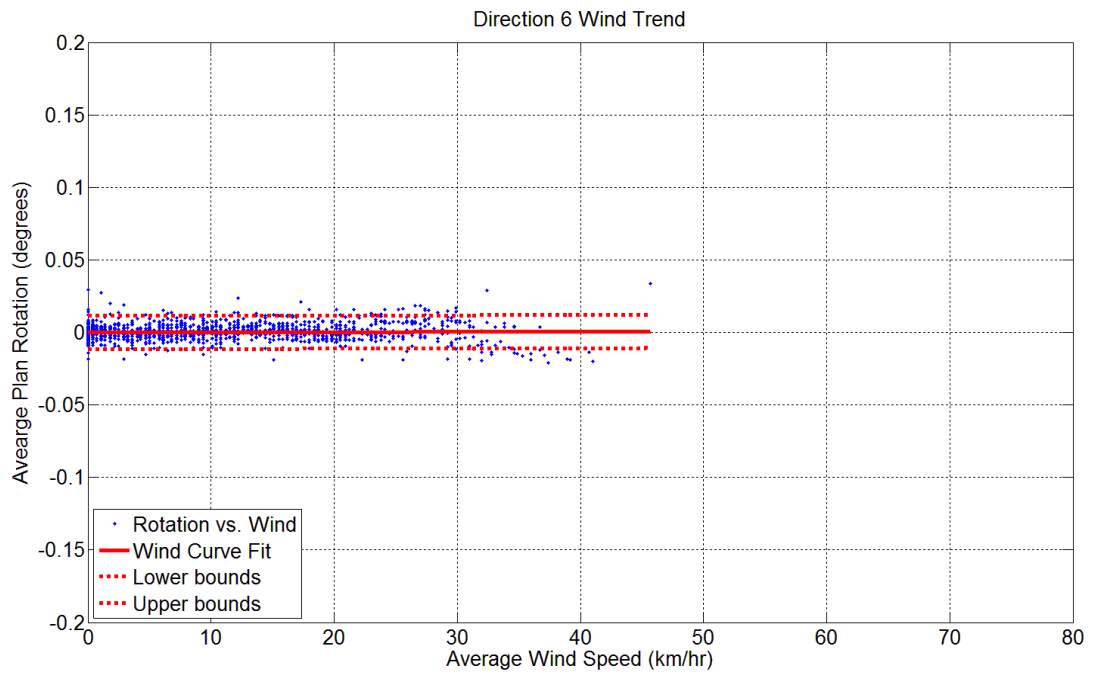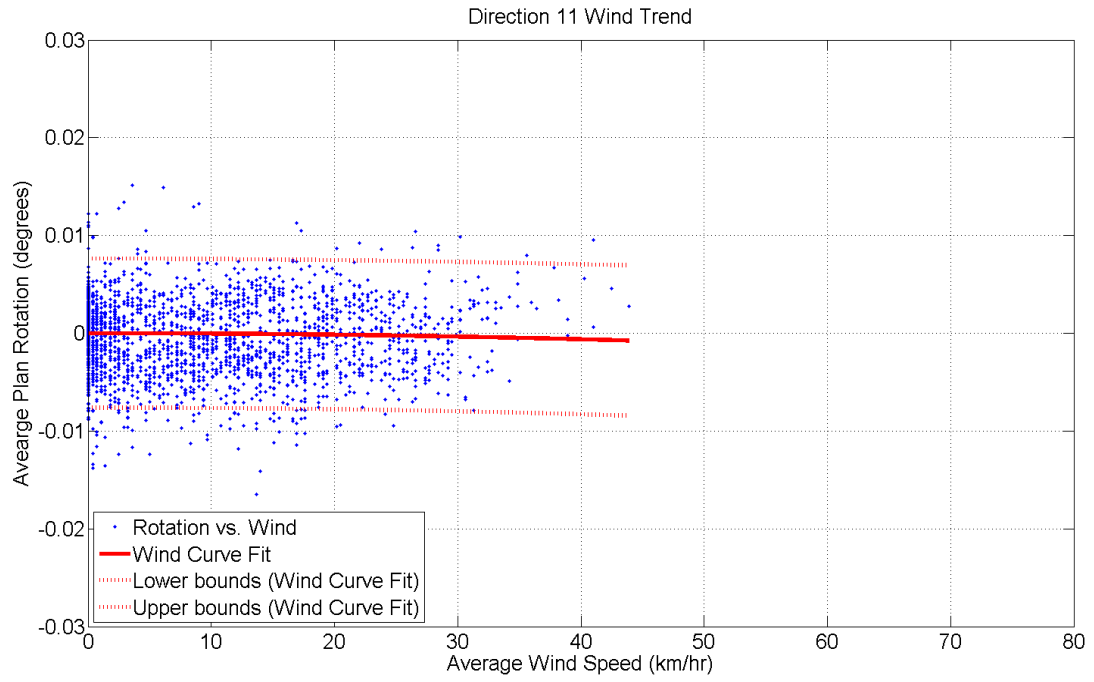

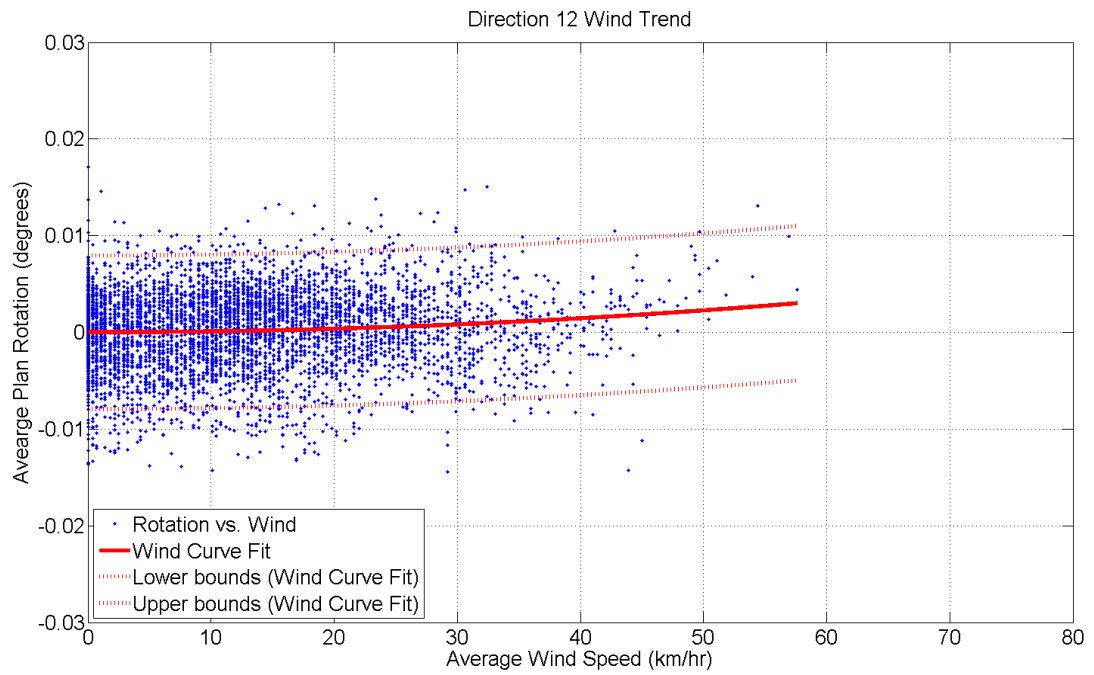**Figure D.24:** Plan rotation wind trend – Direction 6 – HMT MS
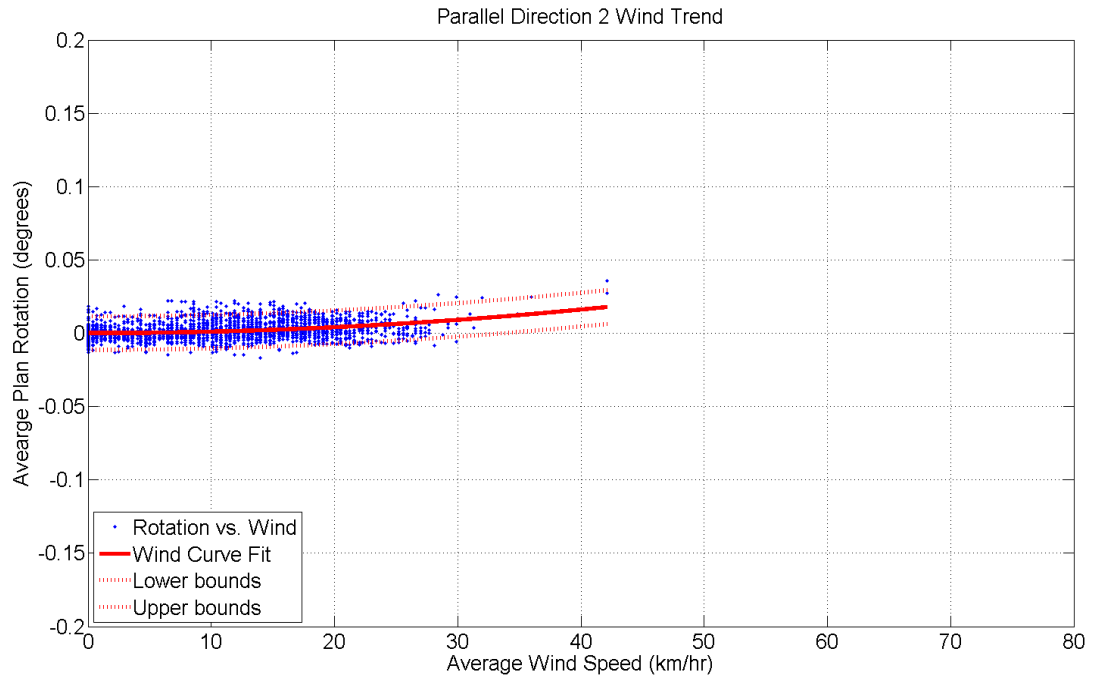
Figure D.25: Plan rotation wind trend – Parallel Direction 2 – HMT MS
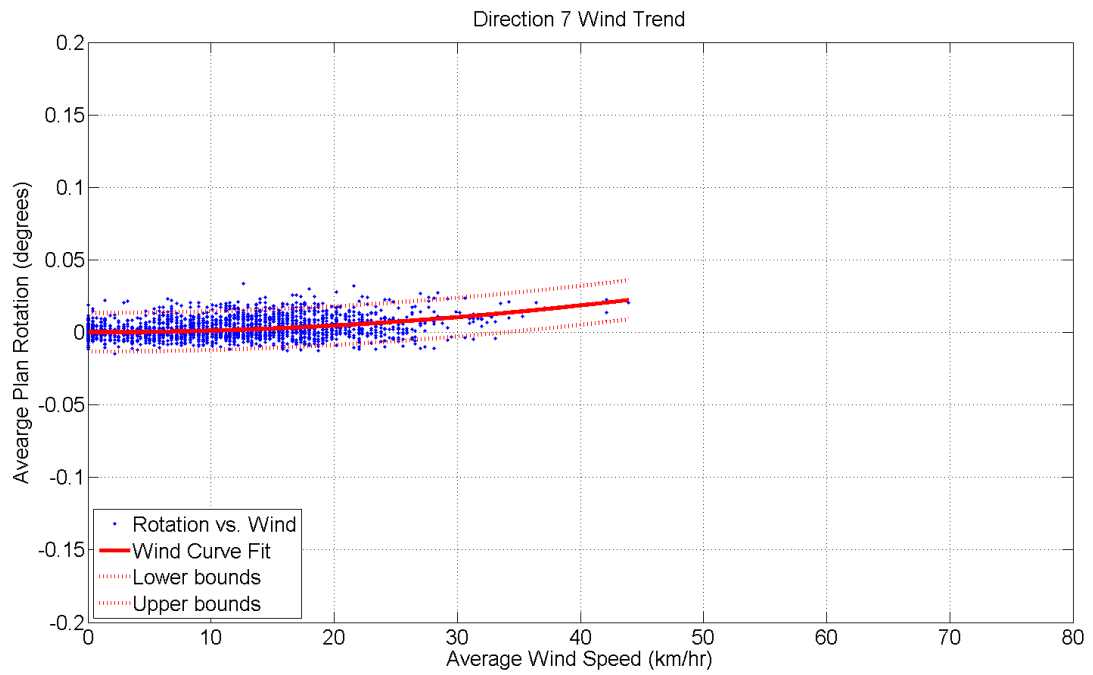
Figure D.26: Plan rotation wind trend – Direction 7 – HMT MS

153
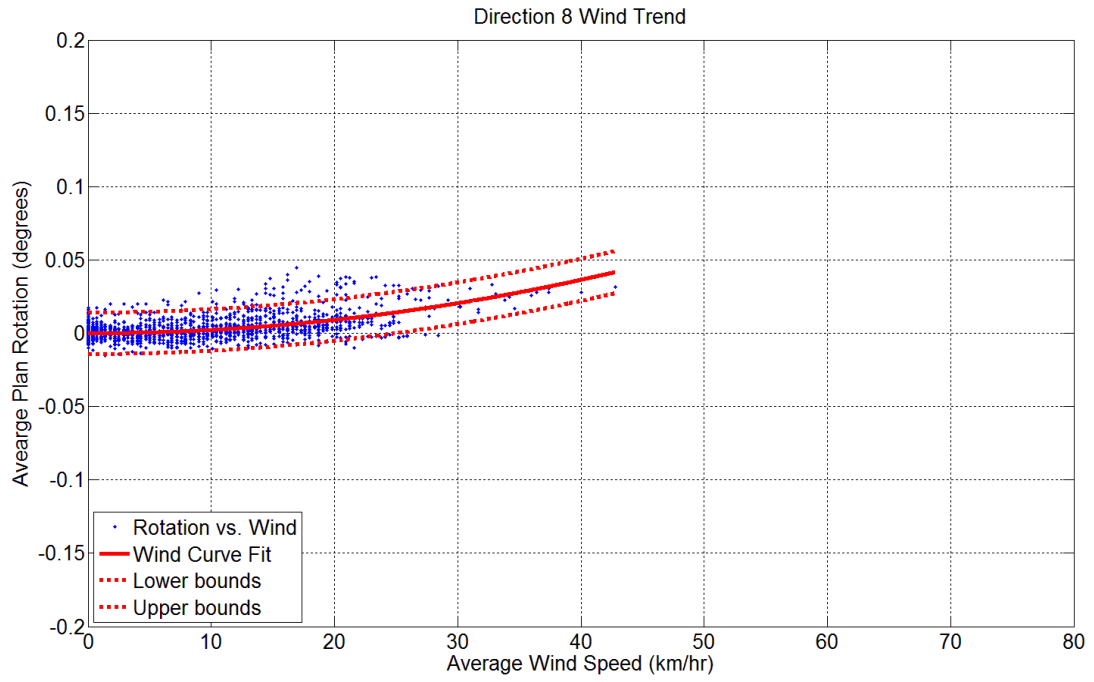
Figure D.27: Plan rotation wind trend – Direction 8 – HMT MS
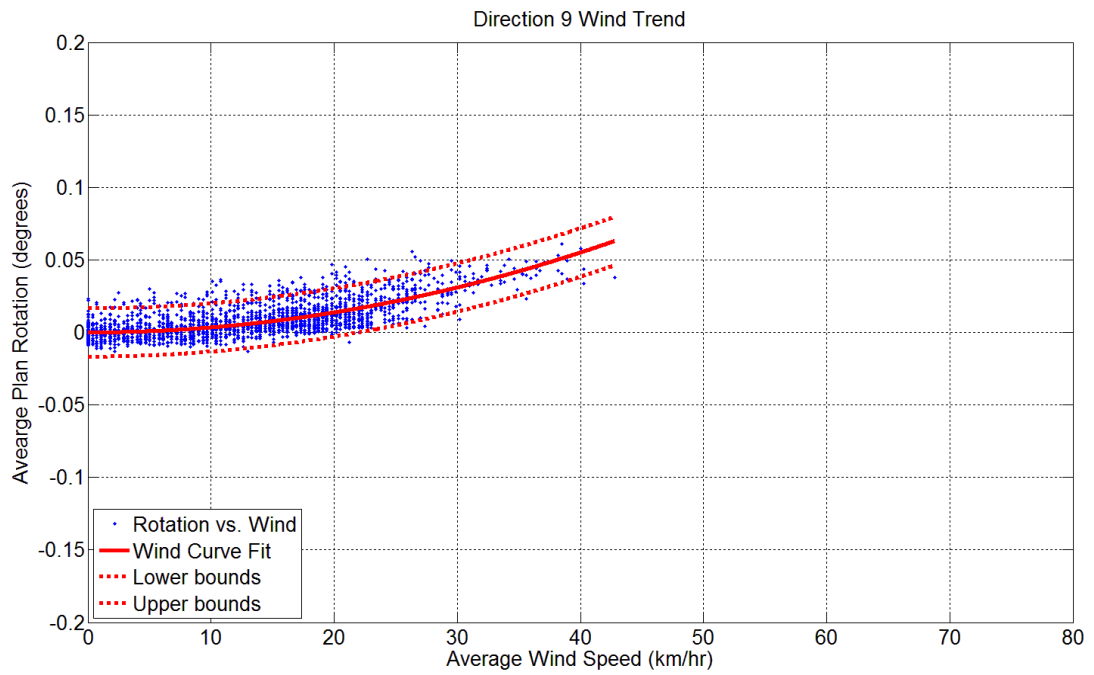
Figure D.28: Plan rotation wind trend – Direction 9 – HMT MS
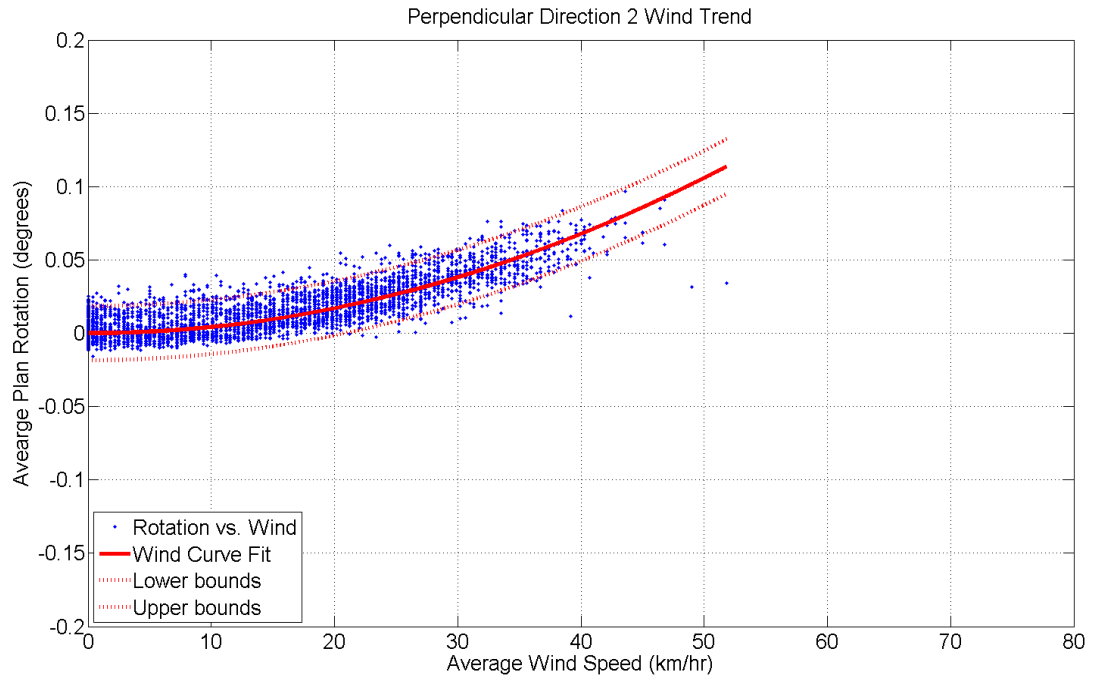
Figure D.29: Plan rotation wind trend – Perpendicular Direction 2 – HMT MS
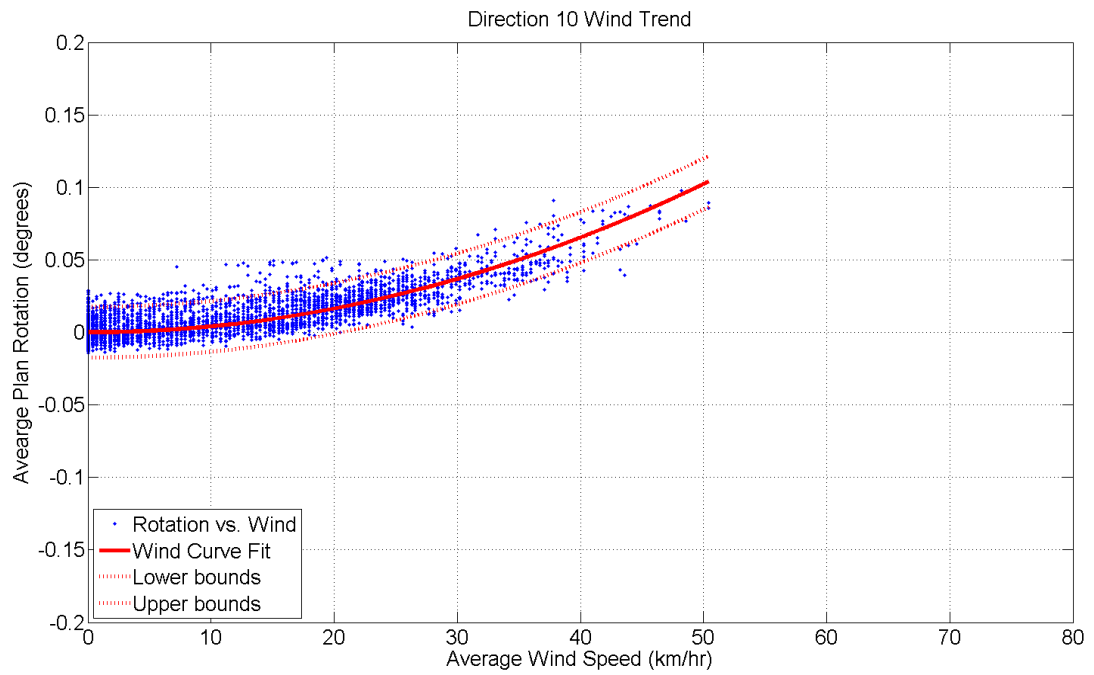
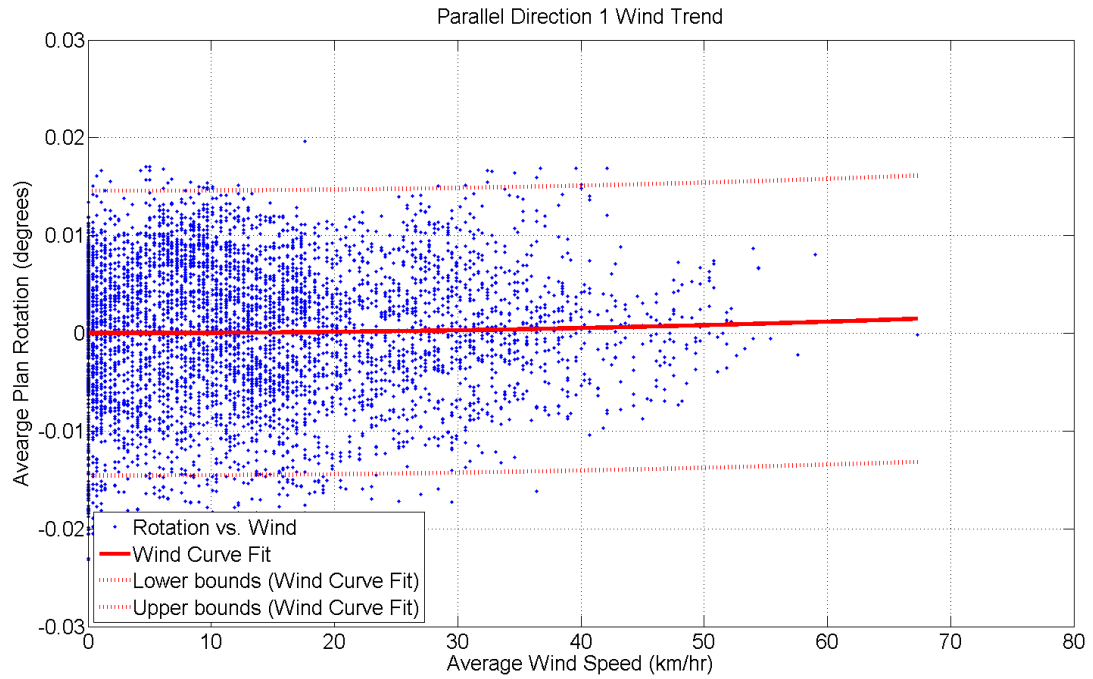**Figure D.30:** Plan rotation wind trend – Direction 10 – HMT MS

155
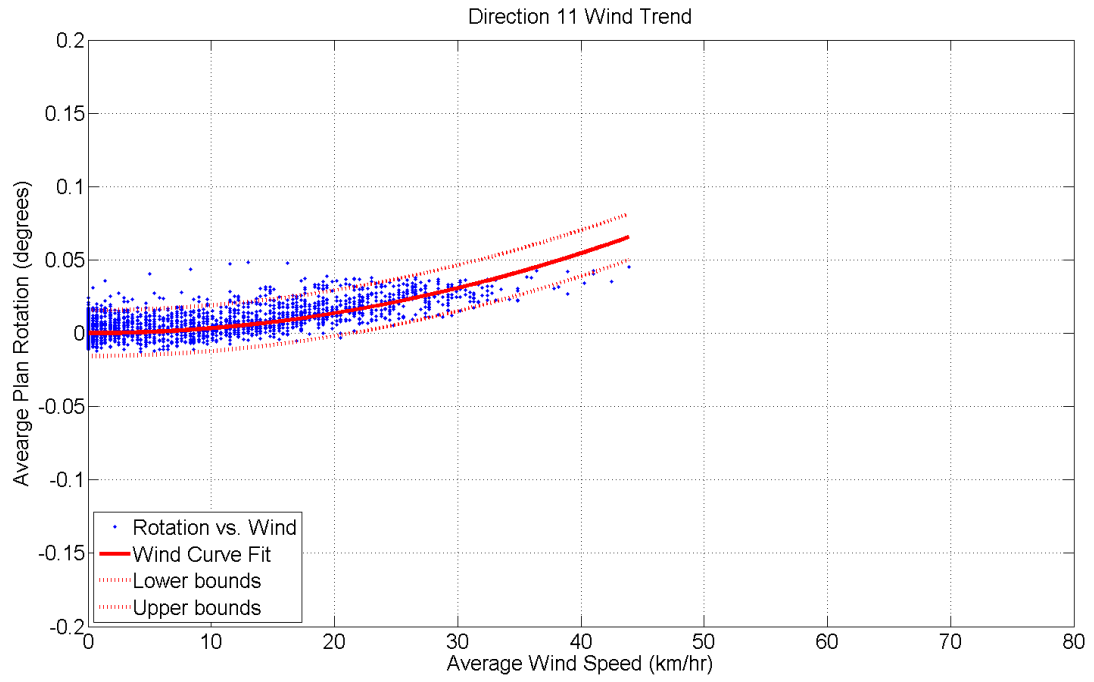
Figure D.31: Plan rotation wind trend – Direction 11 – HMT MS
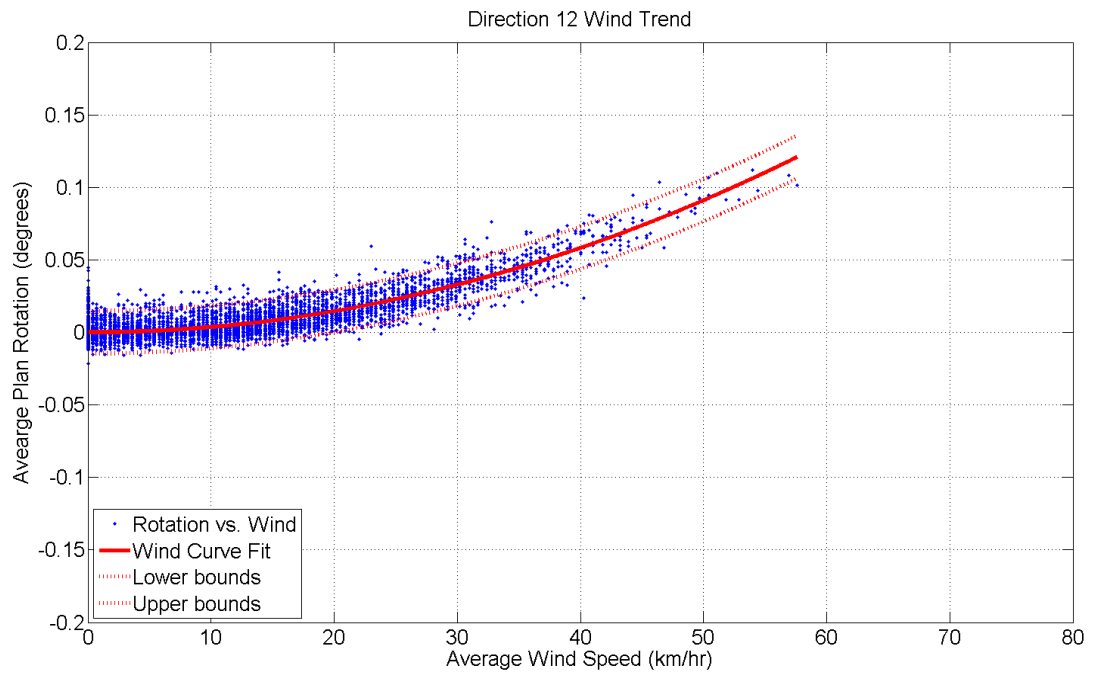
Figure D.32: Plan rotation wind trend – Direction 12 – HMT MS
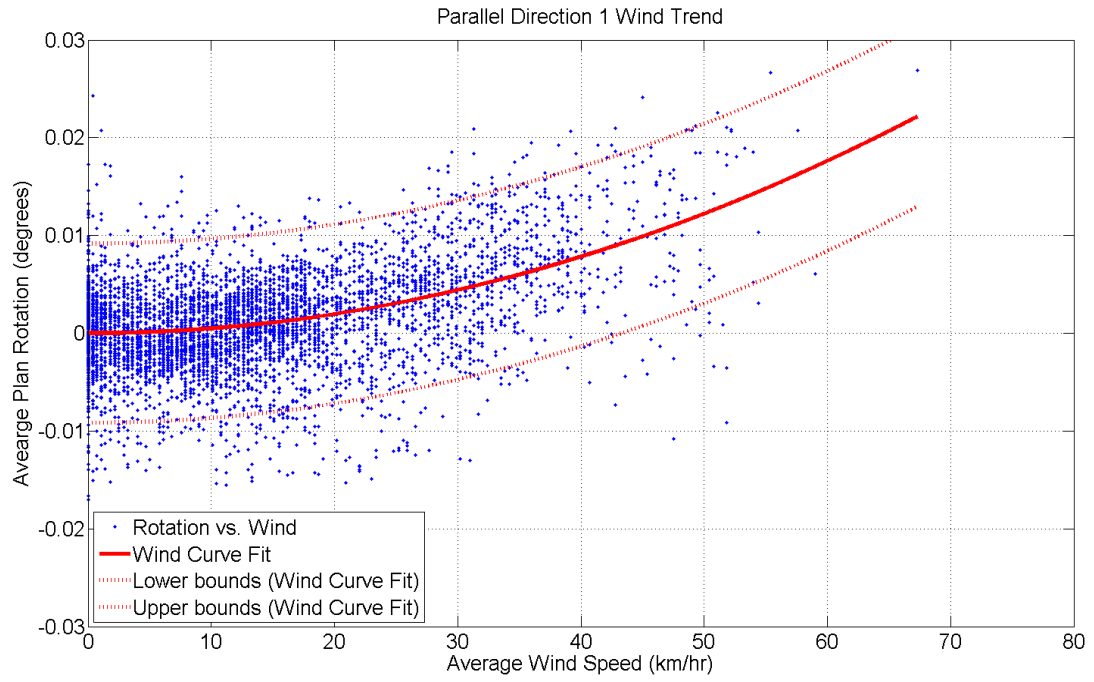
Figure D.33: Plan rotation wind trend – Parallel Direction 1 – DMT SS
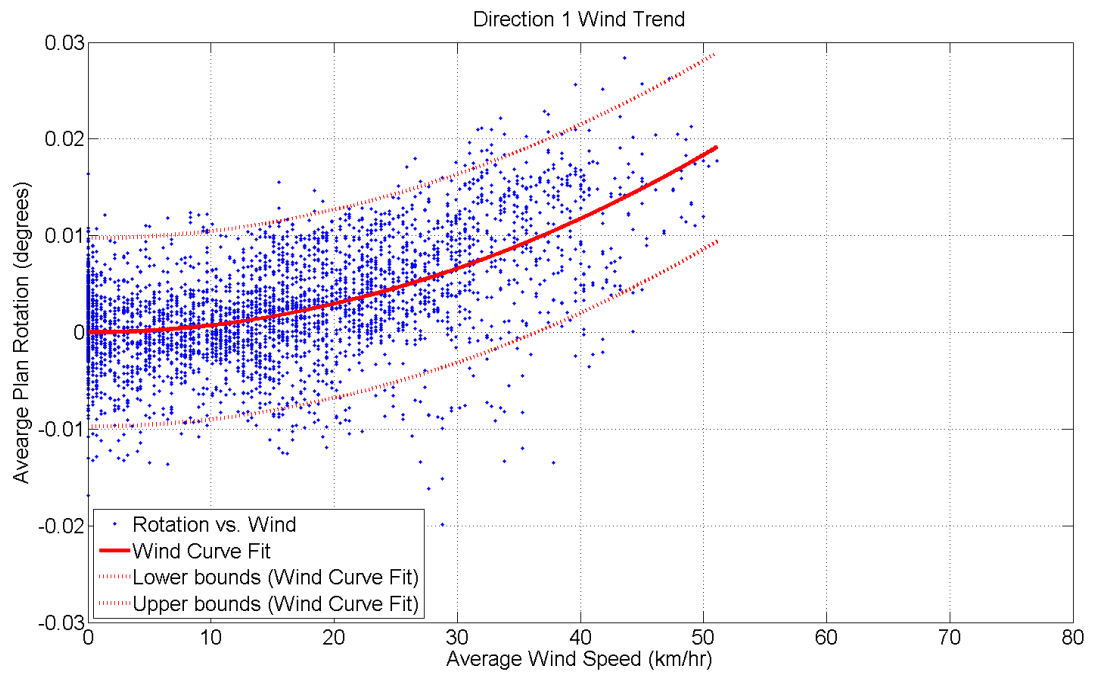
Figure D.34: Plan rotation wind trend – Direction 1 – DMT SS
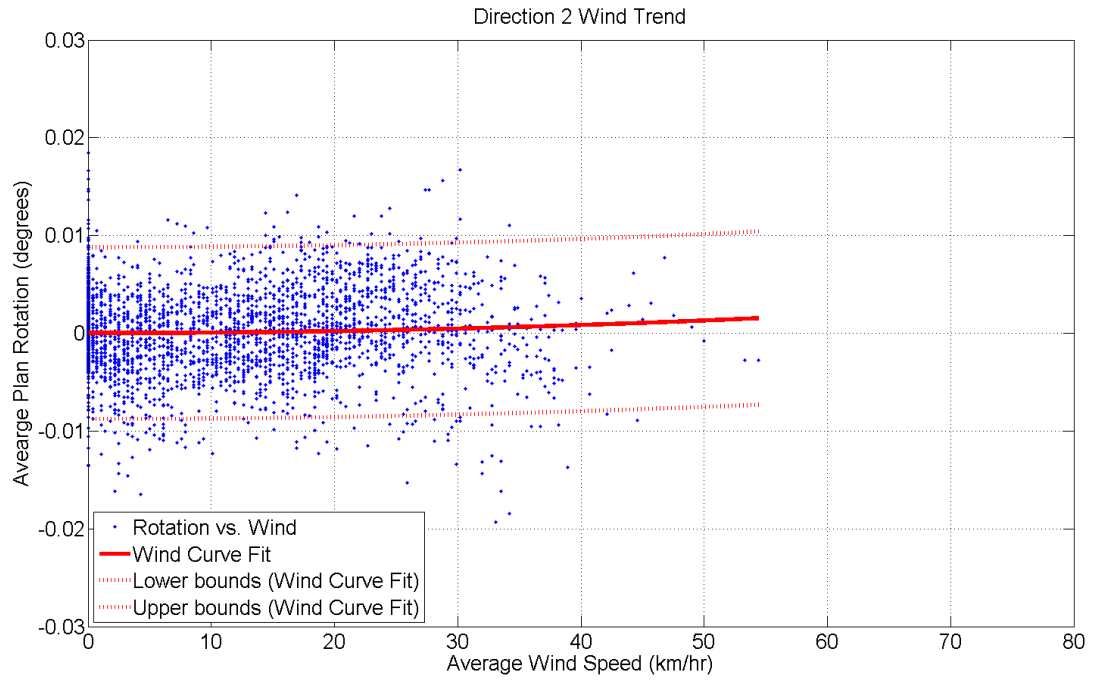
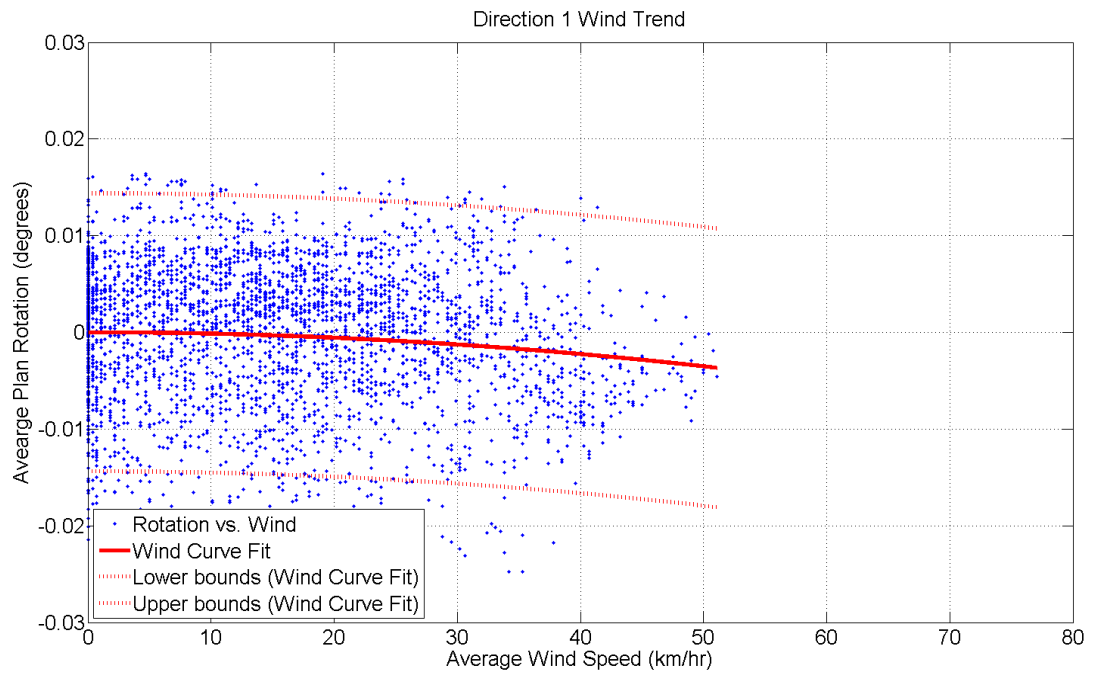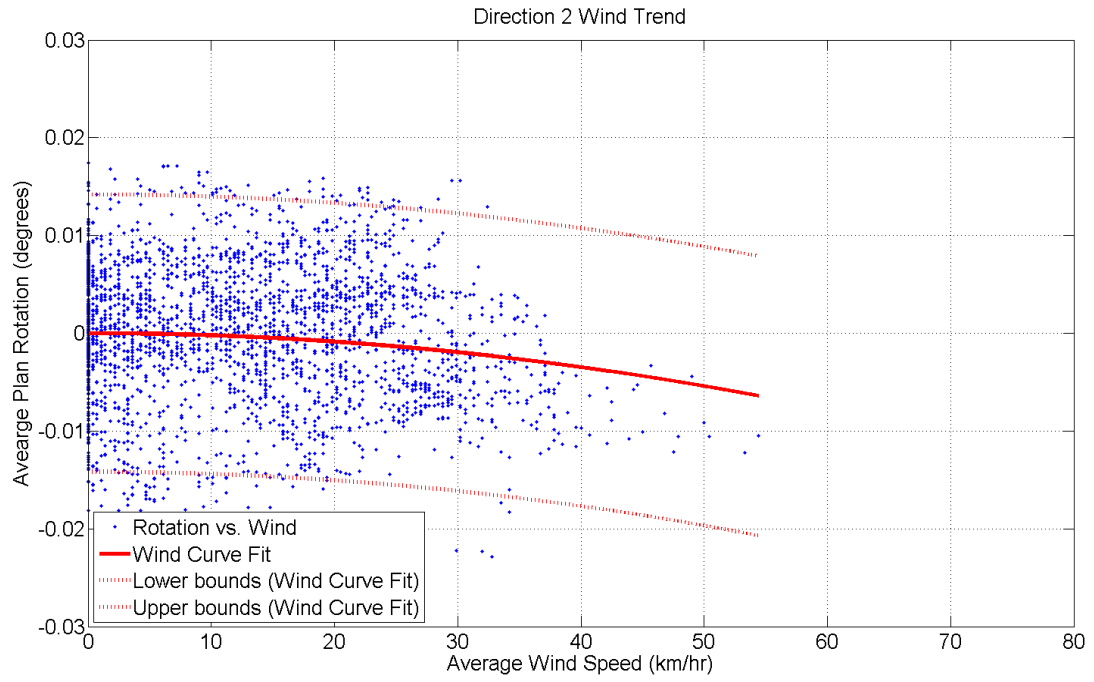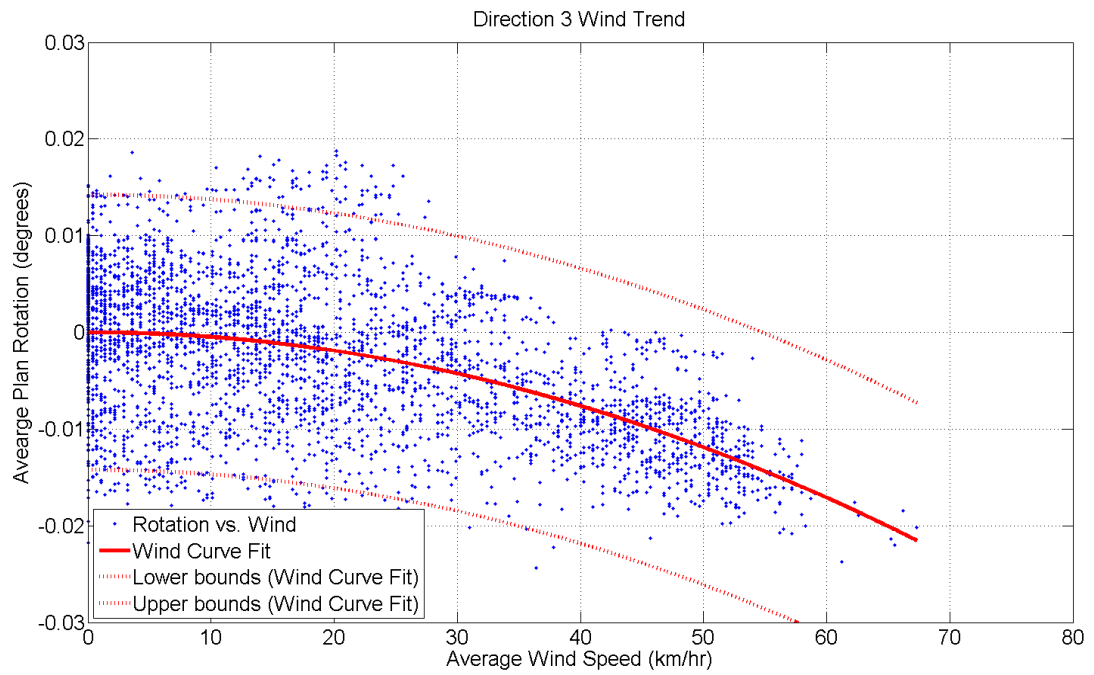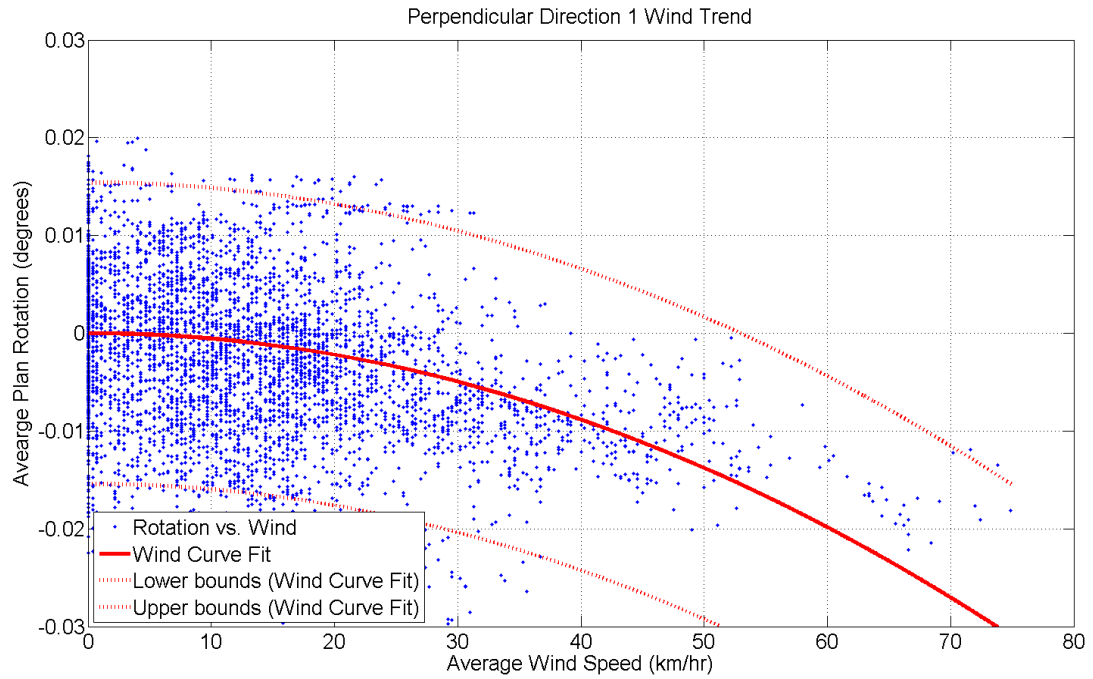**Figure D.35:** Plan rotation wind trend – Direction 2 – DMT SS
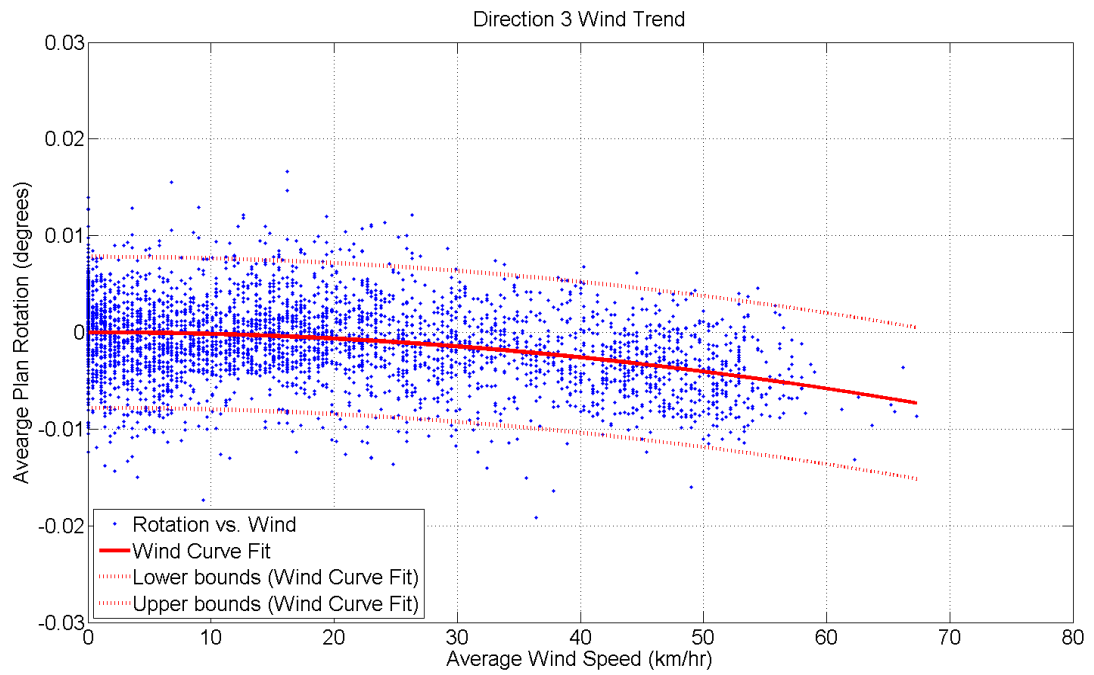
Figure D.36: Plan rotation wind trend – Direction 3 – DMT SS

Figure D.37: Plan rotation wind trend – Perpendicular Direction 1 – DMT SS

Figure D.38: Plan rotation wind trend – Direction 4 – DMT SS

159

Figure D.39: Plan rotation wind trend – Direction 5 – DMT SS

Figure D.40: Plan rotation wind trend – Direction 6 – DMT SS

160

Figure D.41: Plan rotation wind trend – Parallel Direction 2 – DMT SS

Figure D.42: Plan rotation wind trend – Direction 7 – DMT SS
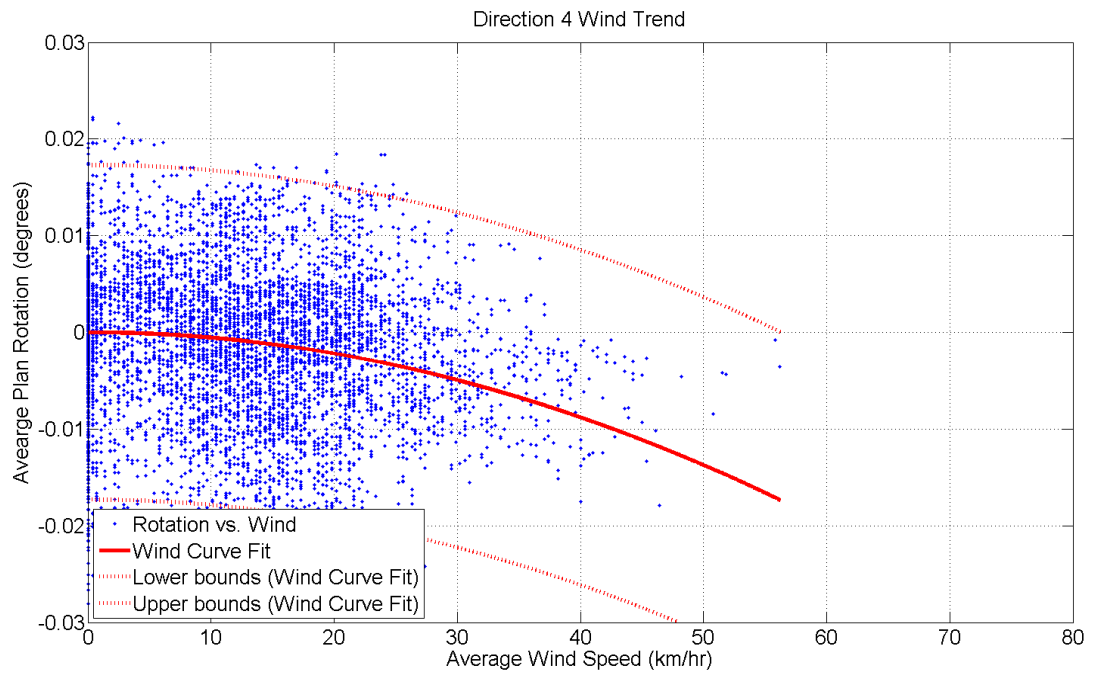
161

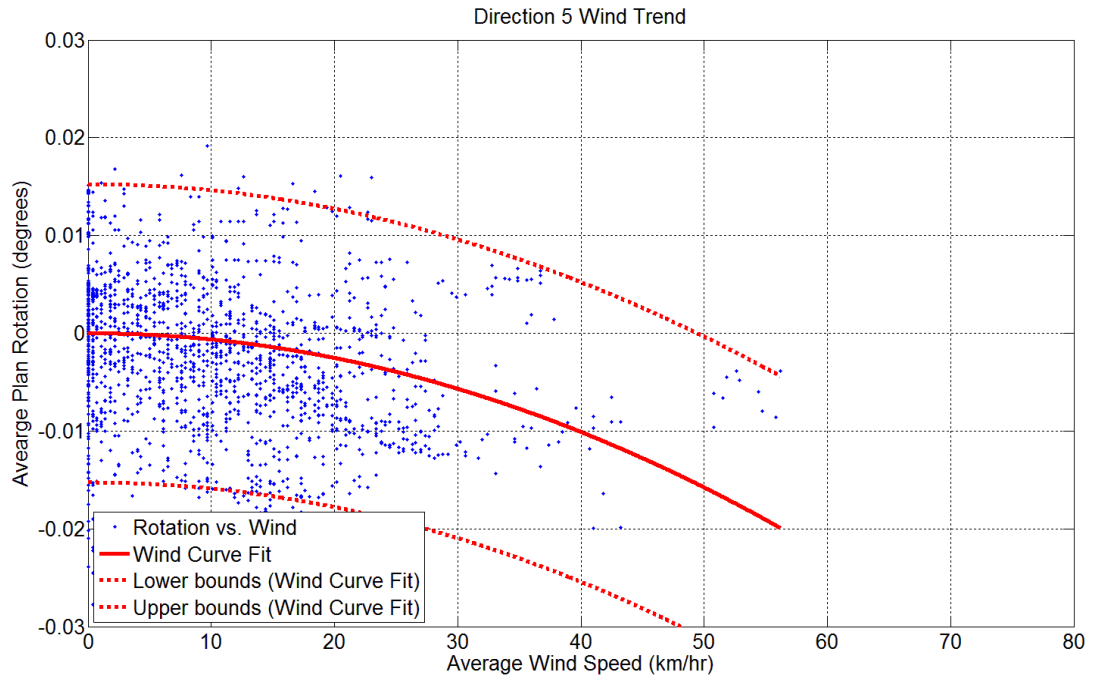**Figure D.43:** Plan rotation wind trend – Direction 8 – DMT SS

Figure D.44: Plan rotation wind trend – Direction 9 – DMT SS

Figure D.45: Plan rotation wind trend – Perpendicular Direction 2 – DMT SS

Figure D.46: Plan rotation wind trend – Direction 10 – DMT SS

Figure D.47: Plan rotation wind trend – Direction 11 – DMT SS

Figure D.48: Plan rotation wind trend – Direction 12 – DMT SS

164

Figure D.49: Plan rotation wind trend – Parallel Direction 1 – HMT SS

Figure D.50: Plan rotation wind trend – Direction 1 – HMT SS

Figure D.51: Plan rotation wind trend – Direction 2 – HMT SS

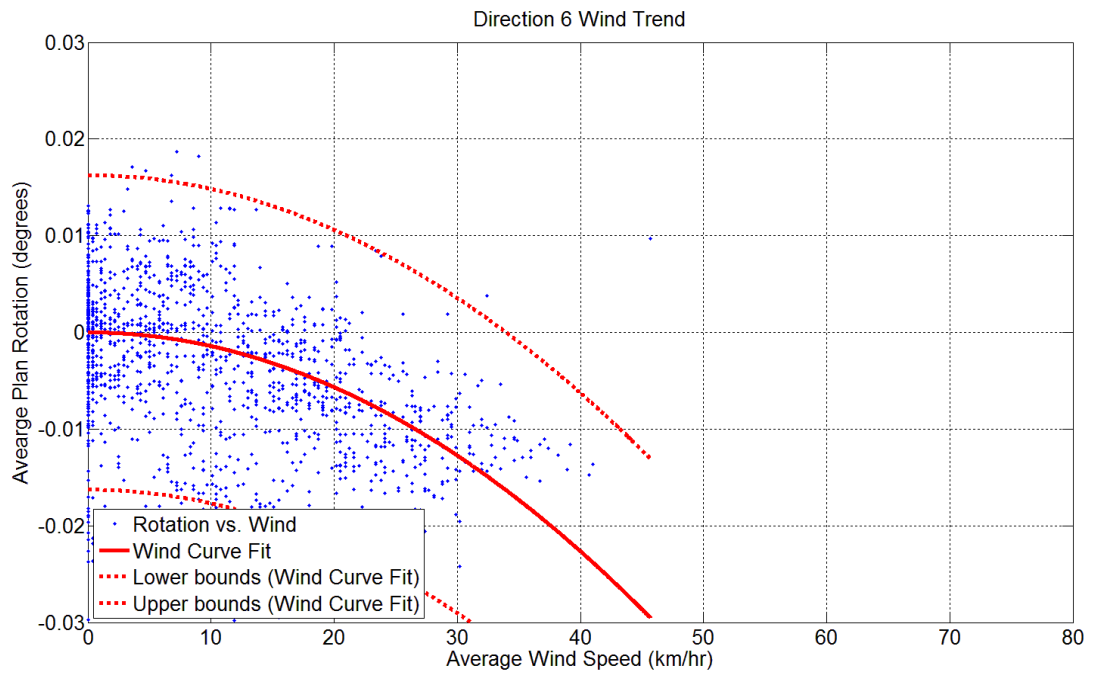**Figure D.52:** Plan rotation wind trend – Direction 3 – HMT SS

166

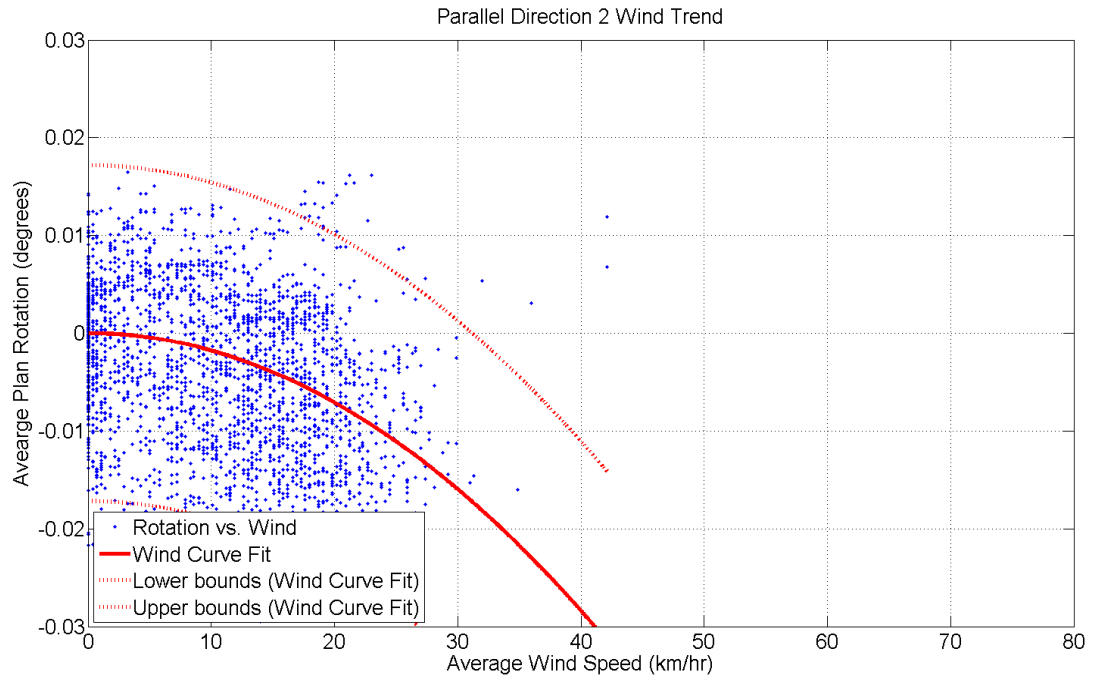**Figure D.53:** Plan rotation wind trend – Perpendicular Direction 1 – HMT SS

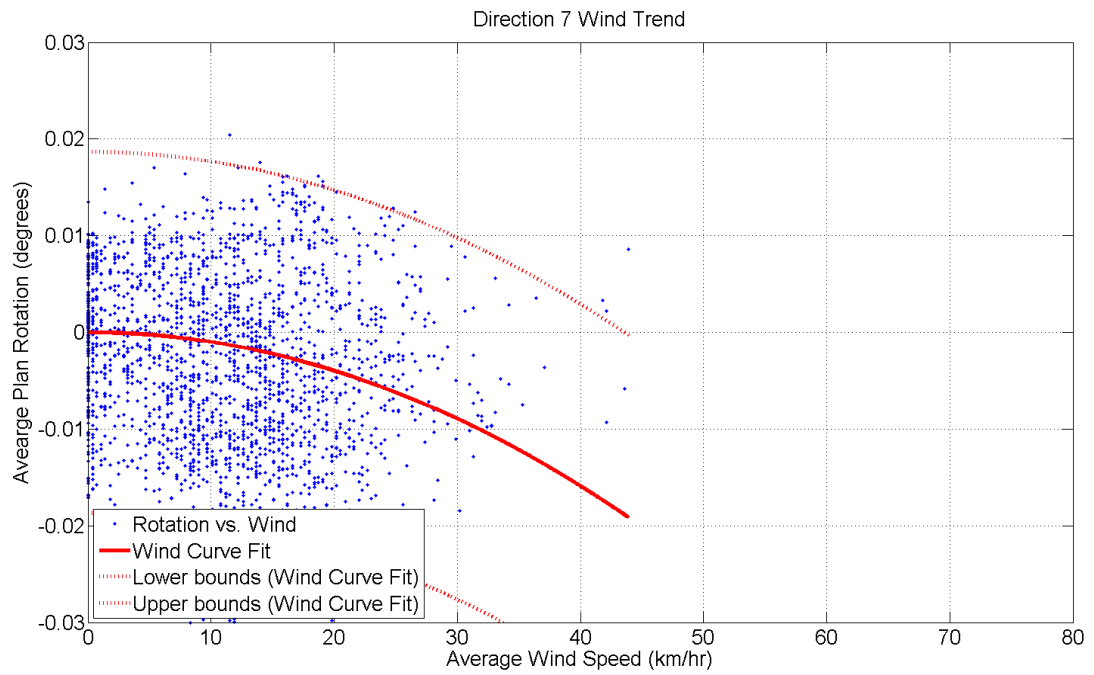**Figure D.54:** Plan rotation wind trend – Direction 4 – HMT SS

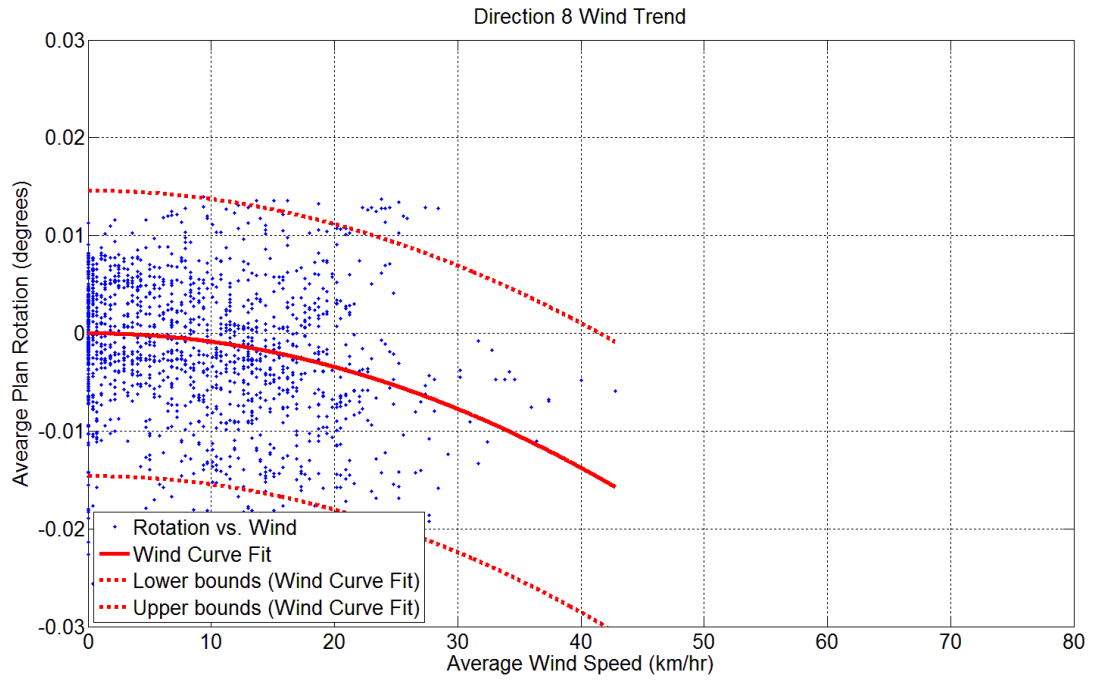**Figure D.55:** Plan rotation wind trend – Direction 5 – HMT SS

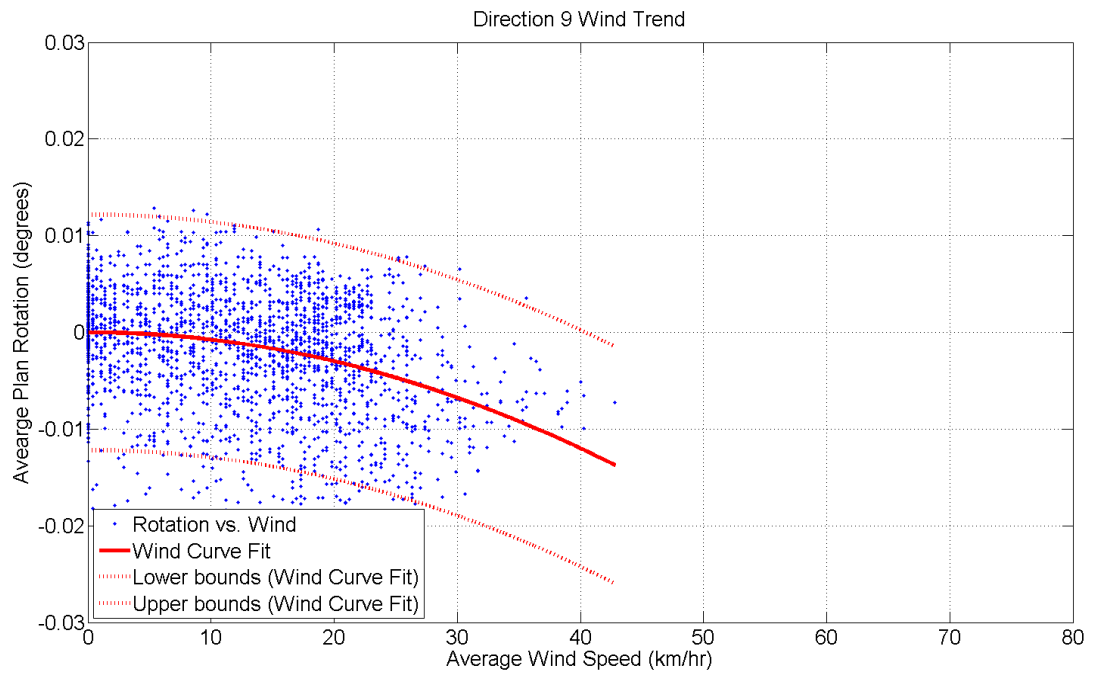**Figure D.56:** Plan rotation wind trend – Direction 6 – HMT SS

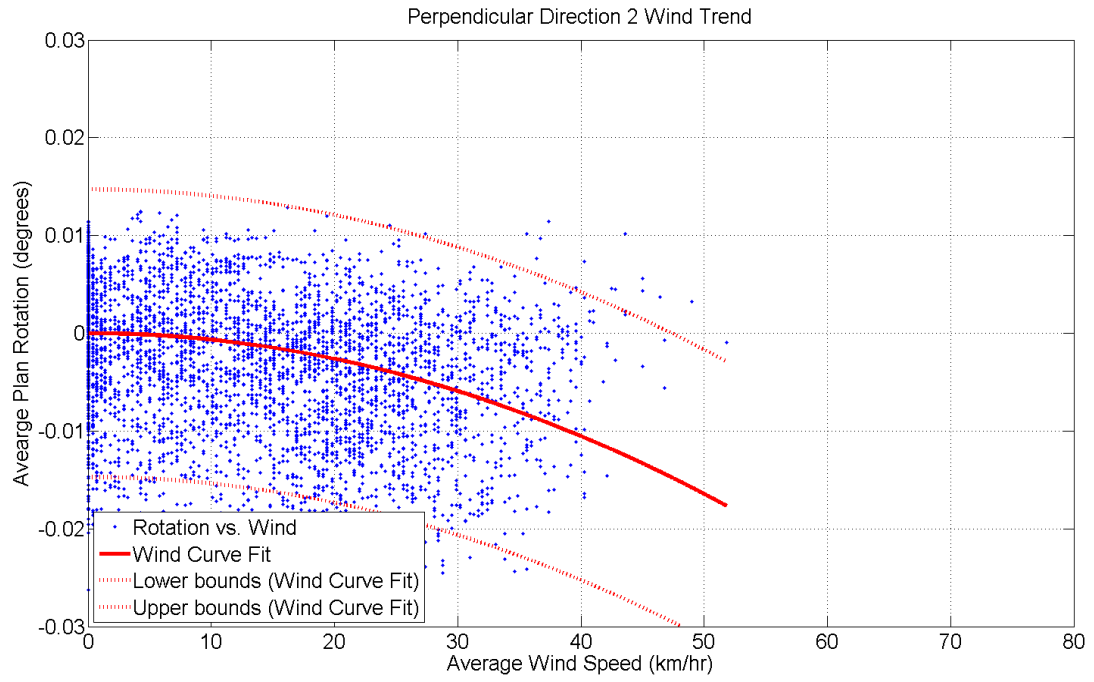**Figure D.57:** Plan rotation wind trend – Parallel Direction 2 – HMT SS

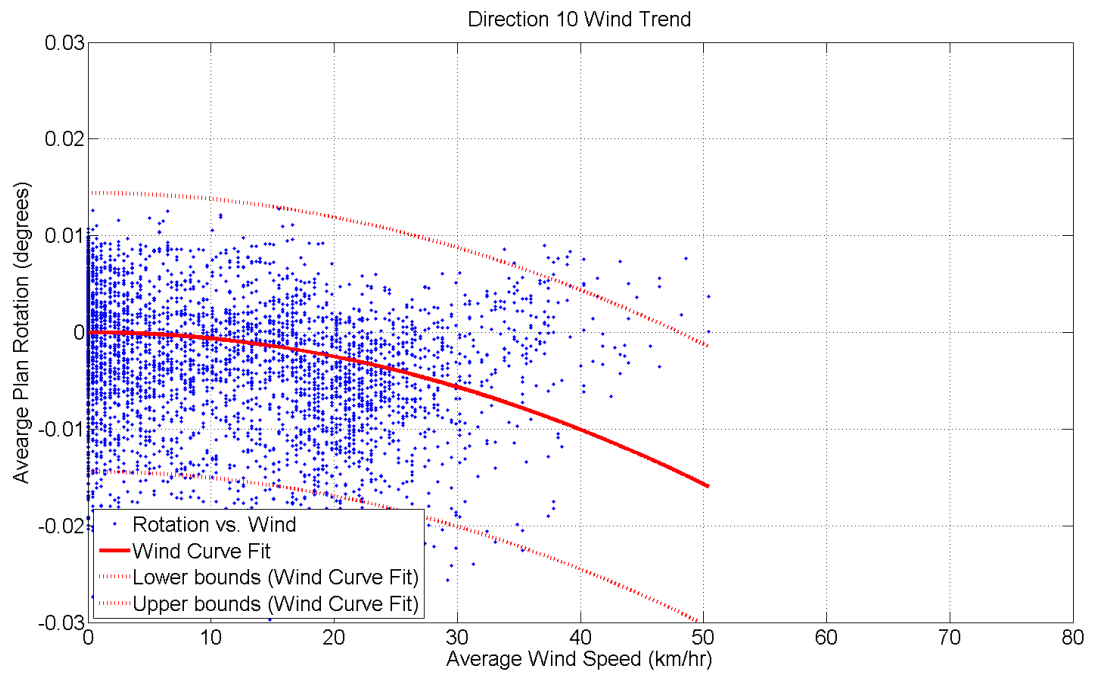**Figure D.58:** Plan rotation wind trend – Direction 7 – HMT SS

169

Figure D.59: Plan rotation wind trend – Direction 8 – HMT SS
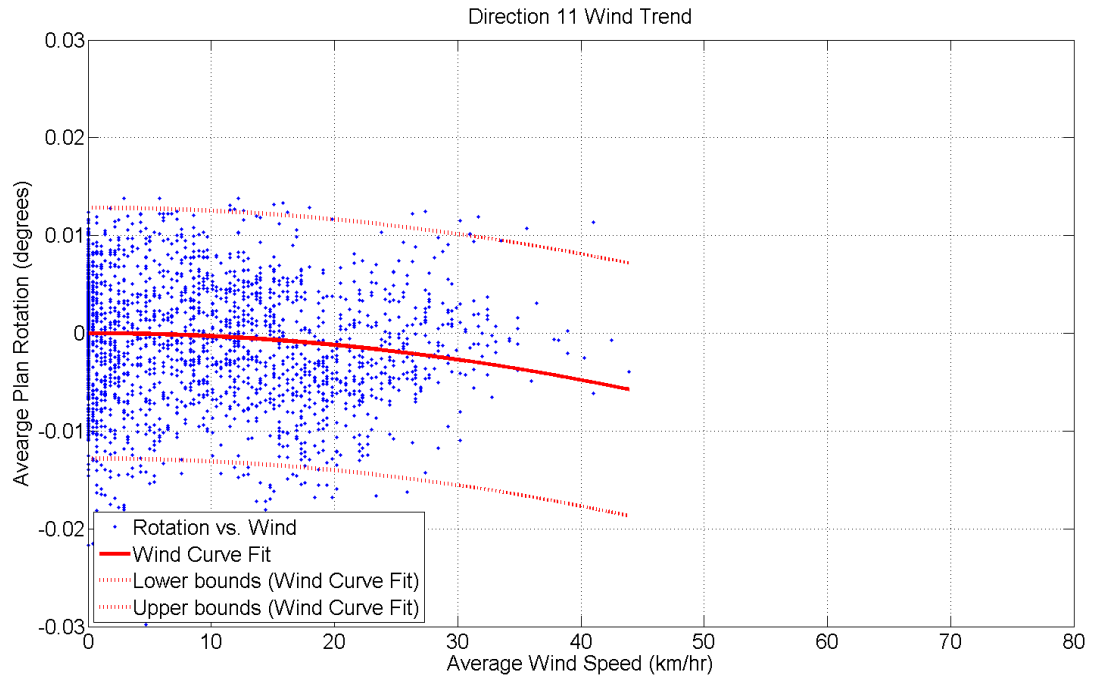

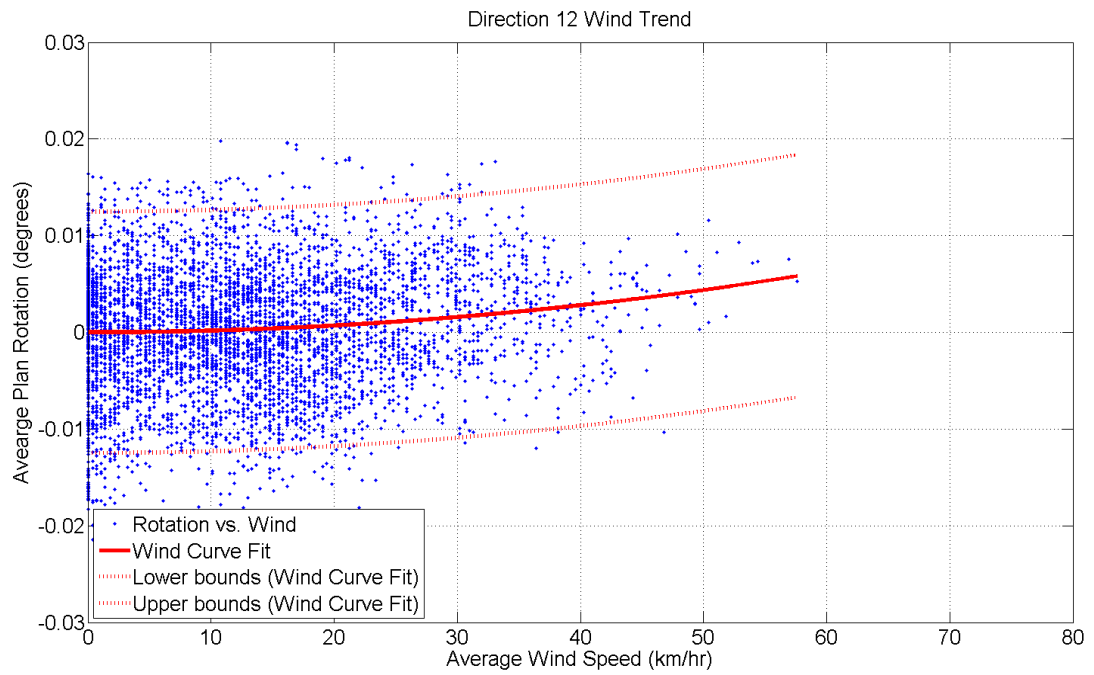**Figure D.60:** Plan rotation wind trend – Direction 9 – HMT SS

Figure D.61: Plan rotation wind trend – Perpendicular Direction 2 – HMT SS

Figure D.62: Plan rotation wind trend – Direction 10 – HMT SS

171

Figure D.63: Plan rotation wind trend – Direction 11 – HMT SS

Figure D.64: Plan rotation wind trend – Direction 12 – HMT SS

Appendix E – Live Load Hourly Averages

Table E.1: Vertical Rotation Hourly Averages - Workday, DMT MS

TIME OF DAY	AVEARGE (Degrees)	STANDARD DEVIATION (Degrees)
12 AM	-0.015	0.021
1 AM	-0.013	0.015
2 AM	-0.025	0.012
3AM	-0.031	0.009
4AM	-0.021	0.015
5AM	-0.015	0.025
6 AM	-0.005	0.043
7 AM	0.035	0.061
8 AM	0.041	0.062
9 AM	0.025	0.061
10 AM	0.011	0.057
11 AM	0.019	0.045
12 PM	0.022	0.043
1 PM	0.015	0.048
2 PM	0.012	0.051
3 PM	0.022	0.055
4 PM	0.041	0.052
5 PM	0.051	0.065
6 PM	0.045	0.061
7 PM	0.035	0.063
8 PM	0.015	0.059
9 PM	0.006	0.042
10 PM	0.010	0.021
11 PM	-0.021	0.032

Table E.2: Vertical Rotation Hourly Averages - Non-Workday, DMT MS

TIME OF DAY	AVEARGE (Degrees)	STANDARD DEVIATION (Degrees)
12 AM	-0.015	0.008
1 AM	-0.013	0.008
2 AM	-0.025	0.007
3AM	-0.031	0.008
4AM	-0.021	0.005
5AM	-0.015	0.009
6 AM	-0.005	0.011
7 AM	0.015	0.012
8 AM	0.011	0.010
9 AM	-0.005	0.010
10 AM	-0.001	0.015
11 AM	-0.016	0.015
12 PM	-0.012	0.016
1 PM	-0.007	0.017
2 PM	0.009	0.018
3 PM	0.012	0.021
4 PM	0.015	0.016
5 PM	0.011	0.014
6 PM	0.013	0.015
7 PM	0.015	0.016
8 PM	0.015	0.014
9 PM	0.006	0.019
10 PM	0.010	0.011
11 PM	0.011	0.005

Table E.3: Vertical Rotation Hourly Averages - Workday, HMT MS

TIME OF DAY	AVEARGE (Degrees)	STANDARD DEVIATION (Degrees)
12 AM	-0.014	0.019
1 AM	-0.013	0.017
2 AM	-0.021	0.013
3AM	-0.034	0.010
4AM	-0.019	0.012
5AM	-0.013	0.021
6 AM	-0.011	0.042
7 AM	0.037	0.059
8 AM	0.029	0.056
9 AM	0.021	0.065
10 AM	0.019	0.061
11 AM	0.019	0.043
12 PM	0.022	0.042
1 PM	0.013	0.047
2 PM	0.009	0.049
3 PM	0.027	0.047
4 PM	0.045	0.055
5 PM	0.050	0.061
6 PM	0.041	0.072
7 PM	0.041	0.059
8 PM	0.021	0.052
9 PM	0.009	0.038
10 PM	0.012	0.027
11 PM	-0.019	0.029

Table E.4: Vertical Rotation Hourly Averages - Non-Workday, HMT MS

TIME OF DAY	AVEARGE (Degrees)	STANDARD DEVIATION (Degrees)
12 AM	-0.015	0.007
1 AM	-0.013	0.006
2 AM	-0.025	0.007
3AM	-0.035	0.010
4AM	-0.022	0.006
5AM	-0.014	0.010
6 AM	-0.009	0.009
7 AM	0.018	0.014
8 AM	0.017	0.011
9 AM	-0.004	0.009
10 AM	-0.005	0.017
11 AM	-0.011	0.021
12 PM	-0.013	0.022
1 PM	-0.007	0.021
2 PM	0.009	0.022
3 PM	0.015	0.025
4 PM	0.016	0.019
5 PM	0.012	0.017
6 PM	0.018	0.017
7 PM	0.012	0.018
8 PM	0.015	0.015
9 PM	0.011	0.017
10 PM	0.010	0.013
11 PM	0.015	0.011

Table E.5: Vertical Rotation Hourly Averages - Workday, DMT SS

TIME OF DAY	AVEARGE (Degrees)	STANDARD DEVIATION (Degrees)
12 AM	-0.009	0.004
1 AM	-0.007	0.003
2 AM	-0.013	0.002
3AM	-0.021	0.003
4AM	-0.019	0.005
5AM	-0.013	0.006
6 AM	-0.010	0.007
7 AM	0.021	0.008
8 AM	0.025	0.010
9 AM	0.027	0.011
10 AM	0.021	0.012
11 AM	0.016	0.013
12 PM	0.018	0.014
1 PM	0.013	0.009
2 PM	0.015	0.011
3 PM	0.016	0.016
4 PM	0.029	0.015
5 PM	0.027	0.018
6 PM	0.031	0.019
7 PM	0.021	0.016
8 PM	0.009	0.010
9 PM	0.005	0.009
10 PM	0.011	0.004
11 PM	-0.015	0.005

Table E.6: Vertical Rotation Hourly Averages - Non-Workday, DMT SS

TIME OF DAY	AVEARGE (Degrees)	STANDARD DEVIATION (Degrees)
12 AM	-0.012	0.005
1 AM	-0.017	0.005
2 AM	-0.021	0.004
3AM	-0.019	0.005
4AM	-0.018	0.004
5AM	-0.014	0.002
6 AM	0.001	0.003
7 AM	0.017	0.006
8 AM	0.012	0.005
9 AM	-0.005	0.004
10 AM	0.005	0.007
11 AM	0.007	0.007
12 PM	-0.011	0.010
1 PM	-0.009	0.009
2 PM	0.007	0.008
3 PM	0.013	0.006
4 PM	0.014	0.007
5 PM	0.009	0.011
6 PM	0.010	0.009
7 PM	0.010	0.008
8 PM	0.011	0.005
9 PM	0.009	0.006
10 PM	0.012	0.005
11 PM	0.008	0.004

Table E.7: Vertical Rotation Hourly Averages - Workday, HMT SS

TIME OF DAY	AVEARGE (Degrees)	STANDARD DEVIATION (Degrees)
12 AM	-0.010	0.005
1 AM	-0.009	0.004
2 AM	-0.011	0.002
3AM	-0.023	0.003
4AM	-0.017	0.006
5AM	-0.011	0.007
6 AM	-0.008	0.009
7 AM	0.022	0.010
8 AM	0.027	0.010
9 AM	0.023	0.010
10 AM	0.017	0.011
11 AM	0.015	0.012
12 PM	0.016	0.015
1 PM	0.014	0.019
2 PM	0.013	0.020
3 PM	0.027	0.025
4 PM	0.025	0.027
5 PM	0.032	0.032
6 PM	0.028	0.031
7 PM	0.022	0.012
8 PM	0.010	0.007
9 PM	0.007	0.005
10 PM	0.013	0.008
11 PM	-0.017	0.007

Table E.8: Vertical Rotation Hourly Averages - Non-Workday, HMT SS

TIME OF DAY	AVEARGE (Degrees)	STANDARD DEVIATION (Degrees)
12 AM	-0.012	0.006
1 AM	-0.017	0.007
2 AM	-0.015	0.004
3AM	-0.017	0.005
4AM	-0.013	0.009
5AM	-0.009	0.005
6 AM	0.001	0.006
7 AM	0.004	0.002
8 AM	0.007	0.003
9 AM	0.001	0.004
10 AM	-0.004	0.005
11 AM	-0.014	0.011
12 PM	-0.010	0.012
1 PM	-0.009	0.009
2 PM	0.014	0.010
3 PM	0.012	0.013
4 PM	0.011	0.005
5 PM	0.010	0.009
6 PM	0.014	0.005
7 PM	0.011	0.010
8 PM	0.013	0.008
9 PM	0.007	0.003
10 PM	0.010	0.004
11 PM	0.006	0.004

Table E.9: Plan Rotation Hourly Averages, DMT MS

TIME OF DAY	AVEARGE (Degrees)	STANDARD DEVIATION (Degrees)
12 AM	-0.0007	0.006
1 AM	-0.0006	0.006
2 AM	-0.0004	0.006
3AM	-0.0007	0.006
4AM	-0.0007	0.006
5AM	-0.0014	0.006
6 AM	-0.0015	0.006
7 AM	-0.0018	0.008
8 AM	0.0015	0.009
9 AM	-0.0013	0.007
10 AM	-0.0005	0.007
11 AM	-0.0004	0.007
12 PM	0.0016	0.007
1 PM	0.0034	0.008
2 PM	0.0039	0.009
3 PM	0.0032	0.009
4 PM	0.0022	0.012
5 PM	0.0012	0.011
6 PM	0.0017	0.018
7 PM	0.0031	0.014
8 PM	0.0026	0.012
9 PM	0.0004	0.009
10 PM	0.0007	0.007
11 PM	0.0002	0.007

Table E.10: Plan Rotation Hourly Averages, HMT MS

TIME OF DAY	AVEARGE (Degrees)	STANDARD DEVIATION (Degrees)
12 AM	-0.0012	0.007
1 AM	-0.0008	0.006
2 AM	-0.0005	0.005
3AM	-0.0009	0.007
4AM	-0.0010	0.007
5AM	-0.0013	0.006
6 AM	-0.0015	0.006
7 AM	-0.0019	0.009
8 AM	0.0015	0.010
9 AM	-0.0019	0.007
10 AM	-0.0010	0.008
11 AM	-0.0006	0.008
12 PM	0.0012	0.009
1 PM	0.0031	0.007
2 PM	0.0035	0.007
3 PM	0.0029	0.007
4 PM	0.0027	0.008
5 PM	0.0015	0.009
6 PM	0.0014	0.010
7 PM	0.0025	0.009
8 PM	0.0021	0.010
9 PM	0.0004	0.009
10 PM	0.0008	0.008
11 PM	0.0005	0.008

Table E.11: Plan Rotation Hourly Averages, DMT SS

TIME OF DAY	AVEARGE (Degrees)	STANDARD DEVIATION (Degrees)
12 AM	-0.0005	0.004
1 AM	-0.0003	0.003
2 AM	-0.0002	0.002
3AM	-0.0011	0.005
4AM	-0.0012	0.006
5AM	-0.0013	0.007
6 AM	-0.0015	0.009
7 AM	-0.0018	0.010
8 AM	-0.0015	0.005
9 AM	-0.0011	0.004
10 AM	-0.0002	0.003
11 AM	-0.0004	0.003
12 PM	0.0014	0.004
1 PM	0.0021	0.005
2 PM	0.0022	0.006
3 PM	0.0023	0.008
4 PM	0.0022	0.008
5 PM	0.0012	0.008
6 PM	0.0014	0.009
7 PM	0.0029	0.007
8 PM	0.0028	0.005
9 PM	0.0018	0.005
10 PM	0.0014	0.004
11 PM	0.0001	0.005

Table E.12: Plan Rotation Hourly Averages, HMT SS

TIME OF DAY	AVEARGE (Degrees)	STANDARD DEVIATION (Degrees)
12 AM	-0.0006	0.005
1 AM	-0.0005	0.005
2 AM	-0.0008	0.005
3AM	-0.0015	0.004
4AM	-0.0014	0.005
5AM	-0.0014	0.004
6 AM	-0.0014	0.005
7 AM	-0.0019	0.005
8 AM	-0.0014	0.004
9 AM	-0.0008	0.006
10 AM	0.0001	0.005
11 AM	0.0005	0.005
12 PM	0.0012	0.004
1 PM	0.0028	0.006
2 PM	0.0029	0.005
3 PM	0.0026	0.004
4 PM	0.0025	0.002
5 PM	0.0016	0.005
6 PM	0.0019	0.005
7 PM	0.0031	0.005
8 PM	0.0025	0.005
9 PM	0.0016	0.005
10 PM	0.0011	0.005
11 PM	0.0010	0.006

Appendix F – Sensor Comparison Plots
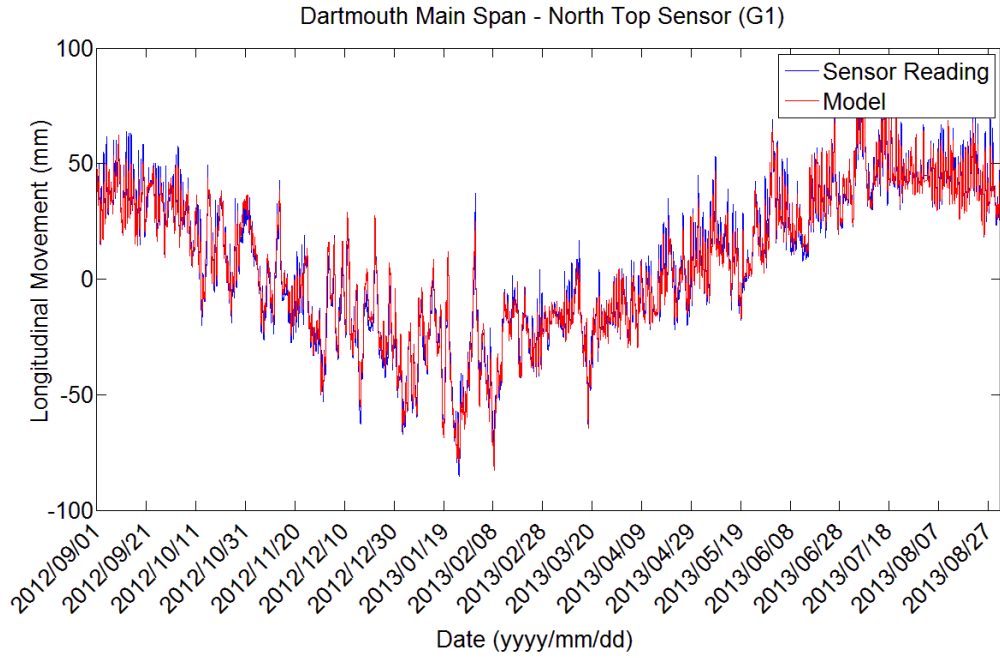
Figure F.1: Model comparison to monitored data, DMT MS Northtop sensor
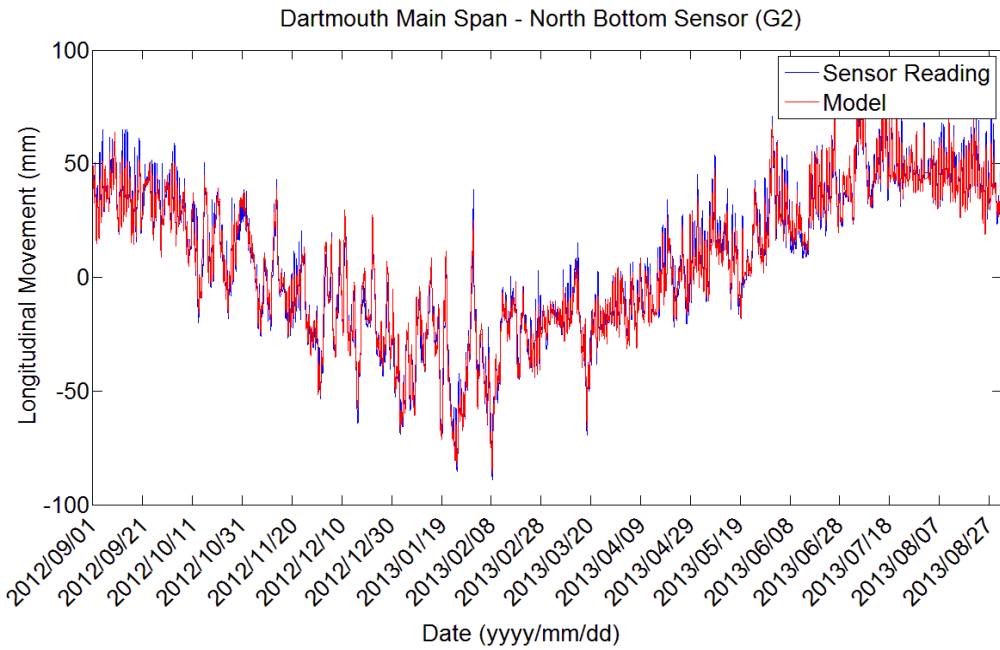
Figure F.2: Model comparison to monitored data, DMT MS Northbot sensor
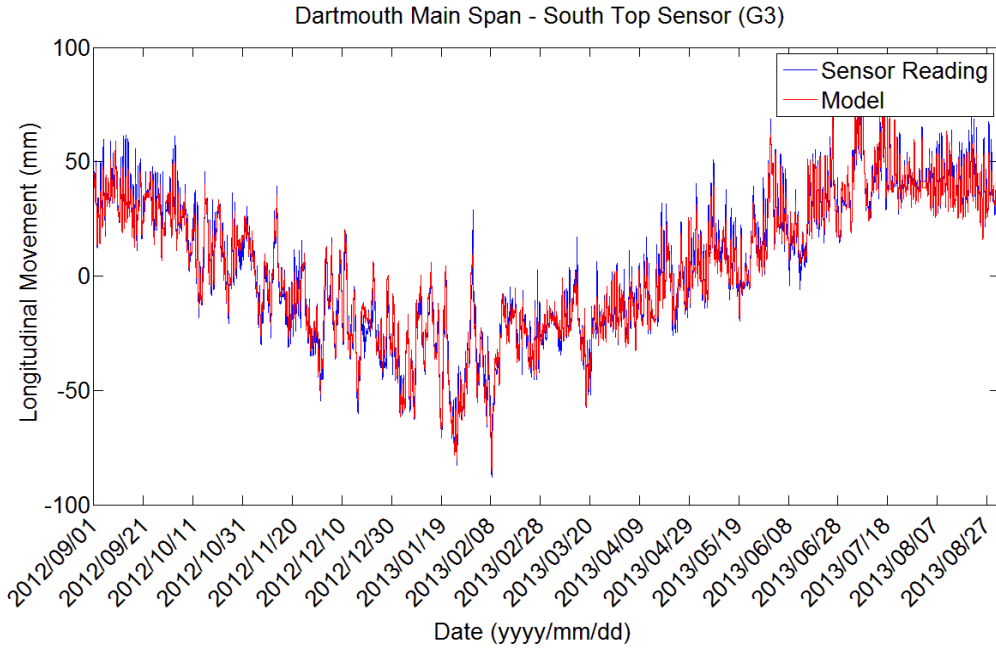
Figure F.3: Model comparison to monitored data, DMT MS Southtop sensor
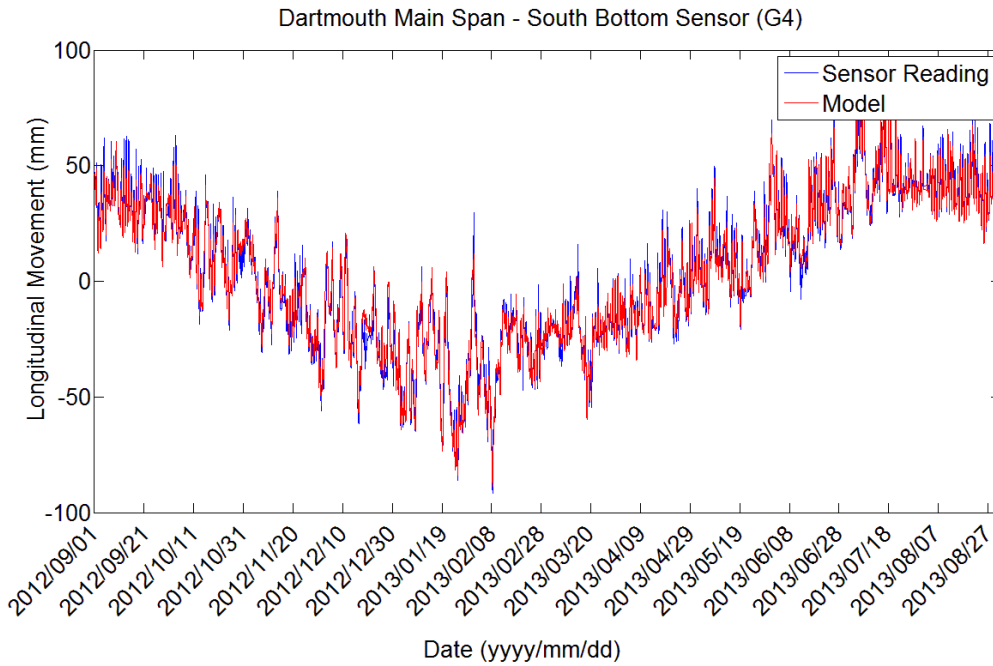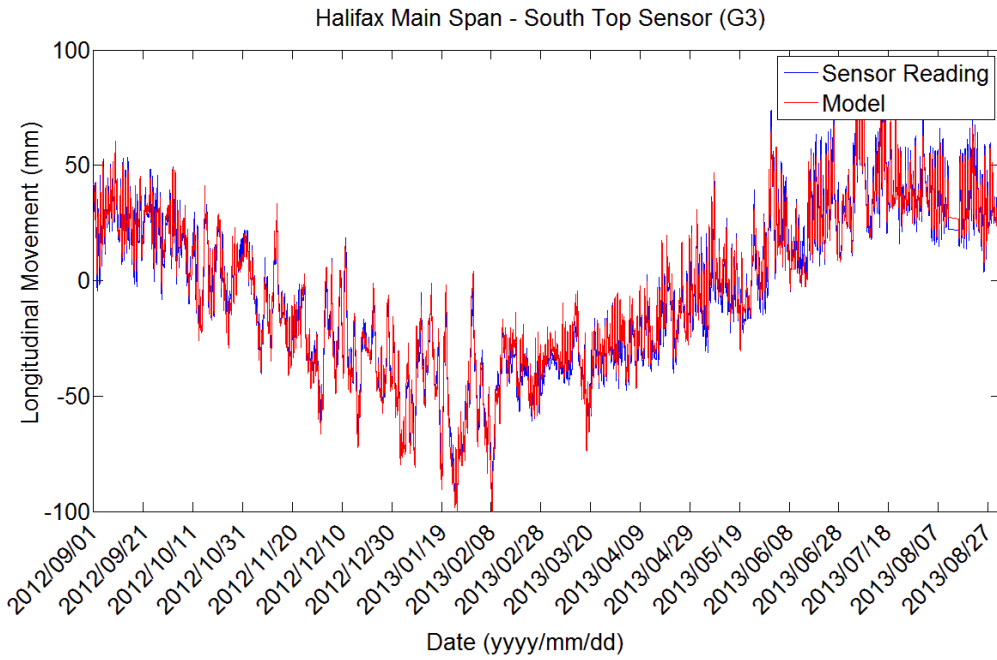

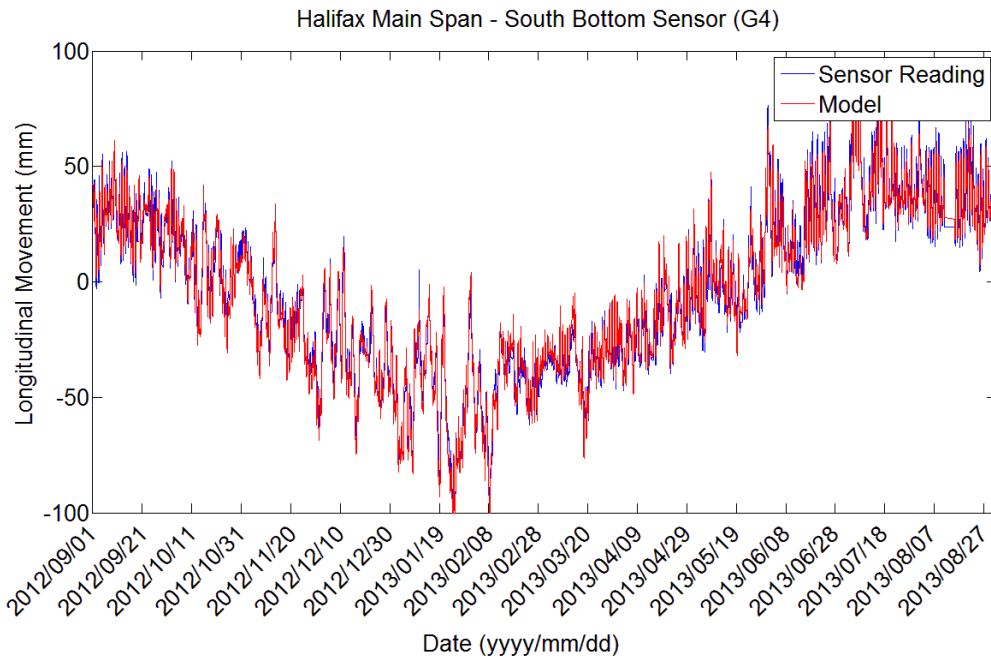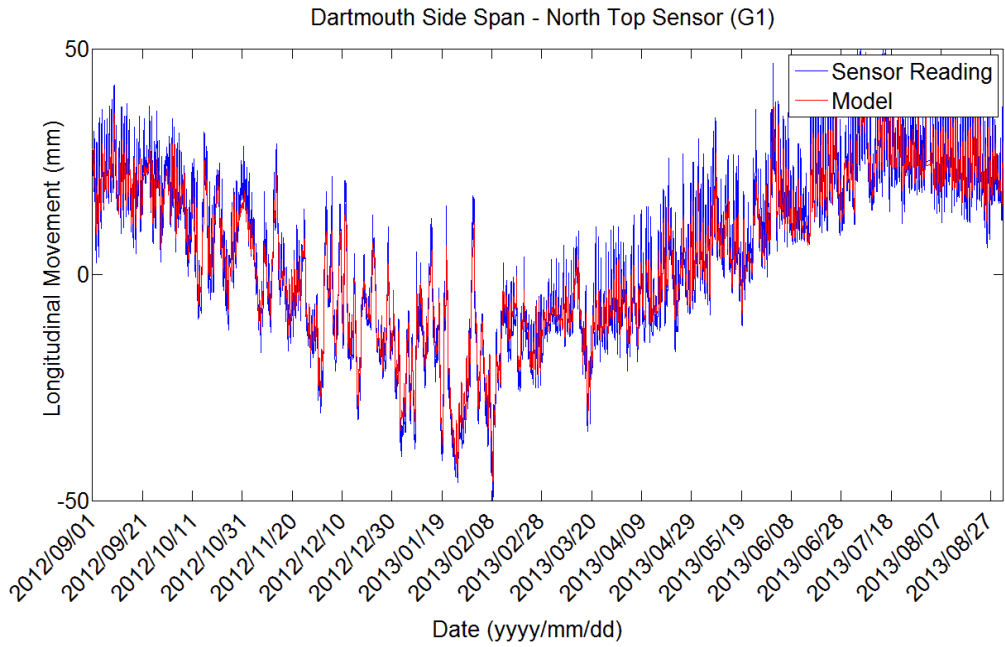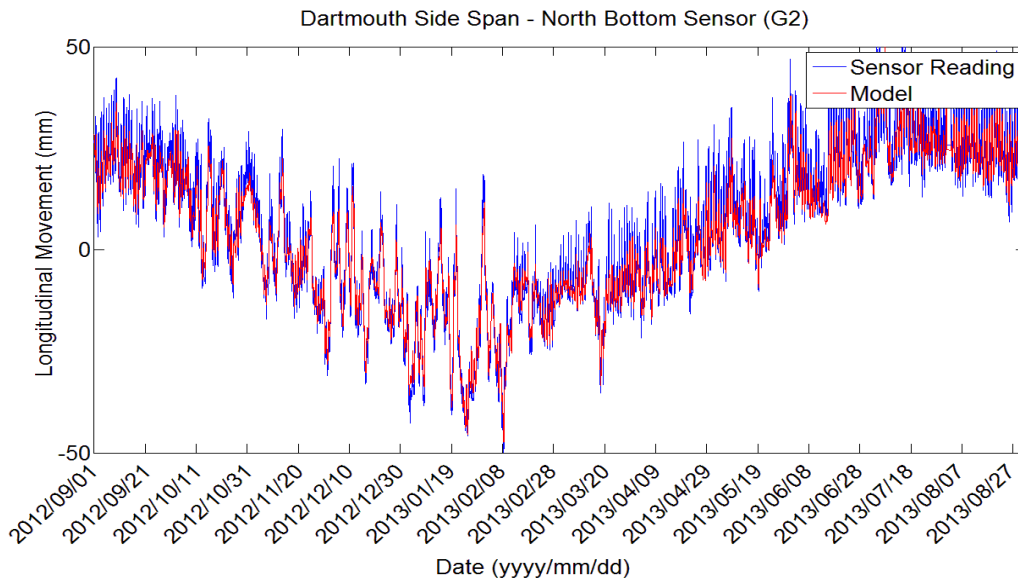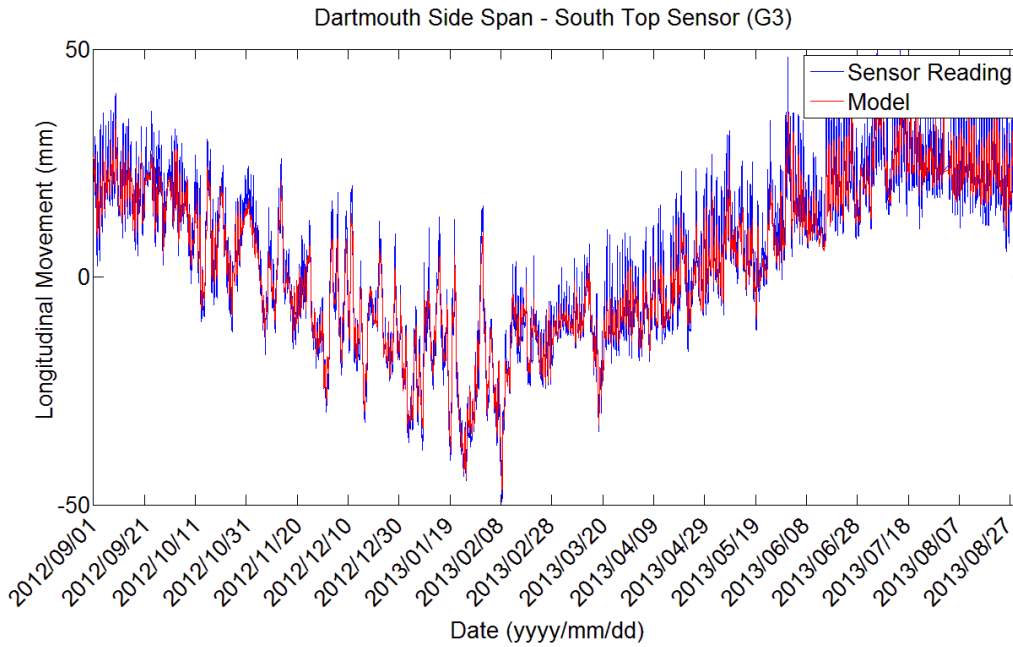**Figure F.4**: Model comparison to monitored data, DMT MS Southbot sensor
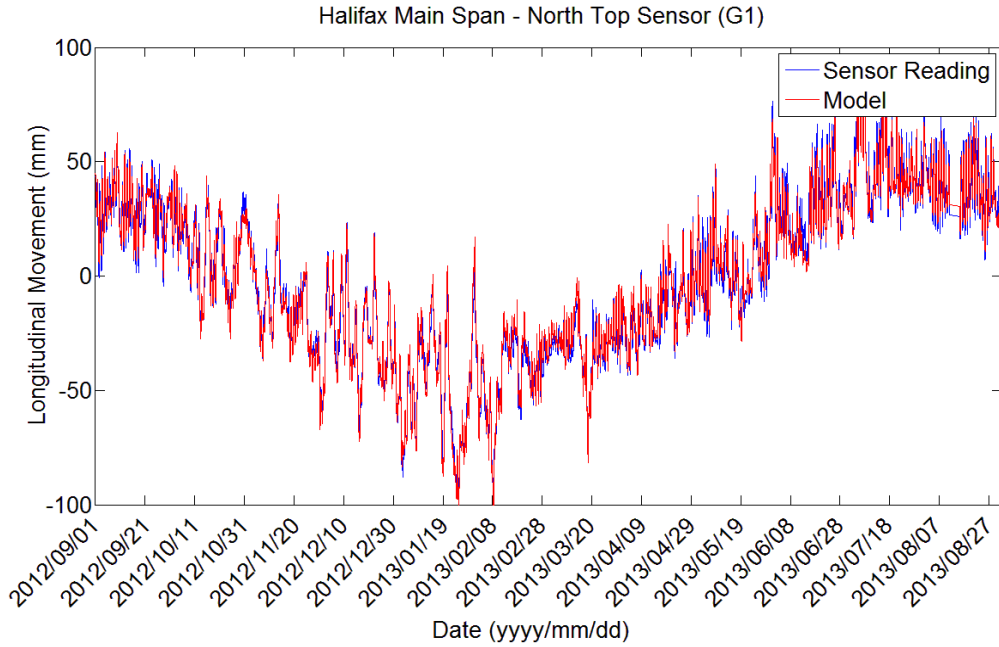
Figure F.5: Model comparison to monitored data, HMT MS Northtop sensor
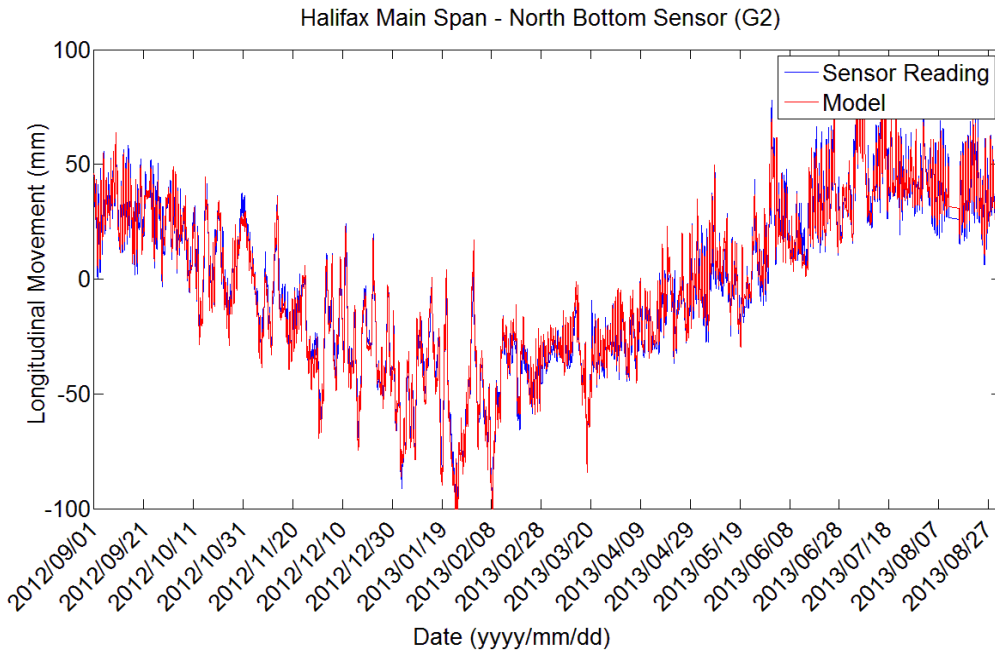
Figure F.6: Model comparison to monitored data, HMT MS Northbot sensor

187

Figure F.7: Model comparison to monitored data, HMT MS Southtop sensor

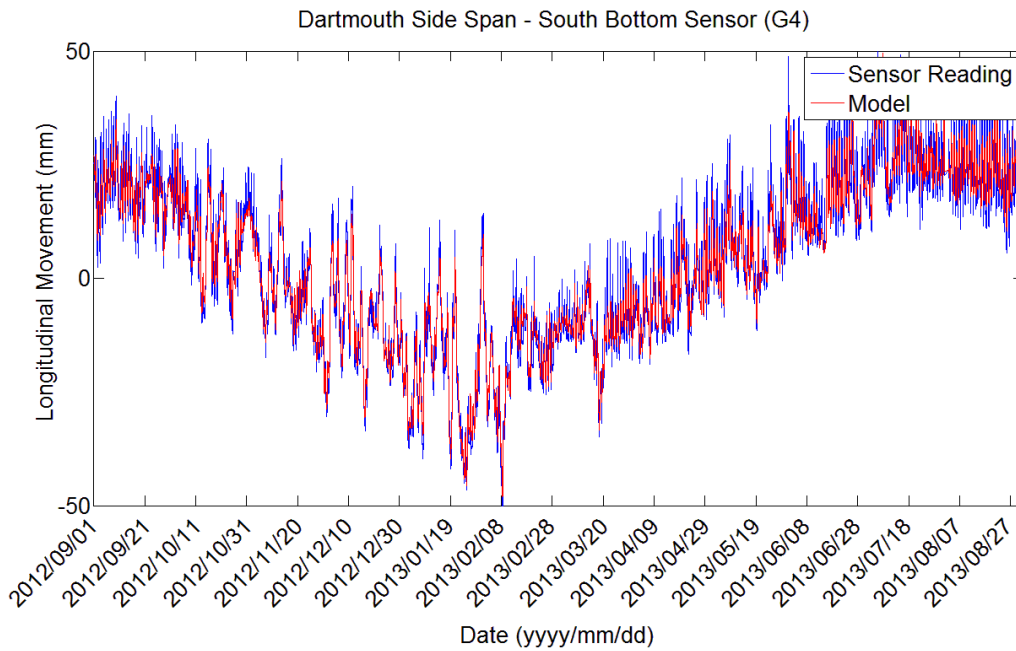**Figure F.8**: Model comparison to monitored data, HMT MS Southbot sensor

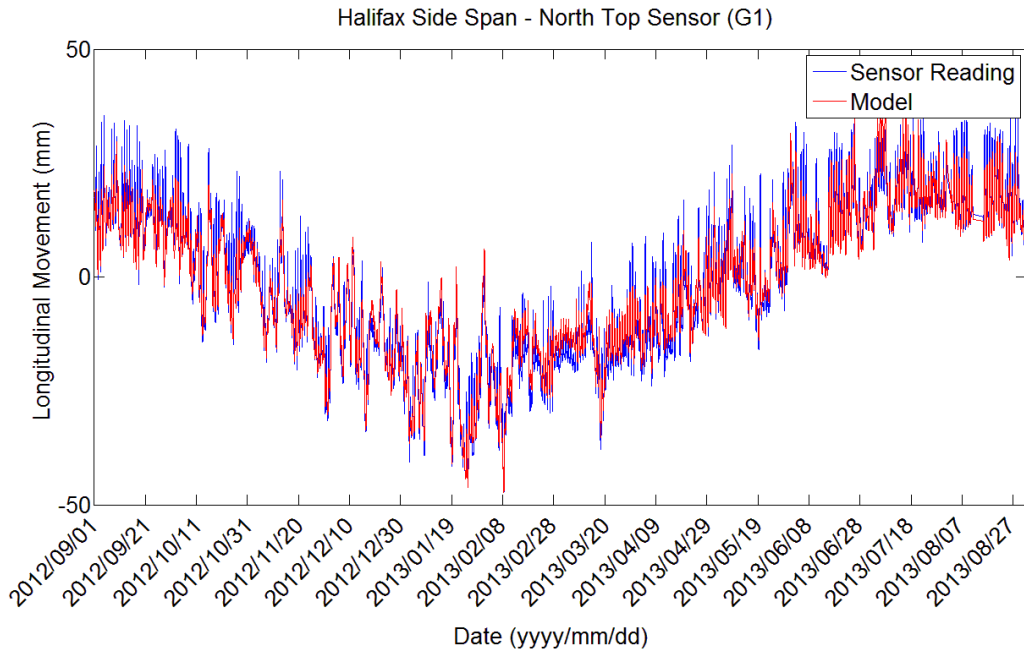**Figure F.9**: Model comparison to monitored data, DMT SS Northtop sensor

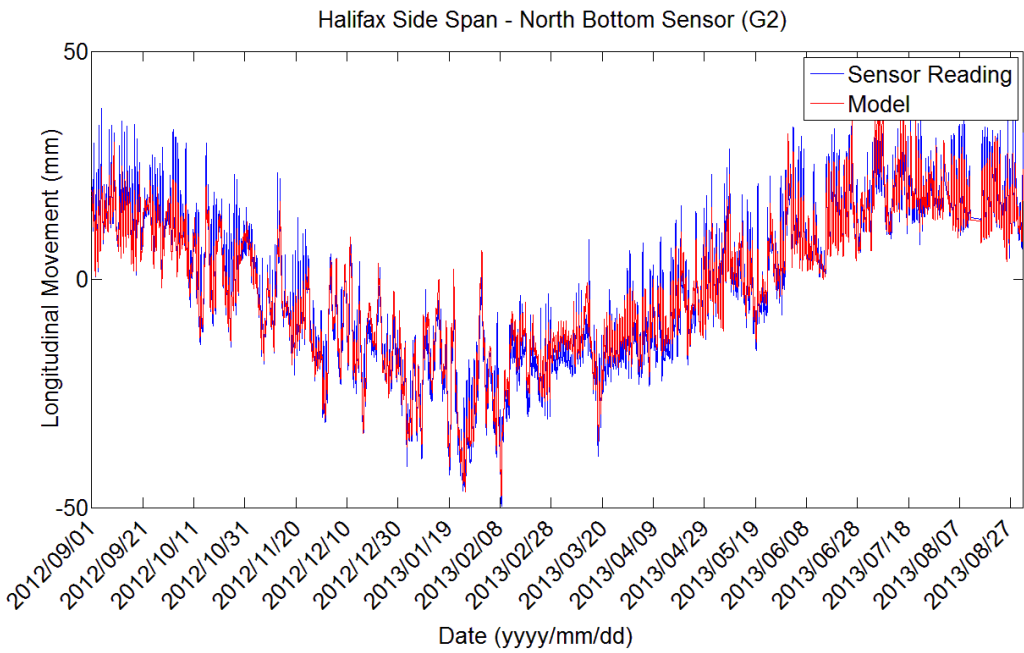**Figure F.10**: Model comparison to monitored data, DMT SS Northbot sensor

189

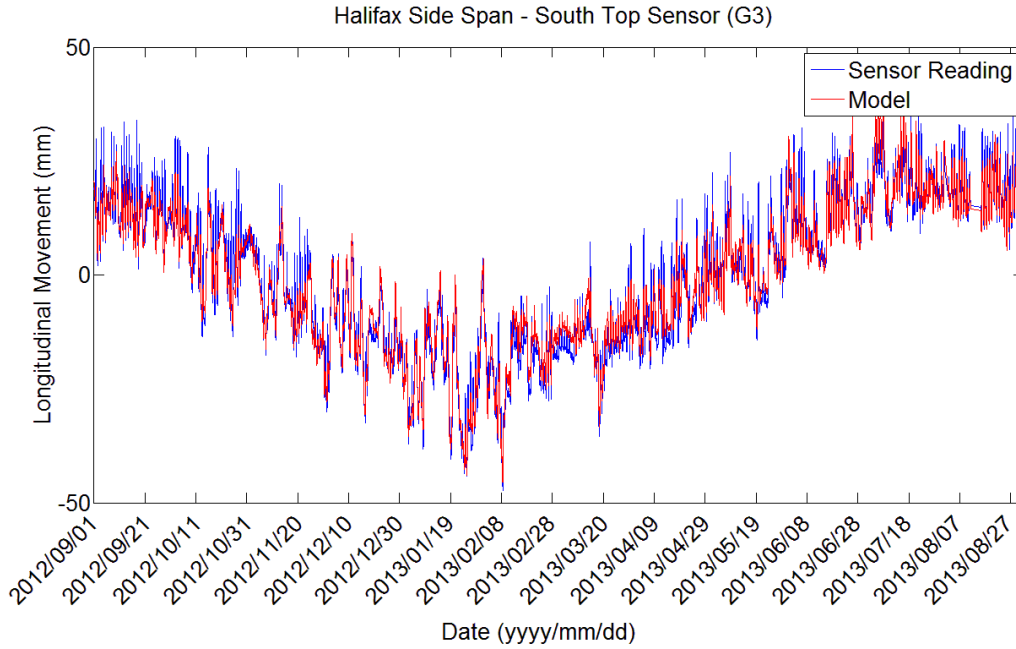**Figure F.11**: Model comparison to monitored data, DMT SS Southtop sensor

Figure F.12: Model comparison to monitored data, DMT SS Southbot sensor
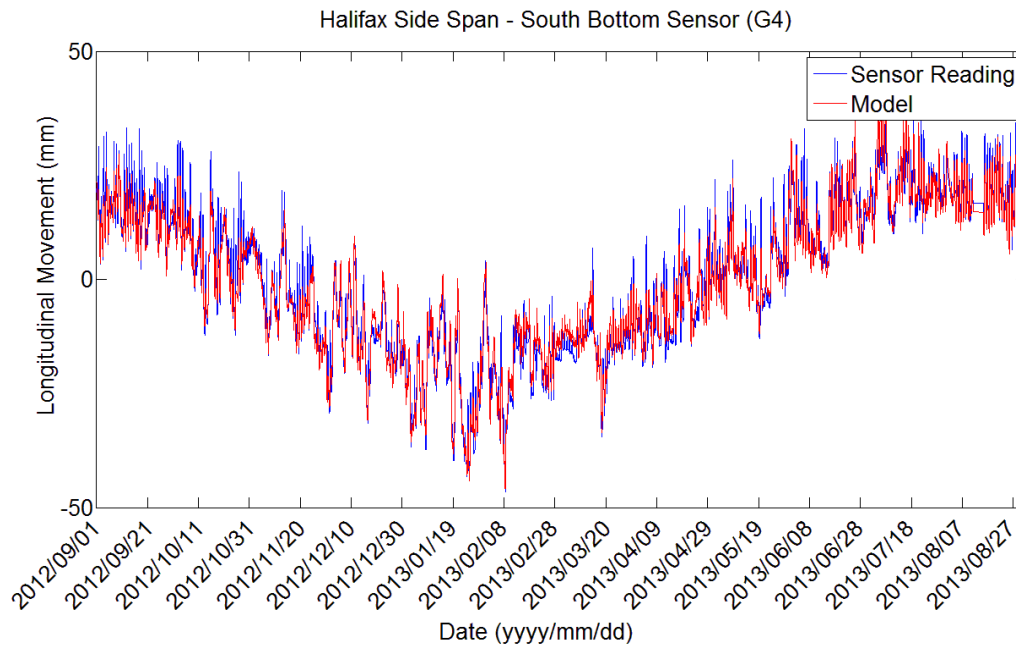
Figure F.13: Model comparison to monitored data, HMT SS Northtop sensor

Figure F.14: Model comparison to monitored data, HMT SS Northbot sensor

Figure F.15: Model comparison to monitored data, HMT SS Southtop sensor

Figure F.16: Model comparison to monitored data, HMT SS Southbot sensor

Table F.1: Distribution of model differences for DMT MS

Difference Bin (mm)	Frequency Count					Percent	
	Northbot	Northtop	Southbot	Southtop	Total		
22.5 to 25	0	0	0	0	0	0	
20 to 22.5	0	2	7	2	11	0	
17.5 to 20	13	12	60	19	104	0	
15 to 17.5	77	48	117	87	329	0	
12.5 to 15	215	211	204	158	788	0	
10 to 12.5	612	585	637	420	2254	1	
7.5 to 10	1027	1096	1475	1266	4864	2	
5 to 7.5	2661	2759	3002	2686	11108	5	
2.5 to 5	7135	8272	7706	7117	30230	14	
0 to 2.5	14000	14162	13991	13195	55348	27	97%
0 to 2.5	14466	13661	13411	14177	55715	27	
2.5 to 5	7098	6394	6865	7519	27876	13	
5 to 7.5	2867	2952	2876	3425	12120	6	
7.5 to 10	1195	1216	1120	1291	4822	2	
10 to 12.5	536	555	472	530	2093	1	
12.5 to 15	220	212	199	242	873	0	
15 to 17.5	69	58	62	69	258	0	
17.5 to 20	22	18	8	10	58	0	
20 to 22.5	0	0	1	0	1	0	
22.5 to 25	0	0	0	0	0	0	

Table F.2: Distribution of model differences for HMT MS

Difference Bin (mm)	Frequency Count					Percent	
	Northbot	Northtop	Southbot	Southtop	Total		
22.5 to 25	0	0	0	0	0	0	
20 to 22.5	0	0	1	1	2	0	
17.5 to 20	14	5	9	6	34	0	
15 to 17.5	54	32	39	16	141	0	
12.5 to 15	173	117	150	146	586	0	
10 to 12.5	583	532	442	510	2067	1	
7.5 to 10	2006	1907	1651	2262	7826	4	
5 to 7.5	5040	5123	4503	5745	20411	10	
2.5 to 5	9362	9419	8763	10189	37733	18	
0 to 2.5	10949	11280	11006	11052	44287	21	95%
0 to 2.5	9577	9769	10037	9029	38412	19	
2.5 to 5	6476	6478	6890	5960	25804	12	
5 to 7.5	3853	3352	3979	3241	14425	7	
7.5 to 10	1902	2044	2137	1862	7945	4	
10 to 12.5	971	881	1144	886	3882	2	
12.5 to 15	414	391	536	433	1774	1	
15 to 17.5	185	192	214	180	771	0	
17.5 to 20	36	82	86	94	298	0	
20 to 22.5	22	23	38	13	96	0	
22.5 to 25	17	7	6	9	39	0	

Table F.3: Distribution of model differences for DMT SS

Difference Bin (mm)	Frequency Count					Percent	
	Northbot	Northtop	Southbot	Southtop	Total		
17.5 to 20	0	0	0	0	0	0	
15 to 17.5	0	0	0	0	0	0	
12.5 to 15	4	13	7	1	25	0	
10 to 12.5	25	32	45	35	137	0	
7.5 to 10	90	142	137	133	502	0	
5 to 7.5	315	558	463	432	1768	1	
2.5 to 5	11020	16401	13056	11715	52192	25	
0 to 2.5	15257	13039	16668	15831	60795	29	91%
0 to 2.5	9987	8243	10033	9952	38215	18	
2.5 to 5	10876	9699	9116	10291	39982	19	
5 to 7.5	2591	2222	1801	2240	8854	4	
7.5 to 10	1374	1202	692	1067	4335	2	
10 to 12.5	536	515	177	435	1663	1	
12.5 to 15	125	127	16	71	339	0	
15 to 17.5	11	18	1	9	39	0	
17.5 to 20	0	0	0	0	0	0	

Table F.4: Distribution of model differences for HMT SS

| Difference Bin (mm)	Frequency Count					Percent	
	Northbot	Northtop	Southbot	Southtop	Total		
17.5 to 20	0	0	0	0	0	0	
15 to 17.5	0	0	0	0	0	0	
12.5 to 15	6	3	4	6	19	0	
10 to 12.5	0	0	0	0	0	0	
7.5 to 10	371	320	307	244	1242	1	
5 to 7.5	1412	1181	1226	1394	5213	3	
2.5 to 5	8263	7676	7229	8839	32007	15	
0 to 2.5	18481	18479	15654	17164	69778	34	90%
0 to 2.5	14184	14406	16327	14443	59360	29	
2.5 to 5	5227	5096	7545	5873	23741	11	
5 to 7.5	2286	2636	2530	2459	9911	5	
7.5 to 10	1000	1300	588	853	3741	2	
10 to 12.5	288	388	186	268	1130	1	
12.5 to 15	106	117	39	90	352	0	
15 to 17.5	13	35	2	4	54	0	
17.5 to 20	0	0	0	0	0	0	

Appendix G – Live Load Gumbel Plots
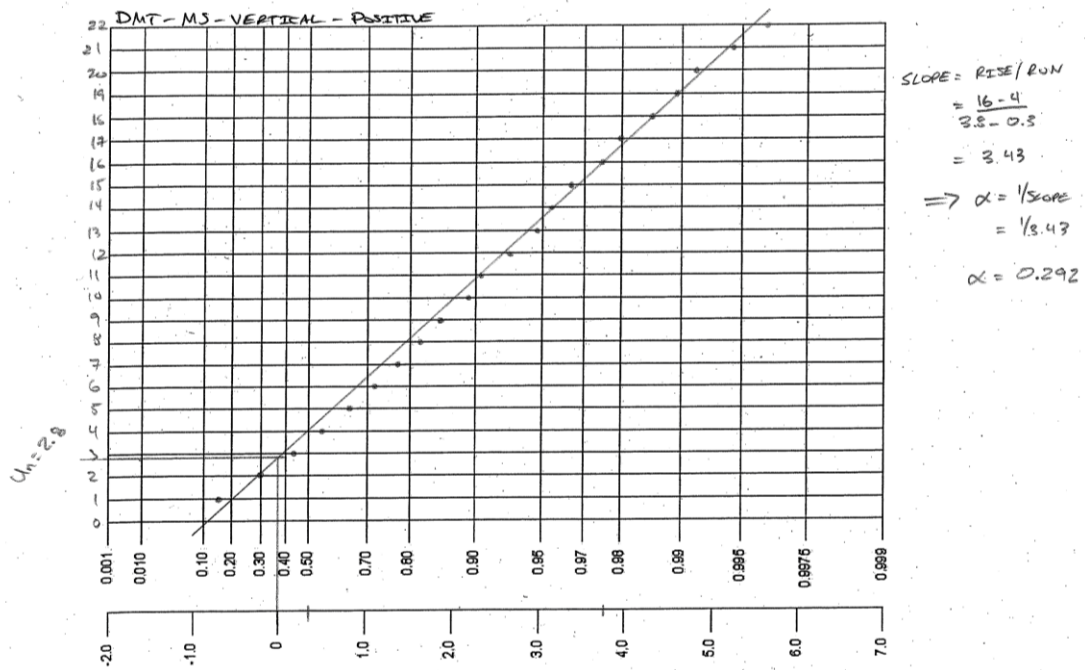
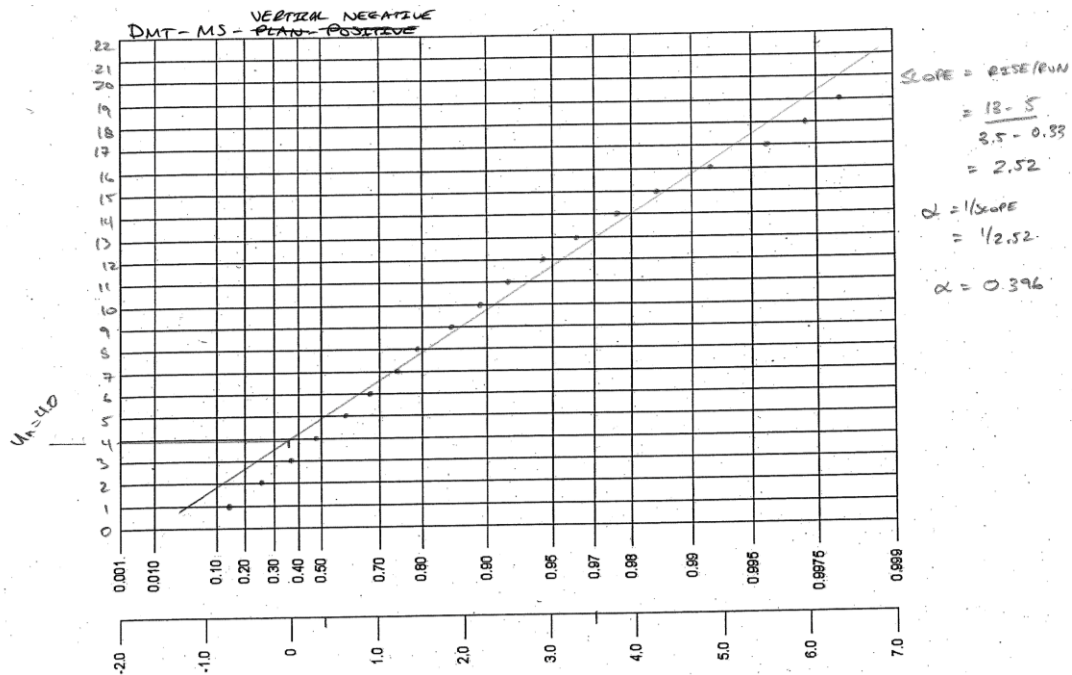**Figure G.1** –Determination of Gumbel parameters, DMT MS Positive Vertical Rotation

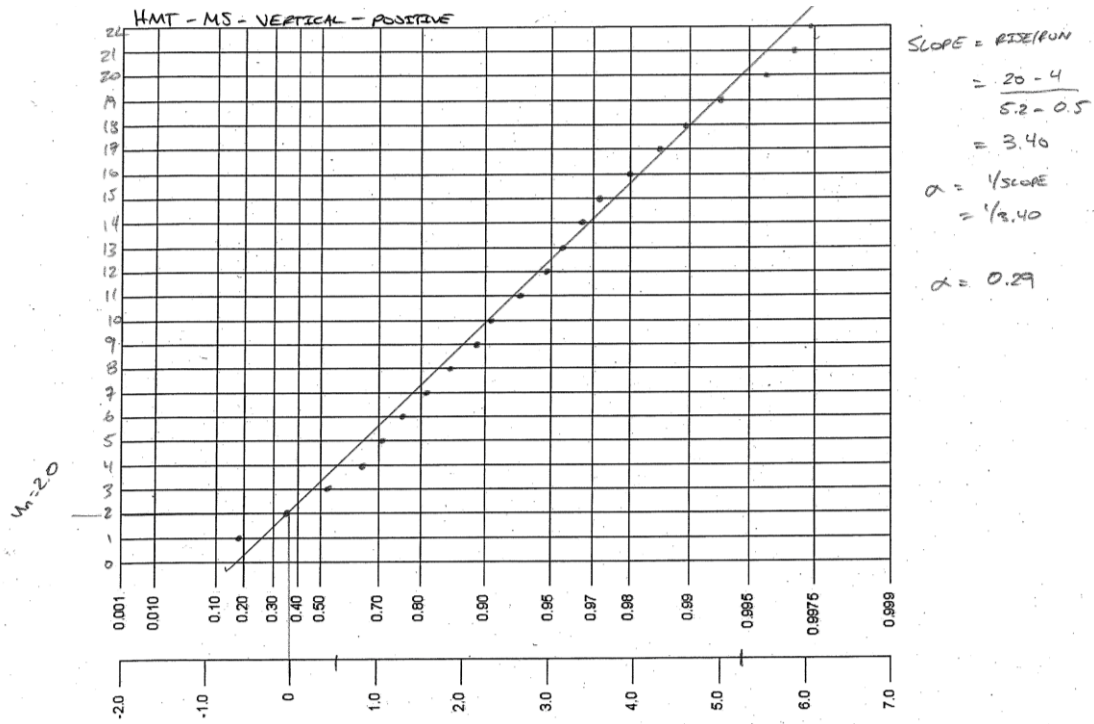**Figure G.2** –Determination of Gumbel parameters, DMT MS Negative Vertical Rotation

Figure G.3 –Determination of Gumbel parameters, HMT MS Positive Vertical Rotation
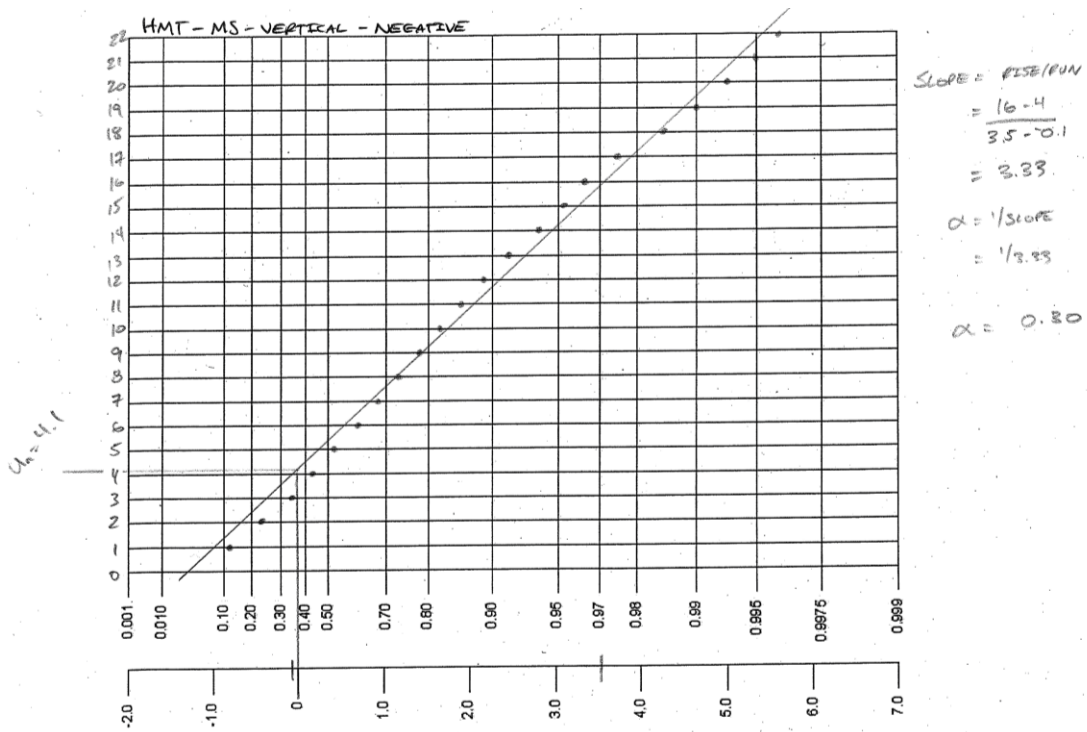

Figure G.4 –Determination of Gumbel parameters, HMT MS Negative Vertical Rotation
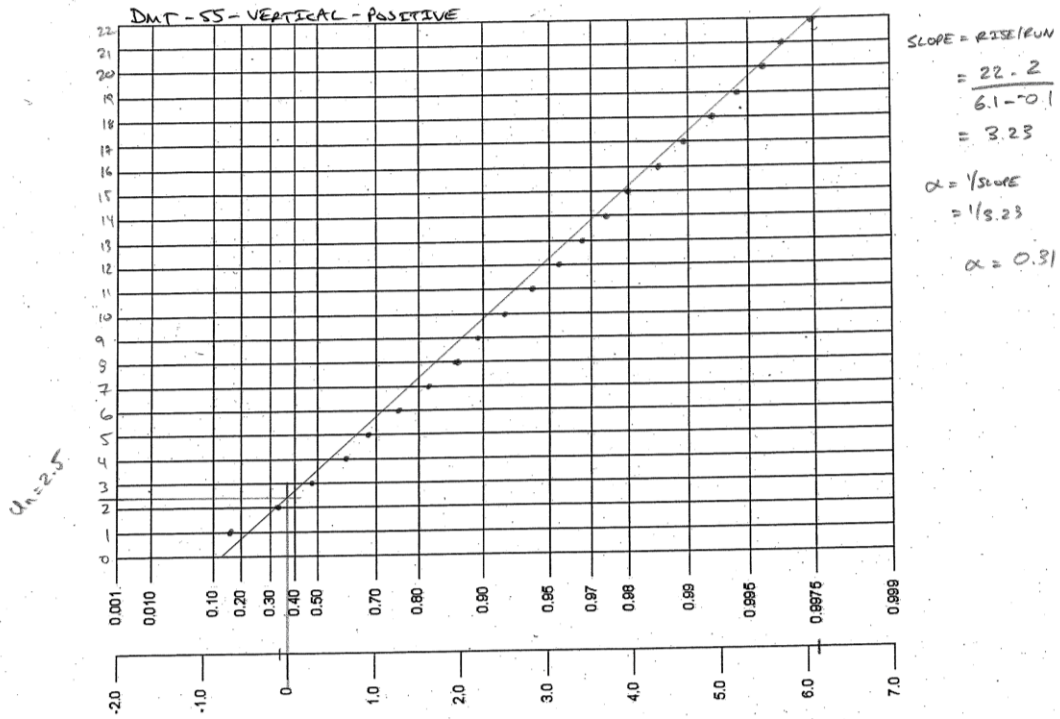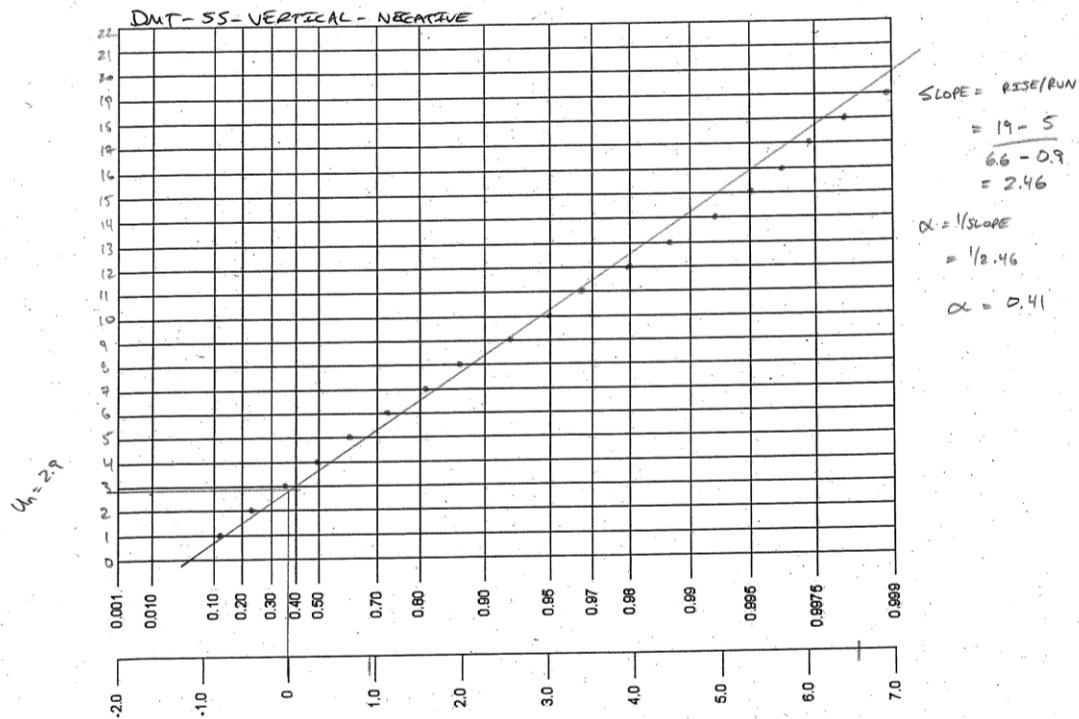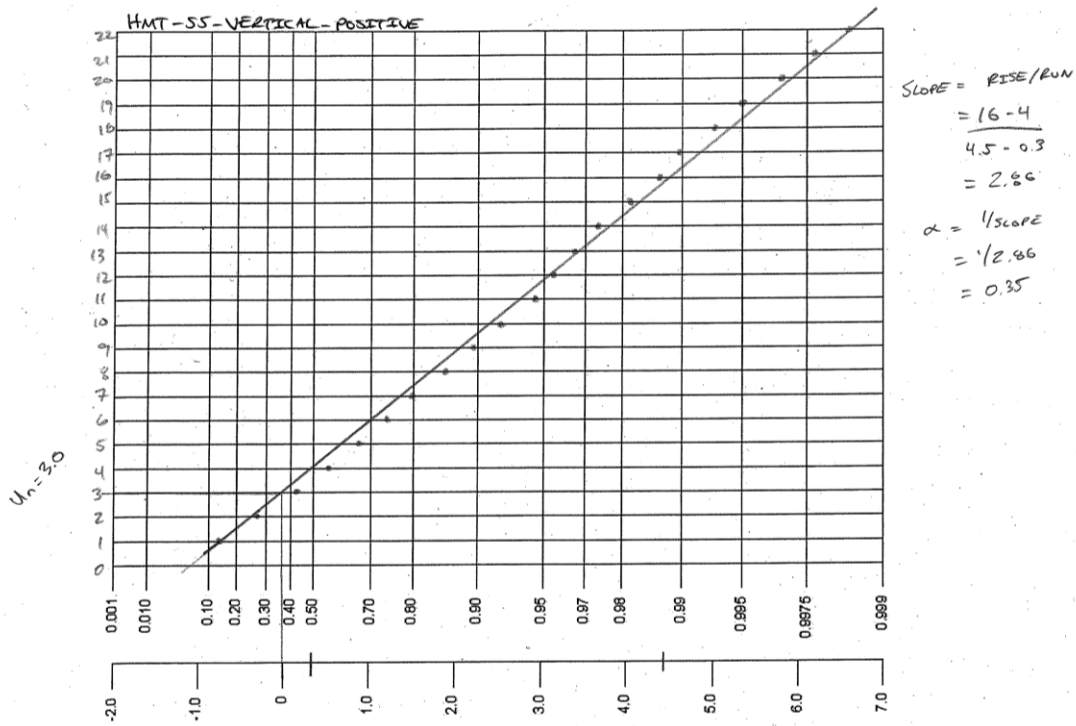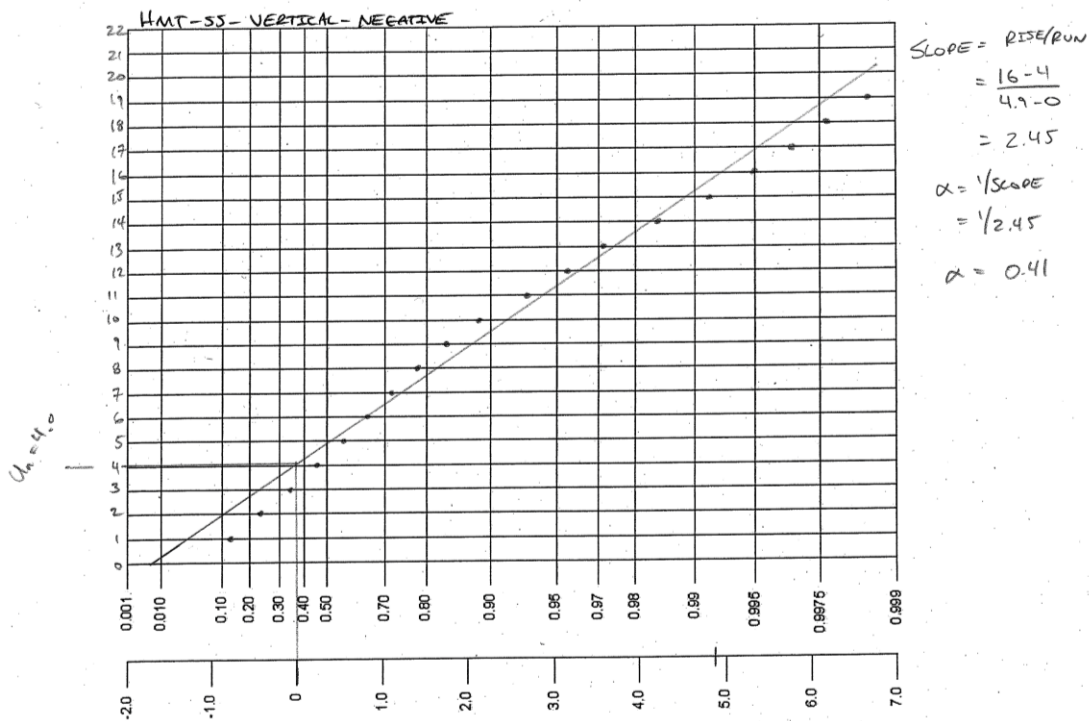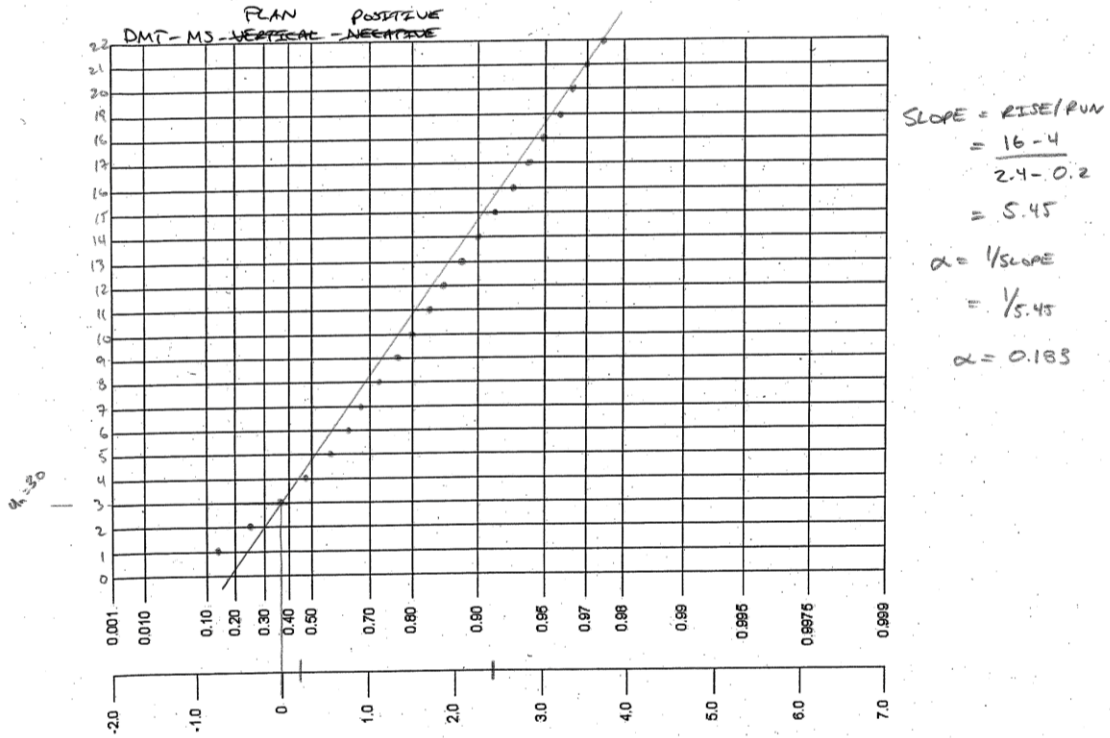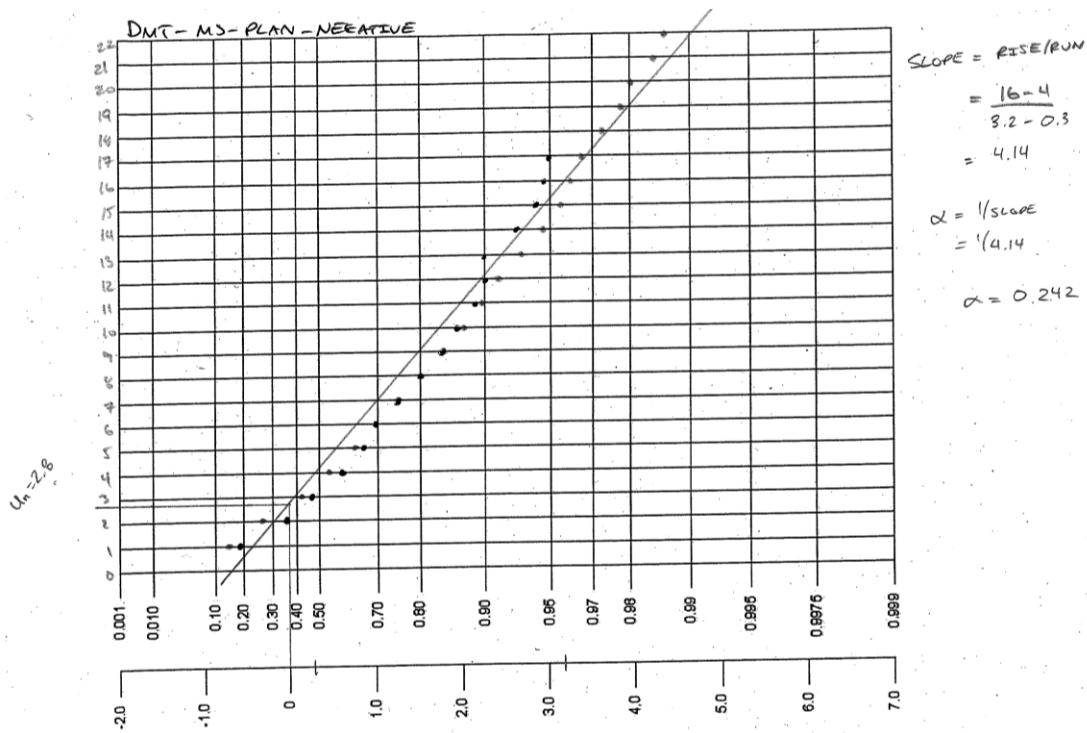
Figure G.5 –Determination of Gumbel parameters, DMT SS Positive Vertical Rotation

Figure G.6 –Determination of Gumbel parameters, DMT SS Negative Vertical Rotation
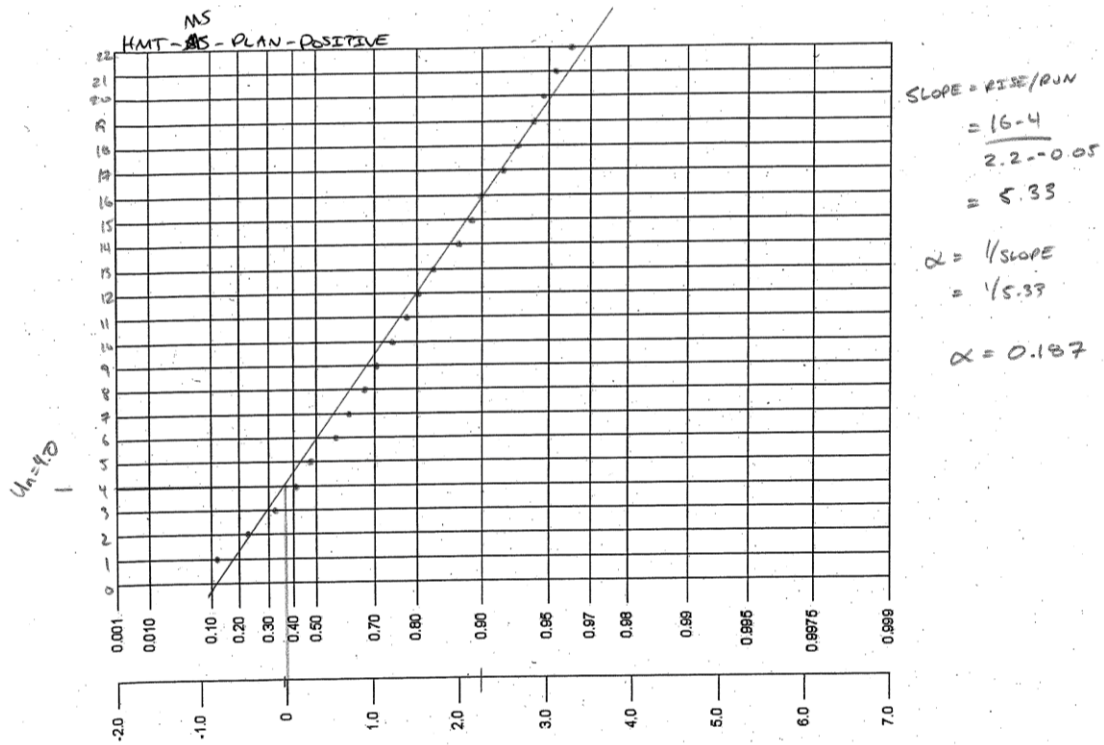
Figure G.7 –Determination of Gumbel parameters, HMT SS Positive Vertical Rotation

Figure G.8 –Determination of Gumbel parameters, HMT SS Negative Vertical Rotation

199

Figure G.9 –Determination of Gumbel parameters, DMT MS Positive Plan Rotation

Figure G.10 –Determination of Gumbel parameters, DMT MS Negative Plan Rotation

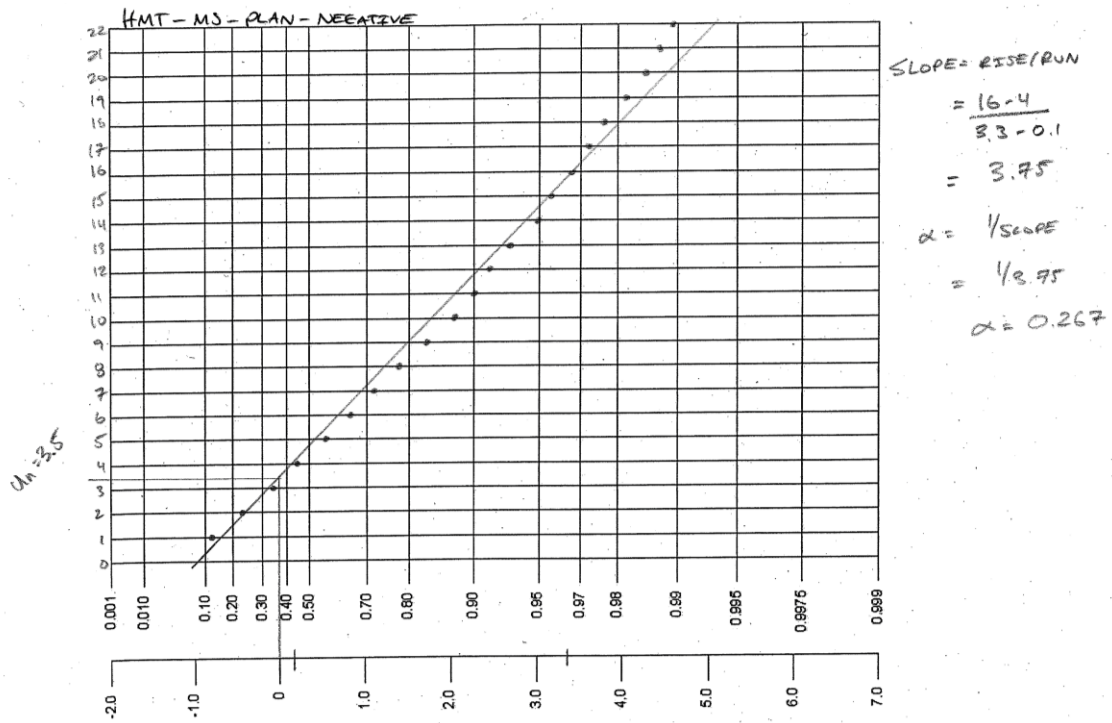**Figure G.11** –Determination of Gumbel parameters, HMT MS Positive Plan Rotation

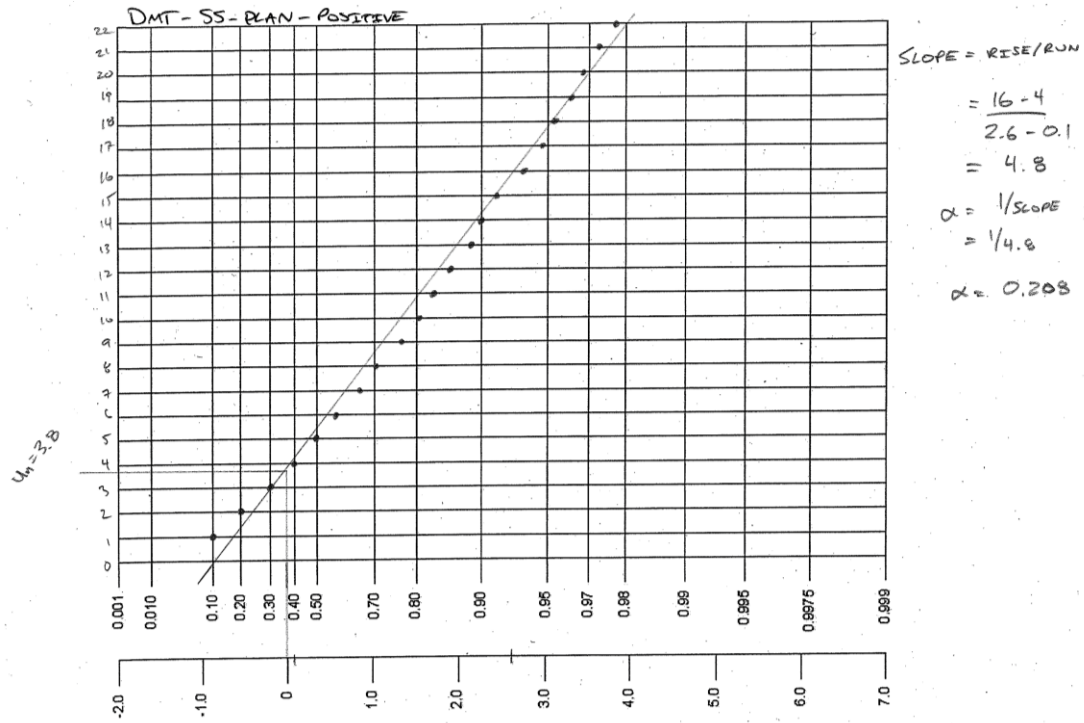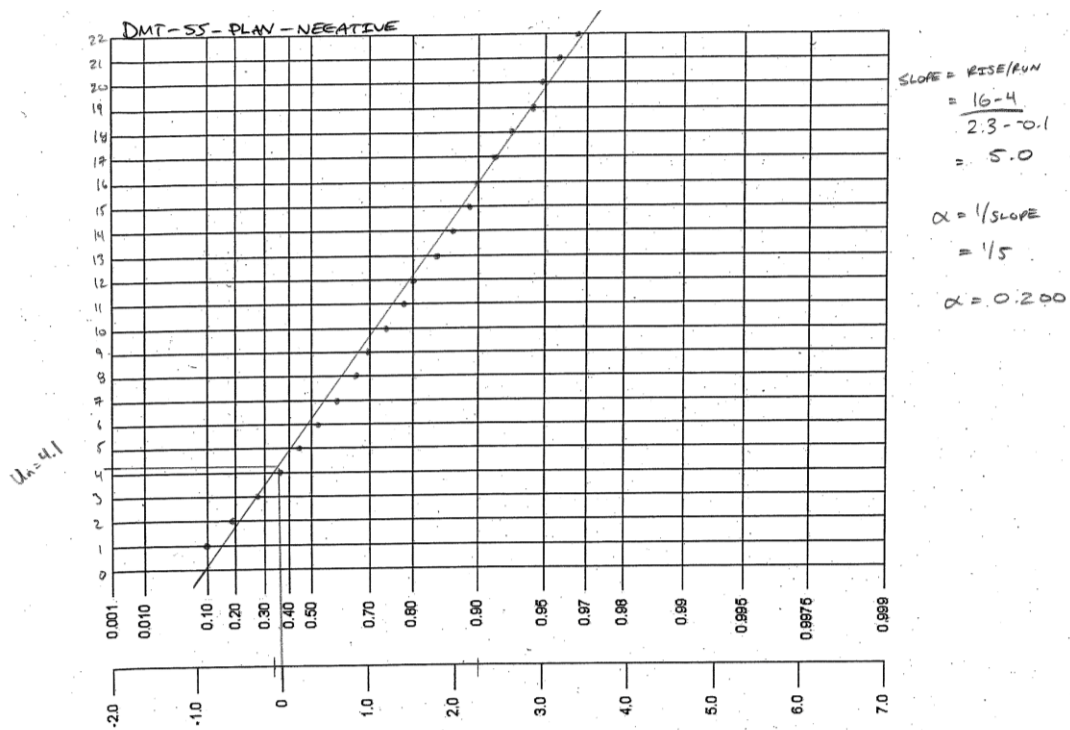**Figure G.12** –Determination of Gumbel parameters, HMT MS Negative Plan Rotation

201

Figure G.13 –Determination of Gumbel parameters, DMT SS Positive Plan Rotation

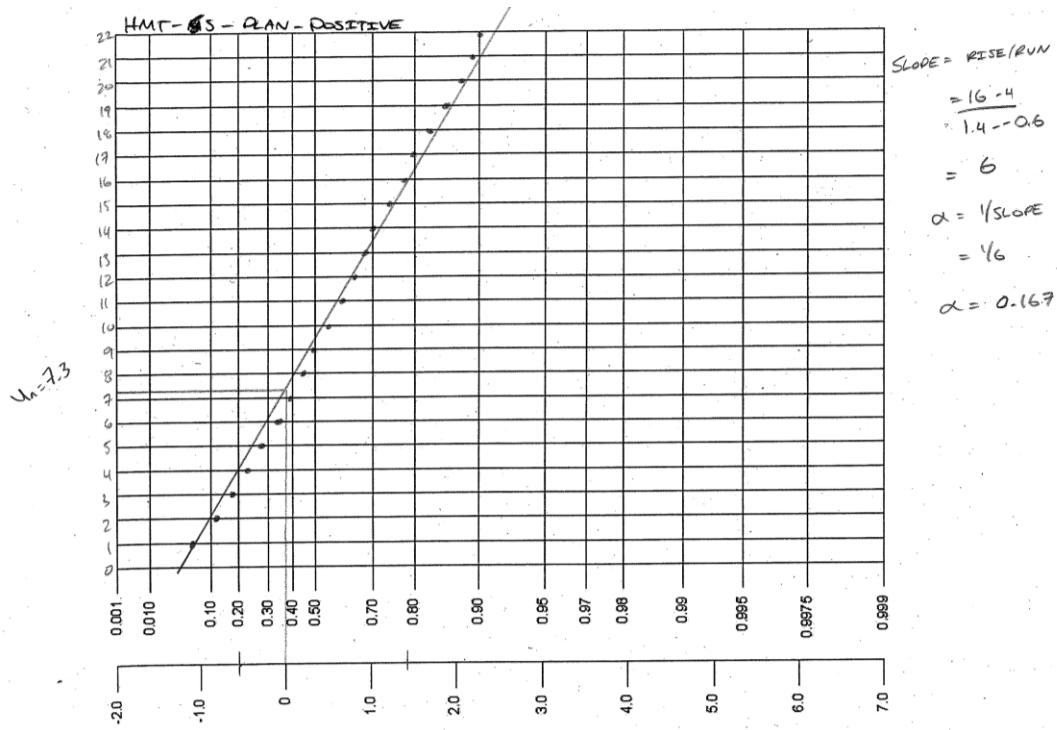**Figure G.14** –Determination of Gumbel parameters, DMT SS Negative Plan Rotation

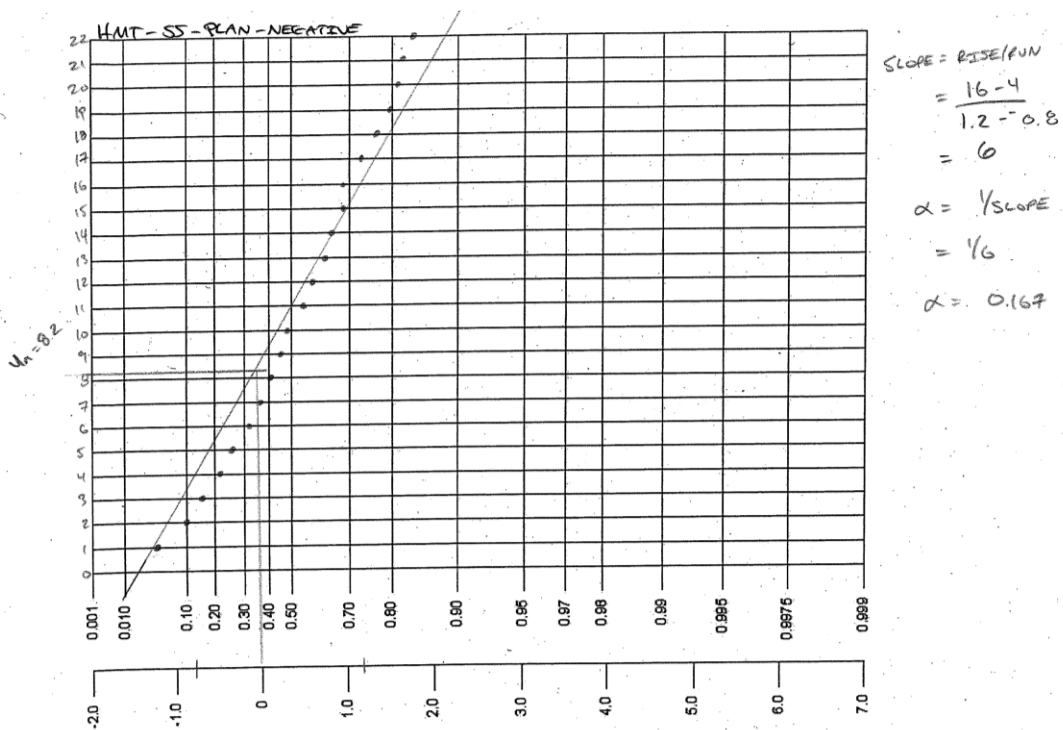**Figure G.15** –Determination of Gumbel parameters, HMT SS Positive Plan Rotation

Figure G.16 –Determination of Gumbel parameters, HMT SS Negative Plan Rotation